Numerical modeling of ODS steel tubes pilgering

Esteban Vanegas

ParisTech
INSTITUT DES SCIENCES ET TECHNOLOGIES
PARIS INSTITUTE OF TECHNOLOGY

MINES ParisTech

Ecole doctorale n°364 : Sciences fondamentales et appliquées

Doctorat ParisTech

T H È S E

pour obtenir le grade de docteur délivré par

l'École nationale supérieure des mines de Paris

Spécialité "Mécanique Numérique"

présentée et soutenue publiquement par

Esteban VANEGAS MARQUEZ

le 13 décembre 2011

Numerical modeling of ODS steel tubes pilgering
-
Modélisation numérique du laminage à pas de pèlerin de tubes en acier ODS

Directeur de thèse : **Roland LOGÉ**
Co-encadrement de la thèse : **Katia MOCELLIN**

Jury

Mme Anne Marie HABRAKEN, Directrice de Recherches, MS^{2}F-ArGEnCo, Université de Liège	Rapporteur
M. José CESAR DE SA, Professeur, Faculty of Engineering, University of Porto	Rapporteur
M. Jean-Claude GELIN, Professeur, ENSMM	Examinateur
M. Yann de CARLAN, Docteur, Service de Recherches Métallurgiques Appliquées, CEA/Saclay	Examinateur
Mme Katia MOCELLIN, Docteur, CEMEF, Chargée de Recherches, Mines ParisTech	Examinateur
M. Roland LOGÉ Docteur, HDR, CEMEF, Chargé de Recherches CNRS, Mines ParisTech	Examinateur
Mme Élise DÉLOYE, Docteur, Valinox Nucléaire	Invité

MINES ParisTech
CEMEF – UMR CNRS 7635
1 Rue Claude Daunesse BP 207 06904 Sophia-Antipolis Cedex, France

T H E S E

Remerciements

Cette thèse a été effectuée au sein du Centre de Mise en Forme de Matériaux (CEMEF) à Sophia Antipolis (06).

Je tiens à remercier la Direction du CEMEF et plus particulièrement Monsieur Yvan Chastel, pour m'avoir accueilli et donné les moyens de réaliser ce travail.

J'exprime toute ma gratitude à Katia Mocellin et Roland Logé, mes directeurs de thèse. Merci de m'avoir fait confiance en me confiant le travail à effectuer dans le cadre du projet Stratotube. Merci pour votre aide lorsque des problèmes se sont présentés ou lorsqu'il a fallu décider des orientations à suivre.

Merci à Madame Anne-Marie Habraken, Directrice de Recherches, MS^{2}F-ArGEnCo à l'Université de Liège, à Monsieur José CESAR de SA, Professeur à l'Université de Porto, et à Monsieur Jean-Claude Gélin, Professeur à l'ENSMM pour avoir accepté d'être rapporteurs de cette thèse et de faire partie de mon jury de thèse.

Je voudrais également remercier Carole Torrin de l'équipe EII. J'ai été un gros consommateur d'espace disque et de temps CPU.

Merci à Benoit Revil-Baudard pour sa collaboration fructueuse avec Forge3. Merci à Marie-Cecile Robin et Pierre-Olivier Bouchard qui m'ont initié dans l'intégration de lois de comportement des matériaux.

Je tiens à saluer aussi les contributions de mes collègues au CEMEF tant pour leur apport technique que pour la bonne ambiance de travail qu'ils ont suscitée.

Grand merci à Marie-Francoise Guenegan, Sylvie Massol et Patrick Coels pour tous les services et conseils administratifs. Sylvie Michel pour sa bonne humeur, disponibilité et ses compétences de terrain.

Je n'oublie surtout pas Gilbert Fiorucci et Alain Le Floch qui m'ont été d'une aide précieuse pour la réalisation des essais mécaniques au CEMEF.

Merci aux autres personnes du CEMEF qui m'ont consacré un peu de leur temps lorsque je suis venu leur poser des questions.

Je remercie très sincèrement Monsieur Yann de Carlan, Docteur au sein du CEA/SRMA, pour son aide précieuse et ses conseils durant ce travail. Je tiens particulièrement à lui exprimer ma reconnaissance pour son dévouement et soutien.

Un grand merci à Louise Toualbi qui a répondu à chacune de mes questions, permettant de fructueuses discussions ainsi qu'à Denis Sornin, Patrick Olier et Didier Bossu, dont l'aide a été très efficace dans l'étude du laminoir à pas de pèlerin de type HPTR.

Je remercie Jérémy Veysset par son travail et son implication dans la simulation numérique du laminoir VMR.

Je tiens à saluer aussi les contributions de mes collègues de Valinox Nucléaire, plus particulièrement Elise Déloye, pour leur apport technique et leurs critiques constructives.

J'ai gardé pour la fin des personnes auxquelles je tiens tout particulièrement. Merci à mes parents qui m'ont toujours soutenu et aidé au maximum et sans qui ce travail n'aurait certainement pas vu le jour. Je souhaite le leur dédier.

Table of content

General introduction

Industrial context

Many of the world's nations, both industrialized and developing, are driving the growth of nuclear energy. The Generation IV International Forum (GIF) is undertaking necessary research and development activities (R&D) to build the next generation of innovative nuclear energy systems. That can replace today's nuclear plants and transition nuclear energy into the long term. Generation IV nuclear energy systems include the nuclear reactor, its energy conversion systems, as well as the necessary facilities for the entire fuel cycle from mineral extraction to final waste disposal.

Six issues are currently under consideration: the new generation reactors have to meet criteria improvements such as safety and reliability of facilities, nuclear non-proliferation, and waste minimization, while remaining profitable and competitive economically. The fast reactor sodium-cooled liquid (SFR) is the reference technology for the fourth-generation reactor program.

In this context, many studies are directed toward the development of innovative metallic materials, fulfilling the design requirements for fission nuclear reactors. Among these are oxide dispersion strengthened (ODS) alloys obtained by powder metallurgy, which are of interest as structural materials due to their creep rupture strength at high temperature and their resistance to severe neutron exposure, compared to the, e.g. conventional ferritic steels. For new fast-neutron sodium-cooled Generation IV reactors, the candidate cladding materials for the very strong rates of combustion are the ferritic and martensitic ODS grades. Classically, the cladding tube is cold formed by a sequence of cold pilger rolling passes with intermediate heat treatments.

It is in this context that Valinox Nucléaire, CEMEF (Center for Material Forming) and CEA (French Alternative Energies and Atomic Energy Commission), gather their efforts and expertise to achieve this ambitious goal. For that purpose, the French National Research Agency (ANR) Stratotube project is a current R&D program within the GIF context. The challenge of this ANR project is to demonstrate the industrial feasibility of thin cladding ODS steel tubes manufacturing.

To produce ODS steel tubes, the Stratotube partners decided to proceed in stages by forming tubes:

i) at the laboratory scale
ii) at the industrial scale

This study focuses on an accurate comprehension of the mechanical behavior of ODS steel tubes under the complex solicitation of the pilgering process at both laboratory and industrial scales. Experiments as well as numerical simulations will be used for this purpose. The final objective is the numerical optimization of the process, looking in particular at the cracking risk.

Fuel cladding tube materials

One of the solutions that may be considered for fuel cladding (Fig. 1), is that for which the widest operational feedback is available. Zirconium alloys are currently employed in pressurized-water reactors (PWR), and austenitic steels in fast reactors (FR). These materials do however carry a number of drawbacks: the former may not be used beyond 400℃, while use of the latter is not to be considered at high doses, owing to their swelling under irradiation (see Fig. 2). There is one other major steel class for which behavior under irradiation is well known: ferritic–martensitic steels. These have many advantages, with respect to fuel element cladding. Indeed, as may likewise be seen from Fig. 3, they exhibit outstanding dimensional stability under irradiation due to their body-centered cubic crystallographic structure, and good corrosion resistance in a variety of environments. When strengthened by a nanometric oxide dispersion [de Carlan *et al.*, 2009], [Inoue *et al.*, 2007], their mechanical strength is greatly enhanced, even at very high temperature (1000-1100℃). Materials of this type are commonly known as oxide-dispersion-strengthened (ODS) materials. In ODS steels, fine oxides block the displacement of dislocations, which are responsible for the material plastic deformation.

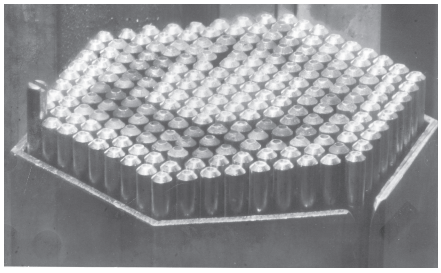

Figure 1. Fuel cladding tube [Dubuisson *et al.*, 2011a].

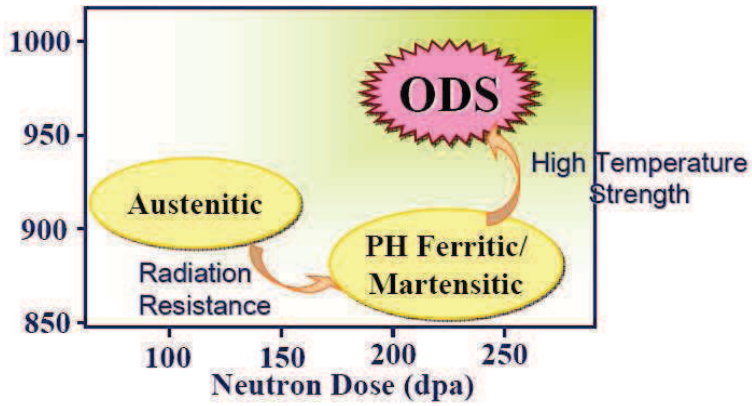

Figure 2. Mechanical performance of several materials as a function of neutron dose and temperature. Oxyde dispersion hardening is effective even over 973 K [Inoue *et al.*, 2007].

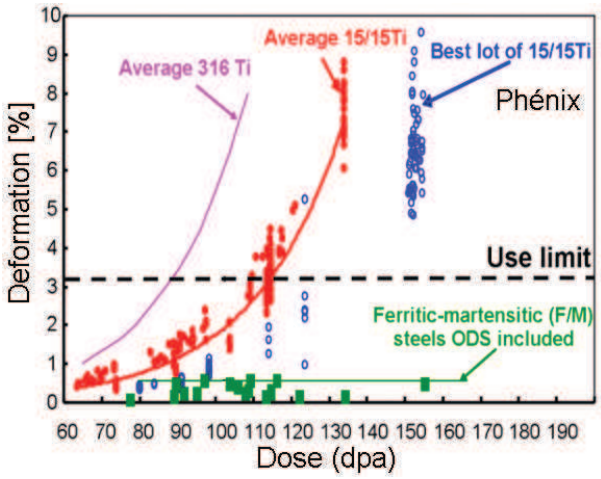

Figure 3. Dimensional evolution, as a function of the dose applied on metallic cladding structures in fuel assemblies used in the core of the Phénix fast reactor [Iracane *et al.,* 2006].

Austenitic steels of the 316Ti type have seen widespread employment, in the past, as cladding "hexagonal" tube material. They have been replaced by an austenitic variant, 15/15Ti, exhibiting slightly greater swelling resistance (see Fig. 3). ODS steels are used for high temperature structural applications and ferritic-martensitic steels have been considered as candidate cladding and structural materials for the Generation-IV fast reactors.

ODS fuel cladding tube forming process

ODS cladding tubes are manufactured by following three main steps [Inoue *et al.*, 2007], [Ratti 2009], [Olier *et al.*, 2009]:

1) Mechanical alloying of the powders.
2) Consolidation of the material usually using hot-extrusion.
3) Manufacturing by means of cold-rolling passes punctuated by intermediate softening heat treatments.

Figs. 4 and 5 set out the schematic for iron-base ODS cladding tube production [Ratti 2009], [Inoue *et al.*, 2007]. First, metal or prealloyed powders, with a few tens of micrometers in diameter, are mixed with a fine yttrium oxide powder, with particle sizes ranging from about 10 nanometers to around 10 micrometers, oxide volume accounting for some 1% of total material volume. These powders are then co-ground, through a succession of mechanical shocks, inside a mill holding grinding balls of various sizes. During this delicate step, which, to a large extent, determines material ultimate quality, the powders are successively work-hardened, welded together, fractured again, welded again and so on. Next, the ground powder is then recovered, and placed in a mild steel container, prior to be carried out using hot extrusion forming, or hot isostatic pressing. This operation allows consolidation of the material, i.e. it makes it possible to obtain, due to the pressure and temperature involved, a material that is dense, free of porosity, and exhibiting a density equivalent to that of a fusion-obtained material [Olier *et al.*, 2009]. During

material consolidation, the dissolved oxides may precipitate again, forming a fine, homogeneous dispersion in the matrix. Depending on consolidation parameters, quality of pulverization, and powder chemical composition, part of the precipitates will be of nanometer size.

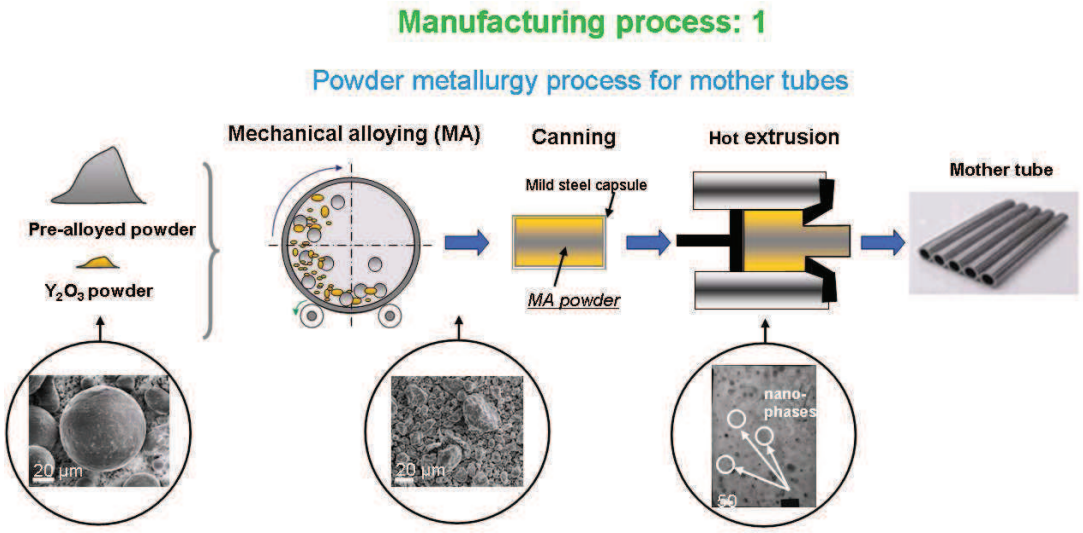

Figure 4. Powder metallurgy for the production of ODS tube from [Ratti 2009].

Subsequently, the cladding tube is cold formed by a sequence of cold pilger rolling passes with intermediate heat treatments. It is on this last stage that this work is focused. The aim is to simulate numerically the forming process.

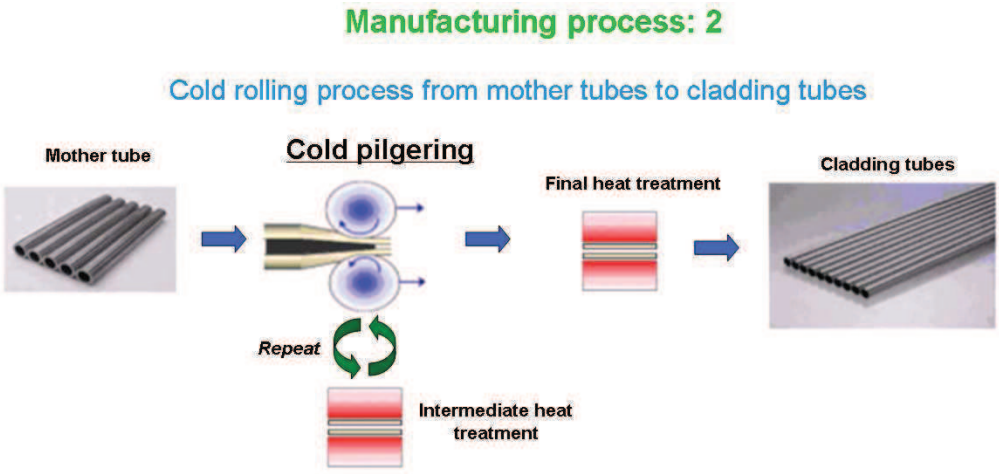

Figure 5. Principle schematic of ODS alloy fabrication through pilgering from [Inoue *et al.*, 2007].

Cold pilgering process

The cold pilgering process is a widespread seamless tube forming operation where the tube is repeatedly rolled over a fixed mandrel by grooved dies. During this process the inner

radius and wall thickness are both progressively reduced. After each back and forth movement (stroke) of the dies, the raw tube is advanced by a small distance and rotated around its axis. It is important that the rotation angle is not multiple of π so as to avoid tube polygonalization. A material volume element undergoes typically several dozens of strokes (see Fig. 6) before deformation is completed [Montmitonnet and Aubin 2008].

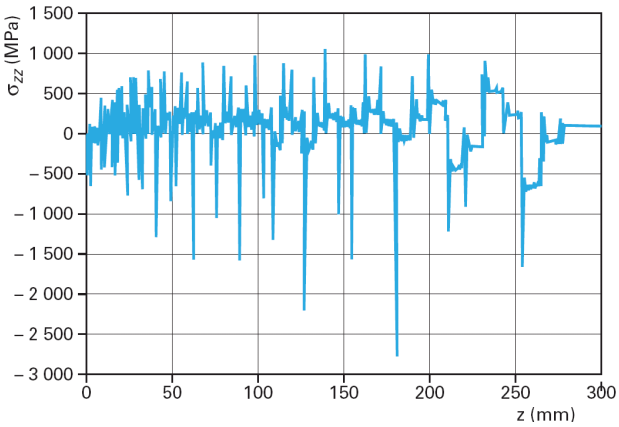

Figure 6. . Axial stress history in pilgering conditions [Montmitonnet and Aubin 2008].

This special forming process is necessary for numerous applications, and cost-effective for many others, for a variety of reasons [Nerino *et al.*, 2011]:

- The cross-section reductions attained are higher than those achieved by other processes. Because the cold pilgering process applies pressure from all sides, it can achieve reductions up to 90 percent for copper; 80 percent for stainless steel, nickel alloys, and Zircaloy; and 75 percent for high-strength titanium alloys.

- The large cross-section reductions help to limit process-related conversion costs, because cold pilgering eliminates additional processes such as cleaning, annealing, pickling, cutting, handling, and straightening between drawing operations.

- The homogenizing material flow in a circumferential direction facilitates substantial reductions in eccentricity. Experience has shown that the higher the eccentricity of the starting tube, the greater is the improvement in eccentricity by cold pilgering.

- The sequence of forming steps improves roundness, stress homogeneity, and surface roughness. Surface defect depths decreases in proportion to the amount of the wall thickness reduction.

- During cold pilgering, practically no material loss occurs. Only the end faces of the finished tubes are out of shape and have to be cut off.

- The cold pilgering process also tends to result in a high Q factor, which is the ratio of the percentages of wall reduction to mean diameter reduction. This is vital in

zirconium cladding because it increases its durability. For comparison, a Q factor greater than 1 is favorable, and a Q factor above 2.5 is very desirable.

The two most common ways to cold-reduce tubes by compression are VMR[1] and HPTR[2] cold pilgering mills. Although both VMR and HPTR dies reduce tubes via compression rather than tension, the complexity of tooling design and manufacturing varies greatly between these machine types. The variable cross-sectional groove of a VMR die requires special expertise and equipment to be designed and built, as does the matching mandrel (conical mandrel). By contrast, the cams, cylindrical mandrels, and constant cross-sectional grooves of HPTR dies are relatively simpler to design and build (see Fig. 7). This allows the production on conventional machine tools, which gives HPTR die owners much more flexibility on sourcing tooling and modification of tool design.

Figure 7. The variable groove on the VMR die (left) requires complex design and manufacturing technology for both dies and mandrel. By contrast, the simple, constant-cross-section HPTR die (right) and similarly simple cams and mandrels allow themselves to conventional manufacturing technologies [Nerino *et al.*, 2011].

HPTR dies run on the same concept as dough rolling, whereby the rolling pin is pressed down into the dough as it is rolled forward, stretching and flattening the dough at the same time. The HPTR dies act as the rolling pin, the cylindrical mandrel acts as the table, and the cams act as the baker's hands (see Fig. 8). Three dies, each paired with a profiled cam, are arranged in a triangle around the tube in what is called the separator, which is itself contained within the housing. The tube's internal diameter is lubricated before loading, and a cylindrical mandrel is inserted.

[1] Vertikaler Massenausgleich Ringwalzei in german or mill by offsetting vertical grooves of the masses
[2] High Pressure Tube Reducer

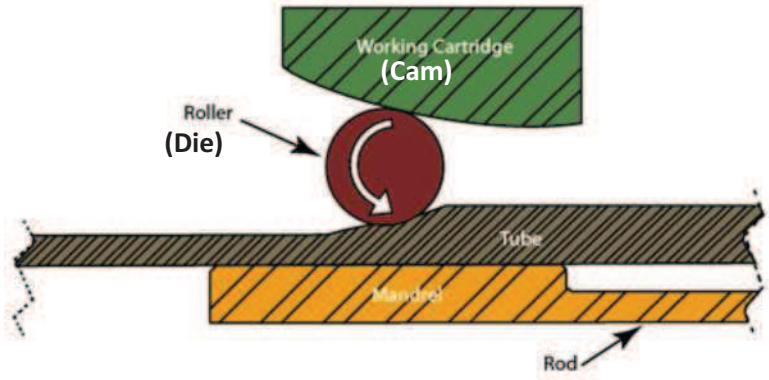

Figure 8. The principle of the HPTR mill's rolling process is based on three components: cams, dies, and mandrel (just one of the three dies is shown here for clarity) [Nerino *et al.*, 2011].

The mill cold-works the tube using a reciprocating motion, following a cycle of four basic steps (see Fig. 9). In step 1, the housing (roller cage) moves forward. This causes the profiled cams (support strap) to push the dies (roller) into the tube, compressing it. In step 2, the housing moves back to the start position, with the dies following the cam until they are once again removed from the tube. In step 3, the tube and mandrel rotate. In step 4, the entire tube is advanced forward slightly. The mandrel is fixed to the rear of the machine and does not advance with the tube. HPTR dies also are capable of producing tubing in special shapes. Among the possibilities are tubes with triangular, square, and hexagonal cross sections.

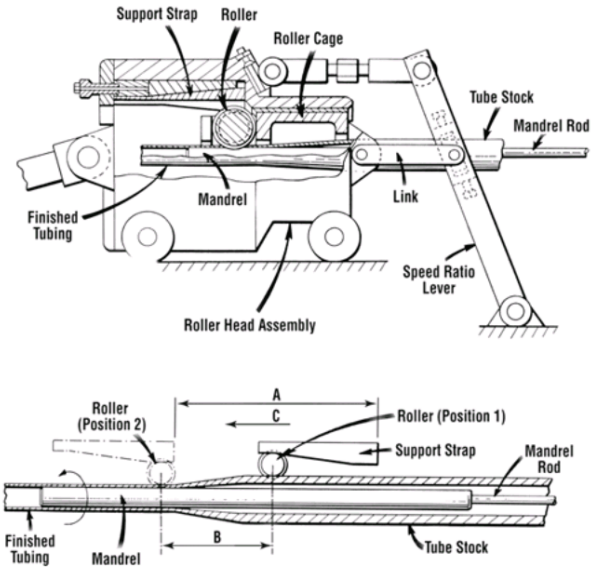

Figure 9. HPTR mill principle of operation [Nerino *et al.*, 2011].

On the other hand, in VMR cold pilgering, the external surface is shaped by two dies with non-axisymmetric grooves, located in a back-and-forth-moving. The die rotation and translation are synchronized by a rack-and-pinion system (see Fig. 10), giving roughly a rolling-without-sliding movement pressing the tube between the die groove and the mandrel. The internal surface is calibrated by a horizontal axisymmetric conical mandrel, held by a mandrel rod. The

evolution of its diameter along the rolling direction ("profile") is one of the parameters controlling the final tube quality. The conjugation of the mandrel profile and the die groove profile controls the evolution of diameter and thickness of the tube. After each back-and-forth movement of the dies, a small length of the tube is fed forward few millimeters and rotated.

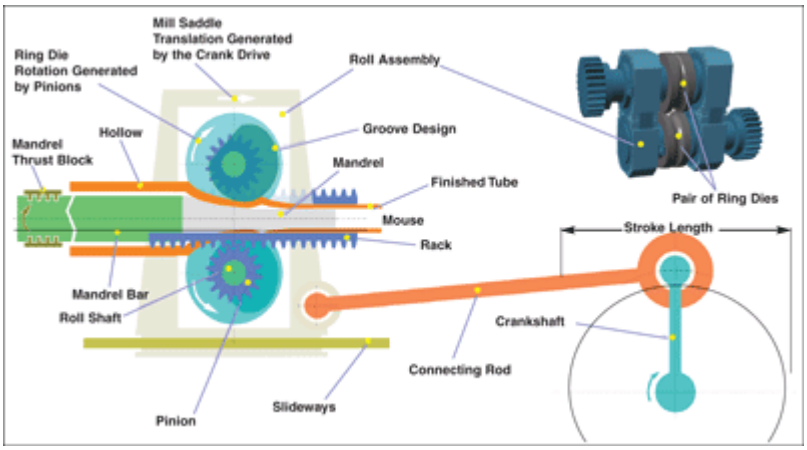

Figure 10. VMR mill principle of operation [Strehlau 2006].

While HPTR dies are simpler in design and operation than VMR dies (Fig. 11), they cannot match the output rates of VMR. As such, modern, high-speed VMR pilger machines have largely taken over the role of HPTR pilger machines in cladding production, as well as other products for which production speed and quantity are important. Sometimes, the HPTR pilger machine is employed in the later cold work passes.

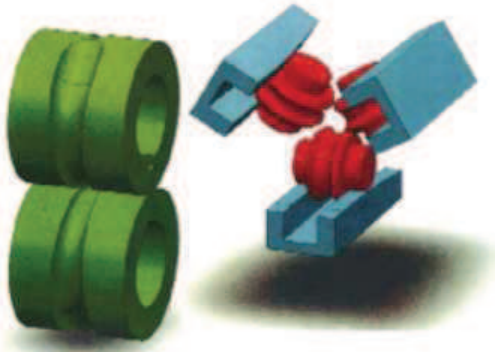

Figure 11. The grooves of VMR dies have a varying cross-section (left). HPTR die (right) has grooves with a single, constant cross section [Nerino *et al.*, 2011].

Fig. 12 displays a comparison between the two cold pilgering processes, i.e. VMR and HPTR.

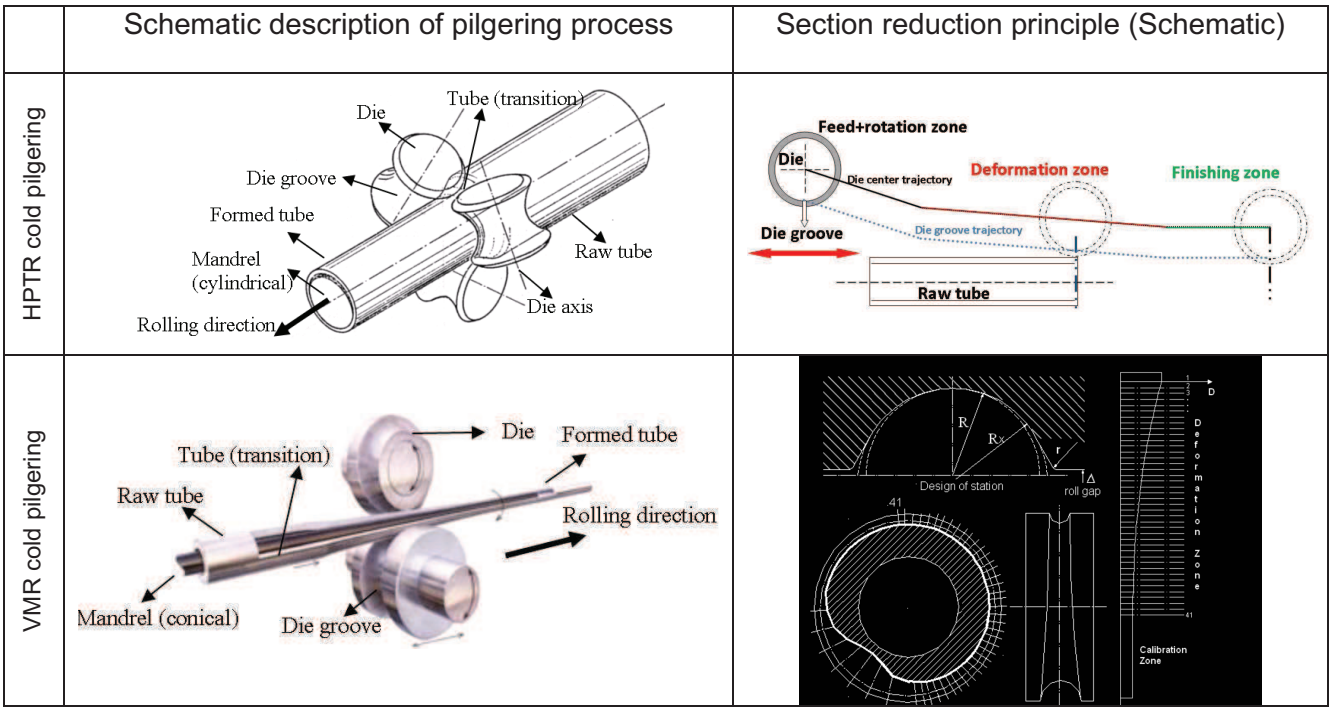

Figure 12. VMR and HPTR pilgering process comparison [Strehlau 2006], [Karas].

Cold pilgering processes induce morphological and crystallographical texture modifications. Grains are elongated by quasi-uniaxial deformation leading to strength anisotropy (see Fig. 13). Moreover, strain hardening due to cold work increases hardness. Therefore, intermediate heat-treatments are necessary to soften the material. Based on previous studies for ODS steels a hardness value below 400 H_{V1} is needed to avoid damage during manufacturing [Inoue *et al.*, 2007].

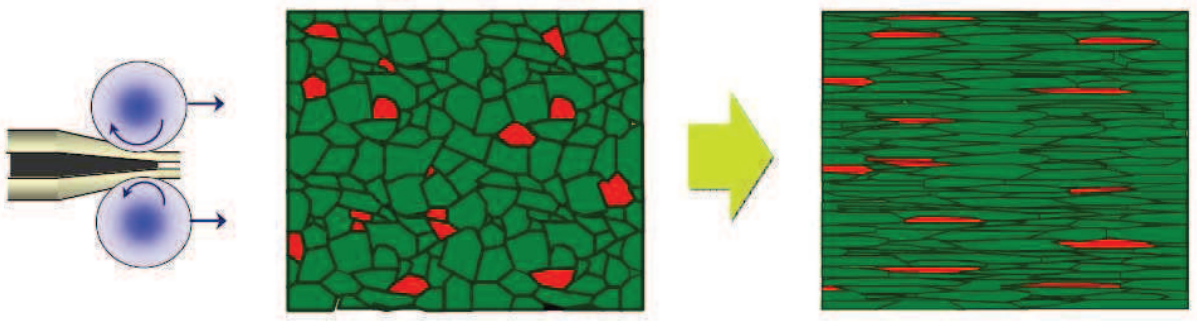

Figure 13. Grains are elongated by uniaxial deformation [Inoue *et al.*, 2007].

Some pilgering process characteristic definitions:

Stroke: corresponds to one back and forth movement of the dies.
Working zone: corresponds to the traveled die distance of one back/forth movement.
Feed increment: tube is moved forward (by small distance) after each stroke.
Rotation angle: tube is turned (by certain angle) after each stroke.
Q *factor:* ratio between thickness reduction and external diameter reduction.

Goals of the thesis

The final objective of this thesis is to investigate the possibility to predict cracking risk from the simulation of ODS tubes HPTR pilgering. For that purpose, it is necessary to model forming operations in a proper way. This requires adaptations and improvements of the Finite Element Method (FEM) software, Forge3®, developed at CEMEF.

Cracking risk prediction in pilgering is linked to the choice of an appropriate constitutive model for modeling the process. Therefore, prior to studying the resistance of ODS steels to this kind of complex, non-proportional multi-axial, and non-periodic cyclic loading using the FEM, a realistic constitutive law is needed.

Furthermore, FEM is quite successful to simulate metal forming processes, but accuracy depends both on (i) constitutive laws and (ii) material parameters identification. Consequently, this thesis aims to assess the impact of the choice of both simulation features and constitutive laws on cracking risk development in pilgering conditions.

The final and robust numerical model will be accurate enough to be used as a design tool for process optimization.

Outline of the study

Considering the previous sections, this work is organized in the following way:

- The following Chapter (Chapter 1) will introduce a bibliographical review useful to understand most of the results presented and discussed in this thesis. Martensitic and ferritic ODS cladding tube manufacturing processes will be addressed first. In a second part, a review will be given for the cold pilgering simulation considering both analytical and FEM (2D and 3D). Special attention is addressed to damage prediction. Finally, the last section will be dedicated to cyclic constitutive laws for both proportional and non-proportional loadings. An effort will be made to highlight the complexity of parameters identification and implementation of some constitutive laws in order to give some clues as how to develop a constitutive model relevant to the pilgering process.

- Chapter 2 is devoted to the mathematical model of forming. The main equations of the discretization by FEM are presented as well as a brief description of the resolution methods used in Forge3®. Subsequently, the results of a complete isotropic simulation of the HPTR cold pilgering will be analyzed. Several sensitivity numerical parameters studies will be presented as well. A comparison between predicted and measured pilgered steady state tube geometry is performed in the last section of Chapter 2.

- ODS steels are considered in this study and a complete understanding of theirs mechanical behavior is required. Hence, mechanical tests in monotonic loadings (classical tensile or compression tests plus shear test), cyclic loadings (classical tension-

compression plus original compression-compression tests), are investigated in Chapter 3. Monotonic and cyclic behaviors are discussed, together with the role of mechanical anisotropy. Different constitutive laws are tested, and calibrated based on the experimental results. Parameters identification is discussed in some details.

- In Chapter 4 a number of experimental observations have been performed (longitudinal strain, number of pilgering marks, micro-hardness) that provide relevant data in order to validate the choice of the constitutive law. Additionally, a deep analysis of the HPTR pilgering process is performed considering each of the constitutive laws identified in Chapter 3. Strains and stresses histories are discussed in detail, together with their probable consequences on the damage, to be correlated with the ODS steel cracking risk.

Chapter 1

Bibliography review

1.1 Introduction

ODS alloys were first developed for gas-turbine aerospace applications because of their very high mechanical strength and corrosion resistance properties at elevated temperature. The high-temperature strength of ODS alloys is due to the presence of fine, stable and uniformly distributed oxide particles which produce direct strengthening by acting as barriers to dislocation motion [Turker and Hughes 1995]. ODS steels are being developed and investigated for nuclear fission and nuclear fusion applications in Japan, Europe, and the United States of America. In addition, commercial ODS products, such as MA957, MA956 and PM2000, are available and have been used in niche applications [Klueh *et al.*, 2005].

Fundamental studies concerning optimization of the mechanical alloying (MA) process as well as effects of alloying elements on high temperature mechanical strength were carried out in cooperation with industrials companies [Ukai *et al.*, 1998]. Based on the results of these studies, the manufacturing of thin-walled cladding tubes was initially attempted using hot extrusion and warm rolling processes in 1989 [Ukai *et al.*, 1998]. Research and development of the ODS ferritic/martensitic steels started in 1987 [Ukai *et al.*, 1998], [Inoue *et al.*, 2008]. Mechanical properties of the tubes have been extensively tested in air and stagnant sodium environments to establish material strength for fuel pin mechanical design. Many works were conducted to develop ODS materials for nuclear applications [Ukai *et al.,* 1993a], [Ukai *et al.,* 1993b], [Ukai and Fujiwara 2002], [Ukai and Ohtuska 2007], [de Carlan *et al.*, 2009], [Fazio *et al.*, 2009], [Dubuisson *et al.*, 2011b], [Kimura *et al.*, 2011], [Baluc *et al.*, 2011]. Specific studies were conducted to propose tube fabrication routes for ODS materials, taking into account the metallurgy of ODS alloys [Ukai *et al.*, 2002], [Ukai *et al.*, 2004], [Narita *et al.*, 2004], [Toualbi *et al.*, 2011], but the determination of constitutive laws to model the cold forming of ODS alloys is a new challenge to improve these fabrication routes. Indeed, ODS constitutive models under cyclic/monotonic loadings are not available at room temperature in the literature, although they are a requisite for the numerical modeling and optimization of cold forming operations.

This bibliography Chapter is organized as follows. In the next section, the ODS ferritic and martensitic cladding tube manufacturing process is described, including the combination of material characteristics. Section 3 is devoted to a general overview of cold pilgering numerical simulation. Section 4 then presents a brief summary of different cyclic constitutive models at room temperature from the simplest to the more complex representation available in the literature.

1.2 ODS cladding tube manufacturing process

The optimization of the fabrication route at the laboratory scale is in progress at the French Alternative Energies and Atomic Energy Commission (CEA) from an experimental and metallurgical point of view. After a few rolling passes, it is necessary to restore the microstructure. Its evolution is closely related to the plastic deformation imposed on the ODS tube material. Heat treatment is performed to reduce the hardness to a level low enough (typically below 400 Hv_1) to

ensure cold forming without risk of tube cracking [Inoue *et al.*, 2007]. The intermediate heat treatments performed during the fabrication are strongly linked to the chemical composition and have a crucial influence on the microstructural and mechanical properties of the final tube [Toualbi *et al.*, 2011]. The alternate thermo-mechanical treatments and deformation steps have to be adjusted to determine a robust fabrication route which allows the manufacturing of ODS cladding tubes with limited crystallographic and morphological anisotropies. Their microstructure depends on the martensitic (Fe-9Cr) or ferritic (Fe-14Cr) structure. Below it is shown that the fabrication route depends on the ODS tube grade.

1.2.1 Martensitic grade

The HPTR cold-rolling process was used by both Japan Nuclear Cycle Development Institute (JNC) and CEA, but the applied fabrication routes included different cross-section reduction ratios, number of passes and intermediate heat treatments.

JNC and CEA independently manufactured the claddings from the same mother tubes of Fe-9CrODS martensitic steel using their own fabrication routes to reach the final dimensions of 6.55 mm outer diameter, 0.45 mm thickness and 1 m length. Fig. 1.1 shows the Fe-9CrODS cladding tube JNC fabrication route. It is composed of 11 cold rolling sequences and 4 heat treatments. Fig. 1.2 shows the Fe-9CrODS cladding tube CEA fabrication route. It is composed of 8 cold rolling sequences and 4 heat treatments.

Process	Tube size	Rd (%)	Temperature (°C)	Time (min)	Hardness (H_v)
CM2 mother tubes	*18.0 mm OD×2.00 mm TH*				*278*
Cold rolling (1st)	16.5 mm OD×1.77 mm TH	18.4			435
Cold rolling (2nd)	15.1 mm OD×1.55 mm TH	19.9			444
Cold rolling (3rd)	13.6 mm OD×1.35 mm TH	21.0			457
Heat treatment (1st)			*1050*	*60 (FC)*	*410*
Cold rolling (4th)	12.3 mm OD×1.16 mm TH	21.9			457
Cold rolling (5th)	11.1 mm OD×1.00 mm TH	21.9			452
Cold rolling (6th)	10.0 mm OD×0.86 mm TH	22.3			473
Cold rolling (7th)	9.2 mm OD×0.77 mm TH	16.9			464
Heat treatment (2nd)			*1050*	*60 (FC)*	*414*
Cold rolling (8th)	8.4 mm OD×0.68 mm TH	19.9			432
Cold rolling (9th)	7.5 mm OD×0.58 mm TH	22.6			467
Cold rolling (10th)	6.7 mm OD×0.49 mm TH	24.6			464
Heat treatment (3rd)			*1050*	*60 (FC)*	*380*
Cold rolling (11th)	6.60 mm OD×0.48 mm TH	4.4			389
Heat treatment (4th)			*1050*	*2 (AC)*	
			750	*60 (AC)*	*368*
Polishing	6.56 mm OD×0.45 mm TH				

FC: Furnace cooling.
AC: Air cooling.

Figure 1.1. Fe-9CrODS cladding tube JNC fabrication route [Ukai *et al.*, 2004].

Process	Tube size	Rd (%)	Temperature (°C)	Time (min)	Hardness (H_v)
CM2 mother tubes	*18.0 mm OD×2.00 mm TH*				*280*
Cold rolling (1st)	15.2 mm OD×1.67 mm TH	30			
Cold rolling (2nd)	12.7 mm OD×1.46 mm TH	27			360
Heat treatment (1st)			*800*	*120*	*347*
Cold rolling (3th)	11.5 mm OD×1.28 mm TH	20			
Cold rolling (4th)	10.0 mm OD×1.04 mm TH	29			355
Heat treatment (2nd)			*800*	*120*	*337*
Cold rolling (5th)	9.0 mm OD×0.86 mm TH	25			
Cold rolling (6th)	8.1 mm OD×0.75 mm TH	21			355
Heat treatment (3rd)			*800*	*120*	*328*
Cold rolling (7th)	7.3 mm OD×0.60 mm TH	27			
Cold rolling (8th)	6.57 mm OD×0.465 mm TH	27			357
Heat treatment (4th)			*1100*	*15 (AC)*	*352*
			750	*60 (AC)*	

Figure 1.2. Fe-9CrODS cladding tube CEA fabrication route [Ukai *et al.*, 2004].

The manufactured cladding tubes exhibited an isotropic grain structure in both longitudinal and transverse cross-sections. Equivalent tensile strength levels were obtained along the axial and radial directions of tubes. This is a very important outcome that assesses the isotropic mechanical behavior of ODS martensitic steels. Similar strength levels in tensile and creep rupture properties were attained for the cladding tubes manufactured by JNC and CEA using HPTR rolling processes, not depending on different fabrication routes.

In [Ukai *et al.*, 2002] and [Ukai *et al.*, 2004] authors proposed manufacturing ranges based on the optimization of thermo mechanical treatments, allowing to both reduce the degree of crystallographic texture in order to ensure the isotropy of mechanical properties of the final tube, and ensure forming without any risk of cracking on the tube.

The authors concluded that the Fe-9CrODS martensitic steels present, during heating, a ferrite to austenite phase transformation around 800 - 900℃ [Ukai *et al.*, 2002]. The critical cooling rate needed to obtain a fully martensitic structure is about 1℃/s. This value implies that only thin products will be easily hardened with a fully martensitic structure. The Y_2O_3 dispersed particles in the matrix stop the grain growth leading to micrometer-sized austenitic grains.

The ferrite to austenite phase transformation, characteristic of martensitic grades, has the advantage of effectively erase the accumulation of work-hardening due to pilgering and deal with a restored material for the next sequence (hardness below 400 Hv_1) as proposed by [Inoue *et al.*, 2007].

Thus, JNC in [Ukai *et al.*, 2004] performed an intermediate heat treatment of 1h at 1050 ℃ carried out every 3 or 4 passes, which reduces t he hardness of around 50 Hv_1. CEA in [Ukai *et al.*, 2004] chose an intermediate heat treatment of 2h at 800 ℃ carried out every 2 passes, allowing a smaller reduction in hardness of about 20 Hv_1. In both cases, intermediate heat treatments are followed by slow cooling so as to ensure a fully ferritic state alloy. This state, which has a hardness lower than the martensitic state, minimizes the risk of cracking during the cold forming [Ukai *et al.*, 2004].

The microstructures observed after the final heat treatment are, in both cases, structured ferritic-martensitic or martensitic, and composed of equiaxed grains. The elongated grain structure was destroyed and rearranged during successive passes in the austenitic phase. Texture measurements before and after thermo-mechanical treatments showed a reduction of the anisotropy of the tube, confirmed by the results of mechanical tests which give equivalent values of yield stress in the radial and longitudinal directions [Ukai *et al.*, 2004]. The ODS martensitic steel tubes produced in this way have a yield stress around 900 MPa at room temperature, and a hardness around 350 Hv_1.

In a more recent work, [Toualbi *et al.*, 2011] studied a fabrication route for a Fe-9CrODS tube. The material was produced by mechanically alloying a pre-alloyed metal powder and an yttrium powder. The resulting powder was sealed into a mild steel can and hot-extruded at a temperature of 1100℃. After degassing, mother tube s with 19mm outer diameter and 2mm wall thickness are obtained. In this work, fabrication routes are determined to reach the final geometry of the cladding tubes: 10,73mm outer diameter and 500µm wall thickness. Cladding tubes were manufactured by means of HPTR cold pilgering. To avoid any damage during cold-working the hardness of the mother tube had to be low enough, therefore, after hot-extrusion the Fe-9CrODS mother tube was homogenized at 1250℃ during 30min and cooled to room temperature with a slow cooling rate of 0.03℃/s. The hardness value o f 250 Hv_1 indicated a ferritic structure which can easily be cold-worked. The mother tube crystallographic texture is shown in Fig. 1.3. The authors concluded that the texture induced by the hot-extrusion process was significantly reduced by the phase transformation characteristic of martensitic grades.

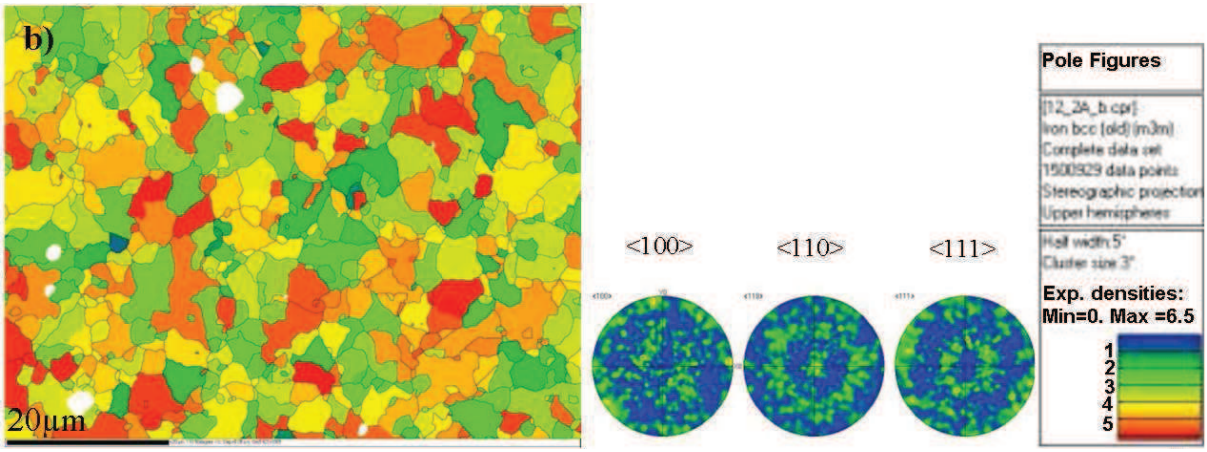

Figure 1.3. EBSD and computed pole figures obtained on the transverse cross-section of mother tube after hot-extrusion and annealing at 1250℃ during 30min [Toualbi *et al.*, 2011].

Fig. 1.4 shows the hardness evolution during the fabrication route used by [Toualbi *et al.*, 2011]. It is noticed in this study that the ferrite to austenite phase transformation allows releasing the internal stresses induced by cold-working.

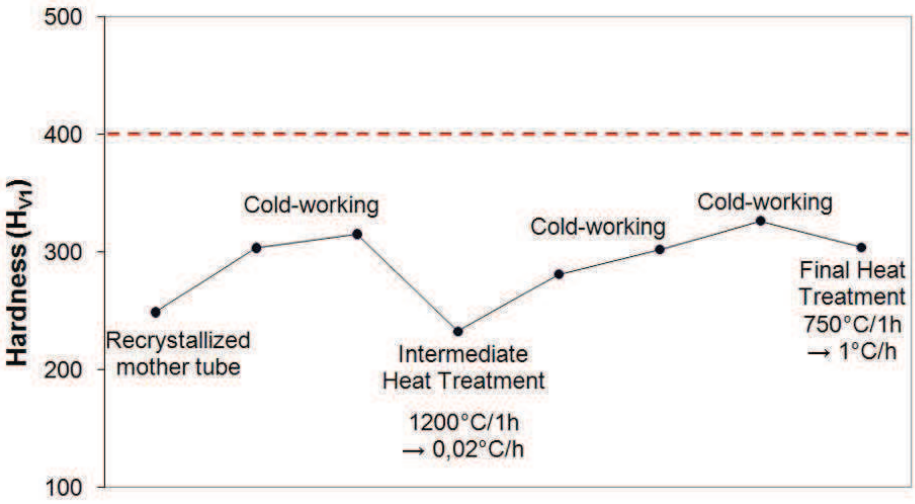

Figure 1.4. Hardness evolution in the course of cladding manufacturing process [Toualbi *et al.*, 2011].

After 3 passes the cold-rolled tube is heat treated at 1200℃ during 1h and slowly cooled in order to transform to a softened ferritic structure. This intermediate anneal causes a significant hardness reduction about 80 Hv_1 which proves the efficiency of the intermediate heat treatment. Fig. 1.5 and 1.6 show the crystallographic texture and pole figures after 3 passes before and after annealing, respectively.

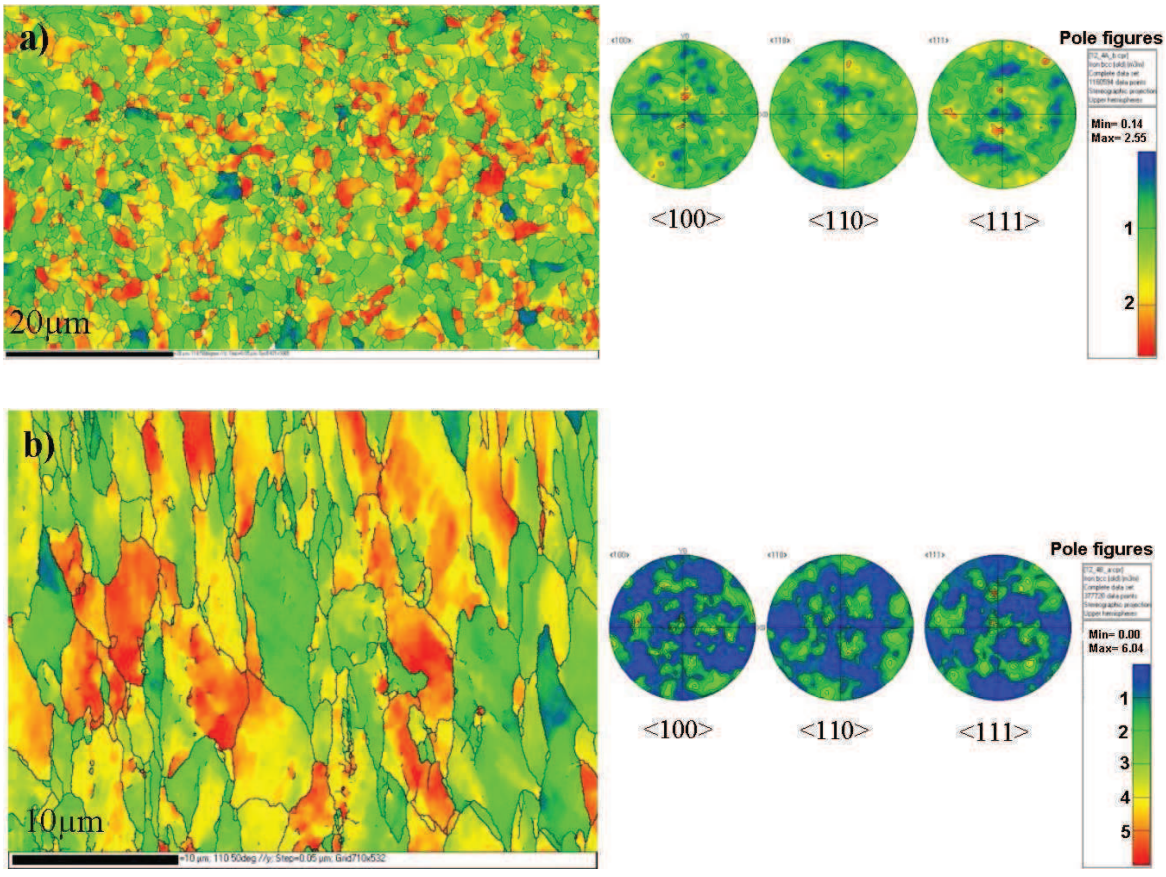

Figure 1.5. EBSD and computed pole figures obtained on the a) transverse and b) longitudinal cross-sections of raw tube after 3 rolling-passes [Toualbi *et al.*, 2011].

Samples taken on the raw tube after 3 rolling passes present slightly elongated grains (see Fig. 1.5) on the longitudinal cross-section sample (around 3-5µm thick and 5-10µm long). After the intermediated heat treatment the elongated grain shape is changed into equiaxial grain shape (see Fig. 1.6) which confirm the efficiency of the phase transformation to reduce the morphological anisotropy introduced by the rolling process [Toualbi *et al.*, 2011]. The grain size remains 7-15µm.

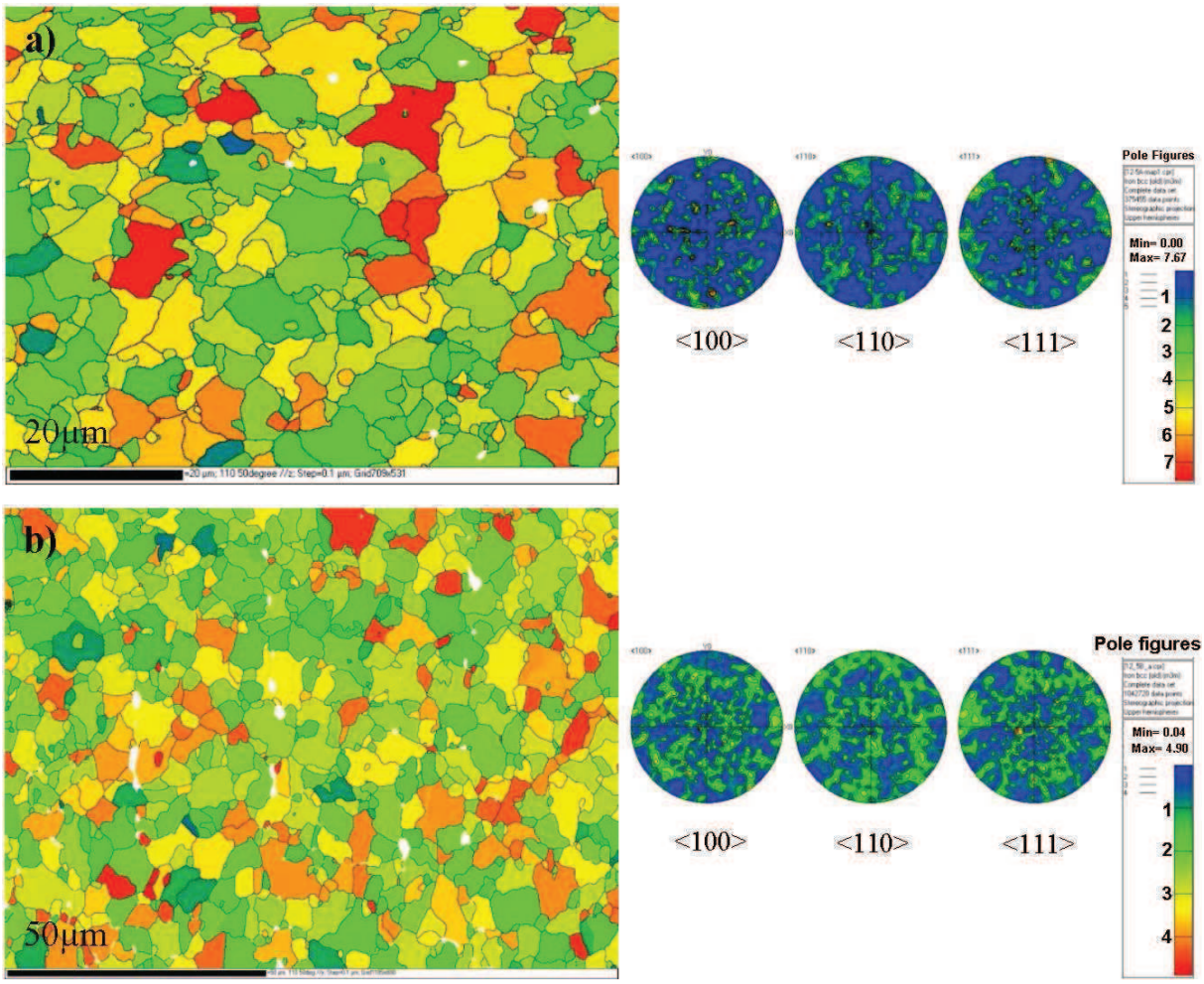

Figure 1.6. EBSD and computed pole figures obtained on the a) transverse and b) longitudinal cross-sections of raw tube after 3 rolling-passes and intermediate heat treatment at 1200℃ during 1h [Toualbi *et al.*, 2011].

1.2.2 Ferritic grade

These grades contain higher levels of chromium that provide improved corrosion resistance of these materials [Ukai and Fujiwara 2002], [Ukai and Ohtuska 2007], [de Carlan *et al.*, 2009]. Unlike the martensitic grades presented in the previous paragraph, ferritic grades show no phase transformation because the matrix remains fully ferritic at all temperatures. To manufacture Fe-12CrODS ferritic steel cladding tubes with coarser and equiaxed recrystallized grains after the final heat treatment instead of the typical elongated structures along the cold

rolling direction, [Narita *et al.*, 2004] propose to optimize the conditions for the intermediate heat treatment after cold pilgering. It was found that the intermediate heat treatment should avoid formation of a recrystallized structure and should restrict to produce recovered structures, because once recrystallization has taken at an intermediated step of the manufacturing process, the recrystallized condition can not be repeated at the final heat treatment. Moreover, [Narita *et al.*, 2004] showed that the conventional heat treatment used to restore the tube microstructure (ferritic grade) is not sufficient to achieve a sufficiently low hardness value (<400 Hv_1) if recrystallization is to be avoided. Therefore, [Narita *et al.*, 2004] developed an original two-step softening heat treatment which reconciled the two conflicting requirements at the intermediate heat treatment, namely, avoiding recrystallization and reducing the hardness to a suitable level for the next cold rolling (see Fig. 1.7)

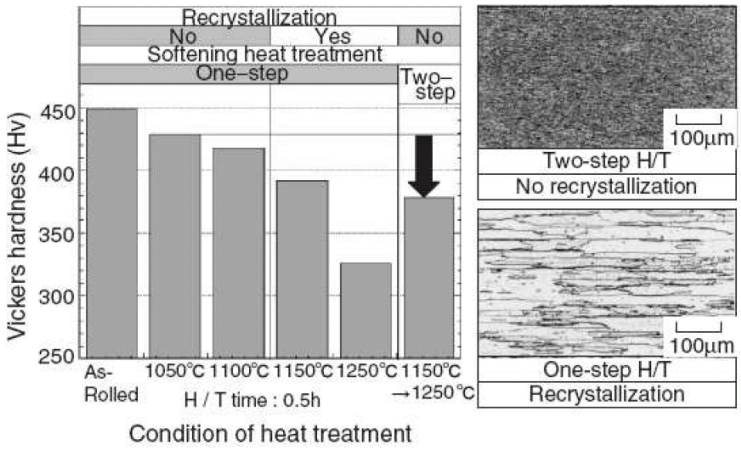

Figure 1.7. The optical microstructures and hardness results for the two steps heat treatment [Narita *et al.*, 2004], as compared to the one-step heat treatment.

The proposed two-step softening heat treatment (see Fig. 1.8) consists first in a heat treatment at temperature (T_1) lower than the recrystallization temperature (T_0) to relieve the strain accumulated during the cold rolling. Following this first heat treatment, the recrystallization temperature, which is highly dependent on the energy stored during the cold work, increases to the value (T_0'). The second heat treatment may be performed at a temperature (T_2) lower than the new recrystallization temperature (T_0') but higher than (T_0), causing a decrease in hardness without recrystallization (see Fig. 1.8). This unique two-step softening heat treatment proposed by [Narita *et al.*, 2004] makes it possible to manufacture good quality Fe-12CrODS ferritic steel tubes.

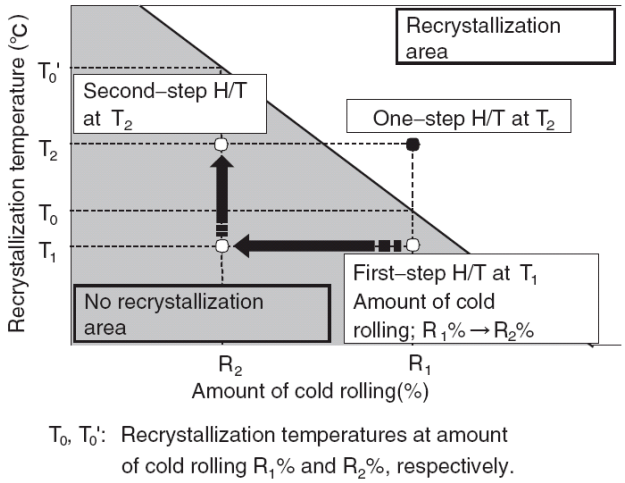

Figure 1.8. Two-step softening heat treatment proposed by [Narita *et al.*, 2004].

Finally, the authors concluded with this approach where recrystallization is not caused by intermediate heat treatments. The result is a finely recrystallized tube whose degree of crystallographic texture is low, ensuring a good isotropy of mechanical properties.

However, both, the work-hardening rate and the Q factor (ratio between thickness reduction and external diameter reduction), characteristic parameters of cold pilgering, have not been optimized in the work of Narita [Narita *et al.*, 2004]. Moreover, it is necessary to adjust the cold-rolling parameters on the chemical composition of the ODS material.

The development of ODS materials for the cladding in sodium fast reactors is a key issue to achieve the objectives required for GENIV reactors. CEA has launched an important program to acquire the harnessing of the fabrication and to understand the properties and mechanical behavior before and after irradiation of such cladding materials [Parmentier *et al.,* 2002], [Alamo *et al.*, 2004], [Alamo *et al.*, 2007], [de Carlan *et al.*, 2009], [Dubuisson *et al.*, 2011b], [Olier *et al.*, 2009], [Ratti *et al.,* 2009], [Oksiuta *et al.,* 2009], [Steckmeyer *et al.*, 2010], [Sornin and Couvrat 2010], [Malaplate *et al.*, 2011], [Toualbi *et al.*, 2011].

1.3 General overview of cold pilgering modeling

Cold pilgering had been modeled and analyzed since the 1950s. Therefore, significant work is available in the literature. First in this section the main works dealing with the analytical approach are presented. Second, works focusing on the finite element methods (FEM) are depicted. Finally, damage models used in the cold pilgering literature are described.

It is pointed out that no literature was found for the HPTR pilgering process. Therefore, all the information presented in this section dealt with the VMR cold pilgering process.

1.3.1 Analytical approach

In the 1950s, simplified 2D models were proposed to calculate the vertical die forces. These models are comparable with those on cold strip rolling. In 1954, [Siebel and Neumann 1954] proposed a model considering only the groove die geometry. They did not take into account the die oval shape. They estimated first the contact length between the groove die and the tube. Afterwards the vertical die force is obtained as the product of the contact length surface by the normal stress. [Geleji 1955] proposed also a 2D model in order to determine the die vertical forces but he considered that the pressure to deform the tube could be divided into the force to reduce the thickness and the force to reduce the diameter since in cold pilgering the inner radius and the wall thickness are both progressively reduced. These models were used to design dies geometries.

Later on, [Yoshida *et al.*, 1975] measured the strain level from deforming grids printed on the transient tube external surface. They also measured rolling vertical and axial force, pressure and contact length. They proposed a 3D simplified model for cold pilgering rolling of copper tubes, based on the experimental observations. The stress tensor was estimated from strain increments measured from the rolled grid via the von Mises criterion. They assumed that the ortho-radial stress was constant over the thickness and neglected the shear stresses. Moreover, they assumed a constant longitudinal strain in the tube cross-section. They showed that the axial stress is compressive in the groove bottom and tensile in the flange area since there is not contact with the die. All the other stresses were described as compressive. They demonstrated that the maximal strain appears during the forward stroke.

[Furugen and Hayashi 1984] developed also a 3D model, following the axial and the orthoradial movement of a metal particle between the groove bottom and the groove flange, due to the rotation and feeding of the tube before starting a new stroke. This model deals with a material point undergoing successive reductions from the raw tube to the final tube. Thus, the principal strain increments can be calculated and, using Huber-Mises criterion and Hencky-Mises flow rule, the stresses were calculated. The authors considered that the gap between the two dies should be taken into account in the geometric description of pilgering. Moreover, the cage mill deformation is considered in the model. Once again, the authors neglect the influence of the shear stresses and strains. The stresses are then integrated to give the rolling force. They found tendencies similar to the measurements in [Yoshida *et al.*, 1975].

[Osika and Libura 1992], created a 2D and 3D strain simulation for copper and brass materials. The computer simulations results for only one stroke are the rolling pressure and the axial force in the tube. An isotropic constitutive law is used in this study. They showed that the numerical results were in good agreement with the experimental results but unfortunately the authors did not describe the approach in details. Fig. 1.9 shows the rolling force comparison for the 2D and 3D models versus the experimental one (named: M-M). Equations are proposed to describe the plastic strain energy consumption, the surface forces energy and the effect of the velocity discontinuity of a kinematically admissible field. Tools shapes were calculated by satisfying a minimum of energy consumption criterion.

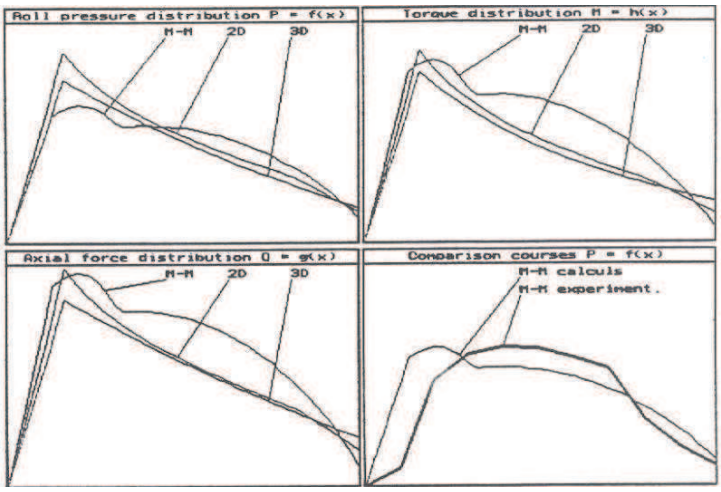

Figure 1.9. Simulations results for the model 2D and 3D [Osika and Libura 1992].

[Huml and Lindegren 1992], [Huml *at al.* 1993], [Huml and Fogelholm 1994], [Huml 1997] developed a computer assisted cold pilgering numerical model able to predict the stress map in the tube, the separating force of dies, the temperature map, using an analytical equation describing the deformation of the tube. In their model the geometry of the pilger rolling process is given analytically (shape of the mandrel and die). The authors do not describe the way to calculate these analytical expressions. They proposed, in neglecting the die groove and the mandrel clearance, that the material can be divided into four zones (see Fig. 1.10).

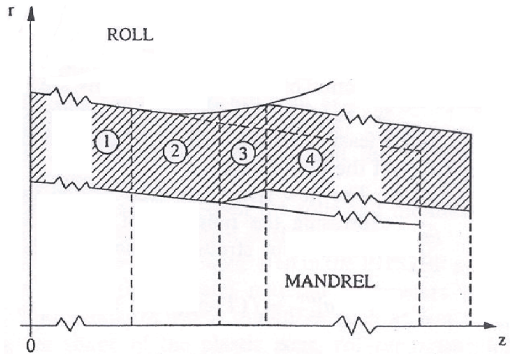

Figure 1.10. The geometry of the plastic zone during a forward stroke in cold pilger rolling tube [Huml and Lindegren 1992].

Zone1 contains a material that has already been rolled down into contact with the mandrel. Zone 2 is a material that is in contact with both the die groove and the mandrel. Zone 3 is a material that is in contact with the die groove only. Material in the zone 4 is not yet deformed by the dies. The successive reductions of the cross-section in zones 2 and 3 must be compensated for by a rigid displacement of zone 4 in the axial direction. In zone 3 the material deformation leads to diameter reduction. In the model it is assumed that the material in zone 3 does not expand in the axial direction because the axial strain increment is neglected in comparison with the radial and the hoop (orthoradial) increments. The deformation of a material point of the tube was computed as a function of its position in the deformation zone and the number of the stroke. The flow stress was related to a characteristic strain increment expressing

the influence of the cyclic multidirectional deformation in terms of a single strain increment value calculated from the strain history:

$$\sigma_{(\varepsilon,T)} = f(T)\sigma_{M(\varepsilon)} + \left(1 - \exp\left(-\frac{\Delta\varepsilon}{\eta}\right)\right)\sigma_{U(\varepsilon)} \tag{1.1}$$

where $f(T)$ is a function of the temperature T, $\sigma_{U(\varepsilon)}$ and $\sigma_{M(\varepsilon)}$ are respectively limiting flow stress curves for the extremes cases of monotonic uniaxial compression, and cyclic loading, and $\Delta\varepsilon$ is the characteristic strain increment detailed in [Huml and Lindegren 1992]. η is a parameter that describes the interpolation between the two extreme flow curves.

The authors calculated die separating force, stress, temperatures, strain increments in the axial direction and the length/shape of contact in order to improve process parameters (e.g. combination of feed and stroke rates). It is pointed out that the authors do not take into account the rotation angle for theirs process improvements. Fig. 1.11 shows the contact length and the shape of the plastic zone.

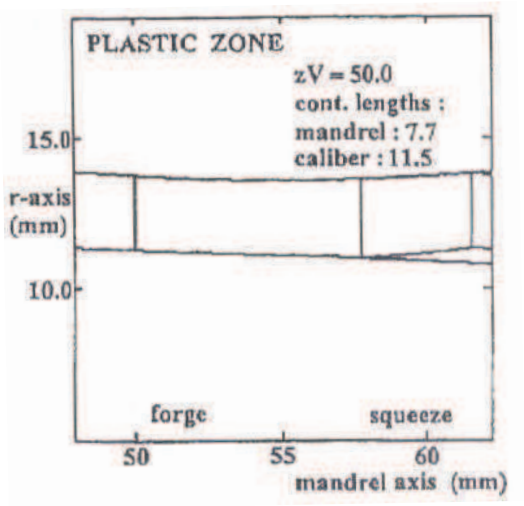

Figure 1.11. Contact length and shape of the plastic zone [Huml *et al.* 1993].

In 1993, [Abe *et al.*, 1993] used the [Furugen and Hayashi 1984] 3D analytical model to understand the origin of the creation of internal surface cracks on Zircaloy-2 tubes during cold pilgering. The authors perform a comparison between 6 dies with a variation of the Q factor defined in the previous Chapter. They inferred the stress conditions in a section of the deformation area that can cause cracks. They concluded that the improvement, for cracking risk, of pilgering is inversely proportional to the ratio $(-\varepsilon_r / \varepsilon_\theta)$. In others words, in the case of good pilgering, the increase of the wall thickness on the flange part, caused by large circumferential compression, is very small even at high area reduction pilgering and, consequently, the frequency of crack occurrence is lower. This crack mechanism is illustrated in Fig. 1.12. Thus, in the tube with less circumferential deformability, larger circumferential compression strain during cold

pilgering tends to produce cracks in the formed tube surface. It is therefore necessary to choose for less deformable tube, a higher Q factor to decrease the radial tensile strain on the flange part during cold pilgering.

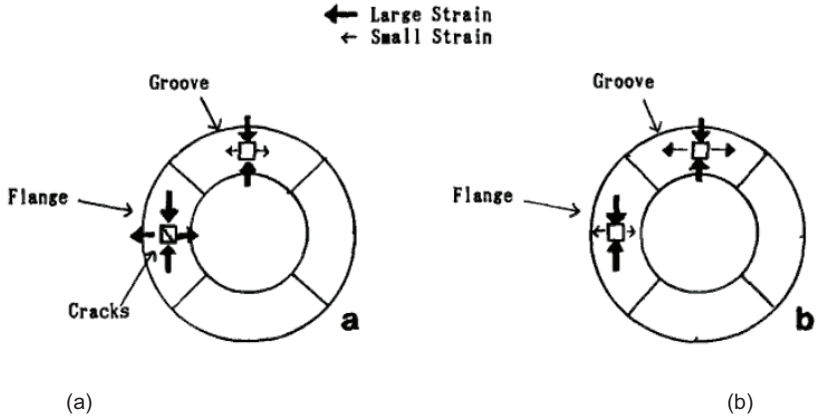

(a) (b)

Figure 1.12. Schematic diagram of crack mechanism: (a) bad pilgering and (b) good pilgering [Abe *et al.*, 1993].

[Girard 1993] in his thesis and [Aubin *et al.*, 1994] in their publication performed a broad experimental and theoretical mechanical study of Zircaloy-4 tubes during cold pilgering. Shear strain was measured by observing the progressive inclinations of inserts through the thickness of the tube wall. A design experiment was used to evaluate the influence of three parameters on the shear strain: the feeding, the die velocity and the type of internal lubricant. It was concluded that shear deformation ε_{rz} can not be neglected and could be the responsible of some defects. ε_{rz} is strongly dependent on the lubrication conditions, e.g. difference in friction conditions between the inner and the outer surfaces of the tube during pilgering. Positive shear, higher friction coefficient on the internal surface compared to the external one ($\mu_{ext} < \mu_{\text{int}}$), was always found, suggesting that external friction is lower than the internal friction. In order to avoid defects the authors proposed to control the pilgering conditions that influence the shear stress. An equivalent friction between internal and external surfaces tends to minimize this shearing. The amount of shear strain $\varepsilon_{\theta z}$ was also measured (see Fig. 1.13). This strain is likely to be responsible of the transformation of a straight line into a helix. It is pointed in this work that shear deformation $\varepsilon_{\theta z}$ is neglected in relation with ε_{rz}. However, the pilgered helix is not a well-understood phenomenon according to the authors.

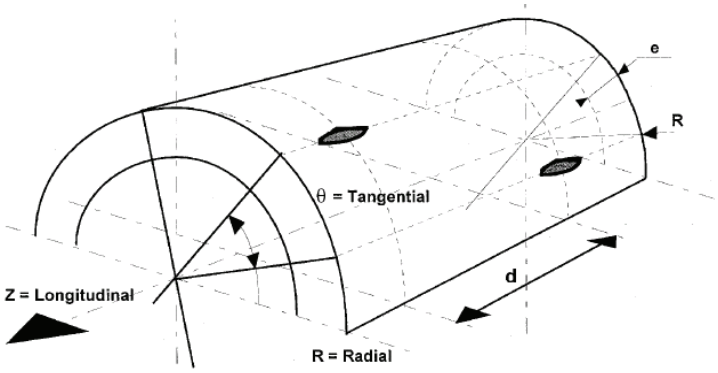

Figure 1.13. Insert position with rolling helix [Girard 1993].

Next in [Aubin *et al.*, 1994] work, a 2D mechanical model is proposed to describe the mechanical conditions that prevail during the pilgering pass of a Zircaloy-4 tube, as a function of the contact length of the die, the tool design, the rolling parameters and the friction. It is based on the geometrical definition of strains that is transformed into stresses via the von Mises criterion and the slab method [Girard 1993]. They included connections to these analytical model corrections on die deformation and horizontal mandrel movement. The die separation forces for the forward and return strokes are calculated. Longitudinal deformation is considered as homogeneous around a cross-section. The strain analysis is improved by a calculation of the contact length between the die and the tube assuming elastic deformation of the die and taking into account the material wave, which increases the contact length. Shear deformation ε_{rz} was taken into account in this semi-analytical model; ε_{rz} was constant over the thickness. [Girard *et al.*, 2001] used the 2D mechanical model proposed by [Aubin *et al.*, 1994]. A stress calculation applied to one particle at each stroke is presented in Fig. 1.14.

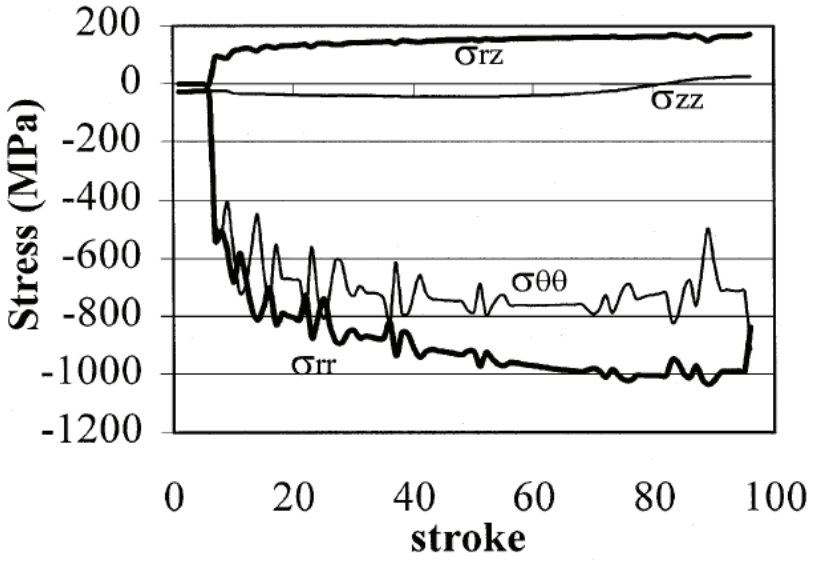

Figure 1.14. Stress components calculation during the last cold pilgering pass of a Zy4 tube [Girard *et al.*, 2001].

The calculation of average strains and stresses in a given perpendicular section of the tube is the major drawback of the 2D mechanical model in terms of accurate tracking of the mechanical history of a material point.

[Girard *et al.*, 2001] proposed to simulate the crystalline texture evolution during cold pilgering using a visco-plastic self-consistent (VPSC) model. This approach was first proposed by [Lebensohn *et al.*, 1996] for zircaloy pilgered tubes. The global strain matrix is defined according to the mechanical model proposed by [Girard, 1993], [Aubin *et al.*, 1994], [Girard *et al.*, 2001]. They arbitrarily divided the simulations: from 0 to 0.5, from 0.5 to 1, from 1 to 1.5% and from 1.5% to 1.75% equivalent strain. The mechanical strain hardening is not taken into account in the simulation. The shear strain ε_{rz} was taken into account in the global strain matrix, a new fact in relation with the approach proposed by [Lebensohn *et al.*, 1996]. A very good agreement is obtained between experimental and simulated pole figures, which underlines the importance of the shear component.

1.3.2 FEM approach

Cold pilgering is a quite complex cyclic forming operation, highly transient, where the material undergoes a long series of small incremental deformations resulting in both diameter and thickness reduction. FEM computation brings a lot of understanding on the mechanical details of this process, can help improving the simple models presented in the previous section and could be used for the process optimization [Mulot *et al.*, 1996]. First, some 2D FEM approaches are described briefly, followed by the 3D approaches.

1.3.2.1 2D models

[Davies *et al.*, 2002] use a 2D FEM model to study the isotropic behavior of a titanium alloy tube. This study investigated the nature of the plastic deformation of the tube during cold pilgering via finite element analysis (Ansys® software). The authors simulated 4 regions of the whole process. Thus, one model was constructed in the rolling area where the material was in contact with the roll dies but not yet in contact with the mandrel. The second finite element model was built in the region shortly after the tube comes in contact with the mandrel. Two additional models were constructed at locations where the overall area reduction was 50 % accomplished and 100 % accomplished. The finite element modeling results presented in this work may be used to qualitatively present an explanation for the direction and the magnitude of the anisotropic hardening that is experienced during cold pilgering. Fig. 1.15(a) is a sample of the results produced during this analysis and shows the equivalent plastic strain imparted to the tube for the given analysis. Fig. 1.15(b) is an illustration of the magnitude of the equivalent plastic strain versus the model angular position at different regions (0%, 7%, 50%, 100%) with all four finite element models included. It is concluded for all 4 models that the maximum plastic strain after one stroke is located on the groove die.

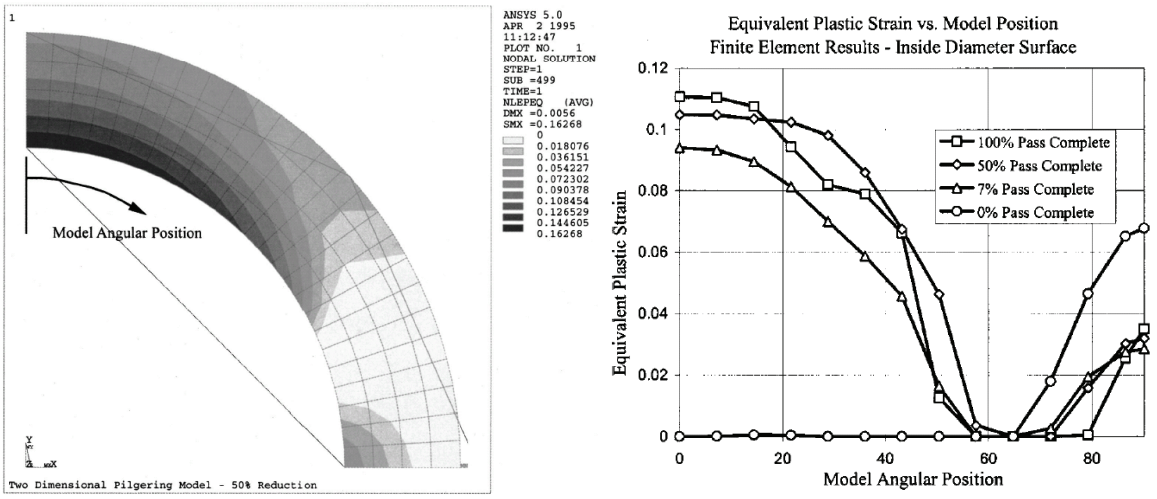

(a) (b)

Figure 1.15. Strain hardening: (a) finite element analysis results (equivalent plastic strain) for the two-dimensional pilgering analysis performed at a point where the total pass was 50% complete; (b) equivalent plastic strain on the inside diameter surface as a function of model angular position. Each curve represents FEA results at a different axial position in the pass [Davies *et al.*, 2002].

Finally, given the significant titanium crystallographic texture and the heterogeneous deformation in a given section of the tube during cold pilgering, the authors carried out an experimental biaxial test (combined axial and internal pressure) to characterize the mechanical anisotropy of the cold pilgered tube. Experimental yield strength data for various ratios of biaxial stress quantified and illustrated the anisotropic nature of titanium alloys developed during pilgering. The Hill equation was used to fit a continuous yield surface to the experimental data. The authors did not implement this anisotropic constitutive model in the 2D FEM cold pilgering simulation.

In [Harada *et al.*, 2005], the authors proposed a generalized plane strain model for the simulation of cold pilgering of cladding tubes for nuclear applications (Zircaloy). In this model, the material is treated as viscoplastic at the loading stage of the pilgering and totally elastic after every stroke. Tools are assumed to be rigid. The authors consider the effect of the tube spring-back after each stroke on the tube deformation in the next stroke. The effect of the spring-back on the die separation force as a function of the rolling displacement (z) is shown in Fig. 1.16. It was concluded that numerical results are improved significantly when considering the effect of the spring-back.

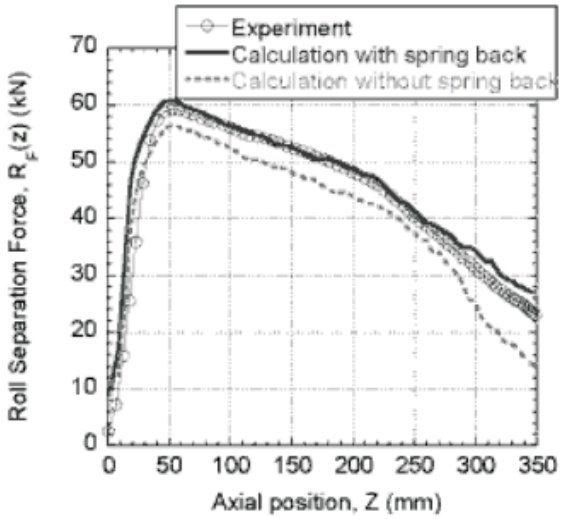

Figure 1.16. Effect of tube spring-back on die separation force [Harada *et al.*, 2005].

1.3.2.2 3D models

[Mulot *et al.*, 1996], [Mulot 1997] firstly used a 3D FEM (LAM3 software) to analyze one forward stroke of a cold pilgering operation on a Zircaloy-4 cladding tube. The main purpose of their study is to evaluate the hypotheses and the results of the 2D simplified mechanical model based upon an estimation of incremental strain components (slab method and length corrected contact proposed in [Aubin *et al.*, 1994], [Girard, 1993]). Because a fully predictive modeling of all the strokes is very CPU time consuming, the authors adapted the approach proposed first by [Hacquin *et al.*, 1996], [Hacquin *et al.*, 1998] for strip rolling. It consisted in estimating the state of the system at the beginning of a representative stroke, when the deformed tube covers the whole mandrel. Therefore, a preform was partly rolled in an industrial mill. Its shape was completely measured on a 3-coordinated measuring machine, from which equations of longitudinal sections and cross sections were determined. Then, the geometry was meshed with 8-node bricks. They considered the entire tool as a rigid body. In these simulations, the tube is assumed to be free from previous strain and stresses, it means without any thermo-mechanical history. An incremental, isotropic elastic-viscoplastic constitutive model is used. It is concluded (i) that 3 nodes only in the thickness are not sufficient for a precise analysis of the internal shear and (ii) 3 or 4 elements in contact with the die and mandrel along the rolling direction is insufficient, at least 10 would be required to obtain good stress and strain distributions. The pilgering helix (already mentioned earlier) was reproduced by the simulation. Moreover, the authors made an interesting conclusion: looking from the rear of the tube, the pilgering helix starts counter-clockwise, then shifts to clockwise; globally, the counter-clockwise rotation seems to dominate in all cases. This is a variance with the experimental observations where the tube in this work is rotated clockwise when fed, and is then twisted further clockwise during the stroke. This may due to some lateral shift of the dies under transverse forces. Progression of the deformation zone along the mandrel is shown in Fig. 1.17. It is noticed how the deformation is propagated as a wave as a

consequence of the die roll along the mandrel. These two last statements confirmed the experimental observations made in [Girard, 1993].

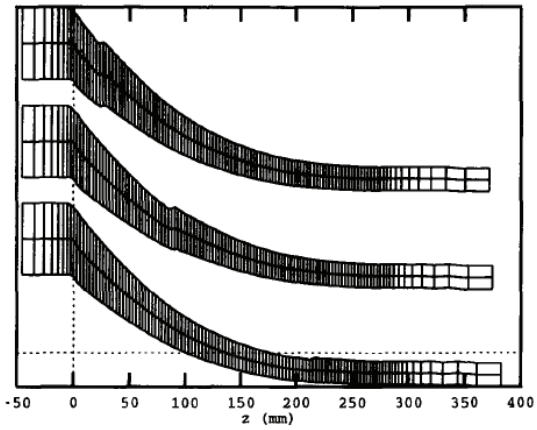

Figure 1.17. Progression of the deformation along the mandrel at different stages of the forward stroke [Mulot *et al.*, 1996].

Fig. 1.18 compares the strain increment on one forward stroke by the slab method and the FEM. The semi-analytical model (slab-method) only gives the average strain. The authors concluded that the average value coincides with the FEM result. But an important conclusion is the significant spread of the accumulated strain through the tube thickness (see Fig. 1.18).

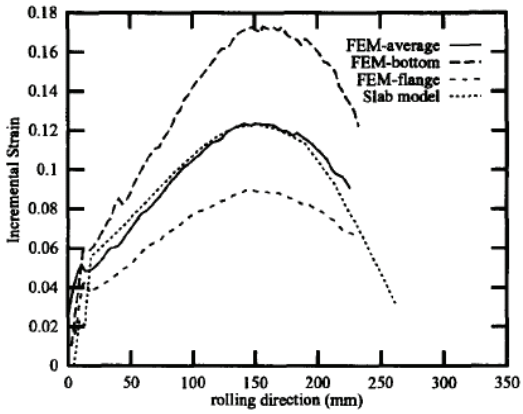

Figure 1.18. Comparison of the incremental strain [Mulot *et al.*, 1996].

Fig. 1.19 shows the ortho-radial distribution of the axial stress which is tensile near the groove flanges and compressive in the groove bottom, as described by [Yoshida *et al.*, 1975], [Furugen and Hayashi 1984]. The authors made deep analyses of the stresses in the pilgered tube.

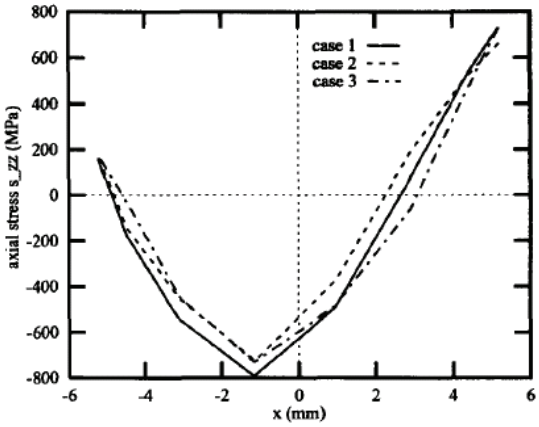

Figure 1.19. FEM simulation: Ortho-radial distribution of the axial stress [Mulot *et al.*, 1996].

Next, this work tested the effect of friction variation between the tube/mandrel and the tube/die interface. In the groove bottom, depending of the friction coefficients, shear may be negative ($\mu_{ext} > \mu_{\text{int}}$) or positive ($\mu_{ext} < \mu_{\text{int}}$), equal coefficients resulting in a symmetric shear. The authors also noticed that the shear is negative at the beginning of the deformation zone ($0 < z \leq 50$), then it either remains negative or becomes positive (see Fig. 1.20). Finally, they concluded that the cumulated effect of strain can be predicted only if the complex shear history is known and accounted for.

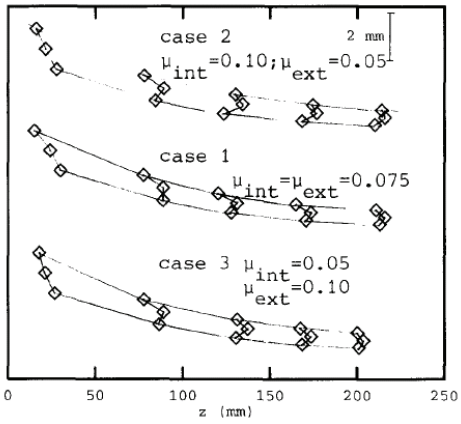

Figure 1.20. Visualisation of the incremental shearing strain ε_{rz} at the groove bottom [Mulot *et al.*, 1996].

[Mulot *et al.*, 1996] studied the anisotropic behavior of Zircaloy-4; they determined the parameters of Hill's criterion at various passes of the cold pilgering. For this, they developed compression and shear tests that allowed calculating the six Hill's criterion coefficients on thick tubes (before rolling). For thin tubes, they used tensile and pipe burst tests. They used a polycrystalline model to predict the Hill's criterion on the whole sequence of cold pilgering passes. The results were promising. Then the Hill's criterion was introduced in the 2D semi-analytical mechanical model. They concluded that the die separation forces are strongly sensitive to the anisotropic yield limit introduced in the mechanical model. This suggests the importance of mechanical anisotropy when dealing with the pilgering process.

Last, [Mulot 1997], [Aubin *et al.*, 2000] proposed a 3D semi-analytical mechanical model based on the 2D semi-analytical model of [Aubin *et al.*, 1994] because the latter does not allow to report the variations of the strain and stress values in a section of the tube since the 2D model computes average values (i.e. it assumes circumferential homogeneity). It is concluded that this 3D model reproduced, qualitatively and quantitatively, the results from the 3D finite element simulation. The 3D semi-analytical mechanical model was validated in relation with measured magnitudes from the industrial mill, as the rolling force, contact length and shear strain ε_{rz}. Fig. 1.21 shows the results for the 2D and 3D semi-analytical models as well as the results of the 3D FEM simulation (maximum FEM equivalent strain: elt1 and minimum FEM equivalent strain: elt6). Fig. 1.22 shows the successive solicitations in tensile and compression pilgering conditions. This cyclic issue is not examined in this work through an appropriate constitutive law. Likewise, the anisotropic Hill's criterion was not introduced in the 3D semi-analytical mechanical model.

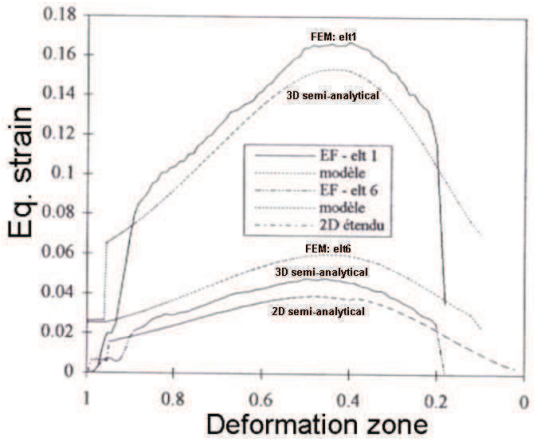

Figure 1.21. Equivalent strain comparison: FEM simulation and analytical method in function of the deformation zone [Mulot 1997].

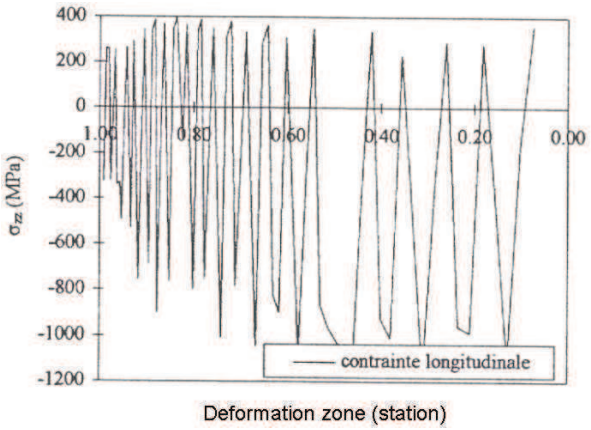

Figure 1.22. Longitudinal stress long the deformation path [Mulot 1997].

[Montmitonnet *et al.*, 2002] have subsequently improved the work of [Mulot *et al.*, 1996]. The authors showed in this study that for a perfect plastic material, the real periodic state of stress can be identified with 2 or 3 strokes when a reasonable initialization of a transient

geometry is performed. The shape of the transition tube at each position z in the rolling direction is determined by the gap between the mandrel and dies when the dies are at z during the stroke. Moreover, to confirm this geometry, similar to [Mulot *et al.*, 1996], the authors performed 3D measurements on a partly pilgered preform (zircaloy tube). Isotropic constitutive behavior is used in this work. They concluded that initializing the stresses to zero has no detrimental consequences. The return stroke had been omitted, because it should be considered purely elastic in the absence of tool deformation (tools are considered rigid). Regarding the numerical model, they used an anisotropic structured mesh. The tube transition mesh and the initial positioning of the simulated system can be observed in Fig. 1.23.

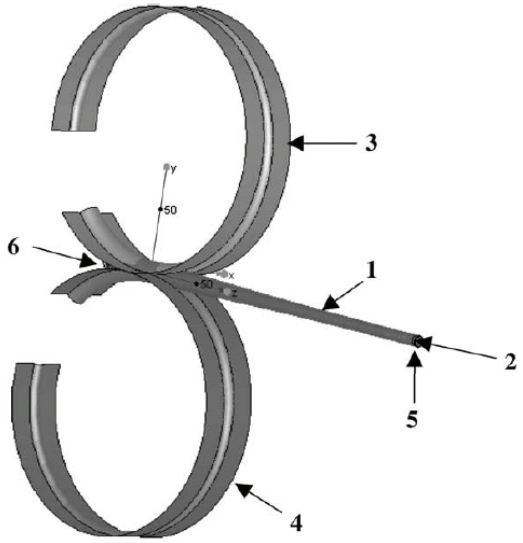

Figure 1.23. FEM model initial set-up: (1) tube transition; (2) mandrel; (3,4) dies; (5,6) represent the boundary conditions at the exit and entry tube, respectively [Montmitonnet *et al.*, 2002].

Strain rate or temperature dependence are not taken into account. Absence of strain hardening is also assumed, to ensure that the initialization does not disturb the development of the geometry and stresses. The analysis is based on the incremental strain imposed by a single stroke. Fig. 1.24 confirms the quasi steady state hypothesis since the geometry and the state of the stress stabilize after 2 strokes. The study was carried out with the commercial software Forge3®.

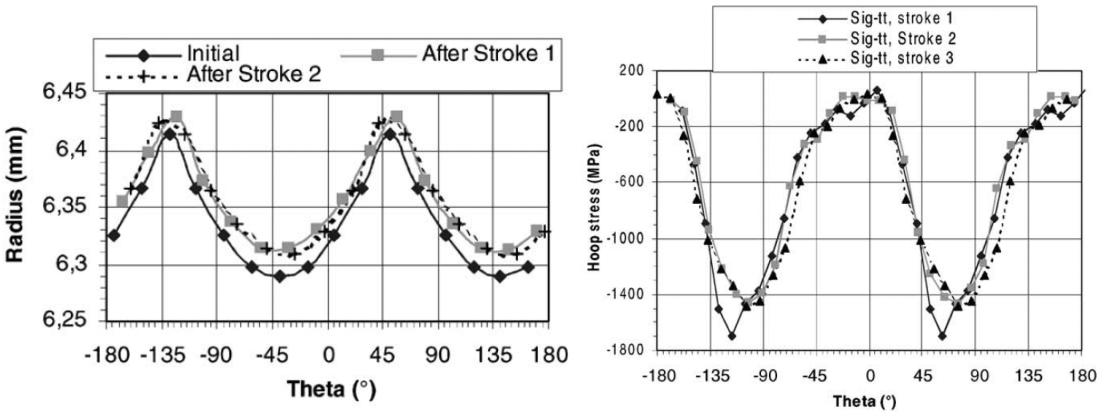

(a) (b)

Figure 1.24. Variables stabilization on a tube cross-section : (a) external surface; (b) orthoradial stress [Montmitonnet *et al.*, 2002].

[Lodej *et al.*, 2006] used the numerical simulation approach of a representative single stroke performed by [Montmitonnet *et al.*, 2002] to develop a post-processing tool to estimate the thermo-mechanical history of a material point. Similarly to the former modeling of steady-state processes, the initial geometry comes from a 3D-measurement of a transition shape. The FEM set-up used in this study is showed in Fig. 1.25.

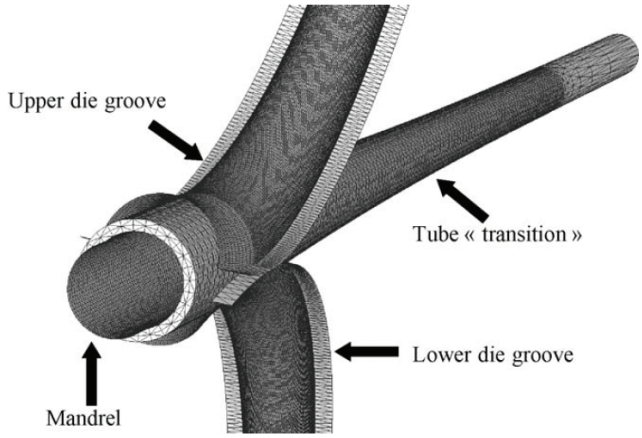

Figure 1.25. Inital FEM model set-up with Forge3® [Lodej *et al.*, 2006].

Anisotropic structural mesh was used and similarly to other work, the tools are assumed rigid. The authors used the same friction coefficient in the internal and external tube surfaces, based on the work of [Aubin *et al.*, 1994]. An isotropic elastic-plastic behavior is assumed for the Zircaloy-4 tube material, but this time accounting for the work-hardening. Consequently, they added a simple initialization of the equivalent strain field (Fig. 1.26) given by:

$$\bar{\varepsilon}(z) = \ln\left(\frac{S_0}{S_z}\right) \tag{1.2}$$

where S_0 is the initial tube section and S_z is the section at a given z position of the transient tube (see Fig. 1.26). The stress field was initialized to zero in this study.

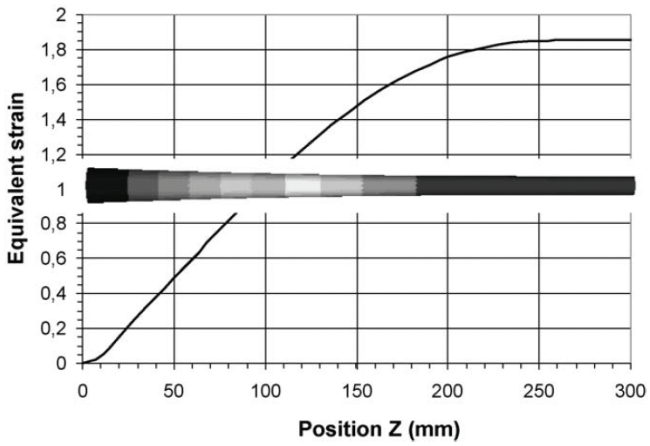

Figure 1.26. Equivalent strain initialisation [Lodej *et al.*, 2006].

Because these initializations are not rigorously exact, some pilgering strokes must be computed until geometry and strain fields have been stabilized leading to the "pseudo-steady state" [Hacquin *et al.*, 1996], [Montmitonnet 2007]. Next, by cumulating the single-stroke displacements and the rigid body motions (feed and rotations) between the strokes, the successive positions of any material point are computed (see Fig. 1.27).

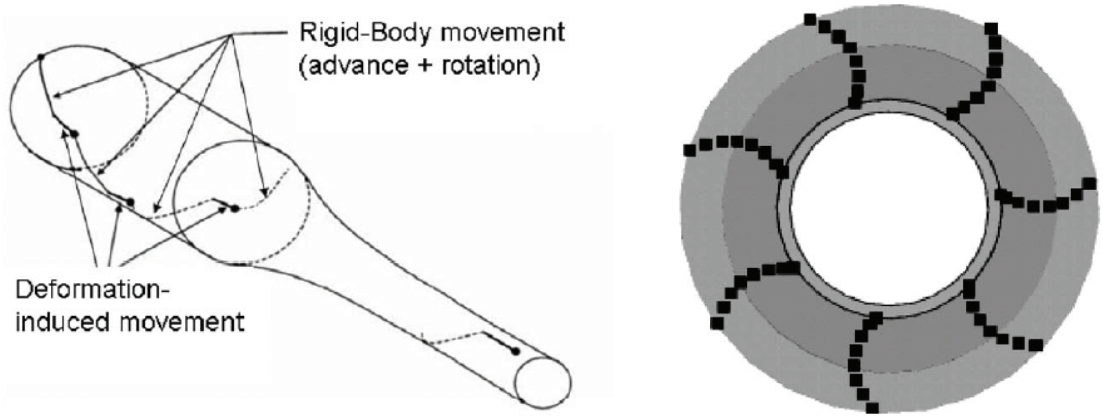

(a) (b)

Figure 1.27. Trajectory determination: (a) principle of position incrementation and (b) seen from behind, the successive positions [Lodej *et al.*, 2006].

The mechanical fields are then interpolated, giving the complete mechanical history of stresses and strains for a volume element. The authors showed the successive tension and compression in all the strain and stresses components (e.g. see Fig. 1.28 for the longitudinal stress).

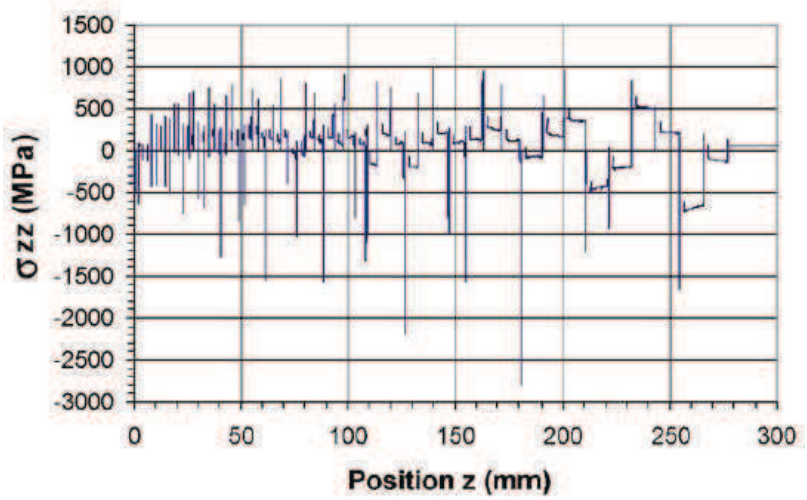

Figure 1.28. Longitudinal stress history of a material point along 56 cycles [Lodej *et al.*, 2006].

The precision is however dependent on the storage frequency. The computation time remains high; one stroke took 38 CPU h on a 2GHz PC for the FEM computations, plus 21 CPU h for the post-processing. The quasi-state approach was estimated to be 10-20 times faster than computing the full 60 or 70 strokes necessary to obtain the periodic state. This study was carried out with the commercial software Forge3®.

[Park *et al.*, 2005] proposed an optimum design of a die shape for the cold pilgering process using FEM analyses considering various processing factors. They concluded that the important design parameters of the pilgering mill machine are the feed rate and the profile of the grooved die. Therefore, an optimum design procedure was conducted in order to investigate various effects on the forming load, as well as the deformed shape as a function of the die surface profiles. Profiles of the die surface for the optimum design were tested with linear, cosine and quadratic curves (see Fig. 1.29). It is pointed out that this work analyzed a cylindrical billet instead of a tube. The results of the analyses showed that the model with the quadratic profile gave the lowest forming load and the proper deformed shape. The material used for FEM analysis was cold OFHC copper. Analyses were conducted for 1/4 model for each profile to minimize CPU time. Three dimensional brick elements were used in the mesh, and computation were carried out with the LS-DYNA 3D® software.

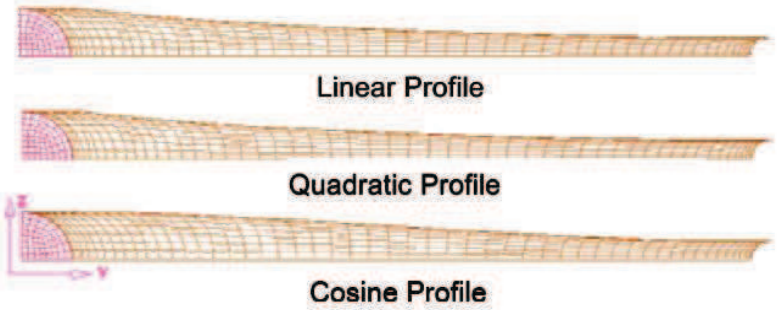

Figure 1.29. Cylindrical billet deformed by 3 different die profile. LS-DYNA 3D software [Park *et al.*, 2005].

In his thesis, [Karas] evaluated the influence of the die geometry on the rolling helices observed experimentally by [Osika and Libura 1992] and [Girard 1993]. Actually, the intrinsic dissymmetry of the tube - dies configuration in the deformation zone brings about both the "pilgering helix" (Fig. 1.30) and spurious torques and transverses forces of large amplitude.

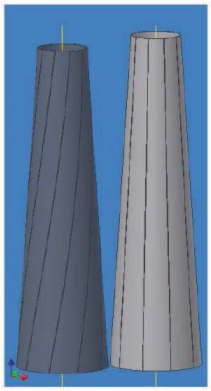

Figure 1.30. Comparison of the material flow in standard and asymmetric die design (schematic) [Karas].

The authors proposed to compensate these effects by an opposite dissymmetry of the dies groove (see Fig. 1.31). The differences in the groove shape make it non-circular and mean that it changes over the mandrel length. [Karas] pointed out the fact that general changes of the groove die cannot be too large, because vibrations effects could appear.

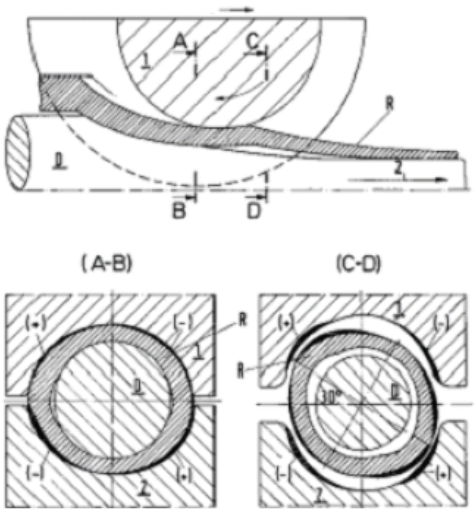

Figure 1.31. Asymmetric die groove [Karas].

In the work of Karas, only 15 strokes are necessary to pilger a copper tube, reaching a deformation close to 95%. Therefore, the author proposes to use an arbitrary Lagrangian-Eulerian formulation (ALE) in the Abaqus® FEM software. ALE adaptive meshing allows to maintain a high quality mesh throughout the analysis, even when large deformation occurs, by allowing the mesh to move independently of the material. The adaptive mesh moves only the

nodes, while the mesh topology remains unchanged. Fig. 1.32 shows the numerical model set up by Karas.

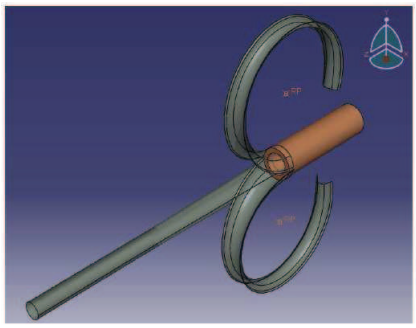

Figure 1.32. FEM model set-up with Abaqus [Karas].

Fig. 1.33 presents the results of equivalent plastic strain after 15 strokes. It is shown that it is possible to find information about rotation of the tube during deformation, because the maximum equivalent plastic strain can be found at each 60°, the rotation angle after each stroke used in this work. It is also concluded that the standard die design deals with higher equivalent plastic strain level (around 8% more) for a similar forming pass.

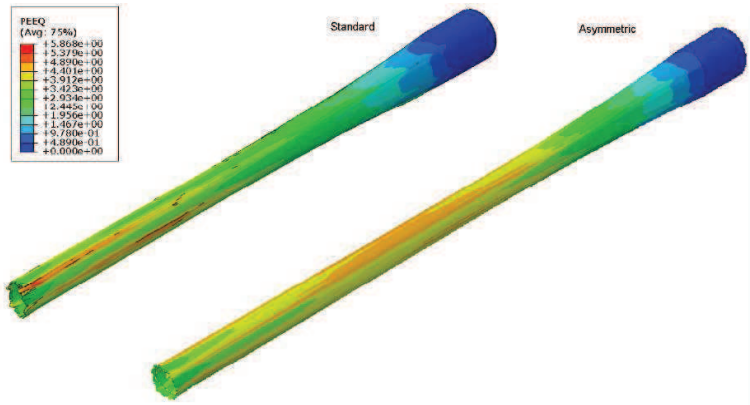

Figure 1.33. Equivalent plastic strain comparison between the standard and the asymmetric model [Karas].

This study showed that the material deformation state is not homogenous in any of the 3 cylindrical coordinates (r , θ , z) (see Figs. 1.33 and 1.34).

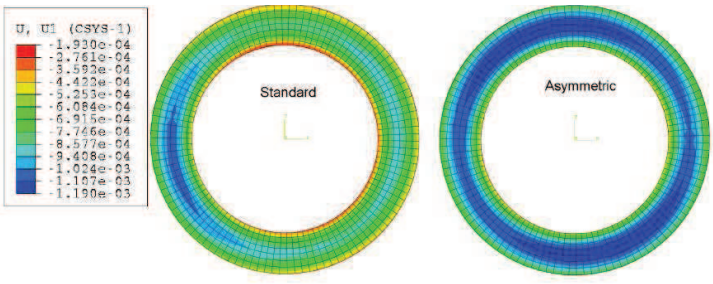

Figure 1.34. Displacement in the radial direction [Karas].

Finally, [Karas] concluded a new asymmetric die design obtained from numerical simulations reduced the rolling force and increased elongation during pilgering. It was possible to observe such effects because well-fitted asymmetric rolls reduced the “pilgering helix”, almost down to “zero”.

1.3.3 Damage function in pilgering

The criterion of Latham and Cockroft (LC) was introduced in [Girard, 1993], [Aubin *et al.* 1994], [Girard *et al.*, 2001] in order to establish a damage function from the principal stresses. Compressive stresses were neglected because they do not have an influence on damage. The damage LC function is the sum of the product of the maximum tensile stress at each stroke with the equivalent strain increment:

$$LC = \sum_{stroke} Max(0, \sigma_I, \sigma_{II}, \sigma_{III}) \Delta\bar{\varepsilon} \,, \tag{1.3}$$

where σ_I , σ_{II} , σ_{III} are the principal stresses (supposed to be active only if tensile) and:

$$\Delta\bar{\varepsilon} = \sqrt{\frac{2}{3}\left(\Delta\varepsilon_{zz}^2 + \Delta\varepsilon_{\theta\theta}^2 + \Delta\varepsilon_{rr}^2 + \Delta\varepsilon_{rz}^2\right)} \tag{1.4}$$

In [Girard *et al.*, 2001] the mechanical model was fed with 3 different experimental values of ε_{rz} . Fig. 1.35 shows the evolution of the damage function with different shear values: (R) curve represents the ideal rolling conditions with $\varepsilon_{rz} = 0.3$, the (S) curve, a harder friction conditions with $\varepsilon_{rz} = 0.45$ and the (T) curve, the hardest conditions with $\varepsilon_{rz} = 0.6$. These results were in agreement with the experimental campaign carried out by [Girard *et al.*, 2001]. The authors modified the die geometries and the lubrications conditions in order to quantify the defects frequency in relation to their locations in the tube thickness, and the adopted tools. The authors concluded with this experimental and theoretical work that the tool geometry has a very strong influence on damage. However, for a given geometry, the lubricant is very important. The LC, as well as the shear strain ε_{rz} could be used as indicators to predict defects frequency. In particular, effort in reducing the damage rate should be intended at reducing the shear strain ε_{rz} , i.e. improving the friction conditions at the interface tool/tube rather than just focusing on the reduction rate or Q factor. The predictive aspect of this model is limited by the need to separately evaluate the mandrel motion, the wave factor and the shear strain.

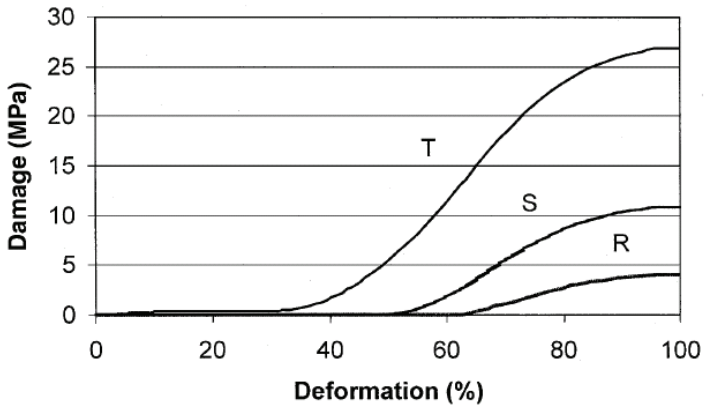

Figure 1.35. Damage function in the reference conditions during the last cold pilgering pass of a Zy-4 tube. (R) curve represents the ideal rolling conditions with $\varepsilon_{rz} = 0.3$, the (S) curve, a harder friction conditions with $\varepsilon_{rz} = 0.45$ and the (T) curve, the hardest conditions with $\varepsilon_{rz} = 0.6$ [Girard *et al.*, 2001].

[Aubin *et al.* 1994] work showed that it is not only possible to predict the severity of the defects, but also to control the pilgering conditions in order to avoid these defects. The improvements were obtained by optimizing the lubricant and pilgering conditions (e.g. feed, Q factor).

In [Harada *et al.*, 2005], the authors assessed the influence of two different tools (Tool-A and Tool-B) on cracking risk. In order to compare Tool-A and Tool-B, the authors use the classical Latham and Cockroft damage function. In this function, the main factors corresponding to the damage are the accumulation of axial stress and the equivalent strain rate.

The differences are based on two process parameters; the first one is the quantity $Q(z)$, given by Eq. (1.5) at a given point z of the pilgering, where t is the thickness and D the diameter. The second parameter $B_0(z)$ deals with the distance between the mandrel centre and the die groove centre.

$$Q(z) = \frac{\ln\left(\frac{t(z+\Delta z)}{t(z)}\right)}{\ln\left(\frac{D(z+\Delta z)}{D(z)}\right)} \tag{1.5}$$

The first tool (named Tool-A) has a relative large $B_0(z)$ and its $Q(z)$ is almost constant. On the other hand, with the second tool (Tool-B); $B_0(z)$ is not large, and its $Q(z)$ is not constant but increases in the rolling direction (see Fig. 1.36).

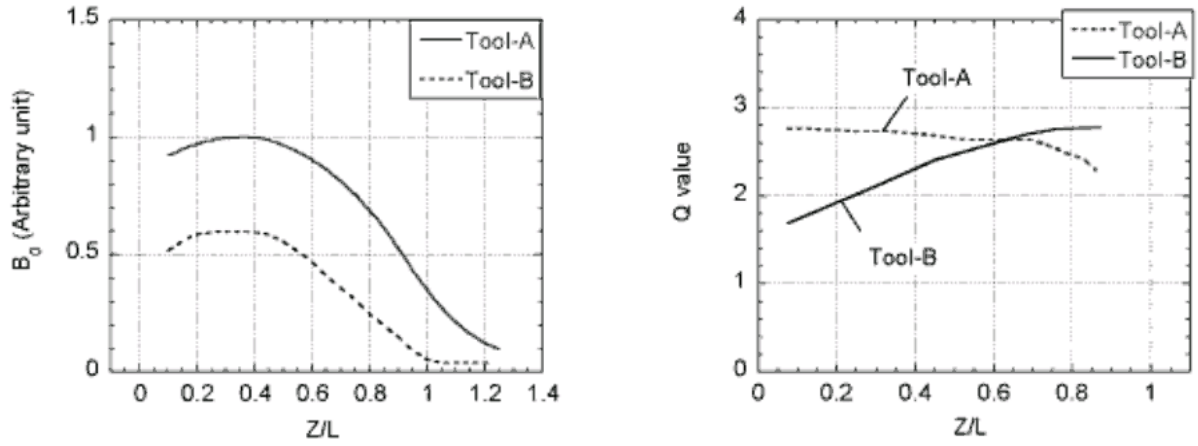

(a) (b)

Figure 1.36. Feature of Tool-A and Tool-B: (a) $B_0(z)$, (b) $Q(z)$ [Harada *et al.*, 2005].

Fig. 1.37 shows the maximum damage function on the outer/inner tube surface at every axial position in pilgering using Tool-A and Tool-B. It has been found that the damage function of the tube inner surface is higher than that on the tube outer surface. Moreover, comparing the effects of Tool-A and Tool-B on the damage, it can be seen that Tool-A brings greater damage than Tool-B does.

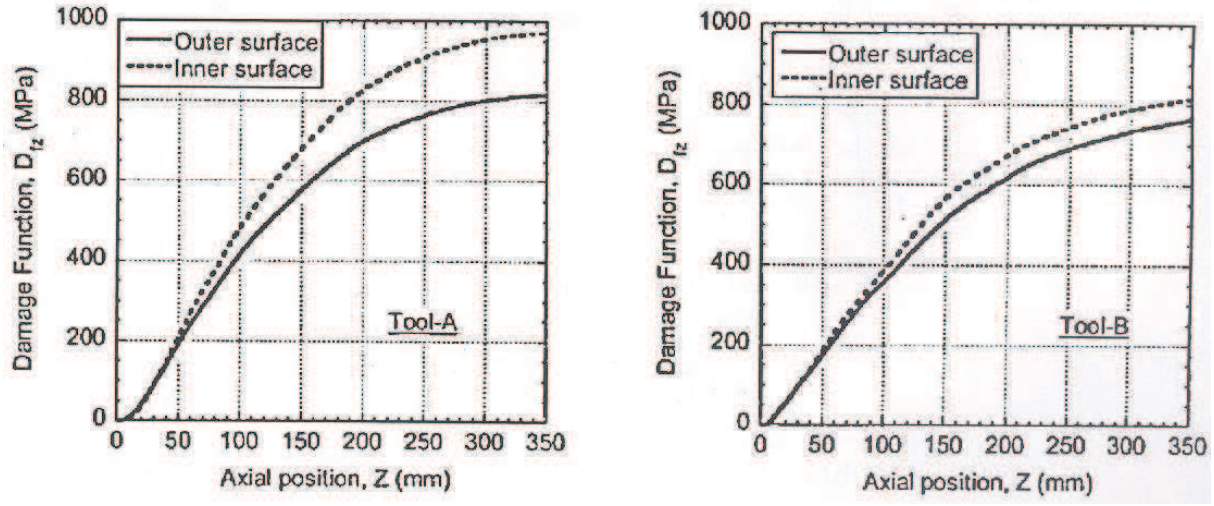

(a) (b)

Figure 1.37. Maximum damage function on tube outer/inner surface considering spring-back : (a) Tool-A, (b) Tool-B [Harada *et al.*, 2005].

Such a damage function (LC) is not supposed to predict accurately the occurrence of a given type of defect, but can be used qualitatively to make comparisons between different rolling conditions.

1.3.4 Summary

2D and 3D analytical approaches have disclosed the main features of pilgering. However, these approaches were semi-predictive only, in that measurements are necessary at least when a new tool is tested in order to check that corrections remains valid. A drawback of analytical approach is the assumption that the mechanical cladding tube states (e.g. stress and strain) are homogeneous over the wall thickness and over the circumference, which is not the case in reality. 2D FEM simulations are low CPU time consuming but the process under consideration is clearly 3D and without obvious symmetries [Montmitonnet *et al.,* 2002]. The mechanical behavior of the pilgering mill can be thoroughly dissected using 3D FEM simulations. The pseudo-periodic (steady-state) approach is addressed to reduce CPU time using trajectory determination from the data of only 4-5 strokes [Montmitonnet *et al.,* 2002]. Nevertheless, the former approach needs approximate initializations of geometry and state variables. 3D FEM simulations are high numerical parameters (e.g. mesh size, time step, contact management, etc.) dependent. Moreover, in all the cases presented in this section, the tool mills are assumed as a rigid body.

The 3D FEM pilgering mechanical analysis carried out in the literature are base on isotropic monotonic constitutive laws. The influence either cyclic or anisotropic constitutive laws on the mechanical history of a material point in pilgering conditions are not reported in the literature.

No data was found in the literature for the numerical modeling of HPTR cold pilgering process.

1.4 Constitutive law

During the cold pilgering process the inner radius and wall thickness are both progressively reduced. After each stroke of the dies, the raw tube is advanced by a small distance and rotated around its axis. A volume element is submitted to several dozens of strokes before deformation is completed. This complex mechanical history is illustrated in Fig. 1.27 and 1.28. The FEM is quite successful to simulate metal forming processes, but accuracy depends both on the constitutive laws used and their material parameters identification [Flores *et al.,* 2007]. Knowledge of the mechanical behavior of materials under complex loadings is necessary to appropriately design mechanical systems.

A large number of cyclic plasticity models have been presented in the literature. According to [Velay *et al.*, 2006], three main approaches for describing a cyclic elastic-plastic constitutive behavior can be distinguished, and are denoted as crystallographic, microscopic or macroscopic.

Crystallographic models are increasingly used even though the associated computing time is high [Nouailhas 1988], [Forest and Cailletaud 1995], [Estrin 1998]. The number of internal variables is typically very large, as it includes a detailed description of the microstructure. Plasticity is described through dislocation slip along crystallographic planes, whose orientation differs from one grain to another. The model formulation is similar to the macroscopic approach (see below), but the stress tensor is applied at the grain scale [Eberl *et al.*, 1998]. The computing

time and the large number of variables limit the use of such models within large scale forming computations.

Microscopic models are based on parameters which can be directly and explicitly related to experimental material microstructural parameters, like dislocation densities and grain sizes [Cailletaud 1992], [Cailletaud *et al.,* 2003], [Cailletaud and Sai 2008], [Bari and Hassan 2001]. The considered scale is typically much smaller than that of the macroscopic representative volume element. Microscopic models can catch the essential phenomena dominating the deformation based on the underlying physics of the deformation coupled to microstructure evolution. However, the models are again very expensive in terms of computing time, when coupled with large scale forming simulations.

Macroscopic models consider, in general, that yield surfaces evolve according to kinematic and isotropic hardening processes. One of the challenges is to be able to capture the sometimes complex hardening kinetics with a reduced number of parameters in the evolution equations. In order to represent plastic behavior of steels, a phenomenological (or macroscopic) elastic-plastic approach is commonly used [Chaboche and Cailletaud 1996], [Chaboche and Cailletaud 1986], [Chaboche 1986], [Chaboche 1996], [Chen and Jiao 2004]. It is then typical to employ a yield function (to describe the yield surface). The yield surface, defined in the stress space, corresponds to the elastic limit and the beginning of the plastic flow.

Concerning the elastic properties, it is often considered that the material can simply be modeled by an isotropic behavior, governed by Hooke's law:

$$e_{ij} = \frac{1+\nu}{E} s_{ij}\,, \tag{1.6}$$

where E is the elastic modulus and ν the Poisson's ratio, $\underline{s}_{ij}$ and $\underline{e}_{ij}$ respectively the components of the deviatoric tensor of stress and strain. From Eq. (1.6), the elastic behavior is written in a matrix form thanks to the matrix $\underline{C}$:

$$\underline{e} = \underline{C}\,\underline{s} \tag{1.7}$$

Several models of plastic behavior can be considered. Table **1.1** summarizes the options depending on the desired degree of accuracy.

Table 1.1. Various constitutive laws governing plasticity [Lemaître and Chaboche 1994].

Plasticity criterion	Hardening	State variables
Isotropic	Isotropic	p
Isotropic	Kinematic	$\underline{X}$
Anisotropic	Isotropic	p
Anisotropic	Kinematic	$\underline{X}$
Isotropic	Isotropic + Kinematic +Anisotropic	$p, \underline{X}, \underline{\varepsilon}^p$
Anisotropic	Isotropic + Kinematic +Anisotropic	$p, \underline{X}, \underline{\varepsilon}^p$

In Table **1.1** p is the accumulated plastic strain, $\underline{X}$ is the kinematic (back-stress) hardening tensor and $\underline{\varepsilon}^p$ is the plastic strain tensor. Isotropic and anisotropic yield criteria are detailed below, before addressing specifically the issues related to cyclic constitutive law.

1.4.1 Yield surface

To describe the yield surface it is typical to employ a yield function ($f(\underline{\sigma})$). The former is usually associated to a hardening law. The yield surface ($f(\underline{\sigma})$) is convex and the state of stress ($\underline{\sigma}$) inside the yield surface is elastic. The yield surface, defined in the stress space, corresponds to the elastic limit and the beginning of the plastic flow and is written in the following way:

$$f = \bar{\sigma}(\underline{\sigma}) - \sigma_y \tag{1.8}$$

In this Equation, $\bar{\sigma}(\underline{\sigma})$ is the effective or equivalent stress and σ_y is the material yield stress.

When the stress state lies on the surface the material is said to have reached its yield point. Further deformation of the material causes the stress state to remain on the yield surface, even though the surface itself may change shape and size as the plastic deformation evolves. Almost all rate-independent theories of continuum plasticity postulate that for a given state of a material, there exists a function $f(\underline{\sigma})$ of the stress such that the material is elastic for:

$f(\underline{\sigma}) \le 0$, or for $f(\underline{\sigma}) = 0$ and $\dfrac{\partial f}{\partial \sigma_{ij}} \dot{\sigma}_{ij} < 0$

and plastic for: $f(\underline{\sigma}) = 0$ and $\dfrac{\partial f}{\partial \sigma_{ij}} \dot{\sigma}_{ij} \ge 0$

where $\dot{\sigma}_{ij}$ is the stress rate. The normality rule associated to the yield function expresses relationships between the stress and plastic strain rate tensor ($\dot{\underline{\varepsilon}}^p$). The yield function gives the stress at which yielding occurs for a given stress state and its gradient (normality rule) gives the direction of the plastic strain rate:

$$\dot{\underline{\varepsilon}}^p = \dot{\lambda} \frac{\partial f(\underline{\sigma}, \bar{\varepsilon}^p)}{\partial \underline{\sigma}}, \tag{1.9}$$

where, $\dot{\lambda}$ is the plastic multiplier.

The hardening law expresses the evolution of the yield surface during deformation. Isotropic and kinematic hardening represent, respectively, the yield surface homothetic dilation and translation.

The yield function itself can be either isotropic (von Mises, Tresca, Hosford…) or anisotropic (Hills, Hosford, Barlat…). The next section introduces briefly some standard yield functions.

1.4.1.1 Isotropic yield function

Isotropic yield functions describe materials with isotropic plastic properties. The equation of the boundary of the yield function involves all components of the stress tensor and the hardening variable is reduced to a scalar variable in the case of isotropic hardening. In this section the most common isotropic plasticity criterion (von Mises) is presented, further details can be found in [Lemaître and Chaboche 1994].

1.4.1.1.1 Von Mises criterion

The von Mises Criterion [Mises 1928], also known as the maximum distortion energy criterion, octahedral shear stress theory, or Maxwell-Huber-Hencky-von Mises theory, is often used to estimate the yield of ductile materials. Since the trace of the stress tensor does not play an active role in plasticity, a simple idea consists in using the second invariant of the deviatoric stress. This produces an ellipsoid in the space of the symmetric stress tensors with a criterion which is independent of the hydrostatic pressure. Denoting σ_y the yield stress in tension, $\underline{s}$ the deviatoric stress tensor, and s_I, s_{II}, s_{III} the principal deviatoric stress components, the yield surface is given by:

$$f(\underline{s}) = ((s_I - s_{II})^2 + (s_{II} - s_{III})^2 + (s_{II} - s_{III})^2)^{1/2} - \sigma_y \tag{1.10}$$

1.4.1.1.2 Tresca criterion

The von Mises criterion involves the maximum shear in each principal plane, $(s_i - s_j)$. On the contrary, the Tresca criterion [Tresca 1868] takes only the largest. As in the previous case, hydrostatic pressure does not modify the value of the criterion. Instead of having a regular surface like von Mises, the Tresca criterion is only piecewise linear.

$$f(\underline{s}) = \max_{i,j=I,II,III} \left| s_i - s_j \right| - \sigma_y \tag{1.11}$$

Fig. 1.38 represents the superposition of the two criteria in generalized plane stresses. These criteria coincide under some loading conditions: uniaxial tension-compression, biaxial tension-compression. However, the criteria disagree in shear loading (second bisector), i.e. the ratio between shear and tensile stress is different (1/2 vs. 1/√3). Fig. 1.38 shows no Bauschinger effect as σ_y in tension equals σ_y in compression. The isotropy is characterized by the symmetry of bisectors.

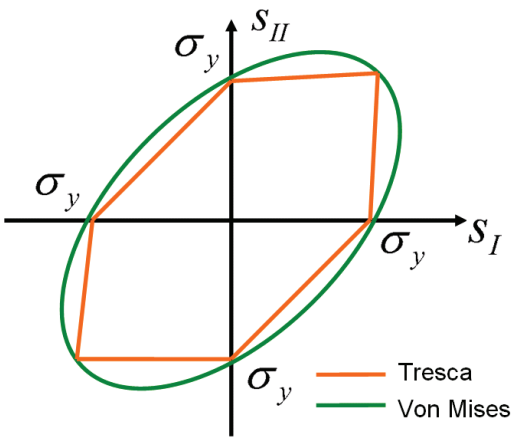

Figure 1.38. Comparison of Tresca and the von Mises criteria in biaxial tension.

1.4.1.1.3 Hosford criterion

The Hosford yield criterion for isotropic materials is a generalization of the von Mises yield criterion [Hosford 1972]. This is also a criterion independent of the hydrostatic pressure. It has the following form:

$$f(\underline{s}) = (|s_I - s_{II}|^n + |s_{II} - s_{III}|^n + |s_I - s_{III}|^n)^{1/n} - \sigma_y \tag{1.12}$$

where s_i, $i = I, II, III$ are the principal stresses, n is a material-dependent exponent.

When $n = 1$ or n goes to infinity the Hosford criterion reduces to the Tresca yield criterion. When $n = 2$ the Hosford criterion reduces to the von Mises yield criterion. This criterion gives possible intermediate descriptions of the plastic behavior, between the von Mises and Tresca criteria. Exponent n depends on the type of crystal (bcc, fcc, hcp, etc.) and has a value usually much greater than 2. Common values of n are 6 for bcc materials and 8 for fcc materials.

1.4.1.2 Anisotropic yield functions

It is shown in the literature that the experimental yield surfaces of metallic alloys determined after plastic deformation exhibit an expansion, a translation and a distortion [Lemaître and Chaboche 1994]. The first two events are taken into account by isotropic and kinematic hardening (see section 1.4.2.1). This is not the case for the last one, which is not described by classical models. Kinematic hardening and isotropic hardening induce themselves anisotropy, but the distorted shape of the yield surfaces is due to textures, which are a direct outcome of plastic deformation. As a consequence, many authors proposed new or modified criteria which describe better the shape of the yield surface, as compared to isotropic criteria. Most of them assume the symmetry of the mechanical behavior in tension and compression and as in the case of isotropic criteria, they are independent of the hydrostatic pressure.

1.4.1.2.1 Hill quadratic criterion

The first yield function accounting for orthotropic anisotropy was introduced by R. Hill in 1948 [Hill 1948] and is based on von Mises work. To introduce anisotropy, R. Hill kept the von Mises quadratic form, but added six coefficients to describe the direction-dependent plastic flow properties:

$$f(\underline{s}) = (F(s_{22}-s_{33})^2 + G(s_{33}-s_{11})^2 + H(s_{11}-s_{22})^2 + 2Ls_{23}^2 + 2Ms_{13}^2 + 2Ns_{12}^2)^{1/2} - \sigma_y \quad (1.13)$$

The 6 anisotropy parameters are the F, G, H, L, M, N variables. Even today, its easy FEM implementation and identification based only on tensile and shear tests allow it to be the most important criterion used in the industrial context. Writing the fourth-order tensor like a 6x6 matrix gives:

$$f^2 = \begin{Bmatrix} S_{11} \\ S_{22} \\ S_{33} \\ S_{12} \\ S_{23} \\ S_{13} \end{Bmatrix}^T \begin{bmatrix} G+H & -H & -G & 0 & 0 & 0 \\ -H & F+H & -F & 0 & 0 & 0 \\ -G & -F & F+G & 0 & 0 & 0 \\ 0 & 0 & 0 & 2N & 0 & 0 \\ 0 & 0 & 0 & 0 & 2L & 0 \\ 0 & 0 & 0 & 0 & 0 & 2M \end{bmatrix} \begin{Bmatrix} S_{11} \\ S_{22} \\ S_{33} \\ S_{12} \\ S_{23} \\ S_{13} \end{Bmatrix} - \sigma_y \quad (1.14)$$

The contribution of the anisotropic behavior through the Hill matrix $[H]$ is shown in Fig. 1.39. The plot of isotropic and anisotropic yield surfaces shows different yield strengths depending on the orientation of the loading, e.g. by comparing σ_0 in the rolling direction σ_0 and σ_{90} in the transverse direction.

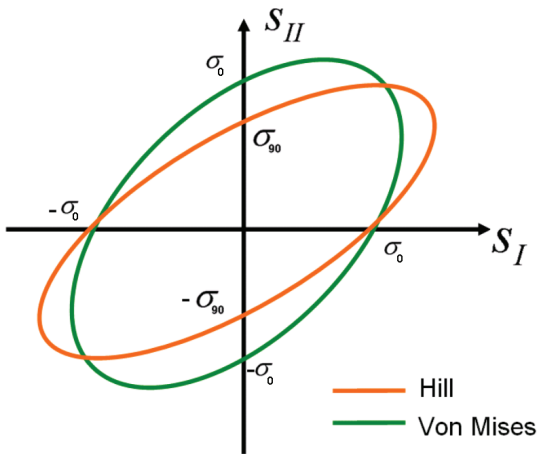

Figure 1.39. Graphic representation of both, Hill 1948 and von Mises plasticity criterions, in the framework of principals stresses (S_I and S_{II}).

Others quadratic criteria have been developed from Hill's (see e.g. [Hu 2007]). They can refine the description of the yield surface from phenomenological or crystallographic considerations. However, the number of experiments needed to identify the yield surface must be kept reasonable.

1.4.1.2.2 Hill non quadratic criterion

In 1979, R. Hill [Hill 1979] developed a non-quadratic criterion from his quadratic criterion, considering a symmetric behavior in tension and compression. The expression of this criterion in plane stress is:

$$f(\underline{S}) = \left|S_{11}+S_{22}\right|^{m} + \left(\frac{\sigma_t^m}{\tau_c^m}\right) + \left|(S_{11}+S_{22})^2 + 4S_{12}\right|^{m} + \left|S_{11}^2 + 2S_{22}^2 + S_{12}^2\right|^{m/2-1}\left\{-2a(S_I^2 - S_{II}^2) + b(S_I - S_{II})^2\right\} \quad (1.15)$$

where a, b, m are dimensionless parameters that must be identified from experimental tests. σ_t and τ_c are the yield points in traction and shear, respectively.

1.4.1.2.3 Other anisotropic functions

From this date, many yield criteria have been proposed to accurately predict the flow behavior of various materials enhancing the yield surface description and taking into account more and more experimental results. Reviews on these improvements can be found in [Hu 2007]. Many authors must be cited, who tried to give accurate anisotropy predictions: [Barlat and Brem 1991], [Karafillis and Boyce 1993], [Banabic *et al.*, 2003], [Barlat *et al.*, 2003], [Cazacu *et al.*, 2006]. In their approaches, anisotropy is introduced by means of a linear stress transformation (combinations of the stress components, based on linear transformation, used in yield function). The main advantage is the easy development of convex formulations which lead to numerical simulations stability, as explained in [Rauch *et al.,* 2011].

All of these formulations are more and more complicated and some of them cannot even take a completely analytical form. For this reason, many authors still prefer to use Hill's quadratic criterion rather than developing new theories. In his paper, [Hu 2007] presents a complete list of these authors using models based on Hill's function and explains that if the selected experimental results are obtained under conditions close to those of applications, Hill's criterion remains a reasonable choice. Moreover if the stress states of applications can be restricted within a specific range, Hill's model can predict the physical process at an acceptably accurate level. However, a problem appears when the real physical problem involves many kinds of stress states and needs a continuous yield model. This explains why [Hu 2007] proposes a new model that uses multiple yield systems which are able to generate a continuous yield surface in stress space.

After defining the shape of the yield surface, one must now define its evolution over the cyclic plastic deformation, as the case in cold pilgering.

1.4.2 Cyclic behavior

Cyclic behavior is often distinguished from the loading conditions (see Fig. 1.40). In the first case, the simplest, the device is subjected to a uniaxial stress field. Laboratory tests often use uniaxial conditions, however, most of the time; service conditions impose multiaxial stress fields.

In multiaxial loading, the case of proportional loading is characterized as follows [Caillet 2007]: at any point M of the solid, on a cycle, the stress tensor $\underline{\sigma}(M,t)$ is proportional to a tensor $\Gamma(M)$ independent of time; the proportionality factor is a monotonic function of time α (t) such as:

$$\alpha(0)=0 \text{ and } \underline{\sigma}(M,t)=\alpha(t)\Gamma(M) \tag{1.16}$$

Under these conditions, the principal directions of the stress tensor (variables at each point) remain constant during loading. In this context a uniaxial load is necessarily proportional. If the previous conditions (Eq. 1.16) are not fulfilled, the loading is called non-proportional. Finally, the load may be periodic, which is the case most frequently encountered in the literature, or random (see Fig. 1.40).

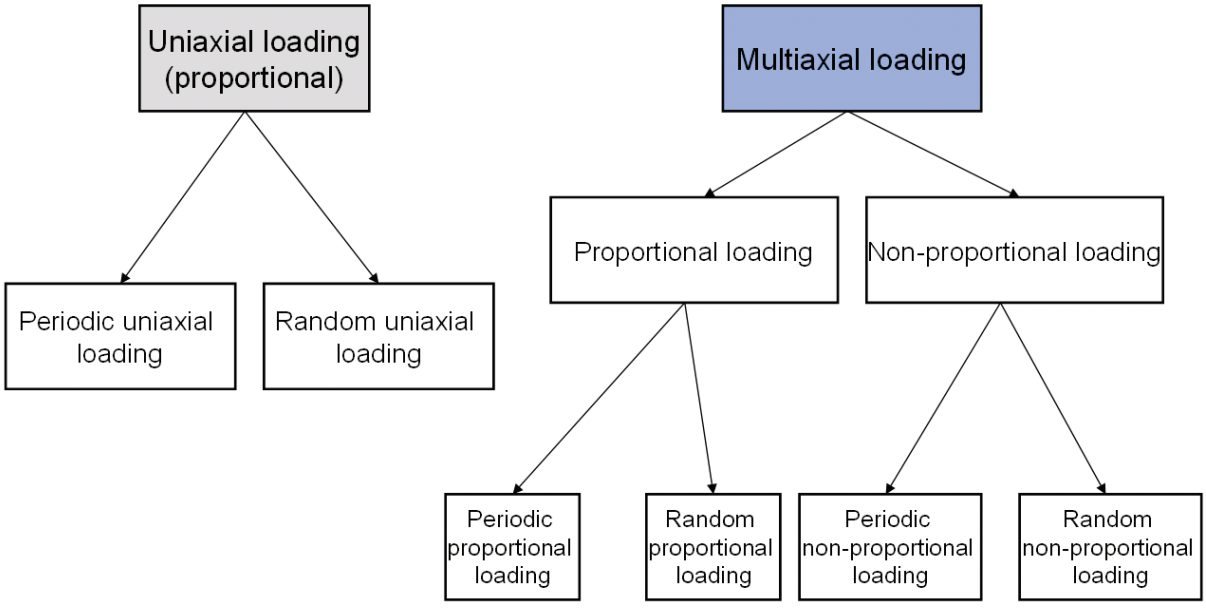

Figure 1.40. The different types of cyclic loading [Caillet 2007].

1.4.2.1 Uniaxial cyclic loading

Uniaxial loading is a particular case of proportional loading. Prescribing a strain path with symmetrical bounds in tension and compression is the basic experiment used to characterize cyclic plasticity. Expressing the effect of hardening is a very complex task, which closely depends on the class of material. Some materials even present hardening and then softening behavior during cyclic loading, for example. In addition, the nature of the hardening can be modified under complex loading paths or by aging of the material. In uniaxial cyclic loading, the main types of hardening usually considered are the isotropic and the kinematic hardening [Lemaître and Chaboche 1994].

1.4.2.1.1 Isotropic hardening

The isotropic hardening model is based on the assumption that the yield surface expands uniformly in the stress space as yielding occurs. The surface does not translate or change shape.

Isotropic hardening is generally used to express the cyclic evolution of the material strength with respect to the plastic flow. The isotropic hardening R is related to the density of dislocations or flow arrests and it represents the growth/decrease in size of the yield surface. The dimension control of the elasticity domain is often given by a law of type [Chaboche *et al.*, 1979]:

$$\dot{R} = b(Q - R)\dot{p} \tag{1.17}$$

or

$$R = Q(1 - \exp(-bp)) \tag{1.18}$$

with b and Q being temperature-dependent material parameters.

This law is obtained from conventional tensile tests or other tests to identify the behavior in large deformations such as shear, torsion test or bulge test [Lemaître and Chaboche 1994]. Fig. 1.41 shows a representation of the 3D evolution of the yield surface in the case of isotropic material flow.

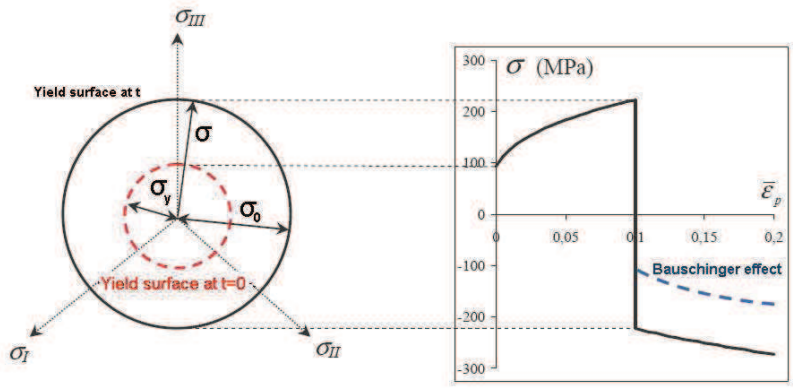

Figure 1.41. Schematics of the isotropic hardening. Left: in the deviatoric plane; right: the stress vs plastic response [Lange 2006].

An isotropic hardening law is generally not enough in situations where components are subjected to cyclic loading. For example, it does not account for the Bauschinger effect, whereby, material yields at lower stress when the direction of loading is reversed (see Fig. 1.41) [Lange 2006].

The behavior under cyclic loading induces a review of the evolution of the amplitude of stress during the cycles depending on the strain amplitude imposed. It is often possible to distinguish two stages of consolidation cycles: a stage of rapid changes in the stress amplitude, and a saturation stage during which the stress amplitude remains constant or almost constant. This is illustrated in Fig. 1.42, where $\Delta\sigma/2$ is the half stress amplitude. A better approximation, given in [Chaboche *et al.*, 1979], [Velay 2003], [Velay *et al.*, 2006], consist in adding several isotropic models such as (Eq. 1.19) allowing the expression to be valid for different saturations rates:

$$R = \sum_{i=1}^{n_2} R_i \qquad R_i = Q_i(1 - \exp(-b_i p)) \tag{1.19}$$

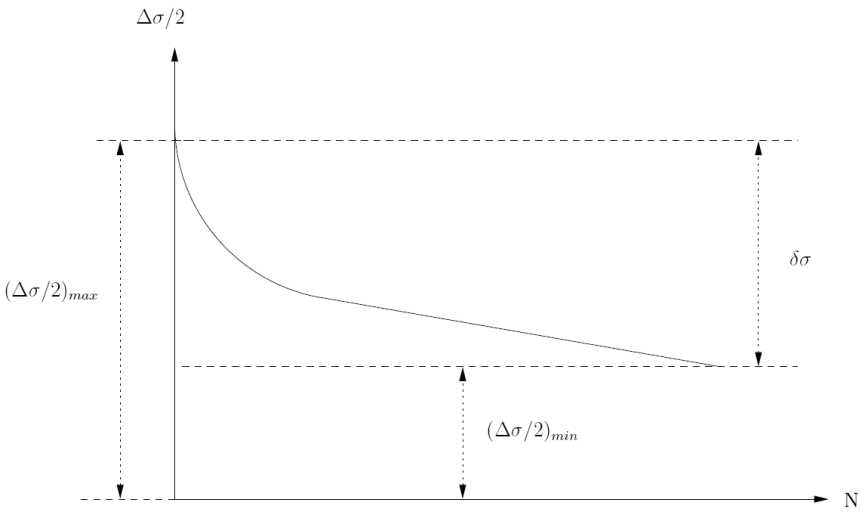

Figure 1.42. Schematic cyclic softening curve [Velay 2003].

1.4.2.1.2 Kinematic hardening

Kinematic hardening rules were developed to model the Bauschinger effect. The model is based on the assumption that the yield surface translates in stress space but does not change size, shape, or orientation as yielding occurs. The kinematic stress tensor $\underline{X}$ represents the center of the yield surface in the stress space (see Fig. 1.43). The kinematic hardening is related to the state of internal (micro) stresses [Chaboche 1989].

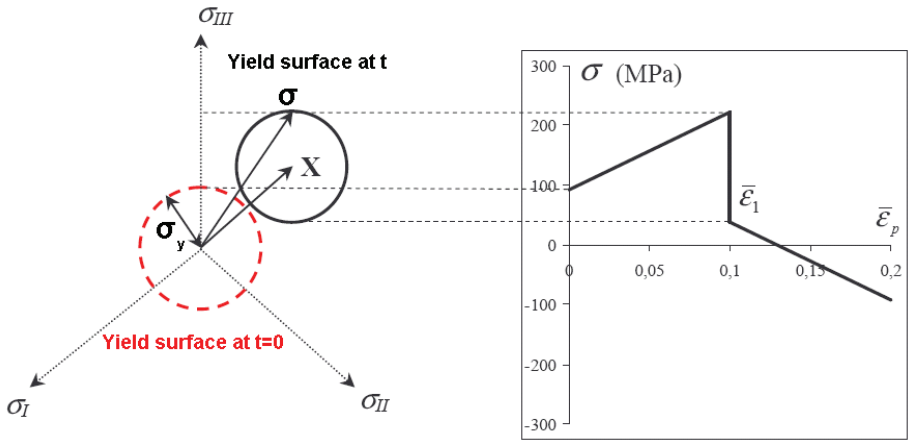

Figure 1.43. Schematics of the Prager's kinematic hardening. Left: in the deviatoric plane; right: the stress vs plastic strain response [Lange 2006].

The simplest model is Prager's linear kinematic hardening [Prager 1945], in which the evolution of the kinematic variable $\underline{X}$ is colinear with the evolution of the plastic strain:

$$\dot{\underline{X}} = \frac{2}{3} C \dot{\underline{\varepsilon}} \tag{1.20}$$

The linearity associated with the stress-strain response (Fig. 1.43) is rarely observed (except perhaps in the regime of significant strains). A better description is given by the model proposed initially by [Armstrong and Frederick 1996] introducing a second term, called dynamic recovery:

$$\dot{\underline{X}} = \frac{2}{3} C \dot{\underline{\varepsilon}} - \gamma \underline{X} \dot{p} \tag{1.21}$$

The second term is colinear with $\underline{X}$ and is proportional to the norm of the plastic strain rate. The evolution of $\underline{X}$, instead of being linear, is then exponential for a monotonic uniaxial loading, with saturation at a value C/γ.

A better approximation, given in [Chaboche *et al.*, 1979], consists in adding several kinematic models such as in (Eq. 1.22), allowing the expression to be valid in a larger domain, and a better description of the soft transition between elasticity and the plastic flow. Fig. 1.44

shows, for the 35NCD16 hard steel, the significant improvement obtained with only two variables, one being linear, with $\gamma = 0$.

$$\underline{X} = \sum_{i=1}^{n_1} \underline{X}_i \qquad \dot{\underline{X}}_i = \frac{2}{3} C_i \dot{\underline{\varepsilon}} - \gamma_i \underline{X}_i \dot{p} \tag{1.22}$$

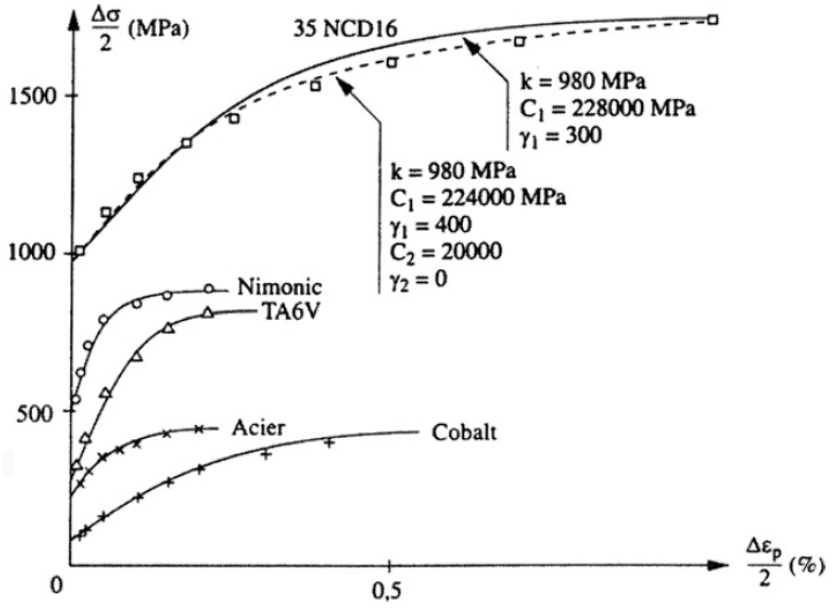

Figure 1.44. Cyclic curves on various materials and their interpretation by the Armstrong and Frederick rule or the multikinematic model [Chaboche 2008].

k in Fig. 1.44 represents the yield stress (σ_y in the thesis notation). More complex combinations can be used, and can be found in [Cailletaud and Saï 1995], [Ohno 1997] for example.

1.4.2.1.3 Mixed hardening

Rather than considering purely isotropic or purely kinematic hardening, real-life materials show in general a combination of both phenomena; that is, under plastic straining, the yield surface expands/reduces and translates simultaneously in stress space. Thus, more realistic plasticity models can be obtained by combining the above laws of isotropic and kinematic hardening [Lemaître and Chaboche 1994].

A hardening model that includes both translation and expansion of the yield surface was proposed first by Hodge (1957) [Lemaître and Chaboche 1994]. This model reproduces well the permanent softening upon reverse loading but not the smooth elastic/plastic transition. A more refined model was then proposed by [Chaboche 1989]. The general equation of the yield surface in the case of coexisting kinematic and isotropic hardening is given by:

$$f = J_2(\underline{\sigma} - \underline{X}) - R - \sigma_y = 0 \tag{1.23}$$

In Eq. (1.23), σ_y is the initial yield stress, $\underline{X}$ the kinematic hardening tensor (or back stress tensor), and R the isotropic hardening.

$J_2(\underline{\sigma} - \underline{X})$, is the second invariant, is defined from the von Mises criterion:

$$J_2(\underline{\sigma} - \underline{X}) = [\frac{3}{2}(\underline{s} - \underline{X}) : (\underline{s} - \underline{X})]^{1/2}, \tag{1.24}$$

where $\underline{s}$ is the deviatoric part of the Cauchy stress tensor $\underline{\sigma}$.

Fig. 1.45 illustrates the mixed hardening in the stress space with the displacement of the center of the yield surface and the dilatation. This model allows describing efficiently the Bauschinger effect. The model parameters can be identified using a semi-automatic identification process [Lange 2006]. This process is performed using an inverse optimization algorithm.

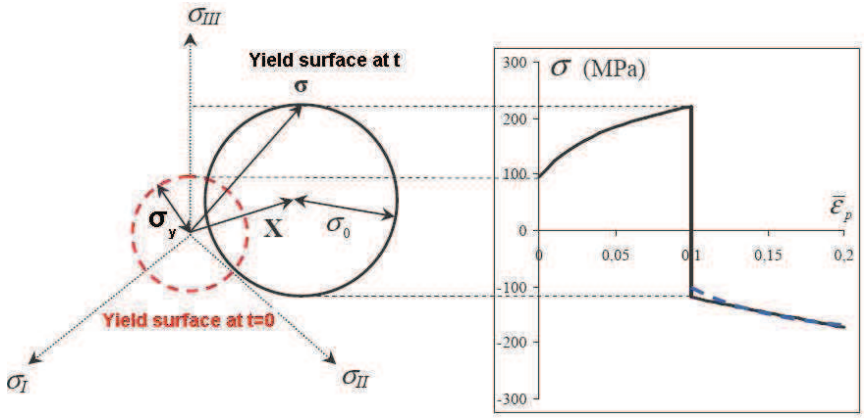

Figure 1.45. Schematics of the Chaboche's mixed hardening. Left: in the deviatoric plane; right: the stress vs plastic response (good representation of Bauschinger effect) [Lange 2006].

1.4.2.2 Multiaxial cyclic loading

The previous section looked at uniaxial testing conditions, and in particular at tension-compression tests, which are the most common and easy to analyze. These tests are however not fully representative of the actual stress fields applied to structural parts. To account for the multiaxial loading, different types of tests have been set up. Multiaxial fatigue has been conducted since the early stages in the history of fatigue testing. Cylindrical tube specimens were first used. They were subjected to solicitations in traction-compression/torsion or traction-compression/ internal pressure or tension-compression /torsion /internal and external pressures [Calloch and Marquis 1999], [Aubin 2001], [Bocher *et al.,* 2001]. These specimens have the advantage of having an almost uniform distribution of stresses and distortions in the active area. Further development continued with bi-traction tests [Aubin 2001], [Bouchou and Delobelle1996a], [Bouchou and Delobelle1996b] or triaxial tension-compression [Calloch and

Marquis 1997]. The former test is complex to analyze because the stresses and strains are not homogeneous in the specimen useful area, it is necessary to use a structural examination to analyze the results.

In uniaxial fatigue, different factors influence the behavior of the material, especially the history of loading, the strain rate and temperature. It will be seen in this section that the hardening under multiaxial loading depends strongly on the loading path. The shape of the loading path and the nature of direction changes have a dominant influence.

1.4.2.3 Loading path influence

For materials that harden cyclically, if non-proportional multiaxial loadings are applied, the cyclic hardening effect can be drastically increased and the stabilized cyclic response can be much more resistant than under equivalent proportional conditions [Chaboche 2008]. One can observe, Fig. 1.46, the responses obtained on a stabilized 316L steel for a tension-compression loading path and a circular loading path of the same amplitude of total controlled strain. At a strain amplitude of 0.5%, the stabilized response is 1.7 times higher for the circular loading path than for the tension-compression loading path.

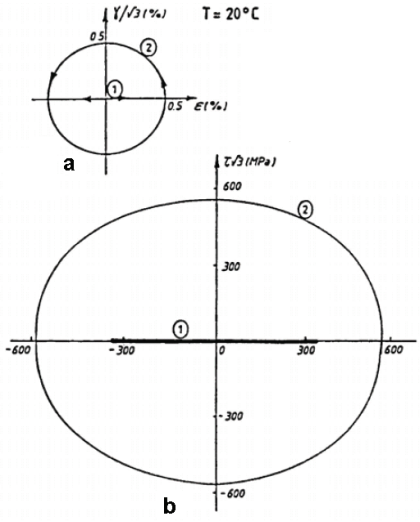

Figure 1.46. Additional hardening in non-proportional loading. (a) Strain path: cyclic proportional loading up to the stabilized cycle (1) followed by a circular path (2) at the same equivalent strain range. (b) Comparison between the stabilized cycle for path (1) and for the path (2) [Benallal and Marquis 1987].

This fact was observed for the first time in OFHC copper, and has been reproduced later on several other materials, especially stainless steels [Tanaka *et al.*, 1985], [Benallal *et al.*, 1989], [Cailletaud and Sai 1995]. Many studies have been carried out to quantify the influence of different loading paths and to classify these paths (see Fig. 1.47) considering the *extra-hardening* under tension-torsion mainly [Tanaka *et al.*, 1985], [Benallal and Marquis 1987], [Benallal *et al.*, 1989], [Tanaka 1994], [Cailletaud and Sai 1995], [Aubin *et al.*, 2003b]. Such effects can be understood from crystal plasticity and dislocation behavior. Under a non-proportional multiaxial

cyclic loading, more slip systems are activated, which increase the number of obstacles for subsequent slip to take place [Chaboche 2008].

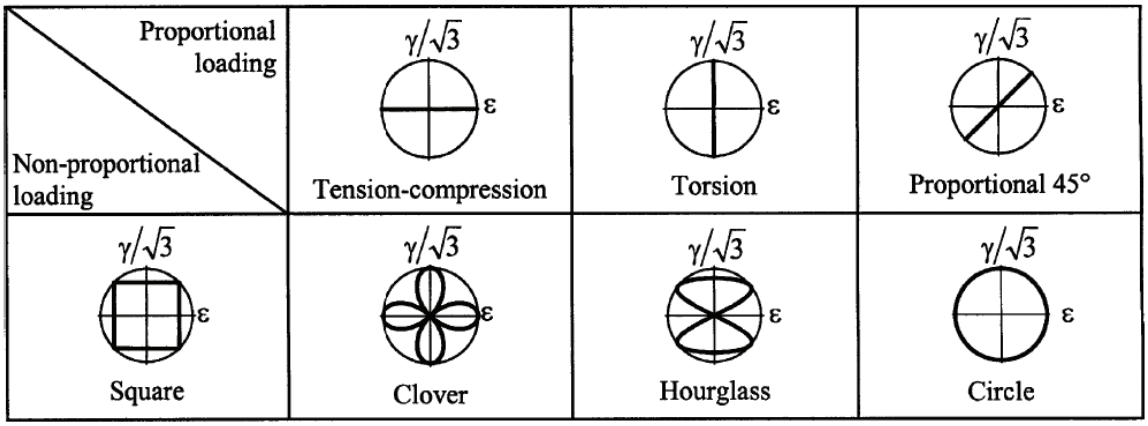

Figure 1.47. Loading paths in the $(\varepsilon, \gamma/\sqrt{3})$ plane [Aubin *et al.*, 2003b].

Fig. 1.48 illustrates the *extra-hardening* in a duplex stainless steel, due to the loading type, when keeping a constant strain amplitude.

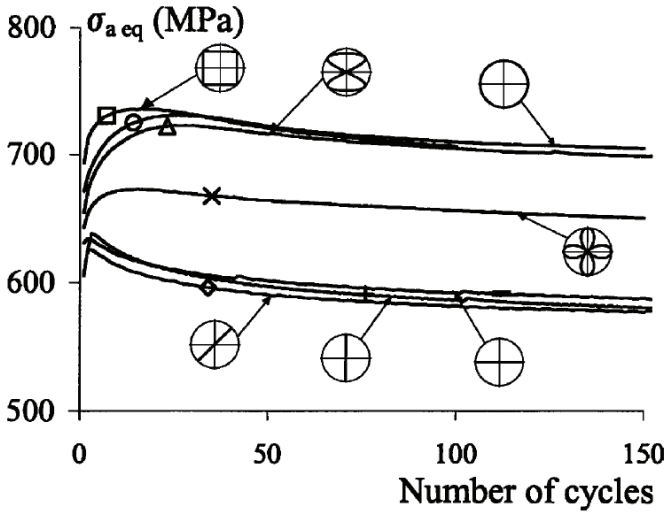

Figure 1.48. Duplex stainless steel hardening - softening curves with strain amplitude of 0.5% [Aubin *et al.*, 2003b].

1.4.2.4 Strain range memory effects

After cyclic hardening and stress amplitude stabilization, and regardless of the type of loading path, some stainless steels can harden again when subjected to a new solicitation with a larger strain amplitude (Fig. 1.49). A new stabilization of the stress amplitude occurs. Several authors have observed that the second stress amplitude stabilization is somewhat affected by the previous cycling, the amplitude of stress on the stabilized cycle is not the same as if the test had been performed directly on a virgin specimen [Tanaka *et al.*, 1985], [Benallal *et al.*, 1989].

Similarly, if the first strain amplitude is imposed again, stress amplitude stabilization occurs at a different level from that reached the first time (Fig. 1.49). This is a memory effect of the strain amplitude. For such materials the cyclic curve (relation between stress range and plastic strain range under stabilized conditions) is no longer a unique relationship and clearly depends on the previous loading histories.

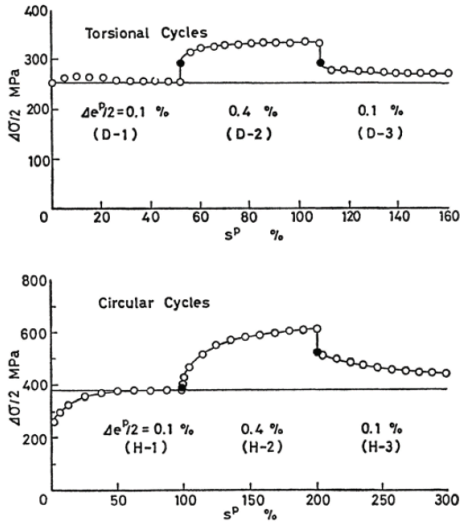

Figure 1.49. 316L steel strain range memory effects at 20℃ for a torsion and circle loading path [Tan aka *et al.*, 1985].

To take into account the plastic strain range memorization, a simple method was proposed in [Chaboche *et al.*, 1979]. Authors introduced a new internal state variable, called q. The memory surface (F) in plastic strain space proposed by [Chaboche *et al.*, 1979] is introduced through:

$$F = \sqrt{\frac{2}{3}\left(\underline{\varepsilon}^p - \underline{\xi}\right):\left(\underline{\varepsilon}^p - \underline{\xi}\right)} - q \le 0 \tag{1.25}$$

Translation of the strain based memory surface is governed by the variable, $\underline{\xi}$ as follows:

$$d\underline{\xi} = \left(1 - \eta_{mem}\right)\left(\underline{n} : \underline{n}^*\right)\underline{n}^* dv \tag{1.26}$$

where η_{mem} is a material parameter and the normal to the strain memory surface ($\underline{n}^*$) is defined as follows:

$$\underline{n}^* = \frac{\underline{\varepsilon}^p - \underline{\xi}}{q}, \tag{1.27}$$

and the exterior unit normal to the yield surface at the loading point is defined as:

$$\underline{n} = \frac{\underline{s} - \underline{X}}{\sqrt{\left(\underline{s} - \underline{X}\right):\left(\underline{s} - \underline{X}\right)}} \tag{1.28}$$

The quantity q is the radius of the memory surface (F) size which is equal to the stabilized plastic strain amplitude for the uniaxial loading. Via this definition, q is in fact equal to the equivalent plastic strain magnitude for any loading path under a constant amplitude loading. The following evolution for changes in the yield surface is proposed in [Chaboche *et al.*, 1979]:

$$Q = Q_0 + (Q_m - Q_0)\left(1 - e^{-2\mu q}\right) \tag{1.29}$$

where Q_m, Q_0, μ are material parameters. Such a memory variable is taken into account in the plastic flow rule by its influence on the asymptotic value of isotropic hardening Q parameter, which now becomes a varying quantity $Q(p)$, p being the accumulated plastic strain (see Eq. 1.17).

The plastic strain range memorization evolution rule, given below, and sketched in Fig. 1.50; takes into account a progressive memorization of the current plastic strain range (under any multiaxial conditions) provided it is larger than those previously encountered:

if $\underline{n} : \underline{n}^* < 0$,

$dq = 0$ and $d\underline{\xi} = \underline{0}$

if $\underline{n} : \underline{n}^* > 0$ and $F = \sqrt{\frac{2}{3}\left(\underline{\varepsilon}^p - \underline{\xi}\right) : \left(\underline{\varepsilon}^p - \underline{\xi}\right)} - q > 0$,

$dq = \eta_{mem}\left(\underline{n} : \underline{n}^*\right)dv$ and $d\underline{\xi} = (1 - \eta_{mem})\left(\underline{n} : \underline{n}^*\right)\underline{n}^* dv$

if $\underline{n} : \underline{n}^* > 0$ and $F < 0$,

$dq = -0.1\eta_{mem}\left(\underline{n} : \underline{n}^*\right)dv$ and $d\underline{\xi} = \underline{0}$

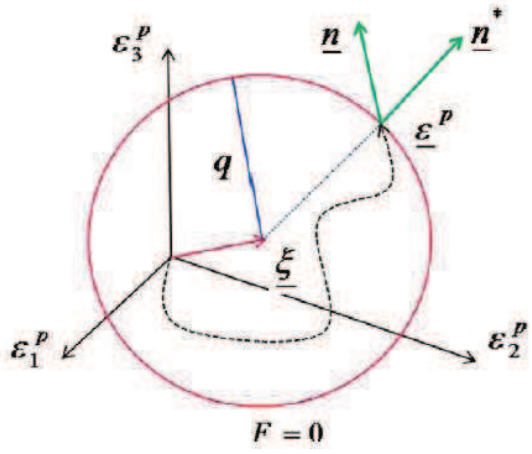

Figure 1.50. Concept of the memory in the plastic strain space from [Chaboche *et al.*, 1979].

In [Nouailhas *et al.*, 1985a-1985b], a more sophisticated model, in which some part of the memory was slowly evanescent, was used in order to describe both monotonic and cyclic hardening of (annealed) 316 stainless steel, but also, with the same model parameters, many

different cold worked initial conditions of the same stainless steel. Chaboche's model in [Chaboche *et al.*, 1979] performs well in simulating uniaxial ratcheting responses, i.e. proportional loading responses [Bari and Hassan 2000], but it fails when performing simulation of multiaxial and quasi-random non-proportional loadings. [Bari and Hassan 2002] proposed an improved kinematic hardening rule incorporating one multiaxial parameter into the Chaboche model. This modified Chaboche model improves the performance in simulating ratcheting responses under multiaxial loading.

1.4.2.5 Non-proportional loading

Non proportional cycles generally induce more significant hardening than proportional ones. In order to distinguish the proportional loadings from the other paths, the angles between vectors representing stress, plastic strain or the rates of these vectors can be introduced. Indeed, in the deviatoric plane, proportional loadings are such that all these angles are null, and for non-proportional loading, they are not. For the description of the non-proportionality, still using macroscopic models (e.g. Chaboche's model), several attempts have been made in the eighties [Tanaka *et al.*, 1985], [Benallal and Marquis 1987]. Benallal and Marquis's model propose that the extra-hardening is completely based on isotropic hardening. On the other hand, some other constitutive models considered the influence of the non-proportionality to be represented in the saturation amplitude of stress due either to kinematic or both isotropic and kinematics hardening [Krempl and Lu 1984], [McDowell 1985], [Abdul-Latif 1996], [Saanouni and Abdul-Latif 1996], [Abdul-Latif and Saanouni 1996], [Taleb *et al.*, 2006], [Abdel-Karim 2009], [Abdel-Karim 2010a], [Abdel-Karim 2010b]. A few examples of literature models are given below.

1.4.2.5.1 Benallal model

One of the simplest and best rules was proposed by Benallal and Marquis [Benallal and Marquis 1987], using a scalar parameter A based on the current tensorial product of the strain and stress rates.

$$A = 1 - \cos^2 \alpha \tag{1.30}$$

where if, $\sqrt{\frac{3}{2}\dot{\varepsilon}_{ij}^{p}\dot{\varepsilon}_{ij}^{p}} \neq 0$, (1.31)

$$\cos\alpha = \frac{\dot{\varepsilon}_{ij}^{p}\dot{s}_{ij}}{\sqrt{\frac{3}{2}\dot{\varepsilon}_{ij}^{p}\dot{\varepsilon}_{ij}^{p}}\sqrt{\frac{2}{3}\dot{s}_{ij}\dot{s}_{ij}}} \tag{1.32}$$

Benallal and Marquis tested also as parameter the angle α between $\underline{\varepsilon}^{p}$ and $\dot{\underline{\varepsilon}}^{p}$; $\underline{X}$ and $\dot{\underline{X}}$; $\underline{s}$ and $\dot{\underline{s}}$. They have concluded that for low values of A, the angle α must be that between the tensors $\underline{X}$ and $\dot{\underline{X}}$, because it is not sensitive to elastic variations.

For proportional loading $\alpha = 0$ and $A = 0$ whereas for a non-proportional loading $0 < A \leq 1$.

The asymptotic value Q of R, which represents the size of the yield surface is a constant in the classical formulation (see Eq. 1.17) and is considered here as a new variable. Its evolution law, which depends on the non-proportionality parameter A defined above, is:

$$\dot{Q} = [(d - f)A + f](Q_{AS} - Q)\dot{p}\,, \tag{1.33}$$

with

$$Q_{AS} = \frac{gAQ_{\infty} + (1 + A)Q_0}{gA + (1 + A)}\,, \tag{1.34}$$

d, f, Q_{∞}, Q_0, g are material dependent parameters.

To improve capabilities of the Chaboche model concerning the description of the isotropic non-proportional hardening, the simplified version of Benallal and Marquis is chosen by many authors, e.g. [Calloch and Marquis 1999], [Bari and Hassan 2000], [Kang *et al.*, 2002], [Kang *et al.*, 2004], [Taleb *et al.*, 2006], it is described below.

It takes: $g = 1$, $Q_0 = 0$ and $f = 0$ which leads to:

$$\dot{Q} = dA[Q_{AS} - Q]\dot{p} \tag{1.35}$$

with,

$$Q_{AS} = AQ_{\infty} \tag{1.36}$$

The non-proportional effect interacts with the flow rule by increasing the limit of isotropic hardening $Q(A)$ in a similar way to the method of strain range memorization discussed in section 1.4.2.4. However, accuracy reduces as the degree of non-proportionality in a loading cycle changes abruptly (e.g. Fig. 1.49). Benallal and Marquis's parameter computation of non-proportionality is instantaneous and lacks memory features. It was demonstrated by [Jiang and Kurath 1997] that Benallal's determination of non-proportionality was unreasonable for some strain cycling paths, such as the butterfly path.

Nonetheless, this model is frequently chosen for its simplicity despite certain drawbacks (creep test and cross hardening test where the angle between the deviatoric stress and the plastic strain rate is zero between the sequences). For more details about these drawbacks the reader may refer to [Taleb and Cailletaud 2010].

1.4.2.5.2 Tanaka model

Another interesting approach was given by [Tanaka 1994], introducing a structural tensor as well as a non-proportionality parameter. This model links the magnitude of the cross effect to

the accumulated plastic strain. Tanaka introduces an internal state variable $\underline{\underline{C}}$ describing the internal dislocation structure. $\underline{\underline{C}}$ describes the directional characters of the structure and is a fourth order tensor. $\underline{\underline{C}}$ evolves gradually during the cyclic loading process. The evolution equation is given by:

$$\dot{\underline{\underline{C}}} = c_c\left(\underline{u} \otimes \underline{u} - \underline{\underline{C}}\right)\dot{p}\,, \tag{1.37}$$

where c_c is a material constant, the symbol $\otimes$ indicates the tensor product and $\underline{u}$ is the normalized plastic strain rate vector:

$$\underline{u} = \frac{\dot{\underline{\varepsilon}}^p}{\left\|\dot{\underline{\varepsilon}}^p\right\|} \tag{1.38}$$

The components of the tensor $\underline{\underline{C}}$ have zero values for an initially isotropic material and gradually reach the target value $\left(\underline{n} \otimes \underline{n}\right)$ that depends on the plastic strain direction of the loading increment [Tanaka 1994].

Then, Tanaka proposes an associated non-proportionality parameter A (similar to Benallal):

$$A = \sqrt{\frac{tr\left(\underline{\underline{C}}^T\,\underline{\underline{C}}\right) - \underline{n}\,\underline{\underline{C}}^T\,\underline{\underline{C}}\,\underline{n}}{tr\left(\underline{\underline{C}}^T\,\underline{\underline{C}}\right)}} \tag{1.39}$$

A and $\underline{\underline{C}}$ are memory parameters [Tanaka 1994], [Jiang and Kurath 1997]. The tensor $\underline{\underline{C}}$ describes the slow evolution of the internal dislocations structure induced by plastic deformation. If a material is loaded in tension-compression, then the dislocation substructure is formed in a particular direction. After the end of these loading cycles, if the material is subjected to torsion, then the previous dislocation structure is destroyed and a new structure is formed (e.g. see Fig. 1.51). This loading sequence is incorporated in the tensor $\underline{\underline{C}}$ by [Tanaka 1994].

$A = 0$ represents the proportional loading and the maximum value of $A = 1$ represents the highest degree of non-proportionality for the 90-degree out of phase loading. For an intermediate degree of non-proportionality, A varies between 0 and 1.

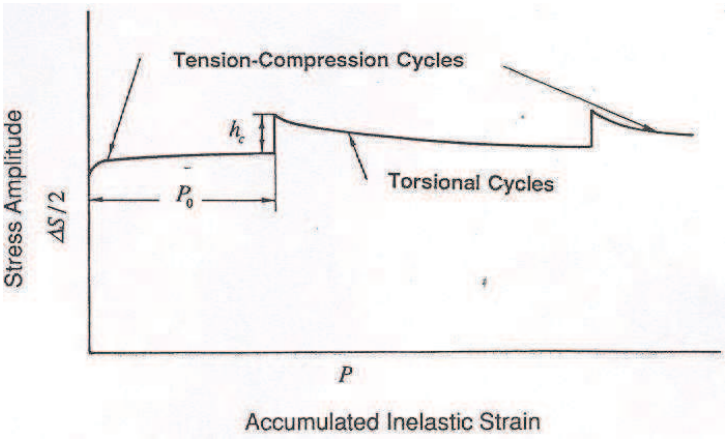

Figure 1.51. Schematic figure of the cross-hardening phenomena [Tanaka 1994].

The evolution of the isotropic hardening surface depends not only on the accumulated plastic strain (p), but is also function of another variable q , which allows to take into account the strain range. $\underline{Y}$ is the center of this surface and q its radius. The introduction of this variable $\underline{Y}$ allows taking into account the cyclic stress relaxation under non-symmetric loadings.

$$\dot{\underline{Y}} = r_y\left(\underline{\varepsilon}^p - \underline{Y}\right)\dot{p} \tag{1.40}$$

$$q = \left\|\underline{\varepsilon}^p - \underline{Y}\right\| \tag{1.41}$$

The asymptotic isotropic hardening value then depends of the loading strain range through the equations:

$$\dot{R} = b(Q - R)\dot{p} \tag{1.42}$$

$$Q = A\left(q_N(q) - q_p(q)\right) + q_p(q) \tag{1.43}$$

$$q_P(q) = a_P q + b_P\left(1 - e^{(-c_P q)}\right) \tag{1.44}$$

$$q_N(q) = a_N q + b_N\left(1 - e^{(-c_N q)}\right) \tag{1.45}$$

q_N is the target value for the case of non-proportional hardening ($A = 1$), and q_P , on the other hand, is the value for proportional hardening ($A = 0$). a_P , b_P , c_P , a_N , b_N , c_N are material parameters.

Satisfactory stress predictions were obtained for all multiaxial strain paths investigated in this work for two materials (1050 QT steel and 304L stainless steel), employing the non-proportionality parameter proposed by [Tanaka 1994] coupled with a simplified form of the Armstrong-Frederick incremental plasticity model [Armstrong and Frederick 1966].

1.4.2.5.3 Abdul-Latif model

For some materials, the size of the yield surface varies slightly. This is the case of ODS steels, which will be analyzed in details in this work. Therefore, the isotropic hardening is low, even when dealing with non-proportional loadings. Benallal and Marquis and Tanaka models are based on the dependence of the isotropic hardening on the non-proportional loading. These models allow to simulate the extra-hardening but not the physical mechanisms.

Abdul-Latif [Abdul-Latif and Saanouni 1996] observed for the Waspaloy, that both the isotropic and kinematic hardening depend of the non-proportional loading. For that reason, the authors modified the Benallal and Marquis model. The isotropic hardening R and the kinematic hardening $\underline{X}$ were then both depending of the Benallal and Marquis's parameter A.

1.4.2.6 Remarks

The most suitable model including non-proportionality effects appears to be the Tanaka model, which can describe the mechanical behavior of 316 stainless steel, 304L stainless steel and 1050 QT steel at room temperature under almost all loading conditions except the mechanical ratcheting and cyclic creep. The implementation of Tanaka type models remains rather complex and involves a large number of parameters, which is an issue in the context of FEM simulations of pilgering.

One can conclude that cyclic plasticity models deal in general with an important number of parameters and require calibration from various types of test. For example, 304 stainless steel requires 47 model parameters in [Krishna *et al.*, 2009] to account for different mechanical effects (ratcheting, strain range dependence, non-proportional loading and memory effect). The model parameters are determined using responses from: uniaxial stress controlled test, uniaxial tensile/compression strain controlled test, shear ratcheting and tension-torsion ratcheting tests, 90° out-of-phase strain/stress-controlled experimen ts [Hassan *et al.*, 2008] and finally, triaxial tension-compression test [Calloch and Marquis 1999].

1.5 Conclusions

This Chapter has been dedicated to a bibliography review in order to present the scientific background of the thesis. Three main parts have been presented.

In the first section it is noticed that the fabrication route proposed with pilgering passes and intermediate heat treatments is efficient to ensure a safe manufacturing of Fe-9CrODS and Fe-14CrODS cladding tubes. For Fe-9CrODS steel the role of the phase transformation is crucial to reduce the morphological and the crystallographic anisotropies induced by the manufacturing process. The intermediate heat treatments are efficient in softening the raw tube and changing the elongated grain structure into an equiaxed grain structure. On the contrary, for Fe-14CrODS, it is concluded that if recrystallization took place at intermediate stages of the fabrication route a

recrystallized microstructure cannot be obtained at final heat treatment. A two-step annealing is useful to soften the cold-rolled tubes without premature recrystallization in intermediate heat treatments. Based on previous studies a hardness value below 400 Hv_1 is needed to avoid damage during manufacturing. Reduction ratio per pass is limited approximately to 20% - 25%. However, fabrication routes leading to different work-hardening rates and Q factors (characteristic parameters of cold pilgering), have not been optimized yet. A robust numerical cold pilgering model could be useful to address this task.

In the second part, a literature survey of 2D and 3D analytical models and 2D and 3D FEM cold pilgering models was carried out. It is pointed out that all the models, either analytical or FEM were performed for VMR pilgering mills. No literature was reported on the modeling of HPTR pilgering mills. It seems to be a new issue.

The first analytical models were intended to find the vertical die forces, in order to better design the tooling. The 2D analytical approach is an outcome of the strip rolling method. The 3D analytical approach is more rigorous, and based on the plasticity theory. These simple approaches have disclosed the main features of the process, but due to the geometrical complexity of pilgering, the details of the stress patterns must be determined by the finite element method. Some authors have focused on a better understanding of the material flow to minimize the defects on the tubes or to predict the mechanical characteristics of the formed tube. The effect of the plastic shearing ε_{rz} on damage and texture evolution is underlined. ε_{rz} is strongly dependent of the lubrication conditions. [Aubin *et al.*, 2000], [Girard *et al.*, 2001] concluded that the Latham and Cockroft damage function is a relevant model to detect defects frequency. Additionally, [Girard *et al.*, 2001] performed texture evolution simulations under pilgering, using a visco-plastic polycrystalline self-consistent model [Lebensohn and Tome 1993]; their numerical results are in agreement with the experimental ones. [Davies *et al.*, 2002] for titanium, [Mulot 1997] for Zircaloy, carried out experimental tests in order to quantify the cladding tubes anisotropy. They showed that the anisotropic Hill's model is well-adapted to describe the cladding tubes yield surface. However, Hill's model was not included in reported FEM numerical simulations.

An original approach to steady-state (or pseudo-steady state) isotropic elastic-plastic flow computation proposed by [Montmitonnet *et al.*, 2002], [Lodej *et al.*, 2006] must be highlighted. It saves computation time and allows optimized meshes to be used; cold pilgering can be simulated at a reasonable computational cost. A drawback of this approach is the "transition long tube geometry" difficult to obtain experimentally, and any change in the fabrication route, would lead to a new one.

Mainly three materials were studied: Zircaloy, titanium and copper. For the time being ODS steels are not yet modeled in pilgering conditions.

It is concluded in [Lodej *et al.*, 2006] that 3D FEM computation can bring a lot of understanding on the mechanical details of this complex process and can be used to carry out parameters process optimization. Nevertheless, a lack of realistic constitutive laws is noticed regarding literature. Actually, most of the 3D FEM simulations used isotropic and monotonic constitutive models. Anisotropy due to crystallographic and morphological textures is however inherited from the hot extrusion process or from intermediate cold pilgering. Furthermore, the

complex, non-proportional, multi-axial, and non-periodic strain path must have an important influence on the mechanical response of the material.

The last section of the bibliography review is assigned to describing pertinent steel constitutive laws. Tresca's and von Mises' isotropic yield functions are too simple to correctly predict output geometries and plastic properties for complex deformation path. Anisotropic yield functions have been developed based on new criteria. Yield functions are more and more complicated and many mechanical tests are sometimes required to correctly identify the model parameters. When dealing with cyclic loading, different effects must be taken into account: multi-axiality, loading path, strain range memory, and even dislocation structure. The ODS steels mechanical behavior has not been studied yet in these conditions, according to the literature.

1.6 Résumé en français

Ce Chapitre est consacré à une revue bibliographique, afin de présenter le contexte scientifique de la thèse. Trois parties principales ont été présentées.

Dans la première partie, il a été constaté que la gamme de fabrication proposée avec des passes de laminage et les traitements thermiques intermédiaires, est efficace pour assurer une fabrication des tubes de gainage en Fe-9CrODS et Fe-14CrODS. Pour l'acier Fe-9CrODS, le rôle de la transformation de phase est crucial pour réduire la morphologie et les anisotropies cristallographiques induites par le laminage à pas de pèlerin. Les nuances martensitiques subissent une transformation de phase de ferrite α en austénite γ vers 800-900℃, qui présente l'avantage de permettre d'effacer efficacement l'accumulation de l'écrouissage due au laminage, et d'obtenir un matériau restauré qui sera ensuite facilement déformable. Les traitements thermiques intermédiaires réalisés entre les passes de laminage, doivent ainsi permettre de repasser dans le domaine austénitique. La nuance Fe-14CrODS ne présentant aucune transformation de phase, la restauration de la microstructure est plus complexe. Il est conclu pour l'acier Fe-14CrODS, que si la recristallisation a eu lieu aux stades intermédiaires de la gamme de fabrication, une microstructure recristallisée ne peut pas être obtenue dans le traitement thermique final. Un processus en deux étapes de recuit est utile pour adoucir les tubes laminés à froid sans recristallisation dans les traitements thermiques intermédiaires. Sur la base des études précédentes, une valeur maximal de dureté de 400 H_{V1} est nécessaire pour éviter des dommages pendant le laminage. L'écrouissage par passe est limité approximativement à 20% - 25%. Cependant, les gammes de fabrication menant à différents taux d'écrouissage et à des facteurs *Q* (paramètres caractéristiques de laminage à froid), n'ont pas encore été optimisées. Un modèle numérique robuste de laminage à pas de pèlerin à froid peut être utile afin d'aborder cette tâche.

Dans la deuxième partie, une étude bibliographique des modèles 2D et 3D analytiques et des modèles 2D et 3D FEM du laminage à pas de pèlerin à froid a été réalisée. Il est souligné

que tous les modèles, analytiques ou éléments finis ont été effectués pour les laminoirs de type VMR laminage. La littérature est peu abondante sur la modélisation des laminoirs de type HPTR.

Les premiers modèles analytiques ont eu pour but de retrouver les efforts verticaux de laminage ou efforts de séparations des matrices. Ensuite, les auteurs se sont attachés à mieux connaître l'écoulement du matériau au cours du laminage afin de minimiser les défauts sur les tubes ou de connaître les caractéristiques du tube fini. L'approche 3D analytique est plus précise, elle est basée sur la théorie de la plasticité. Ces approches simples ont divulgué les principales caractéristiques du processus, mais en raison de la complexité géométrique du laminage à pas de pèlerin, les détails du chemin des déformations et des contraintes doivent être déterminés par la méthode des éléments finis. Certains auteurs ont mis l'accent sur une meilleure compréhension de l'écoulement de la matière afin de minimiser les défauts sur les tubes ou de prédire les caractéristiques mécaniques du tube fini. L'effet du cisaillement plastique sur les dommages et l'évolution de la texture sont soulignés. ε_{rz} est fortement dépendante des conditions de lubrification. [Aubin *et al.*, 2000], [Girard *et al.*, 2001] ont conclu que le critère des dommages de Latham et Cockroft est un modèle pertinent pour détecter la fréquence des défauts. En outre, [Girard et al, 2001] ont effectué des simulations sur l'évolution de la texture pendant le laminage, en utilisant un modèle viscoplastique polycristallin auto-cohérent [Lebensohn et Tome 1993]; leurs résultats numériques sont en accord avec les résultats expérimentaux. [Davies *et al.,* 2002] pour le titane, [Mulot 1997] pour le Zircaloy, ont effectué des essais expérimentaux en vue de quantifier l'anisotropie des tubes. Ils ont montré que le modèle anisotrope de Hill est bien adapté pour décrire la surface de charge de tubes. Toutefois, le modèle de Hill n'a pas été inclus dans les simulations FEM.

[Mulot *et al.*, 1996] ont créé un modèle éléments finis 3D du procédé. Il s'agit d'un modèle simulant un seul coup de cage du procédé pour un tube en Zircaloy. Pour cela, un essai expérimental a été lancé et interrompu une fois que le tube recouvrait tout le mandrin. La géométrie du tube a ensuite été mesurée avec une machine haute précision et la géométrie a été implémentée dans le modèle éléments finis. Les auteurs ont ensuite comparé les résultats de cette simulation avec un modèle semi analytique. La simulation a mis entre autre en évidence les variations de la contrainte longitudinale à une section donnée du tube (zones en fond de cannelure sollicitées en compression et zones aux dépouilles sollicitées en traction), ainsi que le chemin de déformation hélicoïdal, la vague de front de matière créée par le passage des cannelures.

[Montmitonnet *et al.*, 2002] se sont ensuite appuyés sur ce modèle pour prédire l'état mécanique du tube au cours de l'intégralité du procédé à partir de la simulation de deux coups de cage. En effet, les auteurs considèrent le procédé comme quasi-périodique, une fois que le tube recouvre tout le mandrin. Ainsi, la simulation d'un coup de cage couplée aux mouvements rigides (avances et rotations du tube) devrait être suffisante pour reconstruire l'histoire mécanique d'un point du tube au cours de l'intégralité du procédé. En réalité, les auteurs ont démontré que la simulation de deux coups de cage était préférable. Pour chaque coup de cage, ils n'ont simulé que l'aller en considérant que le retour induisait des déformations purement élastiques. Ils partent de champs de déformations et contraintes initiaux nuls. Leurs résultats donnent donc l'incrément de déformation causé par le coup de cage. En revanche, cela implique que les contraintes ne sont valables que pour un matériau non écrouissable.

Cette méthode d'extrapolation de l'histoire mécanique du tube a ensuite été reprise [Lodej *et al.*, 2006]. Cette fois-ci, la méthode est étendue aux matériaux écrouissables. Pour cela les auteurs déduisent l'état de déformation du tube à partir de la géométrie obtenue par les mesures. La simulation de quatre coups de cage est nécessaire pour la convergence des résultats initiaux. Un maillage structuré a été utilisé pour le tube afin d'obtenir des champs mécaniques plus réguliers. Dans cette étude, les auteurs ont implémenté un outil de post-traitement qui permet de reconstruire directement les champs de contraintes et déformations du tube au cours de l'intégralité du procédé. Ainsi, ils montrent qu'un point matériel du tube subit au cours du procédé, des phases alternées de compression et de traction, ce qui engendre un phénomène de fatigue oligocyclique.

Un inconvénient de cette approche est la *géométrie de transition du tube long*, difficile à obtenir expérimentalement, et tout changement dans la gamme de fabrication, conduirait à une nouvelle mesure du profil pseudo stationnaire. Trois matériaux ont été principalement étudiés: Zircaloy, titane et cuivre. Pour le moment, les aciers ODS ne sont pas encore modélisés dans des conditions de laminage. Il est conclu dans [Lodej *et al.*, 2006] que le calcul 3D par FEM peut apporter beaucoup de compréhension sur les détails mécaniques de ce procédé complexe et peut être utilisé pour réaliser l'optimisation des paramètres procédés. Néanmoins, une loi de comportement réaliste n'a été jamais utilisée dans la littérature. En fait, la plupart des simulations (3D FEM) ont utilisé des modèles de comportement isotrope monotone. L'anisotropie, due à des textures cristallographiques et morphologiques héritées du procédé d'extrusion à chaud ou à partir de laminage à froid intermédiaire, n'est pas prise en compte dans les simulations numériques. Par ailleurs, le chemin de déformation complexe devrait avoir une influence importante sur la réponse mécanique du matériau.

La dernière partie de l'étude bibliographique est dédiée à la description des lois de comportement des aciers. Le critères (fonctions de charge décrivant l'évolution de la surface de charge) isotropes et anisotropes ont été introduits afin de pouvoir représenter le comportement plastique des matériaux dans un code numérique. Les premiers critères apparus sont ceux de Tresca et de von Mises dans une formulation isotrope, puis ont été étendus afin de mieux correspondre aux résultats expérimentaux. Cependant, dans certains cas, ces fonctions ne permettaient pas encore de prédire correctement les géométries finales et les caractéristiques mécaniques du matériau. C'est pourquoi les critères anisotropes ont été développés. Parmi ces critères, beaucoup sont issus de la modification du critère de von Mises et d'autres ont été créés afin de prendre en compte les résultats expérimentaux. En contrepartie, ces fonctions et l'identification des paramètres sont de plus en plus compliquées.

Lorsque un matériau subi un chargement cyclique à froid, différents effets doivent être pris en compte: la multi-axialité, le chemin de charge, la mémoire des amplitudes de déformation. Le comportement mécanique des aciers ODS n'a pas encore été étudié dans ces conditions, d'après la littérature.

Chapter 2

Process finite element modeling

2.1 Introduction

This Chapter deals with the presentation of different mathematical and numerical modeling conditions of the mechanical problem arising in material forming, through the finite element software Forge3®. This software has been developed since the 80's at CEMEF and is dedicated to forming processes modeling. Its formulation is based on an updated Lagrangian approach and its principal characteristics are:

- a specific software for axisymmetric and plane strain problems,
- a specific software for 3D problems,
- a velocity-pressure mixed formulation,
- a finite element P1+/P1: linear tetrahedron in 3D and linear triangle in 2D with a bubble term, to enrich velocity discretization compared with pressure discretization,
- management of large deformations,
- automatic 2D and 3D remeshing,
- deformable tools,
- Parallel computation for 3D computation, with MPI library for efficient domain partitioning.

The first part of this section will be devoted to the introduction of the mathematical model in material forging. Then, the main equations of the discretization by the finite element method are presented as well as a brief description of the resolution methods used in Forge3®. Next, the results of a full simulation of the HPTR cold pilgering process using an isotropic constitutive law will be analyzed. Several sensitivity studies will be presented as well. A comparison between predicted and measured pilgered steady state tube geometry is made in the last section.

2.2 The mechanical problem

2.2.1 Continuous problem formulation

When forming by plastic deformation is considered, two types of objects are used: non-deformable objects (dies) and deformable objects (billets, tubes, strips…). Each deformable object is considered as a finite domain $\Omega \subset \Re^3$ with its boundary $\partial\Omega \subset \Re^2$. Its behavior is controlled by fundamental principles of continuum mechanics. After introducing the movement description formalism of the point $\vec{x}$ of Ω, the conservation equations governing its equilibrium are developed with the associated boundary conditions. The mechanical problem is shown to be solved using a mixed finite element formulation combining velocity and pressure as primary variables.

2.2.1.1 Movement description

Solving a mechanical problem requires to introduce a formalism for describing the solid displacements. There are two main families. The so-called Lagrangian approach consists in following the evolution of each material point over time, while the Eulerian approach consists in positioning oneself at a point in space and see the material points flow. The approach taken in Forge3® is the updated Lagrangian, which means that the configuration is updated at each time step.

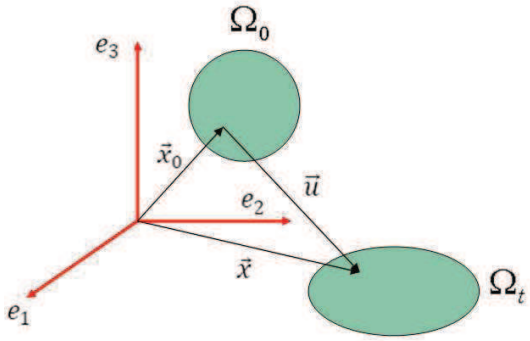

Figure 2.1. Lagrangian displacement description.

At the initial moment $t = 0$, the solid occupies the area noted Ω_0 (Fig. 2.1). By deforming with time, it occupies at the time t the domain Ω_t. To follow the movement of a material point of the solid, there exists a function ϕ, that is a bijection from Ω_0 to Ω_t at any moment t. The position vector $\vec{x}$ of any point of Ω_t, at time t, is given by:

$$\vec{x} = \phi(\vec{x}_0, t) \tag{2.1}$$

Thus the function ϕ defines the position at t of the material point with initial coordinates $\vec{x}_0$. This description is called Lagrangian description of motion, for which it is possible to introduce the Lagrangian displacement field $\vec{u}$ defined by:

$$\vec{x}(\vec{x}_0, t) = \vec{x}_0 + \vec{u}(\vec{x}_0, t) \tag{2.2}$$

The description of motion is completely defined by knowing the initial state and final state of the material point. Forge3® software is based on a movement description of updated Lagrangian type. At each time interval, the movement is defined by a function ϕ^t analogous to (2.1) as:

$$\vec{x}_{t+\Delta t} = \phi^t(\vec{x}_t, t + \Delta t) \tag{2.3}$$

The time-step discretization Δt is chosen small enough to afford the hypothesis of small deformations (between 0.1% and 1% strain at each increment). Under this assumption, the strain rate tensor $\underline{\dot{\varepsilon}}$ and strain $\underline{\varepsilon}$ can be written down as:

$$\underline{\dot{\varepsilon}} = \frac{1}{2}\left(\vec{\nabla}\left(\frac{\partial \vec{u}}{\partial t}\right) + \left(\vec{\nabla}\left(\frac{\partial \vec{u}}{\partial t}\right)\right)^T \right), \qquad \underline{\varepsilon} = \frac{1}{2}\left(\vec{\nabla}\vec{u} + \left(\vec{\nabla}\vec{u}\right)^T\right) \tag{2.4}$$

2.2.1.2 Conservation equations

The equilibrium of the deformable body is governed at all instants by the conservation equations. A first equation is the dynamic equilibrium expressed locally in the Ω domain:

$$div(\underline{\sigma}) + \rho(\vec{\omega} - \vec{\gamma}) = 0 \tag{2.5}$$

In this equation, ρ is the material volume mass, $\underline{\sigma}$ the Cauchy stress tensor, $\vec{\omega}$ the volume forces due to gravity and $\vec{\gamma}$ the acceleration. ρ and $\vec{\gamma}$ terms reflect the inertia effects. It is assumed that those terms are negligible as compared to the forming processes internal efforts. Eq. (2.5) becomes:

$$div(\underline{\sigma}) = 0 \tag{2.6}$$

To this equilibrium equation, other relationships are added to entirely define the mechanical problem:

The constitutive law defined in Ω and connecting the stress tensor $\underline{\sigma}$ to the strain rate $\underline{\dot{\varepsilon}}$. Its numerical integration will be discussed later.

The mass conservation of the elastic-plastic constitutive model integrates the plastic incompressibility and the elastic compressibility in the equation:

$$div(\vec{v}) + \frac{\dot{P}}{\chi} = 0 \tag{2.7}$$

with $\dot{P}$ the hydrostatic pressure rate responsible of the mass compression and χ the compressibility elastic coefficient inferred from de Young's modulus E and the Poisson ratio ν:

$$\chi = \frac{E}{3(1-2\nu)} \tag{2.8}$$

Assuming a small strains framework, the total strain rate tensor is partitioned into elastic and plastic strain rate:

$$\underline{\dot{\varepsilon}} = \underline{\dot{\varepsilon}}^e + \underline{\dot{\varepsilon}}^p \tag{2.9}$$

Combining Eq. (2.6) and Eq. (2.7), the system to solve is:

$$\begin{cases} div(\underline{\sigma}) = 0 \\ tr(\dot{\underline{\varepsilon}}) + \dfrac{\dot{P}}{\chi} = 0 \end{cases} \tag{2.10}$$

The equations may be expressed as a function of two unknowns of the mechanical problem: velocity $\vec{v}$ and pressure P:

$$\begin{cases} div(\underline{s}(\vec{v})) - \nabla P = 0 \\ tr(\dot{\underline{\varepsilon}}(\vec{v})) + \dfrac{\dot{P}}{\chi} = 0 \end{cases} \tag{2.11}$$

where $\underline{s}$ is the deviatoric part of the Cauchy stress tensor.

2.2.1.3 Boundary conditions

Boundary conditions are applied on the boundary domain and govern the solid equilibrium state. The boundary $\partial\Omega$ is decomposed into four parts as described by Fig. 2.2, and can be written is the following way:

$$\partial\Omega = \partial\Omega_l \cup \partial\Omega_T \cup \partial\Omega_v \cup \partial\Omega_c \tag{2.12}$$

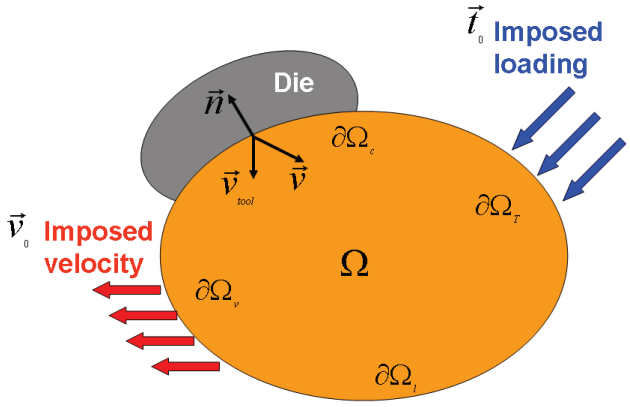

Figure 2.2. Boundary conditions.

Each part correspond to a different type of boundary condition:

- Free boundary ($\partial\Omega_l$) condition:

$$\underline{\sigma}.\vec{n} = 0 \text{ on } \partial\Omega_l \tag{2.13}$$

with $\vec{n}$ the outer normal to the contact surface.

- Imposed velocity ($\partial\Omega_v$) condition:

$$\vec{v} = \vec{v}_0 \quad \text{on } \partial\Omega_v \tag{2.14}$$

with $\vec{v}_0$ the imposed surface solid velocity.

- Imposed stress ($\partial\Omega_T$) condition:

$$\underline{\sigma}.\vec{n} = \vec{T} \text{ on } \partial\Omega_T \tag{2.15}$$

with $\vec{T}$ the imposed normal stress.

- Friction contact ($\partial\Omega_c$) condition:

This condition appears in our case between the solid and tools. This is essential in forming and is divided into two distinct concepts: contact and friction.

-To express the contact condition, it is convenient to introduce pressure contact σ_n defined by the projection of the stress vector on the external normal to the surface of the tool:

$$\sigma_n = (\underline{\sigma}\vec{n}).\vec{n} \tag{2.16}$$

Unilateral contact describing the non-penetration of the material into the dies is written by Signorini's conditions:

$$\begin{cases} (\vec{v} - \vec{v}_{tool}).\vec{n} & \leq 0 \\ \sigma_n & \leq 0 \\ \sigma_n(\vec{v} - \vec{v}_{tool}).\vec{n} & = 0 \end{cases} \quad \text{on } \partial\Omega_c \tag{2.17}$$

In this expression, $\vec{v}_{tool}$ is the tool velocity and $\partial\Omega_c$ is the boundary of the domain Ω on which the unilateral contact condition is imposed. These equations describe a condition of non-penetration. If σ_n is zero then there is no contact and the solid and the tool can have different velocities. In the case where there is contact, then the normal velocity of the solid at the contact point becomes equal to that of the tool, the contact pressure becomes non-zero.

- The friction tangential component is given through the friction law and is defined by relating friction cission $\vec{\tau}$ to the pressure and the relative velocity:

$$\vec{\tau} = \underline{\sigma}\vec{n} - \sigma_n\vec{n} \tag{2.18}$$

The friction laws enable to model the friction on the interfaces between two bodies when a relative sliding movement occurring between them. In the Forge3® software, different friction laws are available for modeling friction with forging tools. The Coulomb limited Tresca friction law is mostly used in cold forming. It is written in the following general form:

$$\vec{\tau} = -\mu\sigma_n \frac{\Delta V_g}{\left\|\Delta V_g\right\|} \text{ if } \left|\mu\sigma_n\right| < \frac{\sigma_0}{\sqrt{3}} \text{ and } \vec{\tau} = -\overline{m}\frac{\sigma_0}{\sqrt{3}}\frac{\Delta V_g}{\left\|\Delta V_g\right\|} \text{ if } \left|\mu\sigma_n\right| \geq \overline{m}\frac{\sigma_0}{\sqrt{3}} \quad (2.19)$$

ΔV_g is the relative sliding velocity between the two bodies. With this relation, the friction shear stress is equal to the normal stress multiplied by the friction coefficient μ or to a fraction of the maximum shear stress sustainable by the material.

2.2.1.4 Constitutive laws

Constitutive laws are critical when modeling the material flow during metal forming. To calibrate a constitutive model, the material behavior following different mechanical and thermal loadings is analyzed. A constitutive model is generally represented as a relationship between the stress tensor $\underline{\sigma}$, the strain tensor $\underline{\varepsilon}$, the strain rate tensor $\underline{\dot{\varepsilon}}$ and temperature $T°$:

$$\underline{\sigma} = \underline{\sigma}(\underline{\varepsilon}, \underline{\dot{\varepsilon}}, T°) \quad (2.20)$$

The stress tensor is decomposed into the deviatoric part $\underline{s}$ and the spherical part $P\underline{I}$:

$$\underline{\sigma} = \underline{s} - P\underline{I} \quad (2.21)$$

$\underline{s}$ is the deviatoric stress tensor, $\underline{I}$ is the unit (second rank) tensor and P is the hydrostatic pressure given by:

$$P = -\frac{1}{3}tr(\underline{\sigma}) \quad (2.22)$$

The one-dimensional representation of the stress and strain are given by:

- von Mises equivalent stress:

$$\overline{\sigma} = \sqrt{\frac{3}{2}s:s} \quad (2.23)$$

- equivalent strain rate:

$$\dot{\overline{\varepsilon}} = \sqrt{\frac{2}{3}\dot{\varepsilon}:\dot{\varepsilon}} \quad (2.24)$$

- equivalent strain:

$$\bar{\varepsilon} = \int_0^{time} \dot{\bar{\varepsilon}}\, dt \tag{2.25}$$

Depending on the loading conditions of the process different types of constitutive laws may be considered. For hot processes the elastic strain is often neglected and the material behavior is modeled by a viscoplastic constitutive law. A cold process, such as pilgering, the elasticity can not be neglected, and an elastic-plastic constitutive law type is therefore considered in this work.

Elastic behavior

The elasticity is characterized by a linear and reversible behavior. The constitutive law of a linear elastic and isotropic material is represented by the Hooke's law:

$$\frac{\partial_J \underline{\sigma}}{dt} = \underline{\underline{C}}\,\underline{\dot{\varepsilon}}^e = 2\mu\underline{\dot{\varepsilon}}^e + \lambda^e\, trace(\underline{\dot{\varepsilon}}^e)\underline{I}\,, \tag{2.26}$$

λ^e and μ are the Lamé coefficients that are constant for a homogeneous material:

$$\mu = \frac{E}{2(1+\nu)} \text{ and } \lambda^e = \frac{E\nu}{(1+\nu)(1-2\nu)}, \tag{2.27}$$

E is the Young's modulus and ν Poisson's ratio. $\underline{\dot{\varepsilon}}^e$ is the elastic strain rate tensor and $\underline{\dot{\sigma}}$ is the stress tensor ratio, $\underline{\underline{C}}$ the resulting fourth rank elastic tensor. The Jaumann derivative of the stress tensor in Eq. (2.26) is defined by:

$$\frac{\partial_J \underline{\sigma}}{dt} = \underline{\dot{\sigma}} - \underline{\omega}\,\underline{\sigma} + \underline{\omega}\,\underline{\sigma} \tag{2.28}$$

where $\underline{\omega}$ is the spin tensor. When the process involves moderate rotations, the simple material derivative can be used in Eq. (2.26) as a satisfactory approximation.

Elastic-plastic behavior

The elastic-plastic constitutive model is used for cold material forming. The elastic-plastic constitutive model can be summarized as follows:

- as the stress $\underline{\sigma}$ is lower than a given stress σ_y the material has a purely elastic behavior described by the Hooke's law (Eq. 2.26).
- when the stress reaches the value σ_y the material starts deforming plastically.

The total strain rate is decomposed into an elastic and a plastic terms (see Eq. 2.9). The elastic part of strain rate is calculated by Hooke's law. The additively is verified for metals where

the elastic strains are small with respect to plastic strains. The yield stress σ_y required to cause plastic deformation is generally determined by a tensile test.

The elastic-plastic behavior is determined by the Prandt-Reuss model [Gay 1995] and is illustrated here with the isotropic von Mises criterion. The plasticity criterion is defined by a yield surface f which, for isotropic hardening, involves the stress tensor $\underline{\sigma}$ and yield stress σ_y :

$$f(\underline{\sigma},\sigma_0) \leq 0 \tag{2.29}$$

As discussed in the previous Chapter,

$$\begin{aligned} &f(\underline{\sigma},\sigma_0) \leq 0 : \text{elastic behavior} \\ &f(\underline{\sigma},\sigma_0) = 0 : \text{plastic behavior} \end{aligned} \tag{2.30}$$

Plastic flow appears when:

$$\frac{2}{3}\sigma_0^2 = trace(s^2) = s:s \tag{2.31}$$

Using the definition of equivalent stress (Eq. 2.23), (Eq. 2.31) leads to:

$$\overline{\sigma} = \sigma_0 \tag{2.32}$$

The yield criterion function f is written finally in the simple form:

$$f = \overline{\sigma} - \sigma_0 \tag{2.33}$$

The Prandt-Reuss model allows determining the direction and the intensity of the plastic flow. The normality rule

$$\underline{\dot{\varepsilon}}^p = \dot{\lambda}\frac{\partial f}{\partial \underline{\sigma}} \tag{2.34}$$

means that plastic flow appears in the normal direction of the yield surface with a intensity given by the scalar $\dot{\lambda}$.

The plastic strain being incompressible:

$$trace(\underline{\dot{\varepsilon}}^p) = 0 \tag{2.35}$$

For a von Mises material Eq. (2.34) becomes:

$$\underline{\dot{\varepsilon}}^p = \dot{\lambda}\frac{3}{2}\frac{\underline{s}}{\sigma_0} \tag{2.36}$$

and the deviatoric stress tensor is given by:

$$\underline{s} = \frac{2}{3}\sigma_0 \frac{\underline{\dot{\varepsilon}}^p}{\dot{\bar{\varepsilon}}^p} \tag{2.37}$$

Summarizing, the elastic-plastic equations are:

$$\begin{cases} \underline{\dot{\varepsilon}} = \underline{\dot{\varepsilon}}^e + \underline{\dot{\varepsilon}}^p \\ \underline{\dot{\varepsilon}}^e = C^{-1}\underline{\dot{\sigma}} \\ \underline{\dot{\varepsilon}}^p = \dot{\lambda}\dfrac{\partial f}{\partial \underline{\sigma}} \\ f = \bar{\sigma} - \sigma_0 \end{cases} \tag{2.38}$$

2.2.1.5 The mechanical problem to solve

The "strong" formulation to be solved is defined by the following system, decomposing $\underline{\sigma}$ in its spherical and deviatoric part:

$$\begin{cases} div(\underline{\sigma}) = div(s(\vec{v})) - \nabla P = 0 & \text{on } \Omega \\ div(\vec{v}) + \dfrac{\dot{P}}{\chi} = 0 & \text{on } \Omega \\ (\vec{v} - \vec{v}_{tool}).\vec{n} \le 0 & \text{on } \partial\Omega_c \\ \vec{\tau} = -\mu\sigma_n \dfrac{\Delta V_g}{\left\|\Delta V_g\right\|} & \text{on } \partial\Omega_c \end{cases} \tag{2.39}$$

2.2.2 Mechanical problem discretization

2.2.2.1 Weak formulation of the continuous problem

The "strong" formulation is transformed into a weak form by multiplying the two equations by $\vec{v}^*$ and P^* quantities and integration. Using the Green's theorem, the problem becomes: *find* $(\vec{v}^*, P^*) \in V$ x P *so that:*

$$\begin{cases} \displaystyle\int_\Omega [\underline{s}(\vec{v}) : \underline{\dot{\varepsilon}}(\vec{v}^*)]d\Omega - \int_\Omega P\,trace(\underline{\dot{\varepsilon}}(\vec{v}^*))d\Omega - \int_{\partial\Omega} \vec{T}.\vec{v}^*\,ds = 0 & \forall\, \vec{v}^* \in V \\ \displaystyle\int_\Omega P^* \left[trace(\underline{\dot{\varepsilon}}(\vec{v}^*) + \frac{\dot{P}}{\chi} \right] d\Omega = 0 & \forall\, P^* \in \mathrm{P} \end{cases} \tag{2.40}$$

where $\vec{T}$ corresponds to external stress vector on the Ω boundary.

2.2.2.2 Space discretization

After continuous domain Ω discretization into finite subdomains Ω_h composed of elements Ω_e, the finite element method defines the interpolation functions over each element in order to define the unknowns of the problem $(\vec{v},P)\in V\times \mathrm{P}$. This approximation leads to solve the weak problem in the finite dimension sub-spaces $V_h \subset V$, $P_h \subset \mathrm{P}$. The discretized weak problem leads to finding the solutions in the finite dimension $(\vec{v}_h,P_h)\in V_h\times \mathrm{P}_h$:

$$\begin{cases} \int_{\Omega_h}[\underline{s}(\vec{v}_h):\underline{\dot{\varepsilon}}(\vec{v}_h{}^*)]d\Omega_h - \int_{\Omega_h}P_h trace(\underline{\dot{\varepsilon}}(\vec{v}_h{}^*)d\Omega_h - \int_{\partial\Omega_h}\vec{T}.\vec{v}_h{}^* ds_h = 0 & \forall\, \vec{v}_h{}^* \in V_h^0 \\ \int_{\Omega_h} P_h^* \left[trace(\underline{\dot{\varepsilon}}(\vec{v}_h{}^*) + \frac{\dot{P}_h}{\chi}\right] d\Omega_h = 0 & \forall\, P_h^* \in \mathrm{P}_h \end{cases} \tag{2.41}$$

P_h and V_h designated respectively the finite spaces of pressure and velocities which are kinematically admissible and defined over Ω_h.

An important issue in the mixed velocity-pressure formulation is the choice of the degree of interpolation functions of the two variables $\vec{v}_h$ and $\vec{P}_h$ in each element. Indeed, the interpolation of the pressure can not be chosen independently of the interpolation of the velocity. For example, if the degree of interpolation of the pressure is higher than that of the velocity, the imposed constraint on the velocity field by the equations of equilibrium and mass conservation are too important and can lead to a wrong solution. Therefore, in order to avoid these “locking” problems, the finite element chosen in Forge3® is a four node tetrahedron with linear interpolation of velocity and pressure. However, the interpolation of the velocity field is enriched with an additional component. This component is called the bubble field and represents an additional node in the centre of the element. This procedure allows satisfying the Brezzi-Babuska (BB) [Babuska 1973] compatibility condition, sufficient for a stable mixed formulation. The bubble field is linear in each of the sub-tetrahedral formed by the central node and three of the other nodes of the element. The tetrahedral element P1+ / P1, shown in Fig. 2.3, is used to discretize the domain. Tetrahedral element enables easy meshing and remeshing operations [Coupez *et al.*, 1998], [Coupez *et al.*, 2000].

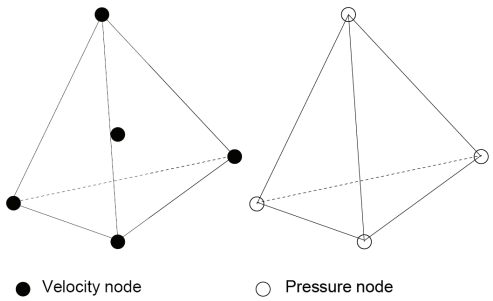

Figure 2.3. P1+/P1 mini-element.

The weak mechanical continuous problem is solved using the finite element discretization. For further details of this system resolution the reader can refer to [Perchat 2000], [Aliaga 2000], [Ben-Tahar 2005], [Boussetta 2005].

2.2.2.3 Contact management

In Forge3® the contact is managed incrementally thanks to a penalty method. The distance between a node and its projection on the tool at time t is denoted $d(t)$. The contact conditions correspond to:

$$d(t) = 0 \qquad \text{on } \partial\Omega_c, \tag{2.42}$$

$d(t) = 0$ if the node is not in contact, $d(t) < 0$ is impossible (non physical).

During simulation, the nodes of the part move with respect to the tools and contact conditions may change. Starting from a known configuration at time t, the condition to be enforced at the end of the following increment is:

$$d(t + \Delta t) \geq 0 \quad \text{on } \partial\Omega_c \tag{2.43}$$

This condition is expressed at time t and linearized [Mocellin 1999]:

$$d(t + \Delta t) \cong d(t) + \frac{\partial d(t)}{\partial t}\Delta t + O(\Delta t^2) = d(t) + (\vec{v}_{tool} - \vec{v}).\vec{n}(t)\Delta t + O(\Delta t^2) \tag{2.44}$$

The unilateral contact condition is written as:

$$(\vec{v} - \vec{v}_{tool}).\vec{n}(t) - \frac{\partial(d(t))}{\partial t} \leq 0 \tag{2.45}$$

This expression is an approximation because the normal $\vec{n}$ and the distance d at the time t are used. However, these quantities vary during the time increment, leading to some errors. This contact algorithm is implicit in the time because the contact conditions are enforced at the end of the increment. From another point of view, it is also explicit because the contact data (distance, normal direction) are computed at time t and are considered constants during the time increment. To take into account the contact condition in the weak formulation, the penalty method is used and the non-penetration condition is imposed thanks to a penalty coefficient (ρ_c). Physically, this method consists in applying a repulsive force to the nodes which penetrate into the die, and this force is proportional to the penetration distance. A node is submitted to penalty only if the distance between this node and the tool is less than $-dPen$. So, a small penetration is allowed. This parameter is chosen depending on the characteristic size of the part, or of the mesh elements. This parameter is fixed by default to $1/100$ of the mesh element size. For more details

on contact management techniques, the reader is invited to consult [Fourment *et al.,* 1999], [Mocellin 1999].

2.3 HPTR cold pilgering process simulation

In this section, a one pass cold pilgering FEM simulation is detailed for a better understanding of the HPTR cold pilgering process. Due to the incremental and non-symmetrical nature of the pilgering process, 3D FEM computation should be used [Lodej *et al.*, 2006] in order to carry out a complete mechanical analysis. The mechanical analysis is performed here with Forge2009®, in 3D.

This work does not use the representative pseudo-periodic state approach described by [Montmitonnet *et al.*, 2002] and [Lodej *et al.*, 2006]. The reasons are:

- First, this approach requires an interrupted pilgered test in order to get the "transition shape" and the initial tube strain field. ODS steels are new and expensive. In addition, the fabrication route is not yet fully determined. Therefore, this methodology can not be used.
- The post-processing interpolation, once the stabilized stroke is reached, has been implemented almost a decade ago in order to save computation time. Since then, metal forming simulations are in continuous progression and have become more reliable and faster due to the simultaneous improvements of resolutions algorithms and computer technology [Chenot *et al.*, 2002].
- Finally, with this approach, the stress and strain fields are considered constant in the tube wall thickness in the initial state. However, in this project the goal is to use a damage criterion, which is not correlated with the assumption of constant stress and strain in the tube wall thickness.

For these reasons the strategy that was chosen is to simulate the whole process, that is to say the full number of strokes. However, only a short part of the tube is considered in order to save CPU time.

2.3.1 Fabrication route simulation

The fabrication route is a combination of rolling passes and intermediate heat treatments. Based on previous studies recommendations for ODS steels the cross-section reduction ratio for each pass is limited to approximately 20% - 25% [Ukai *et al.*, 2004]. Hardness evolution allows adjusting the fabrication parameters. Intermediate heat treatments are performed to ensure a limited increase of the cladding tube hardness, below the critical hardness value of 400 Hv_1. After 2 passes the cold-rolled tube is heat treated. After 6 rolling-passes the final dimensions of the cladding tube are 10,73 mm outer diameter and 500 µm wall thickness. The fabrication route of a Fe-14Cr-1W-ODS (CEA code: J37) tube is showed in Table **2.1**.

Table 2.1. Fe-14Cr-1W-ODS HPTR tube fabrication route at CEA/Saclay.

Grade tube 12: Fe-14Cr-1W-0,3Ti-0,3 Y_2O_3 (Ferritic grade)							
	Outer diameter	Inner diameter	Wall thickness	Pass deformation	Total deformation	Q factor	Hardness*
Raw tube	18.65	16.10	1.28				374
Pass 1	17.44	15	1.22	10.67	10.67	0.66	
Pass 2	15.98	14	0.99	25.01	33.01	2.25	420
Heat treatment							393
Pass 3	***14.35***	***12.70***	***0.83***	***24.81***	***49.63***	***1.63***	
Pass 4	13.28	11.90	0.69	22.15	60.79	2.19	416
Heat treatment							392
Pass 5	12.13	10.97	0.58	22.89	69.76	1.84	
Pass 6	10.73	9.73	0.5	23.65	76.91	1.2	400
Final heat treatment							410

* Applied force: 1kg, time:15s (Vickers)

All numerical simulations performed in this work for HPTR pilgering are based on *pass 3* in Table **2.1**. The raw tube is advanced by 1,7 mm and rotated around its axis by 39° after each stroke, a stroke being defined by one forward and one backward displacement of the rolling dies.

2.3.2 Simulation set up

The cold pilgering process is also used for forming Zircaloy-4 cladding tubes. Therefore, the first feasibility test of HPTR pilgering simulation will consider this material with an monotonic elastic-plastic behavior. The with Young's modulus is E =99GPa, the Poisson's ratio is ν =0.37, and the monotonic strain hardening curve is [Montmitonnet *et al.*, 2002], [Lodej *et al.*, 2006]:

$$\bar{\sigma} = 1000(0.01 + \bar{\varepsilon})^{0.15} \tag{2.46}$$

The time step is considered constant, $\Delta t = 0.001s$, giving a maximal incremental die translation of 0.82mm. The influence of this numerical parameter will be discussed later. All contacts are unilateral. A unilateral contact denotes a mechanical constraint which prevents penetration between two bodies and is usually associated with a gap function which measures the distance between the bodies and a contact force. A Coulomb friction law is assumed with μ =0.1 for both internal and external surface [Montmitonnet *et al.*, 2002]. Another assumption is that the process is isothermal (20℃), or more precisely that the change in temperature of the material does not affect significantly the material behavior. Tools are assumed rigid (which is a strong assumption when dealing with thin tubes). Therefore, only the active die surfaces needs to be meshed. Typical die mesh features are shown in Table **2.2**. Both forward and return strokes are simulated. Dies kinematics and tube mesh are discussed in the next sections.

Table 2.2. Die mesh characteristics.

	Number of elements	Number of nodes	Element type
Dies	3 x 20294	3 x 10199	2D triangles
Mandrel	60000	30100	2D triangles

2.3.2.1 Cold pilgering kinematics

The dies translation velocity (Fig. 2.4) is a sinusoidal function given by:

$$V_z = A\sin(\frac{2*\pi*t}{f}), \tag{2.47}$$

where t is the time, A the amplitude (dies maximal rolling velocity), and f the frequency (for one complete stroke time). V_z is the velocity in the rolling direction.

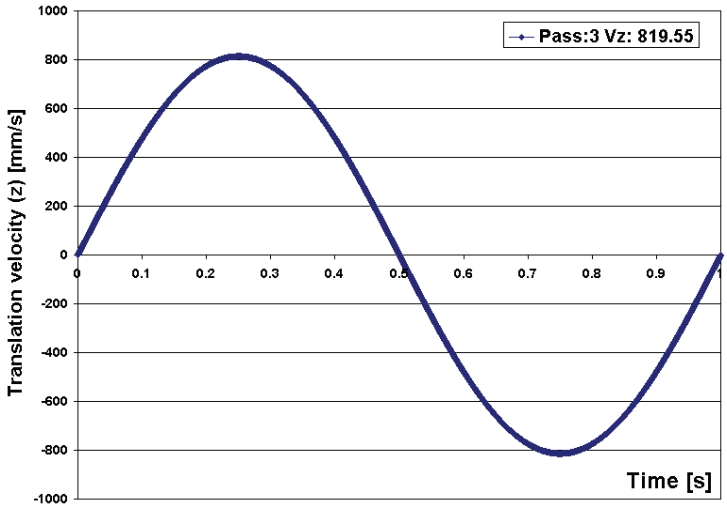

Figure 2.4. Rolling direction dies translation velocity.

In the real HPTR pilgering process, profiled cams push the dies into the tube, which leads to compression [HPTR CEA/LTMEX]. Profiled cams are 3 slopes with different angles (see Annex 1). Therefore, the pilgering model should have also a translation velocity in the radial direction (y). Moreover, cams and dies have a relative motion, which leads to a larger *working zone* than the real cams' length (191mm). This relative motion depends on the final diameter that at the same time depends on the set up of the HPTR mill connecting rod system [see HPTR CEA/LTMEX]. With the assumption that there is not sliding between dies and tube, the dilatation factor (f_x) to apply at the real cam length for the pass 3 is *1.373* (see Annex 2). With this dilatation factor the cams length is nearly 260mm. Homothetic cam is done with fixed slopes angles. Dies move following the slope imposed by the cams and once the final diameter is reached, the die is locked with a hillock in order to calibrate the tube without any slope. Fig. 2.5 displays schematically this

mechanism. The strategy implemented in this work is to simulate only the *working zone*. Finite element simulations can start slightly before this stage, say 2-3 strokes earlier, in order to safely capture the first contact.

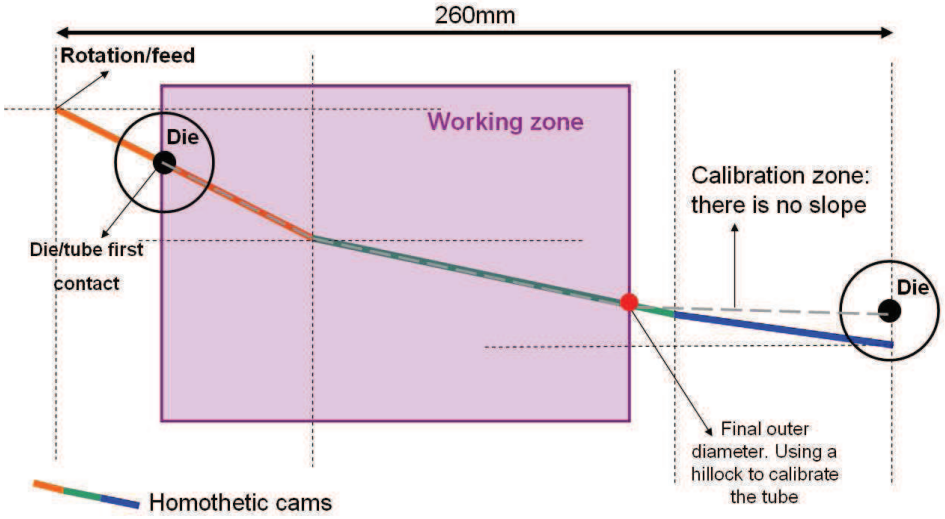

Figure 2.5. Schematic kinematics of the HPTR pilgering process.

Dies compression profile and velocity in the radial (compression) direction (y) are given in Fig. 2.6 and 2.7 respectively.

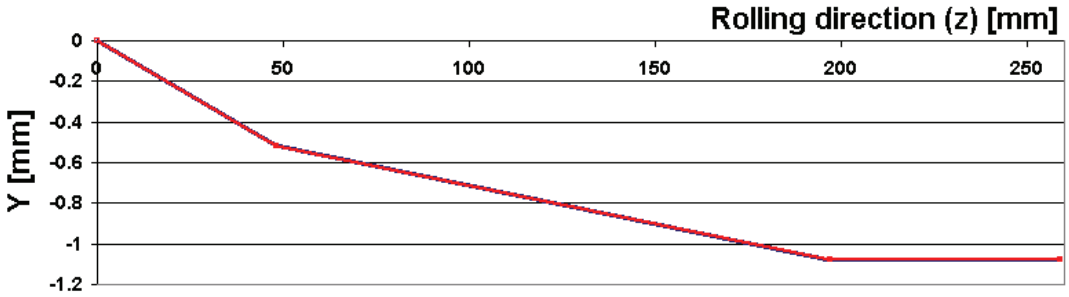

Figure 2.6. Cams profile. Y is the radial die displacement.

Next Figure displays the velocity profile corresponding to the above cam profile (see Fig. 2.6).

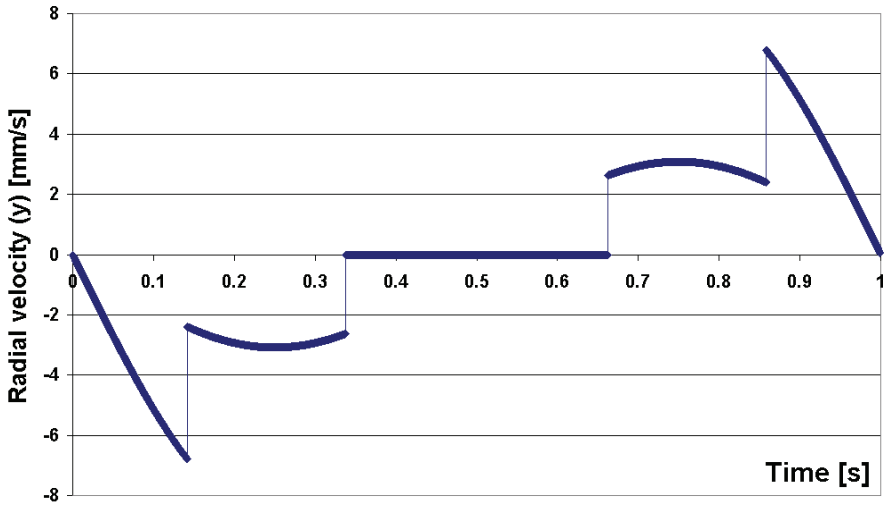

Figure 2.7. Compression dies velocity in the radial direction (y).

Finally, a numerical Forge2009® feature called *manipulator* is used at the rear of the tube to impose boundary conditions. Six degrees of freedom at each node belonging to the tube rear base are set to zero. The six degrees of freedom correspond to 3 rotations and 3 translations. This is consistent with reality since the tube is maintained by jaws, outside of the *working zone*. The tube and the mandrel are coaxial. This is also true in the actual process because the mandrel is also maintained by jaws.

2.3.2.2 Tube length choice

Optimizing numerically the whole process with a *long* tube is simply not feasible at the time being, because of the huge computation time involved. Consequently, a *short* tube is used. The length of this *short* tube must be long enough to be able to achieve steady state thermo mechanical values in the central zone. A numerical study was carried out to obtain the optimal tube length in relation with the numerical accuracy and the computation time (Table **2.3**). 2 elements over the thickness and 100 elements over the circumference are used. The mesh size in the rolling direction is 1mm.

Table 2.3. Tube length influence simulations characteristics

	(a)	(b)	(c)
Tube length [mm]	10	20	40
Number of elements	12000	24000	48000
CPU time (5 cores)	106h	91h	221h

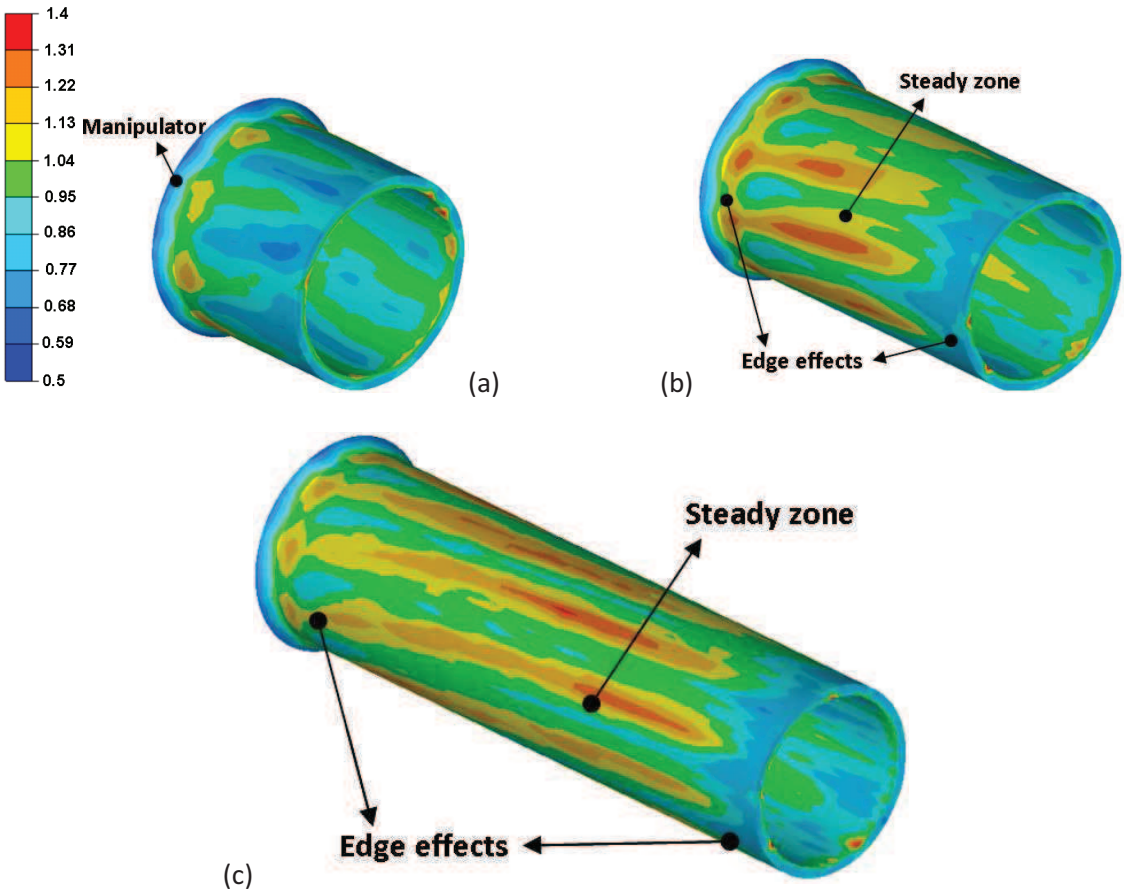

Figure 2.8. Tube length influence study results: equivalent strain isovalues. (a) 10mm (b) 20mm (c) 40mm.

Fig. 2.8 shows the numerical results with 3 different tube lengths. It illustrates the influence of edge effects (manipulator and free end) on the distribution of accumulated strain. Axial rolling marks with a high accumulated equivalent strain also appear. They are due to the die shoulder contact which initially induces local deformations (this point is discussed latter). 20 mm and 40 mm tubes display nearly the same accumulated equivalent strain axial marks in the middle of the tube (steady zone). For 10 mm tube, the steady zone does not exist because of edge effects perturbations. Therefore, the tube of 20 mm is chosen for our simulations because of its acceptable computation time (see Table **2.3**) and numerical accuracy. Moreover, Lagrangian sensors are placed in the thickness of the tube at mid-length (in order to avoid edge effects). They collect the mechanical history undergone by the material point during the whole pilgering process, which provides indications on the nature and the amplitude of the cyclic deformations. The full simulation approach proposed in this work involves with huge amounts of data storage associated to meshes. In this context, Lagrangian sensors allow collecting the essential data for the mechanical analysis of a well chosen materials points.

2.3.2.3 Mesh type choice

Forge3® can perform numerical simulations with structured and unstructured meshes. This section deals with a numerical test comparing 3 types of mesh: structured isotropic,

structured anisotropic and unstructured (see Table **2.4**). 0.5mm mesh size is used for the structured isotropic case. 0.5mm mesh size over the wall thickness and 0.66 mm mesh size in the rolling direction is used for the structured anisotropic case. Unstructured mesh case is performed with a mesh size close to 0.5mm.

The goal is to select the optimal mesh type for future simulations. The initial tube length is fixed to 20 mm. The results are summarized in Fig. 2.9. It can be concluded first, that the unstructured mesh lost strain continuity rolling marks. Additionally, some isolate peak strain values are observed. On the other hand, structured meshes display smooth and continuous axial rolling marks in the steady zone. These marks are also observed experimentally. Therefore, in this particular case, a structured mesh can be used because it gives smoother mechanical fields (see Fig. 2.10). Regarding the isotropic versus anisotropic structured meshes, it can be noticed that mesh size influences the axial rolling marks intensity (see Fig. 2.9), which could be due to the software contact management that itself depends on mesh size. Actually, the more the mesh size decreases the more the equivalent strain field is significant. In section 2.2.5.2 a deeper analysis is done in order to get the optimal anisotropic structured mesh size when considering both computation time and numerical precision.

Additionally to previous comments, the structured meshes allow to control the number of elements in the wall thickness, which is an important issue when analyzing the mechanical field gradient over the wall thickness.

Table 2.4. Mesh type influence on simulations characteristics

	(a)	(b)	(c)
Mesh type	Structured isotropic	Structured anisotropic	Unstructured
Number of elements	86400	43200	53719
CPU time (5 cores)	232h	105h	155h

It is noticed regarding Fig. 2.10 that the longitudinal strain for the isotropic and anisotropic cases are slightly the same. It can be explained by the fact that the sensor (material point) is placed at the middle of the wall thickness. If the sensor is placed close to the external surface, longitudinal strains should be different as showed in Fig. 2.9.

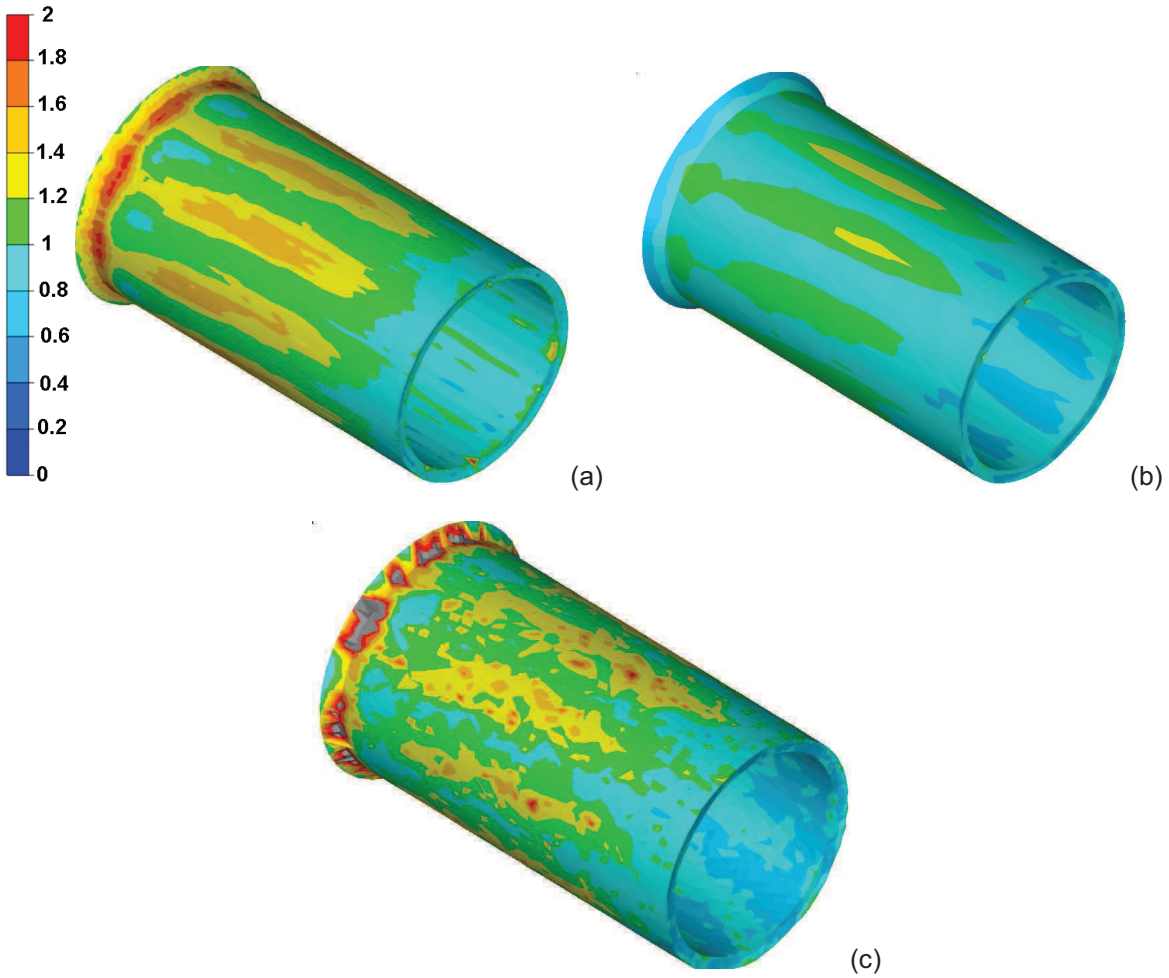

Figure 2.9. Equivalent strain isovalues field. Structured and unstructured meshes influence (initial tube length: 20mm). (a) Structured isotropic mesh (b) Structured anisotropic mesh (c) Unstructured mesh.

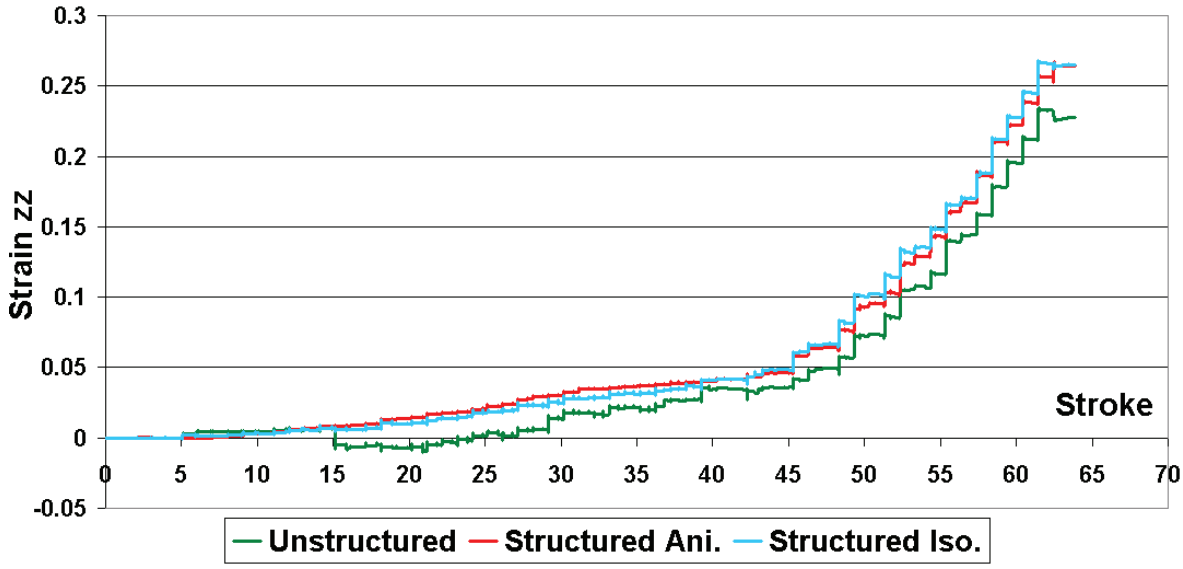

Figure 2.10. $\mathcal{E}_{zz}$ history of a material point in the middle of the tube – mesh type influence.

2.3.3 First numerical results analyses

Taking into account the previous conclusions, an anisotropic structured mesh is chosen for this first numerical results analysis. 3 elements over the thickness, 100 elements over the circumference and 20 elements over the length are used to mesh the 20mm *short* tube. Mesh characteristics are summarized in Table **2.5**.

Table 2.5. Mesh characteristics.

	Number of elements	Number of nodes	Element type
Tube	36000	8400	3D tetrahedral
Dies	3 x 20294	3 x 10199	2D triangles
Mandrel	60000	30100	2D triangles

Meshing and initial position of the simulated systems are displayed in Fig. 2.11.

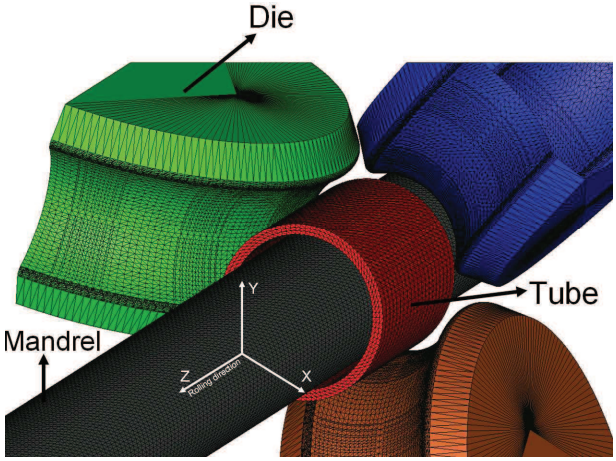

Figure 2.11. FEM simulation set-up.

A Lagrangian sensor is placed at the element Gauss-point located in the mid-thickness of the tube (Fig. 2.12). Placing the sensor in the Gauss-point allows getting the mechanical value without doing any interpolation with the neighboring elements, which is important when using few elements in the tube thickness.

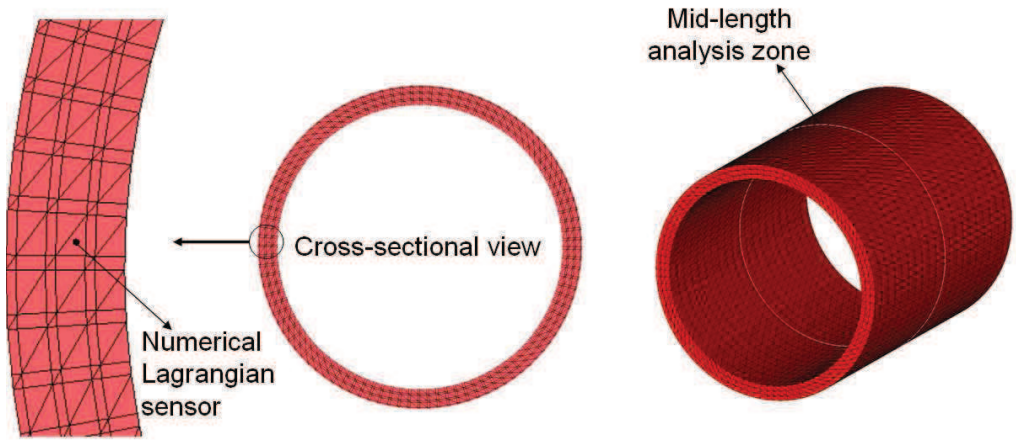

Figure 2.12. Numerical Lagrangian sensor position.

Fig. 2.13 shows the time integrated values of each component of the strain rate tensor in cylindrical coordinates. It is noticed that before the 52nd stroke the dies mainly lead to a diameter reduction of the tube since $\varepsilon_{\theta\theta}$ is incrementally negative.

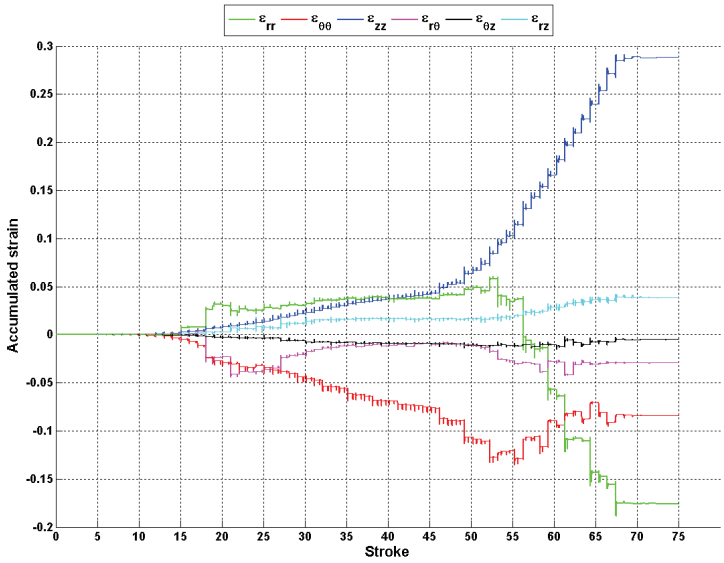

Figure 2.13. Accumulated strain for each component of ε integrated components of the strain rate tensor as a function of the stroke number.

The material constitutive law being elastic-plastic, $Tr(\dot{\bar{\varepsilon}}) \neq 0$. When integrating over the full pass, and combining with numerical errors, which is a little high. Another representation of Fig. 2.13 would consist in plotting and integrating only the plastic part of the strain, with then $Tr(\varepsilon^p) \approx 0$.

Most of the deformation is performed after the 52nd stroke by compression between the grooves dies and the mandrel, and leads to significant extension in the axial (z) direction. As shown in Fig. 2.13 the material can be locally in tension in the finishing zone, because of the side relief. In this case $\Delta\varepsilon_{\theta\theta}$ could be positive.

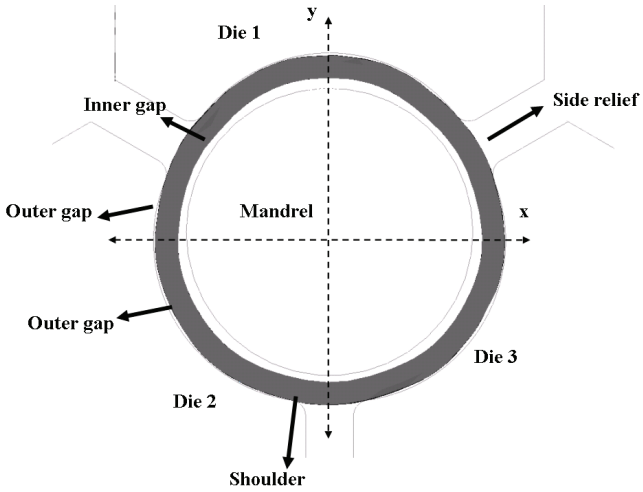

Figure 2.14. Cross-sectional view of the tube at a given position in z in the deformation zone. The shoulder locally deforms the material, creating a tensile stress in the side relief and in the outer gap, and a compressive stress in the shoulder. This leads to a “clover tube”.

From Fig. 2.13, the particular strokes 24, 53, 56, 59, 62, 64 and 67, $\Delta\varepsilon_{\theta\theta}$ is positive, indicating either a tensile stress in the orthoradial direction (Fig. 2.15) or a volume conservation effect.

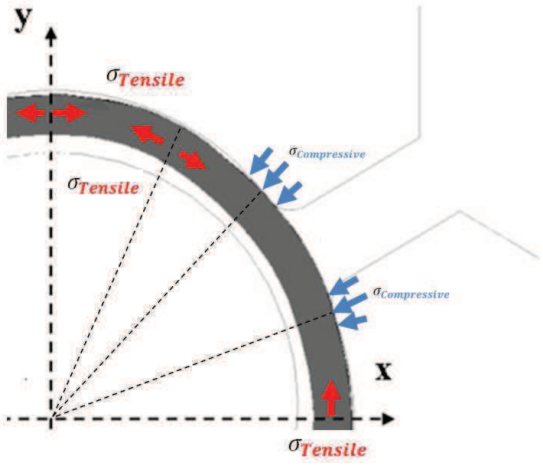

Figure 2.15. Clover geometry caused by the local contact between shoulder and die, and the absence of contact with the die groove.

It is also noticed from Fig. 2.13 that $\Delta\varepsilon_{rr}$ is mostly positive during the first 52 strokes, which is due to the *clover effect*, some parts being in tension (side relief, outer gap) and others parts being in compression (shoulder). This results in an increase of the thickness and is illustrated in Fig. 2.16. From the 52nd to the last stroke, the material comes in contact with the die grooves and with the mandrel, which this time induces a reduction of the tube thickness (Fig. 2.13) with ε_{rr} negative.

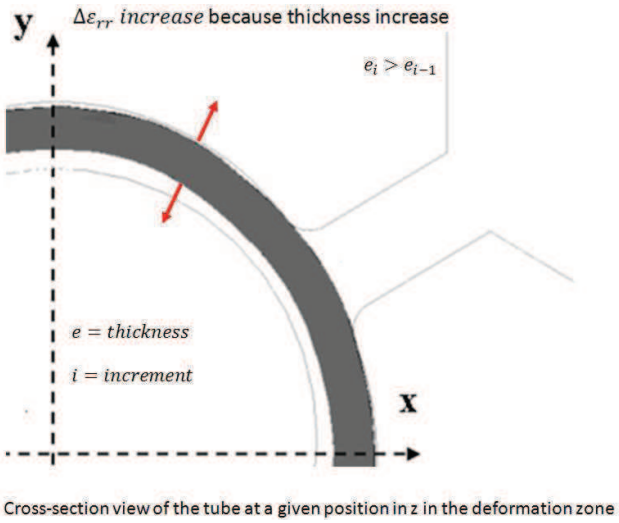

Figure 2.16. Clover effect causing an increase of the thickness.

It is noticed regarding Fig. 2.17 that the thickness reduction is homogeneous in the formed tube despite the intermediate significant *clover* tube shape (see Fig. 2.17 red lines) in the working zone. This fact is explained because of the tube full contact with the die groove and the mandrel at the end of the deformation zone, and because of the small size of the side relief in this zone (sees Fig. 2.18).

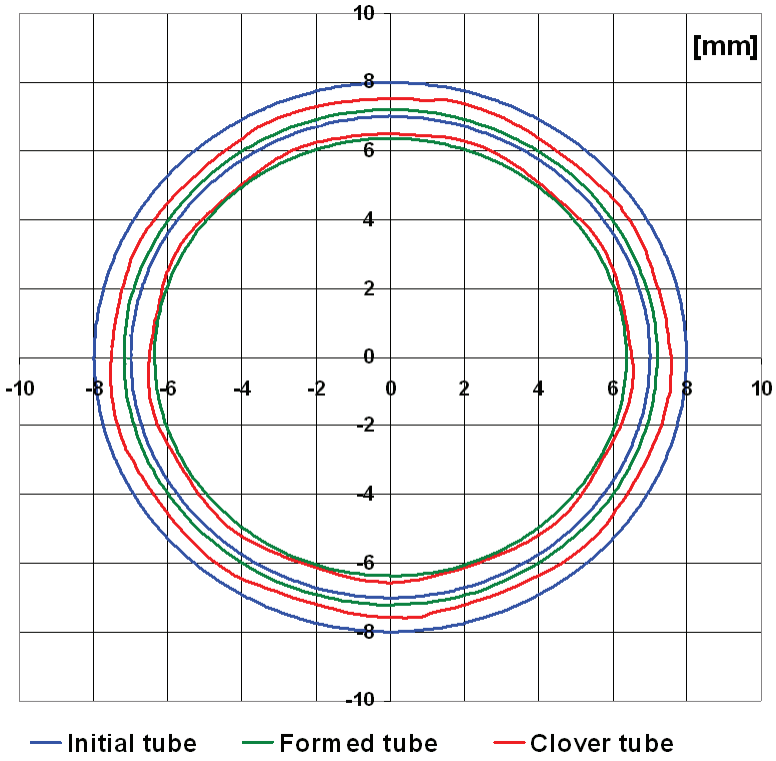

Figure 2.17. Different cross section geometries along the tube length. The clover tube (here in red) is taken from de deformation zone.

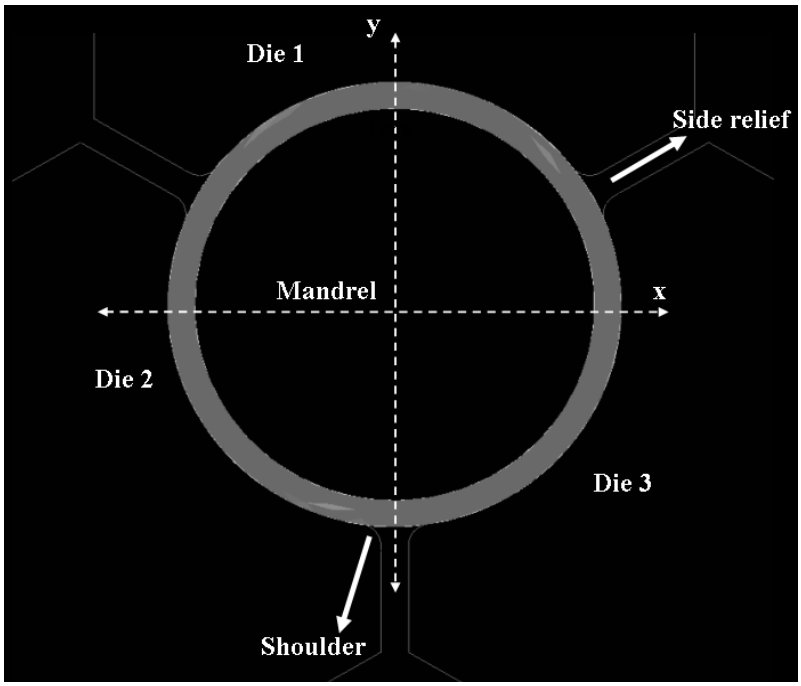

Figure 2.18. Cross-sectional view of the tube at a given position in z in the finishing zone. Note the homogeneous thickness reduction and the small size of the side relief.

The associated deformation in z is positive. The thin walled geometry leads to a stress field dominated by a negative hydrostatic stress (high pressure) leading to a negative stress triaxiality most of the time (Fig. 2.20). The axial stress may however become positive and significant (yield limit: 500 MPa) as illustrated by Fig. 2.19. It means that the stress triaxiality is important but negative as illustrated by Fig. 2.20.

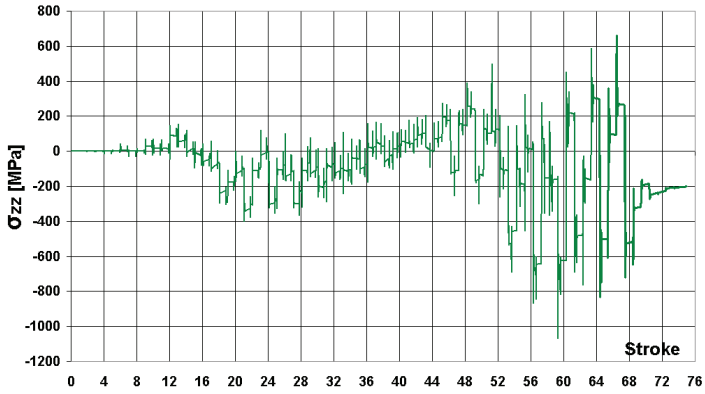

Figure 2.19. Axial stress history (75 strokes).

Regarding Fig. 2.19, this could be linked to damage nucleation, with cracking in the axial direction.

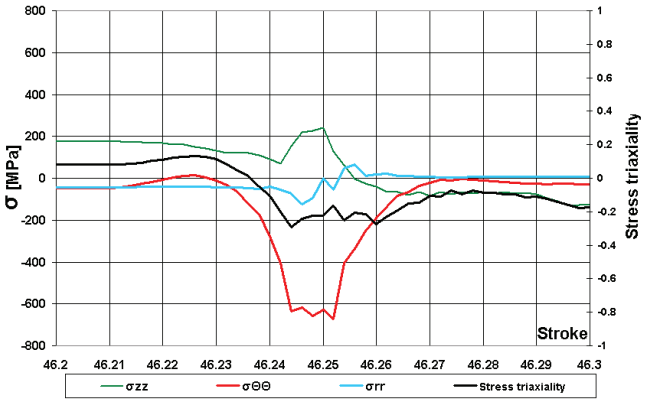

Figure 2.20. Stress components and stress triaxiality. 46th stroke detailing.

More precisely, in the deformation zone under the die, the axial stress is tensile in the side relief area and outer gap area and compressive where the material touches the dies (see Fig. 2.16 gray line). Referring to Fig. 2.21, the reason is clear, the tube is strongly compressed (thickness reduction) underneath the die shoulder, causing axial z-elongation which is necessarily homogenous all around the tube, leading to axial stresses.

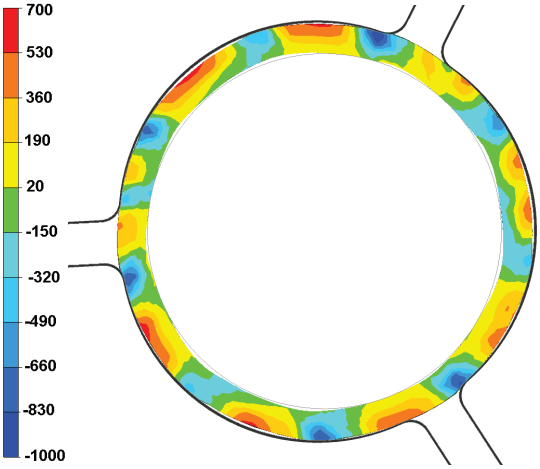

Figure 2.21. 46th stroke cross-section view showing σ_{zz} (in MPa) isovalues at the sensor position (z = 223mm).

This phenomenon is accompanied by an ortho-radial flow. Orthoradial stress $\sigma_{\theta\theta}$ is locally tensile (Fig. 2.22) in the presence of free surfaces (*clover* geometry explained previously).

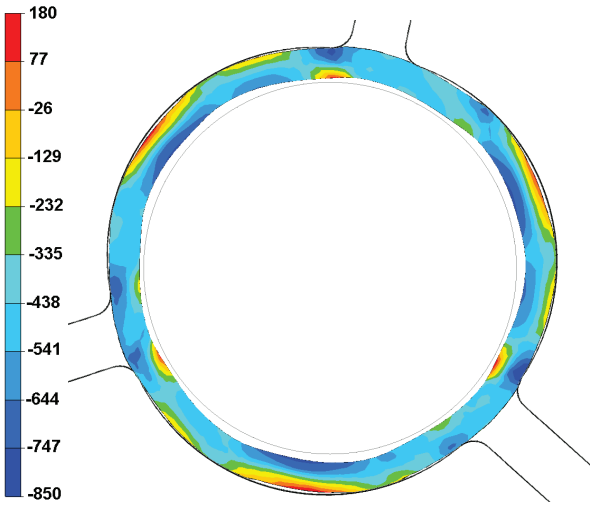

Figure 2.22. 31st stroke cross-section view showing $\sigma_{\theta\theta}$ (in MPa) isovalues (z = 197 mm).

Finally, the radial stress and strain are also positive when free surfaces exist, (outer gaps and side relief). Radial tensile stress values are however small in comparison with the compressive ones. The positive ε_{rr} creates slight bulges in the tube which are illustrated in Fig. 2.23. They correspond with the side relief area of the previous stroke. As these bulges have an increased thickness, contact is made with the dies groove at the next stroke, leading to a compressive stress σ_{rr}.

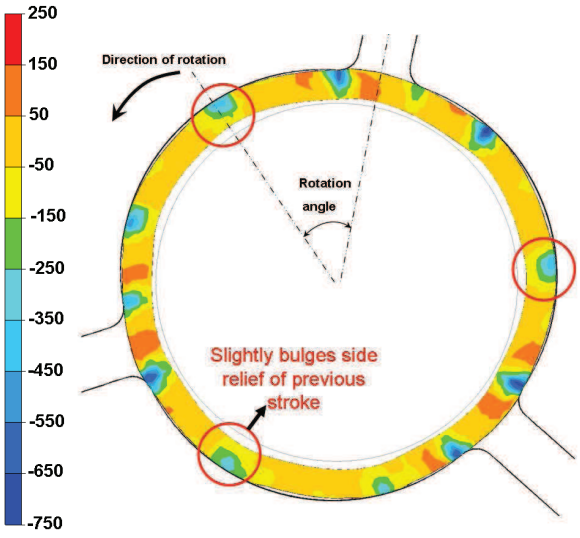

Figure 2.23. 31st stroke cross-section view showing σ_{rr} (in MPa) isovalues (z = 197 mm).

Experimental data indicates a tendency to cracks opening in the axial direction when dealing with ODS steels, hence under the influence of orthoradial loading ($\varepsilon_{\theta\theta}$, $\sigma_{\theta\theta}$). A more detailed analysis of these effects is therefore undertaken.

Fig. 2.24 shows the orthoradial stress and orthoradial strain rate histories at the material point (sensor), described previously. Compression dominates the picture, but some isolated tensile conditions could lead to crack nucleation.

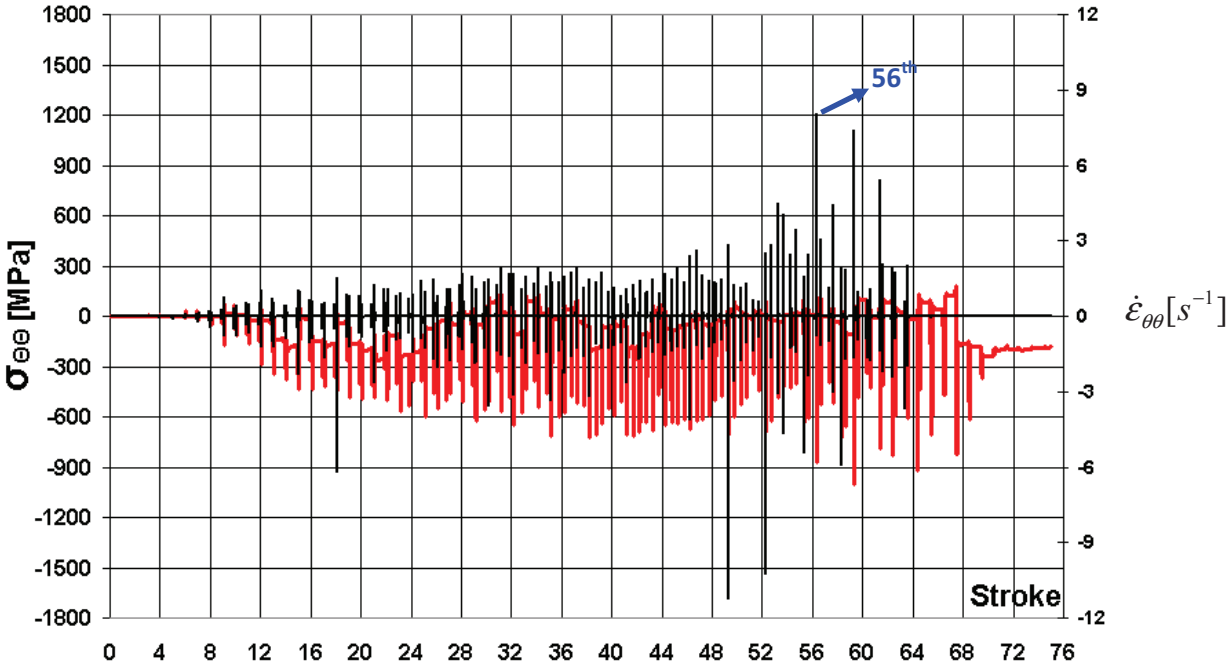

Figure 2.24. Strokes stress and strain rate histories of a material point in the ortho-radial direction. Strain rate is in black.

Fig. 2.25 shows in details the stroke 56 because the maximal positive $\dot{\varepsilon}_{\theta\theta}$ occurs there.

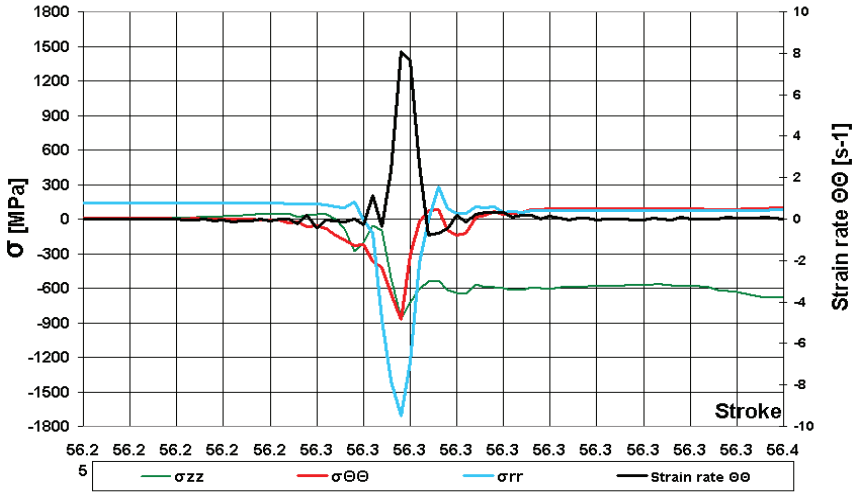

Figure 2.25. 56th stroke detailing.

$\sigma_{\theta\theta}$ in this stroke is negative. Therefore, the origin of this $\Delta\varepsilon_{\theta\theta}$ is the volume conservation ($\Delta\varepsilon_{rr}^{p} + \Delta\varepsilon_{\theta\theta}^{p} + \Delta\varepsilon_{zz}^{p} = 0$).

A more systematic analysis of all cycles can help defining which cycles may contribute to the oligocyclic fatigue of the material. This leads to the need for a damage criterion, which will be addressed in Chapter 4.

It is underlined that such analysis requires appropriate constitutive laws, which will be discussed in Chapter 3.

2.3.4 Adaptative time step

A method of adaptive time step was set up to allow the acceleration of the simulation computing time. Indeed, many iterative processes may occur during the resolution of the mechanical system for elastic-plastic behavior. A small time step is a safe choice but is no more necessary when dies are far from the tube (no contact). In this case it is possible to switch to a higher time step. To come back to the small time step the following condition must be true:

$$d_{contact} \leq d_{tool} \tag{2.48}$$

with,

$$d_{tool} = V_z^{\max} \Delta t \tag{2.49}$$

where $V_z^{\max}$ is the maximum translation velocity of dies, Δt is the time step when dies are not in contact with the tube, $d_{contact}$ is the minimal distance of the tube nodes to the tools calculated by the contact management algorithm. Once $d_{contact} \geq d_{tool}$ the time step is switched again to the small time step and so on. Fig. 2.26 shows an example for a 20 mm length tube. A $\Delta t = 0.001s$ is set when dies are close to the tube and then switched to $\Delta t = 0.01s$ when dies are far from the tube.

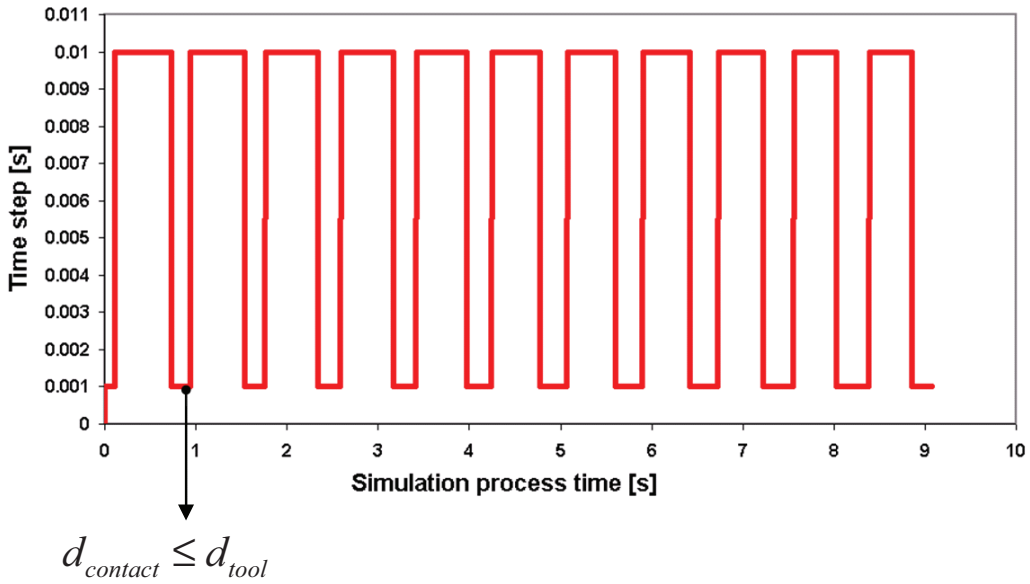

Figure 2.26. Adaptative time step through the simulation of pilgering.

This method accelerates the CPU time by a factor of 2.4 when pilgering a 20 mm length tube. The management of a time step from the tools position is demonstrated in this case and saves considerable CPU time.

2.3.5 Sensitivity studies

The previous mechanical analysis is sensitive to numerical parameters such as:

- Number of elements over the wall thickness
- Number of elements over the tube length
- Time step

This section looks at the quantitative influence of such parameters.

2.3.5.1 Number of elements over the wall thickness

For this sensitivity study the time step is fixed to 0.001s, the Zy4 material behavior is still assumed to be isotropic elastic-plastic (Eq. 2.46). The tube initial length is 20 mm and the number of elements over the tube length is 60 (mesh size in the rolling direction: 0.33 mm). 4 different mesh sizes over the thickness are tested. Their characteristics are summarized in Table **2.6**. The adaptative time step explained in section 2.3.4 is used in this study.

Table 2.6. Simulation characteristics and CPU time.

Assigned simulation name	Number of elements (wall thickness)	Mesh size (wall thickness)	Number of elements	Number of nodes	CPU time
2Th	2 elements	0.495 mm	72000	18300	99 h (6 cores)
3Th	3 elements	0.33 mm	108000	24400	110 h (6 cores)
4Th	4 elements	0.2475 mm	144000	30500	289 h (12 cores)
5Th	5 elements	0.198 mm	180000	36600	447h (12 cores)

Lagrangian numerical sensors have been placed at the mid-length of the tube at different angles (0°-19.5°-39°-90°-180°-270°) and each elemen t of the wall thickness (see Fig. 2.27).

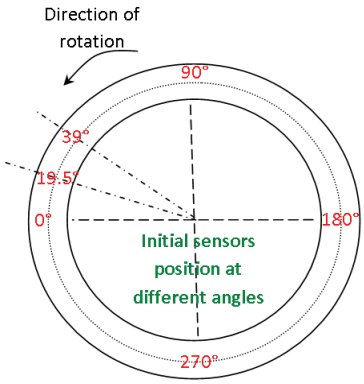

Figure 2.27. Lagrangian numerical sensors placed at the mid-length of the tube at different angles (0°-19°-39°-90°-180°-270°).

The sensors are placed at Gauss-points of some elements. Thus the comparison of different simulations is difficult because the positions of Gauss-points varies depending on the number of elements in the thickness as shown in Fig. 2.28. At each angle, only the sensor closest to the center of the thickness of the tube is considered.

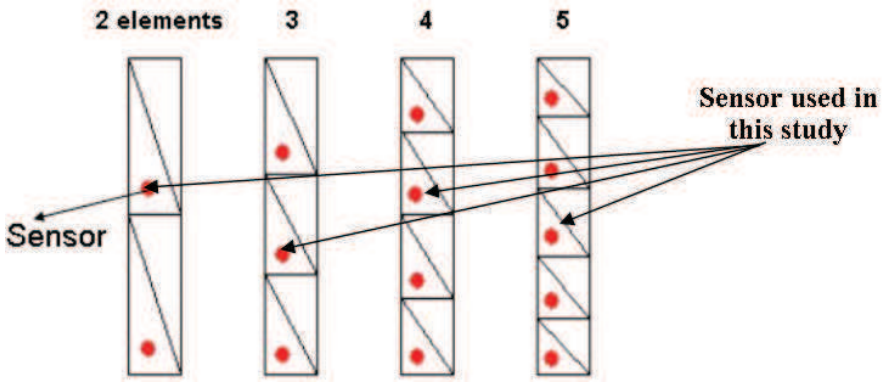

Figure 2.28. Sensors used in this study.

Therefore it is chosen to compare the strain component which is the most homogeneous in the wall thickness of the tube, such that the influence of the difference in position between the sensors is minimized. Figs. 2.29 - 2.31, show that the most uniform strain component over the thickness is ε_{zz}. This strain component is used to compare the simulations in this section.

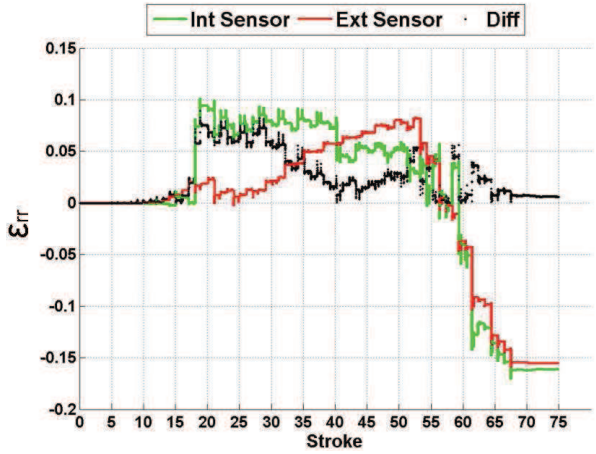

Figure 2.29. Change of $\mathcal{E}_{rr}$ in the wall thickness at angle 0° (5Th simulation – 5 elements over the wall thickness). Diff corresponds to the strain component gradient between the internal and the external sensors.

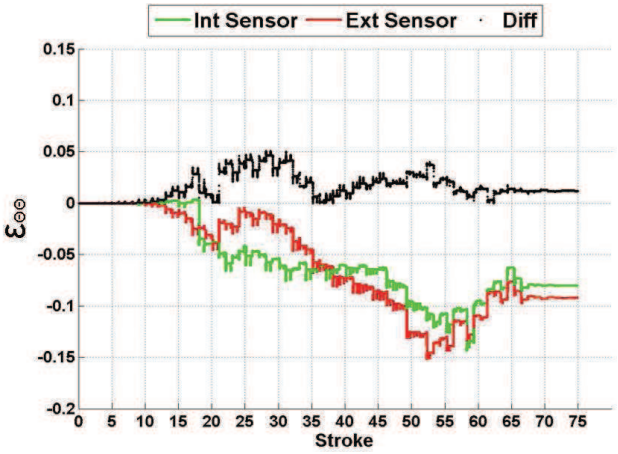

Figure 2.30. Change of $\mathcal{E}_{\theta\theta}$ in the wall thickness at angle 0° (5Th simulation) . Diff corresponds to the strain component gradient between the internal and the external sensors.

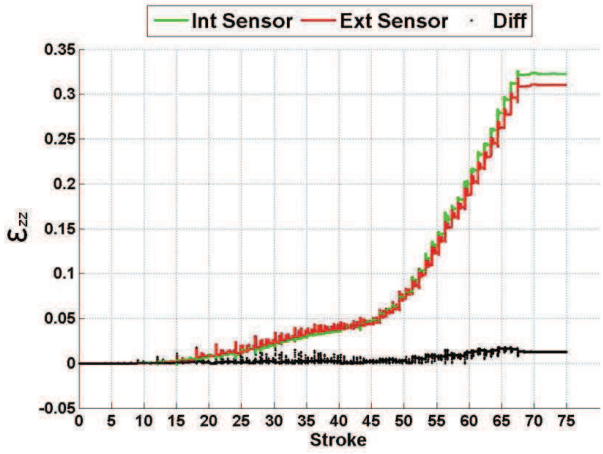

Figure 2.31. Change of $\mathcal{E}_{zz}$ in the wall thickness at angle 0° (5Th simulation) . Diff corresponds to the strain component gradient between the internal and the external sensors.

From Fig. 2.32, the "mid-thickness" results for ε_{zz}, with the assigned simulation name 5Th, are very similar to those obtained with the tube with the simulation 4Th. The convergence seems to be achieved with 4 elements in the wall thickness.

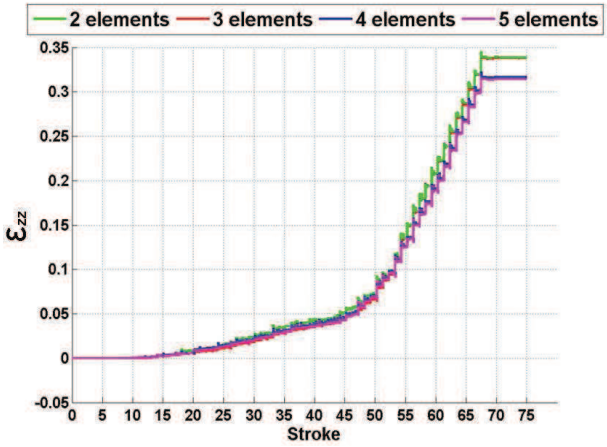

Figure 2.32. "Mid-thickness" value of ε_{zz} comparison at angle 180° in function of the number of elements over the thickness.

This analysis at "mid-thickness" is then done for other components of the strain tensor: ε_{rr}, $\varepsilon_{\theta\theta}$ (see Fig. 2.33 and 2.34). The trend is the same: the convergence seems to be achieved with 4 elements in the wall thickness.

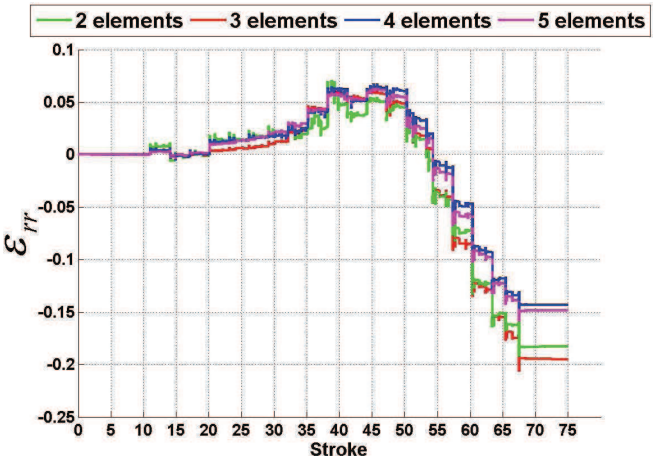

Figure 2.33. "Mid-thickness" value of ε_{rr} comparison at angle 180° in function of the number of elements over the thickness.

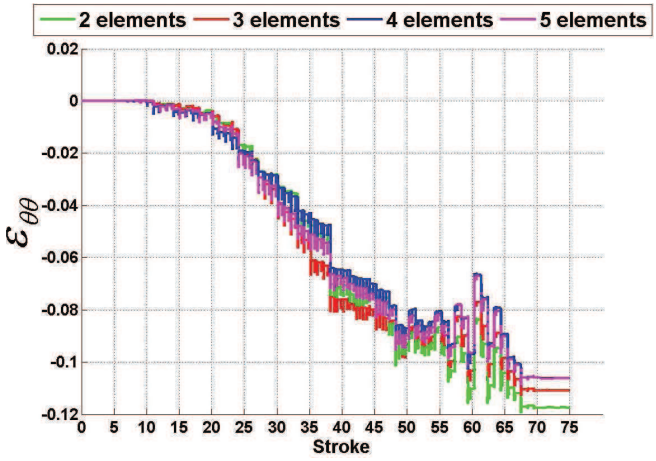

Figure 2.34. "Mid-thickness" value of ε_{rr} comparison at angle 180° in function of the number of elements over the thickness.

2.3.5.2 Number of elements over the tube length

For this sensitivity study the time step is fixed to 0.001s, the Zy4 material behavior is assumed isotropic elastic-plastic (Eq. 2.46). The tube initial length is 20 mm and the number of elements over the wall thickness is 3 (mesh size: 0.33 mm). 4 different size meshes over the length of the tube are tested. Their characteristics are summarized in Table **2.7**. The adaptative time step is used in this study.

Table 2.7. Number of elements over the length tube (simulation characteristics).

Assigned simulation name	Number of elements (length)	Mesh size (length)	Number of elements	Number of nodes	CPU time
20L	20 elements	1 mm	36000	8400	123 h (6 cores)
30L	30 elements	0.66 mm	54000	12400	78 h (6 cores)
40L	40 elements	0.5 mm	72000	16400	76 h (6 cores)
50L	50 elements	0.4 mm	90000	20400	212 h (6 cores)
60L	60 elements	0.33 mm	108000	24400	140 h (6 cores)

Simulations comparisons are carried out with the three values ε_{rr}, $\varepsilon_{\theta\theta}$, ε_{zz} since they were calculated with a mesh tube with 4 elements over the thickness. The sensors are positioned at the same place.

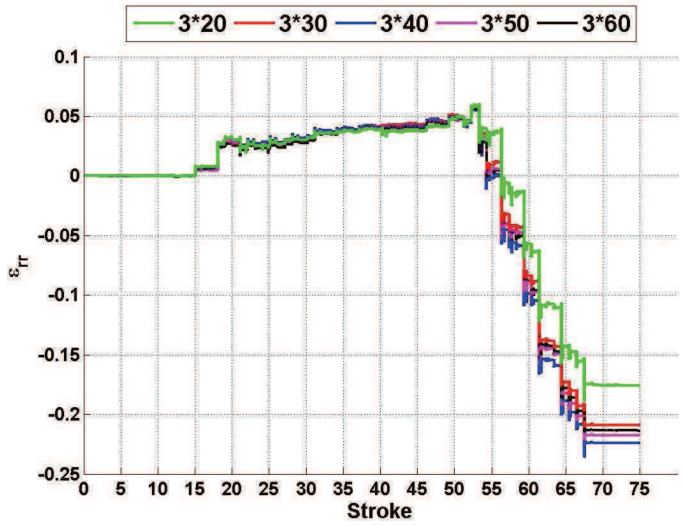

Figure 2.35. $\mathcal{E}_{rr}$ comparison at angle 0° in function of the number of elements over the tube length.

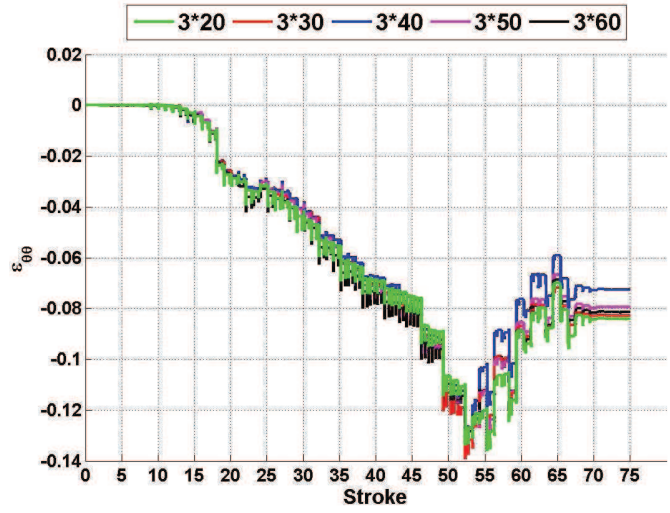

Figure 2.36. $\mathcal{E}_{\theta\theta}$ comparison at angle 0° in function of the number of elements over the tube length.

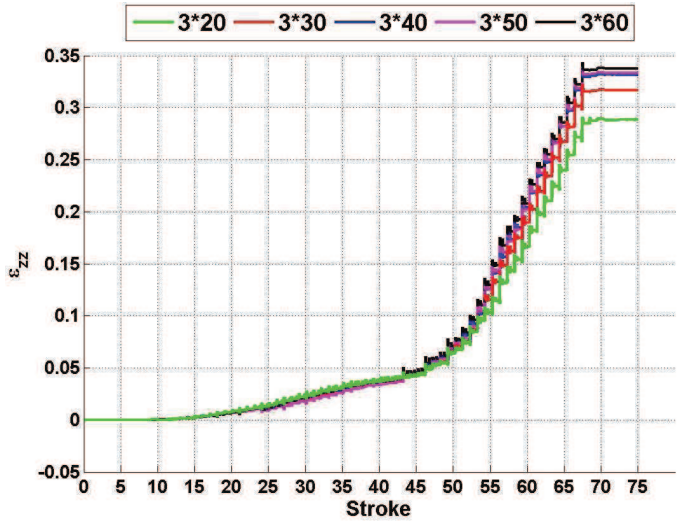

Figure 2.37. $\mathcal{E}_{zz}$ comparison at angle 0° in function of the number of elements over the tube length.

From Fig. 2.37, the higher the number of elements along the length of the tube, the higher the values of ε_{zz} (10-15% more axial elongation). Convergence is achieved from 40 elements along the tube length in this strain direction. The difference is especially noticeable from the 50th stroke since then the tube is in contact with the mandrel. From this point, dies reduce the wall thickness involving a tube elongation in the rolling direction because of mass conservation. It is therefore necessary to put 40 elements in length for a 20 mm tube. It is noticed from Fig. 2.35 and 2.36 that ε_{rr}, $\varepsilon_{\theta\theta}$ values are miscalculated after the 50th stroke when using less than 40 elements. As explained previously, in the working zone, the material can only flow in two directions: the rolling direction or the side relief, therefore a mesh with few elements in the tube length could induce numerical rigidity to the mechanical computation, and lead to a decrease of the computation accuracy. Finally, in this particular case, it is necessary to use at least 50 elements in the rolling direction in order to get good precision.

2.3.5.3 Time step

For this sensitivity study the simulation 4Th (4 elements over the thickness) is used. The set-up of the numerical simulation stays unchanged. 4 different time steps are tested: 5.10^{-3}s, 1.10^{-3}s, 5.10^{-4}s, 1.10^{-4}s. Their characteristics are summarized in Table **2.8**. The adaptative time step is not used in this study.

Table 2.8. Number of elements over the length tube simulation characteristics.

Time step [s]	Number of strokes	CPU time
5.10^{-3}	77	98 h (6 cores)
1.10^{-3}	77	288h (6 cores)
5.10^{-4}	77	869h (6 cores)
1.10^{-4}	51	749h (6 cores)

Simulations comparison is carried out with the three values ε_{rr}, $\varepsilon_{\theta\theta}$, ε_{zz} since they were calculated with a mesh tube with 4 elements over the wall thickness.

Some numerical volume increase is observed during the first 50 strokes. As explained previously, these first 50 strokes deal with the *clover tube*. Fig. 2.38 shows a sensitivity study of this volume increase with the time step. A small time step can prevent this numerical error. But, reducing the time step leads to an increase in the required CPU time (Fig. 2.38 and Table **2.8**).

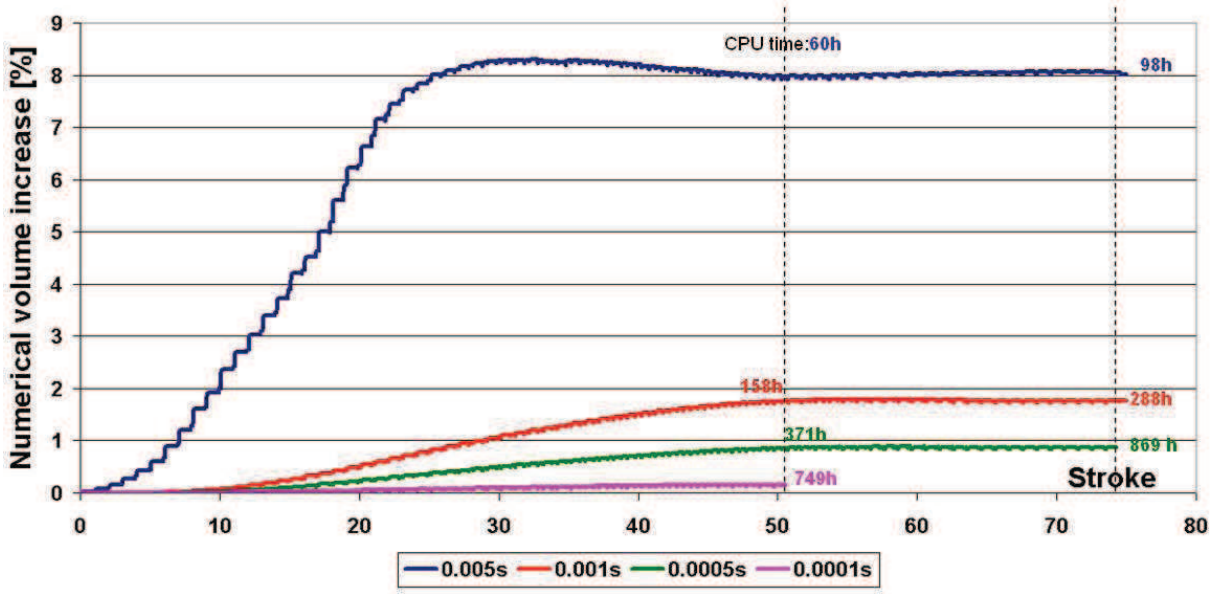

Figure 2.38. Volume increase in the numerical simulation during the HPTR process for various time steps. CPU time with 12 cores. Mesh characteristics: 4 elements over the wall thickness – 60 elements over the tube length.

This numerical volume increase has an impact in the computation of the mechanical values. Figs. 2.39 - 2.41 displays the influence of the time step on one material point (sensor) deformation.

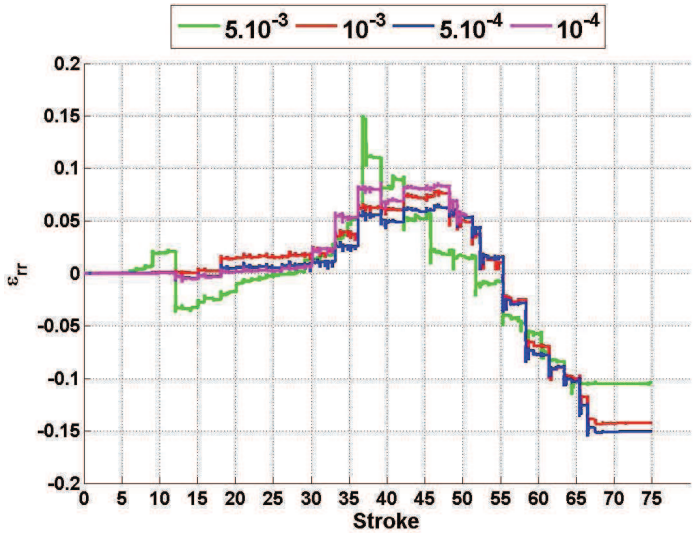

Figure 2.39. $\mathcal{E}_{rr}$ comparison at angle 0°. Time step influence.

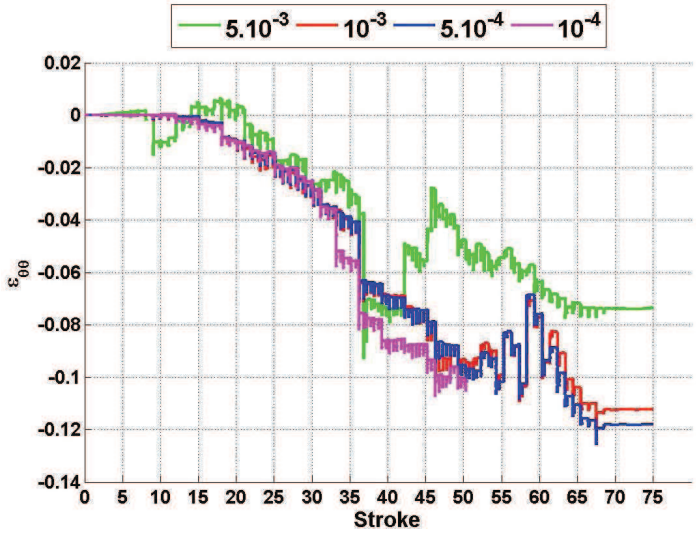

Figure 2.40. $\mathcal{E}_{\theta\theta}$ comparison at angle 0°. Time step influence.

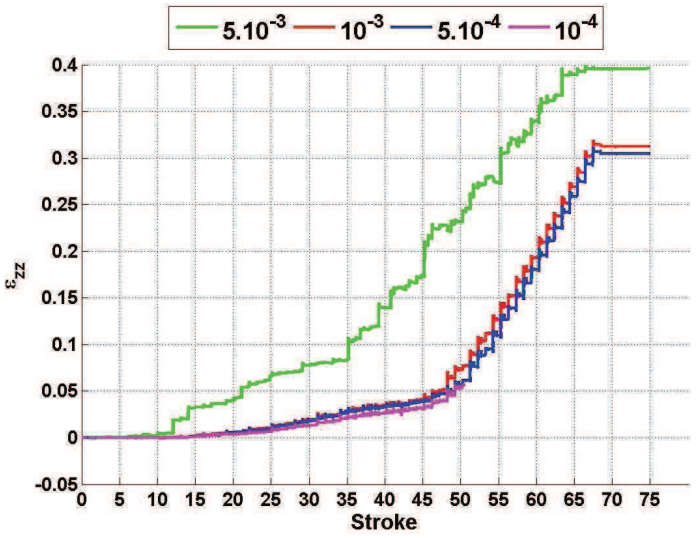

Figure 2.41. $\mathcal{E}_{zz}$ comparison at angle 0°. Time step influence.

It is clear regarding Figs. 2.39 - 2.41 that the simulation with a time step of 5.10^{-3}s is not viable. The tube increasing volume leads to much more contact with dies hence more deformation (e.g. Fig. 2.41). In contrast the simulation with a time step of 1.10^{-3} is very close to that with a time step of 5.10^{-4} in terms of strains. On the other hand, time step of 1.10^{-4}s leads to different strain values in the orthoradial and radial directions, when comparing with the other time step. It can be explained by the fact that the *clover tube* (stroke 30-50) does not increase too much its numerical volume as seen in Fig 2.38. Nonetheless, time step of 1.10^{-4}s leads to a huge CPU time (749h are required for 51 strokes). Due to the minimal difference in the results between time steps of 1.10^{-3}s and 5.10^{-4}s, it is chosen to work with a time step of 1.10^{-3}s, which gives the best compromise CPU time –precision.

2.3.6 Summary

This section dealt with influence of numerical parameters. The following numerical characteristics are chosen for future simulations:

- Time step: 0.001s
- Tube length: 20 mm
- Mesh type: Unstructured anisotropic mesh
- Number of element over the thickness: 4
- Number of element over the length: 50

2.4 Comparison between predicted and measured pilgered steady state tube geometry

The goal of this section is to validate the kinematics of the dies that will be used in the following of this work. CEA/Saclay carried out an interrupted pilgering test in order to know experimentally the tube profile in a steady state. This test dealt with two materials: the ODS steel tube and the Zircaloy-4 tube. A 3D measurement machine, numerically controlled (CNC), allows the acquisition of the coordinates of the points measured in the pilgered steady state tube geometry. Concerning the numerical simulation, *a long tube approach* is used. The latter consists in pilgering numerically a tube at least as long as the real working zone. In this particular case the length tube is 210 mm. Now, dealing with such a tube length, CPU time computation is enormous. In order to reduce the simulation time and, because only the transition geometry is required in this study, a coarse mesh is used: 2 elements over the thickness and 210 elements over the length tube (mesh size in the rolling direction: 1 mm). Simulation mesh characteristics are summarized in Table **2.9**.

Table 2.9. Mesh characteristics.

	Number of elements	Number of nodes	Element type
Tube	176400	44310	3D tetrahedral
Dies	3 x 20294	3 x 10199	2D triangles
Mandrel	60000	30100	2D triangles

The simulation set up is displayed in Fig. 2.42.

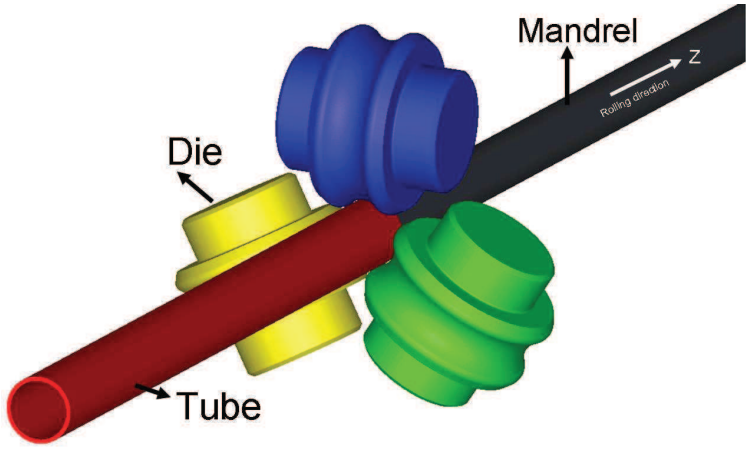

Figure 2.42. The tooling and meshes used in the *long* tube simulation.

The elastic-plastic behavior described in section 2.3.2 is assumed for the tube. Coulomb friction is assumed with $\mu = 0.1$. *Pass 3* of the fabrication route (Table **2.1**) is simulated. The process total time is 98s. The time step is constant during deformation, $\Delta t = 0.001s$, elsewhere the adaptative time step is used. The tube is turned 39° and moved forward (feed) 1.7 mm after each stroke. A material point takes 120 strokes to pass through the working zone. The full 120 strokes computation time remains high: the *long tube approach* took 1560 CPU h (65 days) parallel calculation on a 2x8 cores (AMD Opteron Magny-cours 2.3 Ghz) Linux cluster.

Fig. 2.43 shows how equivalent deformation is distributed in the steady state tube. Dies shoulder first touch the tube, leaving axial rolling marks with a high accumulated equivalent strain. It is noticed also that the strain is not homogeneous over the tube circumference due to the *clover* tube shape imposed in the first dozens of strokes. These two aspects were observed in the experimental test carried out (e.g. Fig. 2.43: Zy4 tube).

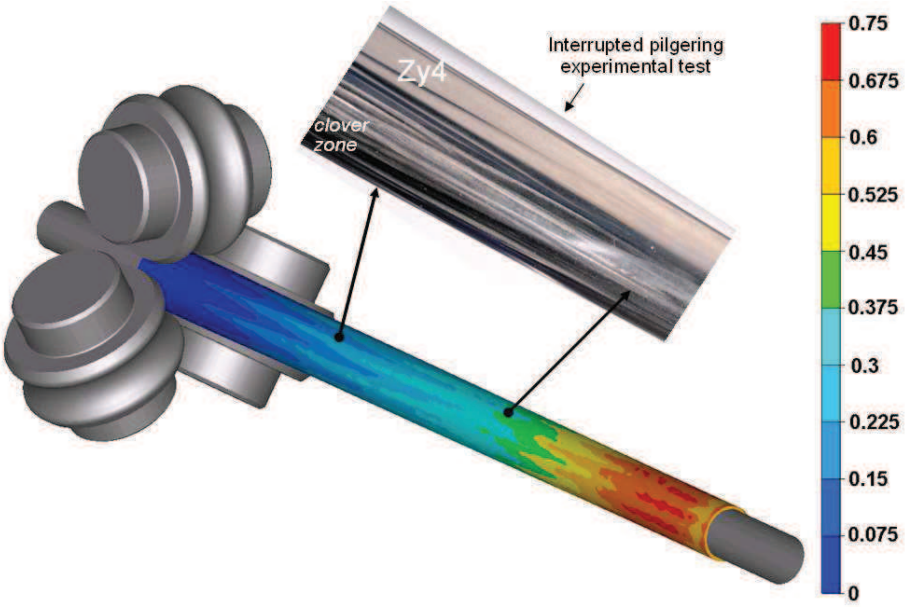

Figure 2.43. Interrupted pilgering test: simulation and experimental. Equivalent strain Zy4 tube isovalues.

Fig. 2.44 displays the calculated distance between the mandrel and the steady state Zy4 tube. It is concluded that nearly the half of the pilgering process in this particular case is done with contact between the mandrel and the tube. Therefore the wall thickness reduction occurs in the last 69 strokes. It means that the Q factor evolves during the HPTR process. In the first fifty strokes the Q factor is smaller than during the last strokes.

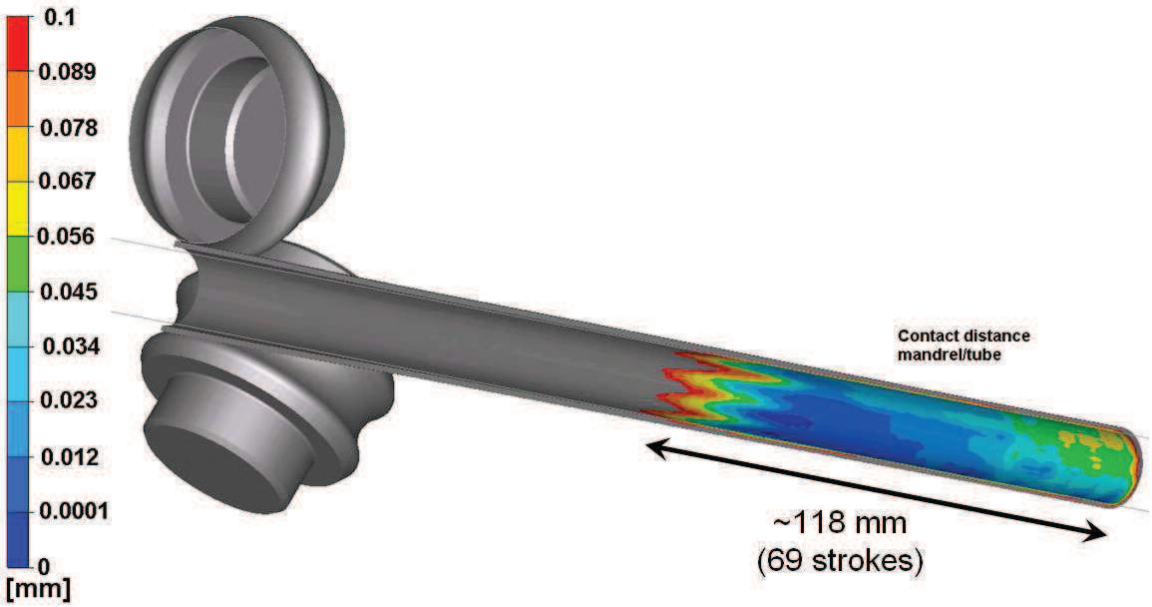

Figure 2.44. Interrupted pilgering test simulation. Contact distance mandrel - Zy4 tube isovalues.

A comparison between the predicted and the measured pilgered steady state tube geometry is illustrated in Fig. 2.45. In this figure the strain of the experimental tube is calculated with the following equation:

$$\varepsilon = \ln\left(\frac{r_0^{\,2}}{r_{(z)}^{\,2}}\right) \tag{2.50}$$

where r_0 is the initial tube radius and $r_{(z)}$ is the radius at a given position z of the tube length.

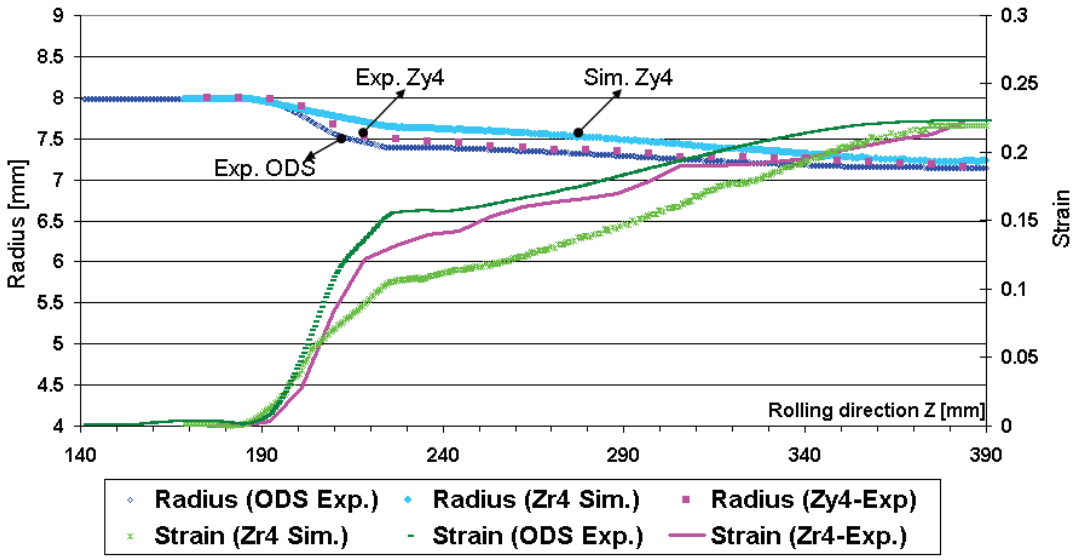

Figure 2.45. Comparison between the predicted and the measured pilgered steady state tube.

It is noticed in Fig. 2.45 that the numerical pilgering model underestimates the intermediate strain values because the steady state *profile* is slightly different between the experimental and the numerical response. It is in the first slope that the difference is more distinct. There are some numerical model assumptions that can explain this dissimilarity: the whole HPTR mill is considered as rigid (the dies and mandrel spring-back is not taken into account), the contact management based in the penalty algorithm is highly dependent of the time step and the mesh size, the numerical volume increase has also an important role in this divergence. Nevertheless, the working zone length is nearly the same as well as the trend of the steady state tube profile and the strain. Additionally, the formed tube geometry of the *pass 3* fabrication route is reached. Fig. 2.46 shows a comparison between the analytical and the calculated formed tube geometry, which coincide very well.

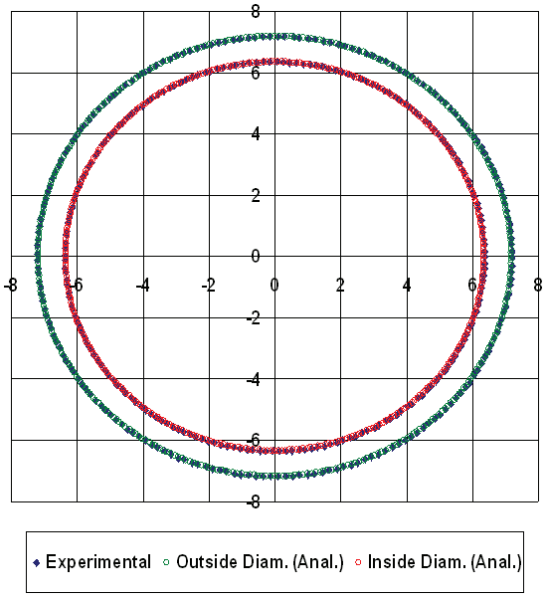

Figure 2.46. Formed tube cross geometry comparison (dimension: mm).

2.5 Conclusions

In this Chapter, complete modeling of HPTR cold forming process, involved in the production of thin tubes, has been analyzed.

In order to better understand numerical results, an introduction to the finite element method (FEM) has been done with the presentation of equations of the mechanical problem. Conservation equations and boundary conditions enable to define the system which has to be solved.

First numerical results have been detailed in a second part. The present study has demonstrated the feasibility of FEM mechanical deep analysis of the HPTR cold pilgering of tubes. Complete simulations of HPTR pilgering of an isotropic material have been presented using a *short tube approach*. In this approach all strokes are simulated. The main results have shown that the formed tube has non-homogenous strain in the radial, circumferential and axial direction. The maximal strain is located on the tube external surface due to the repeated contact with dies. A complex mechanical history undergone by a material point has been detailed. One can follow the overall thinning of the tube (compression along the radial direction), and overall reduction in diameter (compression along the ortho-radial direction), both of them resulting in a significant elongation along the tube axis. It is concluded that some ortho-radial and radial strain positive increments could lead to damage and cracking, even though most of the strain path involves reduced stress triaxiality. A detailed analysis of local stress conditions may explain the nucleation of defects (longitudinal cracks) in low-cycle fatigue regime. The shear ε_{rz} component was found to be not negligible in relation with the others shear strains. Additionally, non-helicoïdal path was found in HPTR pilgering because the component $\varepsilon_{\theta z}$ is nearly zero.

A sensitivity analysis on the mesh sizes, time step, type of mesh and length of the tube was performed in order to assess the accuracy of the current calculations. An optimal set of numerical parameters was chosen: unstructured anisotropic mesh (4 elements over the thickness, 50 elements over the length), tube length of 20 mm, time step of 0.001s. This configuration exhibits the best accuracy-computation time compromise.

Finally, a comparison between predicted and measured pilgered steady state tube geometry was carried out. The *long tube* approach was used. Some discrepancies were found between the numerical and the experimental response. They are mainly due to numerical approximations in the FEM model and assumptions made for the real HPTR kinematics. Nevertheless, general trends have been obtained and the numerical kinematics seems to be accurate enough to be considered in for a more detailed mechanical analysis of the process, using adapted constitutive laws.

2.6 Résumé en français

Dans ce Chapitre, la modélisation complète du procédé de laminage à pas de pèlerin de type HPTR, impliqué dans la production de tubes minces, a été analysée.

Afin de pouvoir interpréter et comprendre au mieux les résultats numériques, une introduction à la mécanique numérique a été faite. Les équations de conservations et les conditions limites ont permis de poser le problème et définir le système à résoudre. Le problème est ensuite discrétisé en temps et en espace afin d'avoir le système final à résoudre. Enfin, la résolution du ce système est brièvement détaillée.

Les premiers résultats numériques ont été présentés dans la deuxième partie de ce chapitre. La présente étude a démontré la faisabilité détaillée de la mise en forme des tubes par le procédé de laminage à pas de pèlerin de type HPTR en utilisant la méthode des éléments finis. Des tendances générales ont été obtenues et ont besoin d'être confrontées à des expériences. La première difficulté pour la simulation de procédés de type laminage à pas de pèlerin est la prise en compte de l'aspect incrémental de la déformation. Certains auteurs ont fait le choix de simplifier la modélisation du procédé en considérant la déformation sur une configuration quasi stationnaire du procédé pour diminuer les temps de calcul des simulations du procédé. On a choisi ici d'étudier l'ensemble des événements de déformation vu par la matière. On se limite simplement à l'étude d'une portion du tube. Les extrémités du tube ne sont pas représentatives de l'histoire du matériau car les conditions de bord libre d'un coté et les conditions de déplacement imposé de l'autre coté entraînent des perturbations. On étudie alors l'histoire thermomécanique du matériau sur la portion intérieure du tube.

Dans cette approche (*tube court*), tous les coups de cage sont simulés. Les principaux résultats ont montré que le tube fini a une déformation non homogène dans les directions radiale, circonférentielle et axiale. La déformation maximale est située sur la surface externe du tube, elle est due au contact répété avec les galets. L'histoire mécanique complexe subie par un point matériel a été détaillée. On peut suivre l'amincissement du tube (compression suivant la direction radiale), et la réduction globale de diamètre (compression le long de la direction ortho-radiale), les deux phénomènes conduisant à un allongement important le long de l'axe du tube. Il est conclu que certains incréments positifs de déformation ortho-radiale et radiale pourraient conduire à des dommages et des fissures, même si la plupart du chemin de déformation implique une triaxialité négative. Une analyse détaillée des conditions de déformations locales peut expliquer la germination de porosités (fissures longitudinales) dans le régime de la fatigue oligocyclique. La composante de cisaillement ε_{rz} a été jugée non négligeable par rapport aux autres déformations de cisaillement. En outre, un chemin non-hélicoïdal a été trouvé dans le laminage HPTR car la composante $\varepsilon_{\theta z}$ est presque nulle.

Une analyse de sensibilité sur la taille de maille, le pas de temps, le type de maillage et la longueur du tube a été réalisée afin d'évaluer la validité des calculs. Des paramètres numériques optimaux ont été choisis: maillage anisotrope non structuré (4 éléments sur l'épaisseur, 50 éléments sur la longueur), la longueur du tube est de 20 mm, le pas de temps est

0.001s. Cette configuration présente le meilleur compromis temps, calcul et précision des résultats.

Enfin, une comparaison entre le profil expérimental et le profil numérique du tube d'un essai interrompu a été réalisée. L'approche tube long a été utilisée. Certains écarts ont été trouvés entre la réponse numérique et la réponse expérimentale. Elles sont principalement dues aux approximations numériques dans le modèle éléments finis et des hypothèses faites sur la cinématique du laminoir HPTR réel. Néanmoins, les tendances générales ont été obtenues et la cinématique numérique semble être assez précise pour être prise en compte dans une analyse mécanique plus détaillée du procédé, en utilisant des lois de comportement adaptées au chargement cyclique.

Chapter 3

Constitutive law

3.1 Introduction

The knowledge of the constitutive equations of materials allows an optimal design involving the proper material at the right place. Building the models calls on a set of equations that must be adjusted to a given material thanks to an experimental database made of mechanical experiments and, possibly, microstructural observations. For this purpose, some experimental mechanical tests have been achieved leading to an identification of three different types of constitutive laws: isotropic monotonic, anisotropic monotonic and isotropic cyclic. The final goal is to assess the influence of the choice of the constitutive model on the mechanical history of a material point under pilgering conditions.

Section 1 introduces briefly the ferritic and martensitic ODS steels considered in this Chapter. Some microscopic observations coming from the literature are discussed.

Section 2 deals with the mechanical response of ODS steels using a classical tensile test. The constitutive behavior of two ODS grades under tensile conditions is modeled with a monotonic constitutive law. Constitutive law parameters are identified using the inverse analysis module available in Forge3®.

Hot extruded ODS steel tubes usually reveal an anisotropic strength in the radial, ortho-radial and longitudinal directions. Anisotropy is due to crystallographic texture and to the strongly elongated grain morphology in the extrusion direction. Identification of Hill's parameters is done in Section 3 using both i) compression tests of cylindrical specimens cut in three different directions (longitudinal, radial and ortho-radial) and ii) shear test parallelepiped specimens; combined with an inverse analysis technique [Vanegas *et al.*, 2011a].

In Section 4, in the framework of a unified plastic constitutive theory, the strain-controlled cyclic characteristics of ODS steels are analyzed and modeled with two different tests. The first test is a classical tension-compression test. The second test consists in alternated uniaxial compressions along two perpendicular axes. It has been developed based on the similarities with the loading path induced by the pilgering process. Since variable strain amplitudes prevail in pilgering conditions, the parameters of the considered constitutive law were identified based on a loading sequence including strain amplitude changes. Next, an elastic-plastic model based on internal state variables is investigated. Its main features and its implementation into Forge3® are discussed. Moreover, a proposed semi automated inverse analysis methodology is shown to efficiently provide optimal sets of parameters for the considered loading sequences. When compared to classical approaches, the model involves a reduced number of parameters, while keeping a good ability to capture stress changes induced by strain amplitude changes. Furthermore, the methodology only requires one test, which is an advantage when the amount of available material is limited [Vanegas-Marquez *et al.*, 2011b].

3.2 Manufacturing ODS steel process

In this study, the mechanical properties of two different ODS steels are presented:

i) ferritic steel (14% by weight of chromium)
ii) martensitic steel (9% by weight of chromium)

Because the amount of ODS is limited, ferritic ODS steels from different origins were used. One designated as *J05* (CEA material code) and the other designated as *J27-M2* (CEA material code). Concerning the martensitic grade, it is designated as *J24* (CEA material code). Theirs manufacturing and microscopy observations are discussed below.

J05 and *J24* were produced at the CEA from powders delivered by Aubert & Duval. Mechanical alloying was performed by Plansee: yttrium oxide powder (content of 0,3 wt.%) was added by milling to the pre-alloyed (Fe, Cr, C, W, Ti….) matrix powder (Table **3.1**). The mechanically alloyed powder is sealed in a soft steel can and hot-extruded in the form of bars at a temperature of 1100℃ and then air-cooled. The produced *J05* ODS bar was then annealed at 1050℃ for 1 h and air cooled. The *J24* bar was then annealed first at 1050℃ for 1 h and water cooled; then annealed at 750℃ and air cooled. They did not undergo any subsequent recrystallization heat treatment.

Table 3.1. Chemical composition of ODS steels (weight %).

CEA material code	Grade	Fe	Cr	W	Ti	Y	O	C	Si	Ni	Mn
J05	Ferritic	83.10	13.65	1.17	0.30	0.26	0.06	0.05	0.27	0.16	0.33
J24-M2	Ferritic	83.10	13.5	0.90	0.40	0.22	0.06	0.05	0.32	0.17	0.27
J24	Martensitic	87.06	8.45	1.10	0.22	0.28	0.06	0.04	0.17	0.35	0.27

J05 ODS steel microstructure characterization was carried out in the work of Steckmeyer [Steckmeyer *et al.*, 2010]. Characterization of the grain morphology using a transmission electron microscope (TEM) showed that the grains were elongated along the extrusion direction (Fig. 3.1(b)) and relatively equiaxed in the bar section (Fig. 3.1(a)). Additionally in Steckmeyer's study, texture analyses were conducted using X-ray diffraction (XRD) techniques. For *J05* steel, they revealed a very strong fiber texture, the preferential crystallographic orientation being <110> along the extrusion direction, as presented in Fig. 3.2. *J05* showed a pole density <110> along the extrusion direction of 28 [Steckmeyer *et al.*, 2010]. Unlike ferritic grades, martensitic grades (*J24*) show a lower crystallographic texture (see Fig. 3.3), with a pole density <110> along the extrusion direction of 3 [Praud 2011]. *J24* grade is much more isotropic than *J05* because of the ferrite to austenite phase transformation (see section 1.2.1), characteristic of martensitic grades, after hot extrusion [Toualbi *et al.*, 2011].

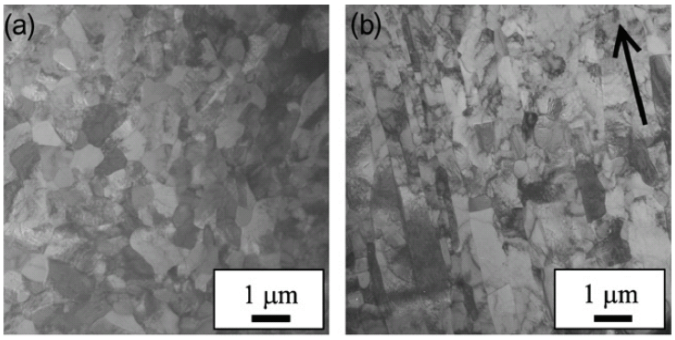

Figure 3.1. Description of the extruded bar microstructure of *J05* steel. TEM images with an extrusion direction respectively (a) perpendicular to the image plane and (b) along the arrow [Steckmeyer *et al.*, 2010].

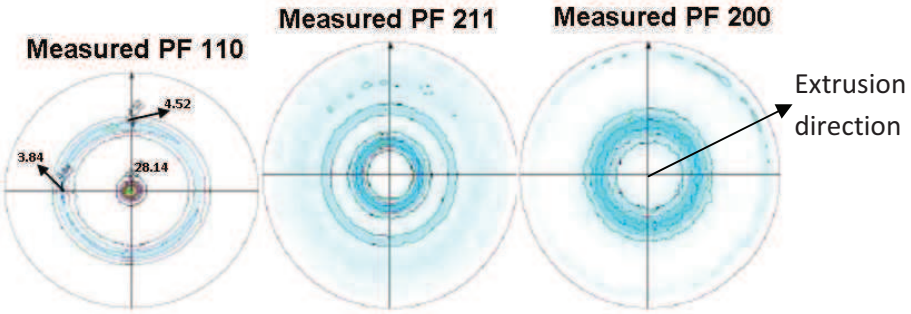

Figure 3.2. *J05* steel pole figure obtained by XRD [Steckmeyer *et al.*, 2010].

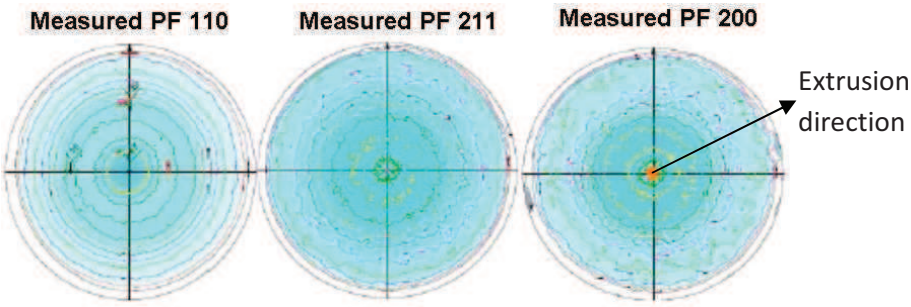

Figure 3.3. *J24* steel pole figure obtained by XRD [Praud 2011].

The other ferritic alloy designated as *J27-M2* was studied in the framework of the Generation IV and Transmutation Materials (GETMAT) European program research project. The alloy, produced at the CEA/Saclay; was hot extruded in the form of bars at 1100℃ and then air cooled. Next, it was annealed at 1050 ℃ for 1.5 ho urs and air-cooled. The chemical composition of the investigated ODS grade is shown in Table **3.1**. It is noticed that chemical compositions of both ferritic grades (*J05* and *J27-M2*) are quite similar. Therefore, *J05* and *J27-M2* ODS ferritic steels have a very close microstructure. This study assumes that *J05* and *J27-M2* ODS ferritic grades have also the same mechanical behavior.

The J27-M2 microstructure looks different depending on the orientation of the plane of observation [Serrano *et al.*, 2011], since grains are elongated in the extrusion direction. A

preferential orientation <110> axes along the extrusion direction (see Fig. 3.4) is observed. Similarly to the bar *J05* described previously (Fig. 3.2). [Serrano *et al.*, 2011] carried out tensile tests on samples machined in the longitudinal and radial direction of a ferritic ODS extruded bar (*J27-M2)*. They have concluded that the observed microstructural anisotropy seems to have a direct effect on the ductility. It was found in this work that the radial orientation was around 50% less ductile than the extruded (longitudinal) direction, while the yield stress and ultimate tensile strength were only slightly affected by anisotropy.

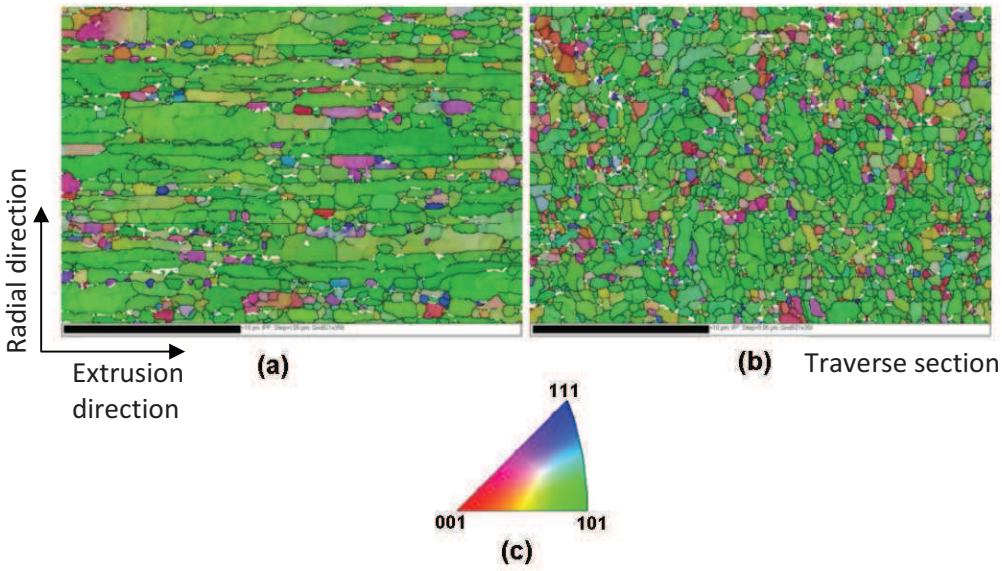

Figure 3.4. *J27-M2* inverse pole figure maps obtained by EBSD on the (a) longitudinal, (b) transverse section of samples and (c) inverse pole figure legend (reference direction is the extruded direction [Serrano *et al.*, 2011].

The available material described previously were mechanically tested as following:

- *J05*: tensile test and cyclic tension-compression test
- *J24*: tensile test and cyclic tension-compression test
- *J24-M2*: cyclic compression-compression test

The above mechanical tests are described, simulated and analyzed in the following sections.

3.3 Monotonic constitutive law

3.3.1 Experimental facilities

3.3.1.1 Tensile test set up

One specimen geometry has been used for grades *J05* and *J24* to characterize the mechanical properties in tension. The tensile direction is parallel to the longitudinal direction of the extruded bar. The specimen geometry has an 11.5 mm gauge length and a 2 mm x 2 mm square section. The specimens were machined from the homogeneous part of the ODS steel bar. Tensile tests were carried out at room temperature. They were strain controlled with a constant strain rate of $7x10^{-4}$ s^{-1}. This experimental campaign was carried out by M. Praud at CEA/Saclay [Praud 2011], [Praud *et al.*, 2011].

3.3.1.2 Tensile test results

Tensile test results are gathered in Table **3.2**. The first highlight is the limited ductility of *J24* in comparison with *J05*. Moreover, *J24* has a yield limit slightly superior to *J05*. The Young's modulus is the same for both grades as expected. Stress-strain curves obtained for *J05* and *J24* are displayed in Fig. 3.5.

Table 3.2. *J05* and *J24* tensile experimental test results.

	$E[GPa]$	$R_{p0.2\%}[MPa]$	$R_m[MPa]$	$\sigma_{y0.2\%}[MPa]$	$\sigma_m[MPa]$	$\varepsilon_{(\sigma_m)}[\%]$	$\varepsilon_{failure}[\%]$
J05	207.7	1072	1158.14	1078.26	1294.6	12.62	21.39
J24	207.7	1083	1183.3	1089	1237	5	14.6

In Table **3.2** E is the Young's modulus, $R_{p0.2\%}$ is the offset yield point, R_m is the tensile strength, $\sigma_{y0.2\%}$ is the yield limit at the offset yield point, σ_m is the ultimate tensile strength, $\varepsilon_{(\sigma_m)}$ is the strain corresponding to the ultimate stress and $\varepsilon_{failure}$ is the fracture point.

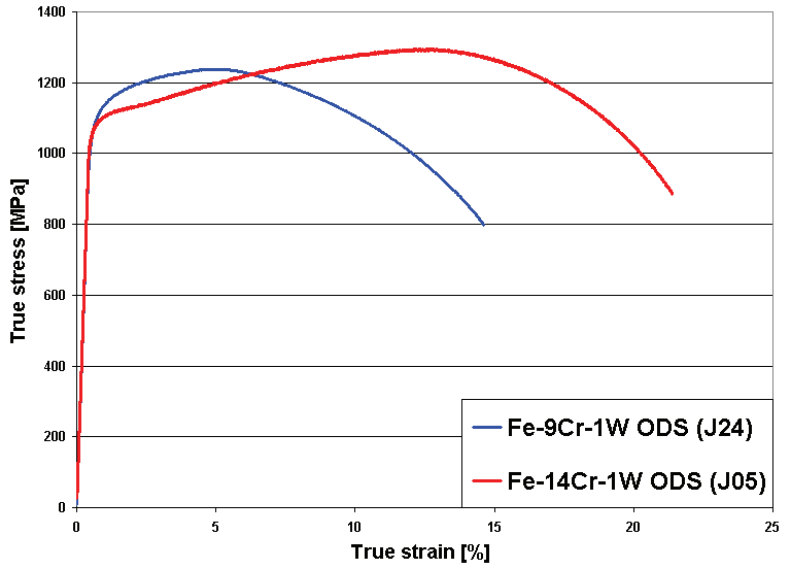

Figure 3.5. ODS steel tensile test experimental results [Praud 2011].

3.3.2 Monotonic constitutive model

A standard constitutive model to described monotonic loadings is the elastic-visco-plastic Hansel-Spittel law described given by:

$$\sigma_0(\bar{\varepsilon}) = A e^{m_1 T} T^{m_9} \bar{\varepsilon}^{m_2} e^{m_4 \bar{\varepsilon}} (1+\bar{\varepsilon}^{m_5 T}) e^{m_7 \bar{\varepsilon}} \dot{\bar{\varepsilon}}^{m_3} \dot{\bar{\varepsilon}}^{m_8 T}, \tag{3.1}$$

where $\bar{\varepsilon}$ is the equivalent deformation (total strain), $\dot{\bar{\varepsilon}}$ the equivalent deformation rate (total strain rate), T is the temperature and A, m_{1-9} are the regression coefficients. The previous tensile test is assumed isothermal (temperature T is constant) and without strain rate effects: parameters m_3 and m_8 are therefore set to zero.

3.3.3 Identification methodology

An inverse analysis method is used to fit the parameters (A, m_1, m_2, m_4, m_5, m_7) of the Eq. (3.1) behavior law. The main interest of these methods is to identify parameters which are hard to estimate by manual fitting. These methods combine experimental and numerical data in order to determine the considered parameters. In a first step, experimental tests are performed and data are collected ($R^{\exp}$). These tests are numerically simulated to provide the numerical data (R^{sim}). Correlation between numerical and experimental data is obtained by minimizing an objective function representing the level of disagreement between numerical and experimental values. The best set of parameters is given thanks to an optimization algorithm based on Meta-model Assisted Evolution Strategies (MAES) [Fourment *et al.*, 2009], [Fourment *et al.,* 2010]. MAES are regarded as quite robust with respect to local extrema. They make possible to solve

complex optimization problems. Evolutionary algorithms (ES) typically consist of three operators: selection, recombination and mutation. Their cost is usually quite high in terms of function evaluations. MAES combines an ES with Kriging meta-models to reduce the number of functions [Ducloux *et al.*, 2010]. The inverse analysis tool based on MAES is used here as illustrated in Fig. 3.6.

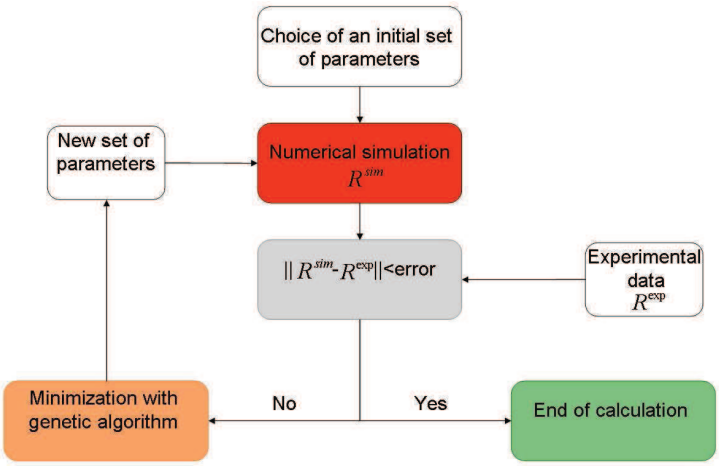

Figure 3.6. Inverse analysis schematic principle.

This method leads to the parameters given in Table **3.3** and to a good correlation between the experimental and the numerical responses (Fig. 3.7). The parameters were identified before necking.

Table 3.3. Parameters values of the numerical Hansel-Spittel law.

	$A[MPa]$	m_1	m_2	m_4	m_5	m_7	$E[GPa]$	Poisson's ratio
J05	1360	-0.01	0.0005	-0.0008	0	3.5	220	0.30

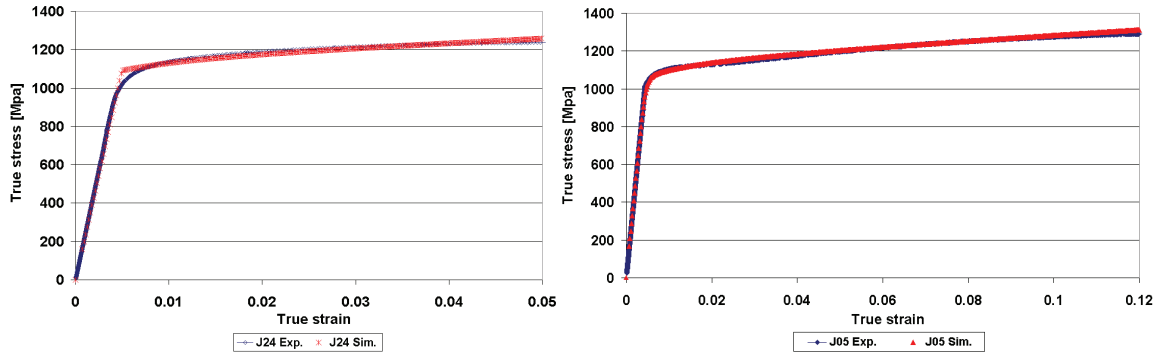

(a) (b)

Figure 3.7. Comparison between the experimental and numerical responses of the tensile test carried out for a) *J24* b) *J05*.

3.4 Anisotropic constitutive law

Plastic anisotropy can be measured through ovalization of cylindrical samples in tension or compression tests. Indeed the difference in the yield stress will favor plastic flows one-cross-sectional direction with respect to the other. The underlying application being cladding tubes undergoing internal pressure, the mechanical properties of the ODS steel in the radial and ortho-radial directions should be studied.

In this section the identification of Hill's parameters (see section 1.4.1.2.1 for Hill48 model description) is presented performing compression tests on cylindrical specimens cut in three different directions (longitudinal, radial and ortho-radial directions in an extruded bar). Additionally to these tests, shear tests are also performed such as to identify all Hill's parameters [Massé 2010].

3.4.1 Experimental facilities

3.4.1.1 Upsetting test set up

Compression tests have been done on a hydraulic testing device Dartec HA250/300 at CEMEF. Samples were cut from the ODS bar by electrical discharge machining with an initial height of 11 mm, and an initial radius of 5 mm. The cutting procedure is displayed in Fig. 3.8. 49% height compression is performed with an hydraulic machine. The sample and tools are lubricated with Molykote® HSC paste. The ram speed for compression is set to 1 mm/s. The ram displacement is 5 mm. For each direction, two samples have been used. The error (L2 error norm) between the experimental curves (force versus displacement) is calculated from Eq. (3.2), $f_{\exp 1}$ and $f_{\exp 2}$ being the experimental force, and i indicating a particular data point in the force versus displacement curves. The mechanical tests are reproducible with a maximum error of 2% (see Table **3.4**).

$$L2_{error-norm} = 100 \times \frac{\left\| f_{\exp 1} - f_{\exp 2} \right\|_{L_2}}{\left\| f_{\exp} 2 \right\|_{L_2}} = 100 \times \frac{\sqrt{\sum_{i=1}^{n} (f_{\exp 1}^{i} - f_{\exp 2}^{i})^2}}{\sqrt{\sum_{i=1}^{n} (f_{\exp 2}^{i})^2}} \tag{3.2}$$

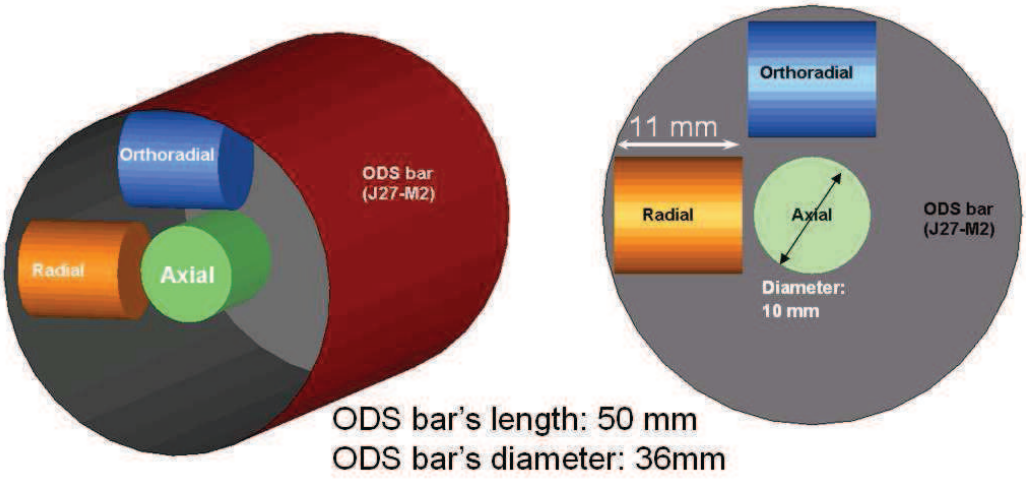

Figure 3.8. Cylindrical specimens cut in three different directions (longitudinal, radial and ortho-radial) of an ODS extruded bar. GETMAT project bar, piece reference: B 1-2.

3.4.1.1.1 Upsetting test results

After compression, the sample cut in longitudinal direction shows no ovalization, proving isotropy in the traverse section (Table **3.4**). Radial and ortho-radial samples show an ovalization which confirms the existence of a crystallographic texture (see Fig. 3.9).

Table 3.4. Samples dimensions evolution after compression.

	Long. a	Long. b	Radial a	Radial b	Ortho-radial a	Ortho-radial b
Major axis	6.51	6.52	6.86	6.85	6.95	6.93
Minor axis	6.50	6.48	6.20	6.19	6.10	6.09
Height reduction	48.2%	48.1%	49.3%	48.8%	48.4%	48.5%

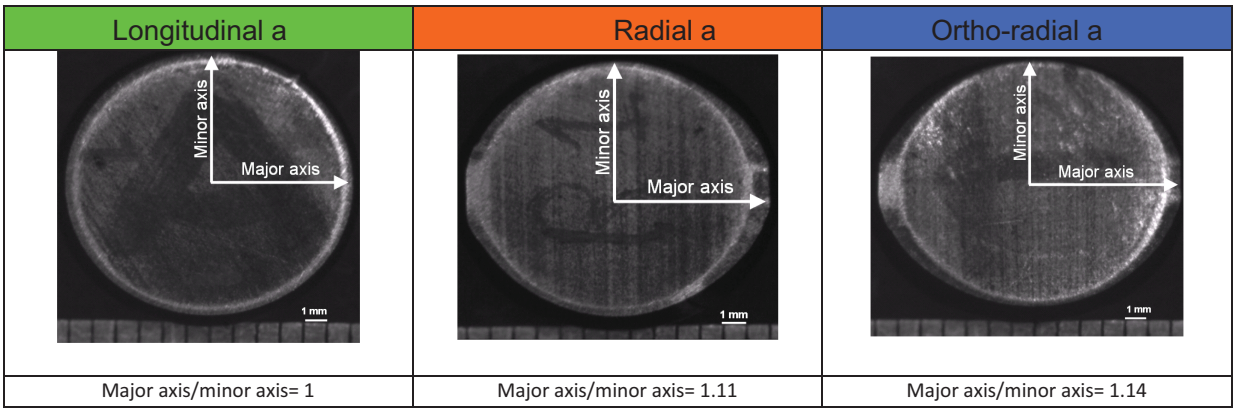

Figure 3.9. Upsetting experimental test results after compression.

When the mean stress-strain curves of the three upsetting tests are plotted (Fig. 3.10), slight differences of the yield stress appear between longitudinal, radial and ortho-radial

directions. Yield stresses are summarized in Table **3.5**. The ortho-radial direction seems to be the hardest one.

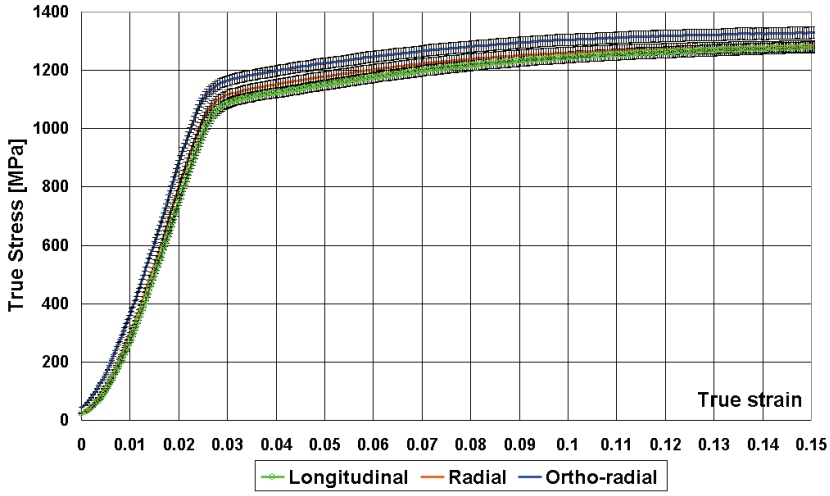

Figure 3.10. Stress-strain compression curves in three directions of samples cut from an extruded bar.

Table 3.5. Upsetting test yield stress comparison.

σ_{0zz} [MPa] Longitudinal	σ_{0RR} [MPa] Radial	$\sigma_{0\theta\theta}$ [MPa] Ortho-radial
1041	1066	1110

3.4.1.2 Shear test set up

Shear tests are performed in order to complete the Hill's parameters identification [Massé 2010]. Shear tests have been done on the same machine as for the compression tests. Dimensions of the samples are 2 x 2 x 14 mm^3, cut from a *J27-M2* ODS extruded bar (described previously) as shown in Fig. 3.11. Samples were again cut from a bar by electrical discharge machining. The ram speed for the shear test is set to 1 mm/s; the test set up is displayed in Fig. 3.12. Their experimental shear response is reproducible with a maximum error (Eq. (3.2)) of 5%.

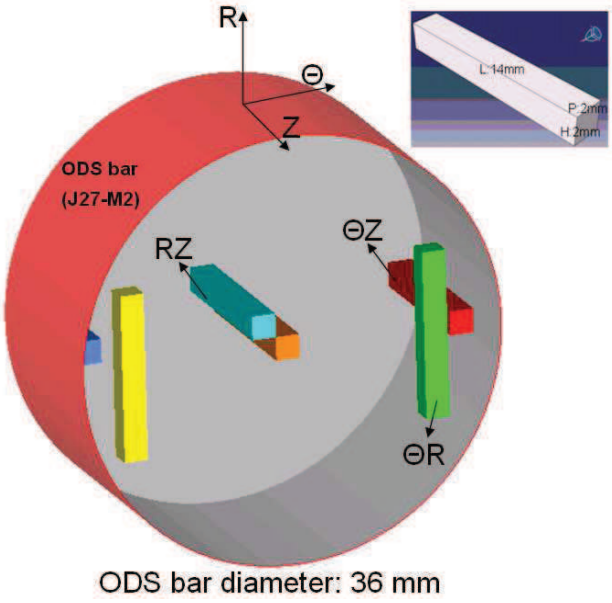

Figure 3.11. Sampling for shear test.

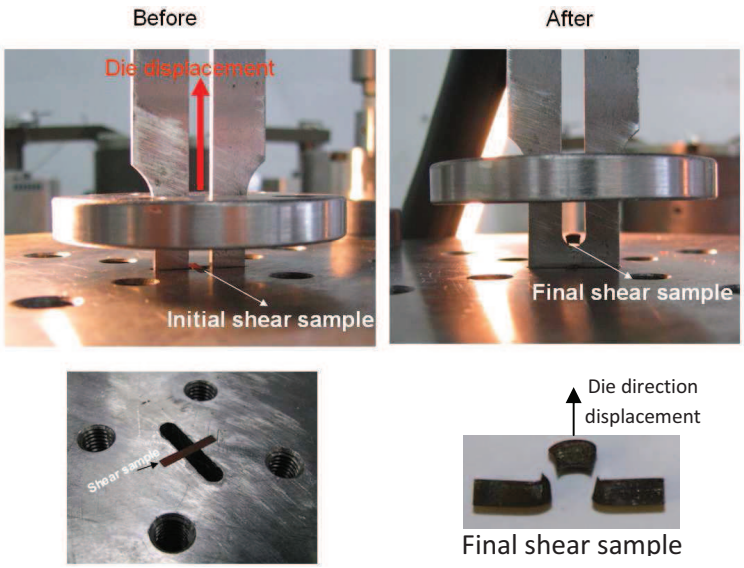

Figure 3.12. Shear test set up, left: before shear, right: after shear. *J27-M2* steel.

3.4.1.2.1 Shear test results

The shear stresses for the three selected orientations are shown in Fig. 3.13. Shear yield stresses are summarized in Table **3.6**. The θR solicitation seems to be the less ductile. The other two, RZ and θZ, lead to similar behaviors.

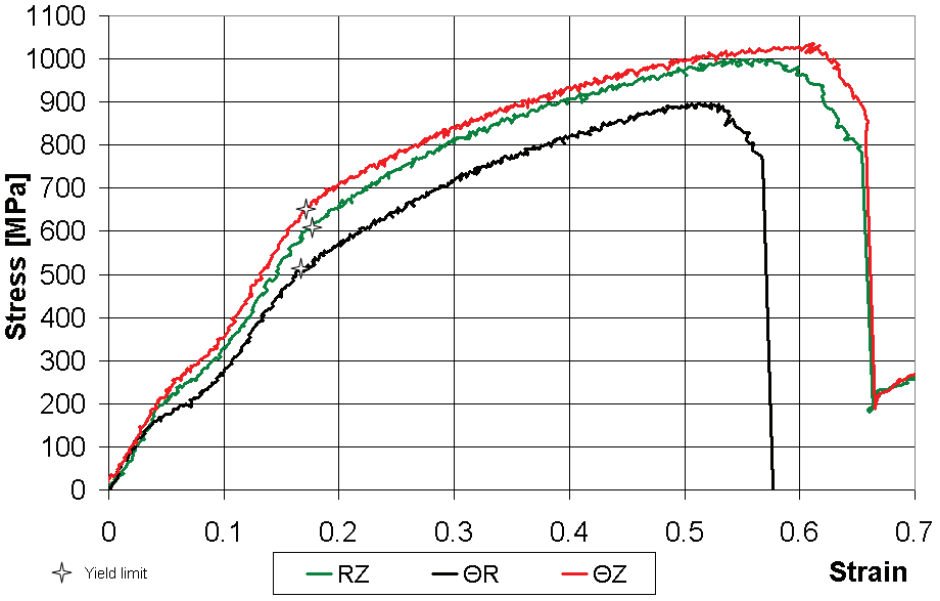

Figure 3.13. Shear curves. J27-M2 steel.

Table 3.6. Shear test yield stress results in three different directions..

$\sigma_{0\theta Z}$ [MPa]	σ_{0RZ} [MPa]	$\sigma_{0\theta R}$ [MPa]
670	605	510

3.4.2 Anisotropic constitutive model

The first yield function accounting for orthogonal anisotropy was introduced by Hill [Hill 1948] and is based on von Mises work. To introduce anisotropy, Hill kept the von Mises quadratic form, but added six coefficients to describe the direction-depended plastic flow properties:

$$1 = F(\sigma_{\theta\theta} - \sigma_{ZZ})^2 + G(\sigma_{ZZ} - \sigma_{rr})^2 + H(\sigma_{rr} - \sigma_{\theta\theta})^2 + 2L\sigma_{\theta Z}^2 + 2M\sigma_{rz}^2 + 2N\sigma_{r\theta}^2 \quad (3.3)$$

These parameters have a physical meaning; they are linked to the axial and shear yield stresses [Massé *et al.*, 2011]:

$$\sigma_{0ZZ} = \frac{1}{\sqrt{F+G}},\ \sigma_{0RR} = \frac{1}{\sqrt{G+H}},\ \sigma_{0\theta\theta} = \frac{1}{\sqrt{F+H}},\ \sigma_{0\theta Z} = \frac{1}{\sqrt{2L}},\ \sigma_{0RZ} = \frac{1}{\sqrt{2M}},\ \sigma_{0R\theta} = \frac{1}{\sqrt{2N}} \quad (3.4)$$

Thus, the equivalent stress can be chosen as [Montmitonnet and Chenot 1995]:

$$\sigma_{eq}^2 = A\cdot[F(\sigma_{\theta\theta} - \sigma_{ZZ})^2 + G(\sigma_{ZZ} - \sigma_{rr})^2 + H(\sigma_{rr} - \sigma_{\theta\theta})^2 + 2L\sigma_{\theta Z}^2 + 2M\sigma_{rz}^2 + 2N\sigma_{r\theta}^2] \quad (3.5)$$

In an anisotropic case, A is taken by convention as [Montmitonnet and Chenot 1995]:

$$A = \frac{1}{2}\sqrt{\frac{3}{\Sigma}} \text{, with } \Sigma = FH + FG + GH \tag{3.6}$$

$F = G = H = 1$ and $L = M = N = 3$ return the von Mises criterion. Hill's criterion therefore appears as the simplest quadratic generalization of von Mises criterion.

Complex anisotropy models developed for sheet forming, previously mentioned in Chapter 1, have not been validated in bulk forming and their numerous parameters are quite difficult to identify [Massé *et al.*, 2011]. This explains the choice for this simple approach. Besides the model is already available in most FEM formulations.

3.4.3 Identification methodology

Ovalization can be characterized by the shape factor of the cross-section after compression (see Fig. 3.14) and related to the anisotropy coefficients [Montmitonnet and Chenot 1995]. G/H can be identified from the radial compression test:

$$\frac{b}{a} = \frac{h_0}{h}^{(G-H)/(G+H)} \tag{3.7}$$

where b, a are the axis of the ellipsoidal cross-section ($b < a$).

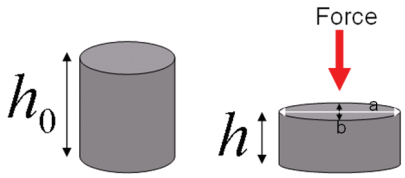

Figure 3.14. Compression test geometry.

Similarly, for the ortho-radial compression test (H/F):

$$\frac{b}{a} = \frac{h_0}{h}^{(H-F)/(H+F)} \tag{3.8}$$

The third equation F/G is issued from the two previous equations. All the experimental (*major axis/minor axis*) values are taken at mid-height of the sample. To fully identify the three coefficients (F, G and H) one more information is required. The yield stress in the axial compression (Eq. 3.4 for σ_{0ZZ}) gives F.

$$F = \frac{(F/G)}{\sigma_{0ZZ}{}^2 (1 + (F/G))} \tag{3.9}$$

Finally, G and H are given by:

$$G = \frac{F}{(F/G)} \tag{3.10}$$

$$H = F*(F/G) \tag{3.11}$$

In practice, L, M and N are determined from shear tests using expressions in Eq. 3.4 for $\sigma_{0\theta Z}$, $\sigma_{0\theta R}$ and σ_{0RZ}. Because of the limitation in the amount of available ODS material steels, shear tests are not always possible. Therefore, in this section it is proposed to identify two anisotropic constitutive laws:

i) Fully identification: F, G and H are identified through Eqs. (3.9) - (3.11). L, M and N are determined from shear tests using Eq. 3.4 for $\sigma_{0\theta Z}$, $\sigma_{0\theta R}$ and σ_{0RZ}. (Designated simulation name: cylinder).

ii) Partial identification: F, G and H like in (i). The values of L, M and N are fixed to 3, as the case for an isotropic material. (Designated simulation name: cylinder_shear_iso).

These methodologies, applied to our experimental tests, leads to the parameters values presented in Table **3.7**.

Table 3.7. Anisotropic Hill criterion material parameters calculated using analytical expressions.

	F	G	H	L	M	N
Cylinder	0.56	1.55	1	2.56	3.19	4.6
Cylinder_shear_iso	0.56	1.55	1	3	3	3

These parameters have been validated by simulating the upsetting test using the identified behavior. Friction was first identified based on barreling [Massé *et al.*, 2011], resulting in Tresca's friction factor $\overline{m} = 0.21$. Some discrepancy is observed between experiment and simulation of the ovalization, when leading in the radial and ortho-radial directions as shown in Fig. 3.15 and Table **3.8** (*Ovalization ratio* is defined as the ratio between a and b, see Eq. 3.7). Hill's constitutive model equations make the assumption that the material is perfectly orthotropic. However, the initial sample height is significant in comparison to the diameter of the raw extruded bar, which leads according to Fig. 3.16 to inhomogeneous texture in the sample. This may correspond to a non orthotropic material. A second limitation of the analytical approach is that it combines strain and stress data to identify the anisotropic parameters. This is known to be incompatible with Hill's theory [Hill 1948], [Hill 1990]. Finally, it is known that friction reduces the magnitude of anisotropic effects [Montmitonnet and Chenot 1995]. The three aspects above may explain the difference between experimental and numerical ovalization results. For this reason a numerical optimization is proposed in the next section in order to have enhanced results.

It is pointed out that the *cylinder* and *cylinder_shear_iso* approaches, performed about the same way, but a slight improvement for the *cylinder* approach (see Table **3.8**).

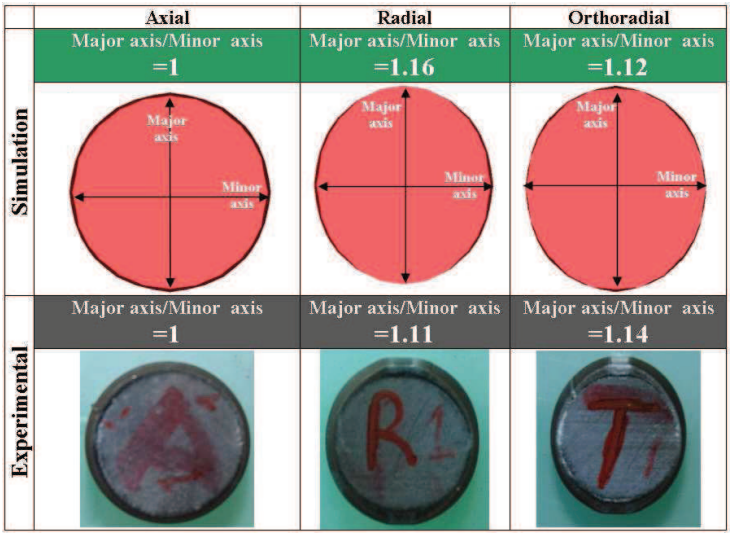

Figure 3.15. Comparison between experimental and numerical ovalization (cylinder case). J27-M2 steel.

Table 3.8. Ovalization ratios comparison.

	Longitudinal	Radial	Ortho-radial
Experimental	1	1.11	1.14
Cylinder	1	1.16	1.12
Cylinder_shear_iso	1	1.17	1.10

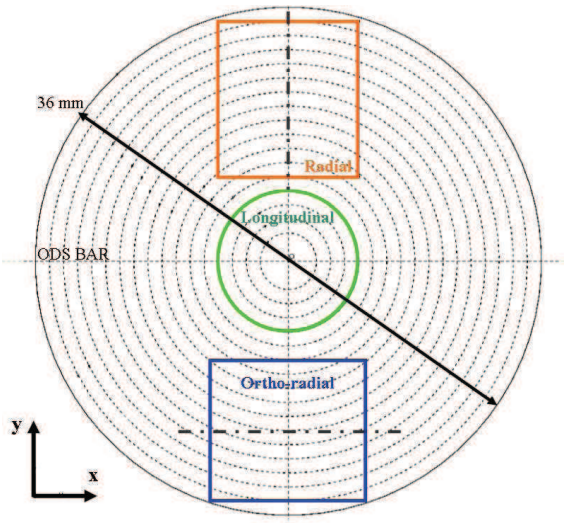

Figure 3.16. Schematic crystallographic texture pattern from side to side of the sample schematic representation.

3.4.3.1 Parameters calculation improvement

In order to improve the ovalization ratio results, for the *cylinder* and the *cylinder_shear_iso* cases, the inverse analysis method explained in section 3.3.3 is used again.

The optimization is done on F, G, H only, i.e. shear parameters remain fixed for both cases. The inverse analysis was carried out for each sample (radial and ortho-radial loading). Enhanced parameter values, for both studied cases, are shown in Table **3.9**. Correlation between numerical and experimental data is obtained by minimizing the deviation between numerical and experimental values (*major and minor axes* of the cross-section). A new ovalization result of the radial and orthoradial samples is shown in Table **3.10** for the *cylinder* case.

Table 3.9. Anisotropic Hill criterion enhanced parameters after numerical identification.

	F	G	H	L	M	N
Cylinder before numerical optimization	0.56	1.55	1	2.56	3.19	4.6
Cylinder after numerical optimization	0.7	1.23	1.27	2.56	3.19	4.6
Cylinder_shear_iso before numerical optimization	0.56	1.55	1	3	3	3
Cylinder_shear_iso after numerical optimization	0.66	1.3	1.6	3	3	3

Table 3.10. *Cylinder* case: experimental and numerical compression test ovalization ratio results.

	Ovalization ratio *before* numerical optimization			Ovalization ratio *after* numerical optimization		
	Long.	Radial	Orthoradial	Long.	Radial	Orthoradial
Simulation	1.001	1.16	1.12	1.001	**1.107**	**1.142**
Experimental	1.001	1.110	1.144	1.001	1.110	1.144

The optimization on ovalization ratios leads, as expected when using Hill's criterion, to errors in the predicted yield stresses [Hill 1990]. The yield stress is not well estimated as seen in Table **3.11**. Errors already existed in the analytical approach. Fitting Hill's coefficient based on ovalization should however give relevant results on deformation predictions during cold forming.

Table 3.11. *Cylinder* case: yield stresses comparison.

	σ_{0ZZ} [MPa]	σ_{0RR} [MPa]	$\sigma_{0\theta\theta}$ [MPa]
experimental	1041	1066	1110
before numerical optimization	1041	947	1211
after numerical optimization	1041	855	969

3.4.4 Further mechanical test

In the previous section it was pointed that the crystallographic texture was not homogeneous in the samples due to the significant size of the sample in relation with the ODS GETMAT bar diameter (36 mm). Therefore, it is proposed in this section to assess the effects of the sample size and of the cut position into the bar. Compressions of mini-cylinders were

performed. Designated names and cut positions of each mini-cylinder are shown schematically in Fig. 3.17(a). This Figure shows also the samples (in red) used in the previous section 3.3.1.

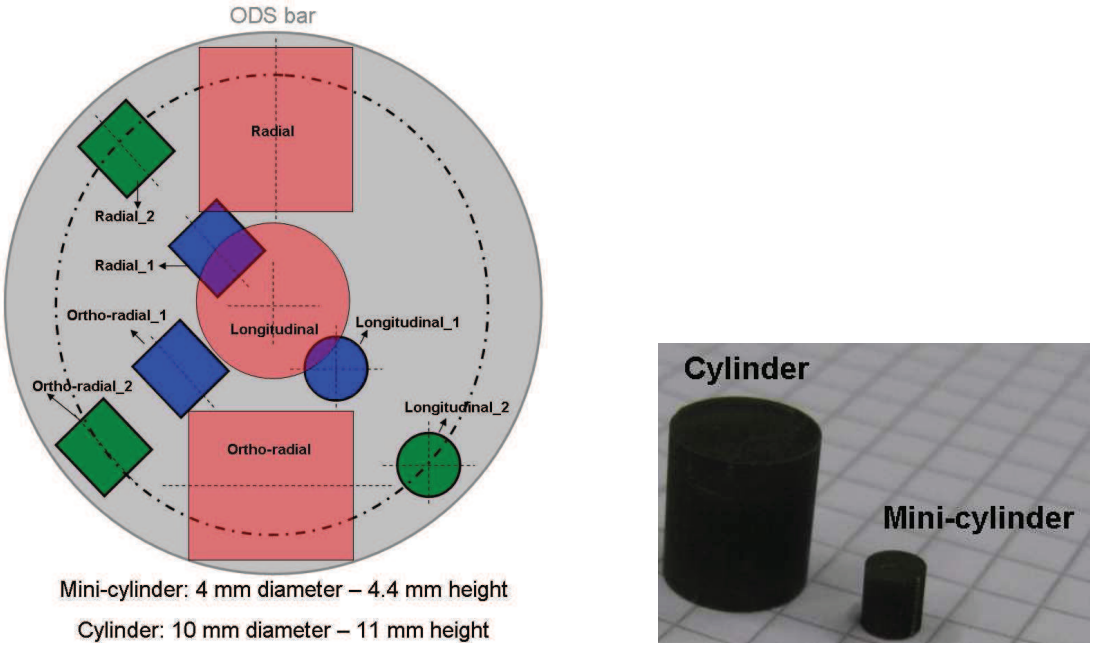

(a) (b)

Figure 3.17. (a) Cylinder and mini-cylinder cut in the extruded bar (not to scale) – (b) Cylinder and mini-cylinder size comparison.

Fig. 3.17(b) shows a comparison between the cylinder and the mini-cylinder sizes. Stress-strain curves for cylinders and mini-cylinders are superposed in Figs. 3.18 - 3.20 respectively for the three loading directions. The yield stresses and ovalization ratios of each test are summarized in Table **3.12**.

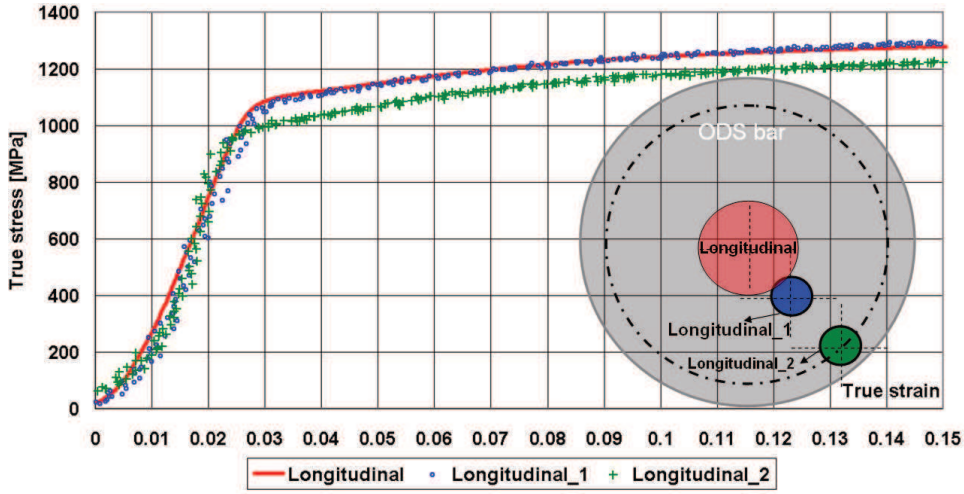

Figure 3.18. Stress-strain compression curves of one cylinder and two mini-cylinders positioned at different points and oriented in the longitudinal (extrusion) direction.

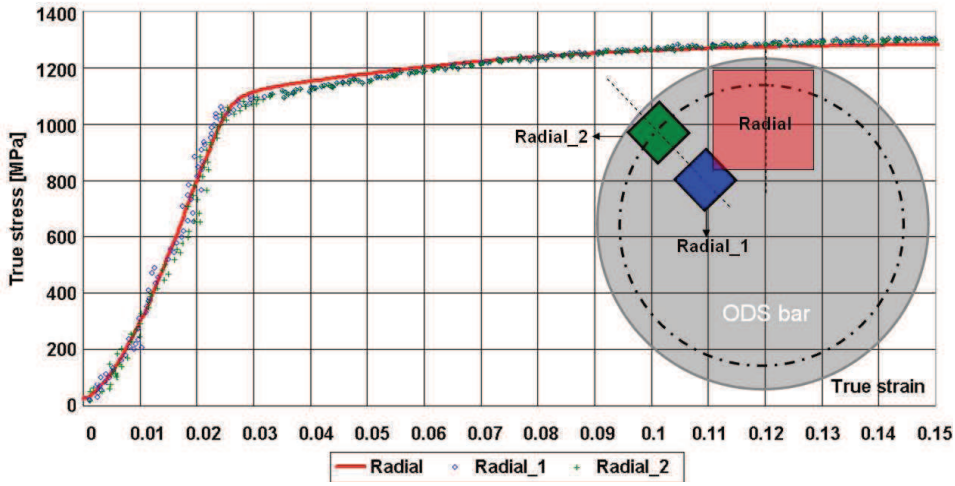

Figure 3.19. Stress-strain compression curves of one cylinder and two mini-cylinders positioned at different points and oriented in the radial direction.

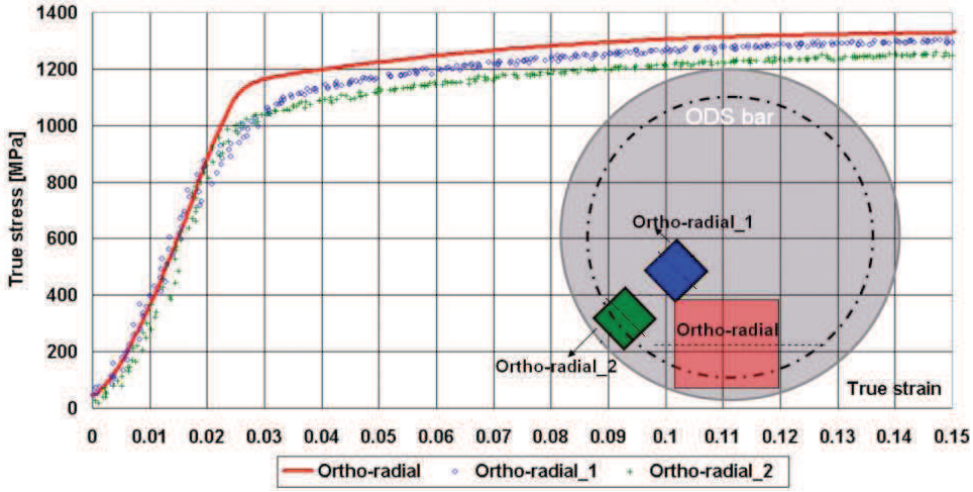

Figure 3.20. Stress-strain compression curves of one cylinder and two mini-cylinders positioned at different points and oriented in the ortho-radial direction.

Table 3.12. Experimental yield stresses and ovalization ratios comparison.

	Yield stress [MPa]	Major axis [mm]	Minor axis [mm]	Ovalization ratio
Longitudinal	1041	12.28	12.18	1.001
Longitudinal_1	1035	5.73	5.66	1.009
Longitudinal_2	958	5.79	5.52	1.044
Radial	1066	13.72	12.36	1.110
Radial_1	1047	6.12	5.08	1.151
Radial_2	1035	5.98	5.38	1.107
Ortho-radial	1110	13.92	12.16	1.144
Ortho-radial_1	1070	6.12	5.39	1.123
Ortho-radial_2	1012	6.07	5.36	1.129

Peripheral mini-cylinders show lower yield stresses in comparison with those located close to the central axis. Moreover, when dealing with mini-cylinders, it can be noticed that the ovalization ratio can vary with the position. In the ortho-radial direction, a systematic difference is noticed as compared to the bigger cylinders.

The parameters identification methodology described in section 3.3.3 was used again for the mini-cylinder compression tests. Results are summarized in Table **3.13**.

Table 3.13. Anisotropic Hill criterion parameters for cylinder and mini-cylinders.

	F	G	H	L	M	N
Cylinder	0.56	1.55	1	2.56	3.19	4.6
Mini-cylinder_1	0.63	1.58	0.91	2.63	3.28	4.73
Mini-cylinder_2	0.69	1.37	1	2.1	2.63	3.78

Mini-cylinder_1 is calculated from: *ortho-radial_1*, *radial_1* and *longitudinal_1*. *Mini-cylinder_2* is calculated from: *ortho-radial_2*, *radial_2* and *longitudinal_2*. The simulation of the upsetting of *mini-cylinder_2* resulted in good agreement on ovalization as shown in Table **3.14**. For *mini-cylinder_1* some discrepancy may still be observed.

Table 3.14. Experimental and numerical compression test ovalization ratio results.

	Cylinder			Mini-cylinder_1			Mini-cylinder_2		
	Long.	Radial	Ortho-radial	Long.	Radial	Ortho-radial	Long.	Radial	Ortho-radial
Exp.	1.001	1.11	1.144	1.009	1.151	1.123	1.044	1.107	1.129
Sim.	1.001	1.16	1.12	1.096	1.222	1.554	1.061	1.079	1.134

Regarding Table **3.13** it is pointed that the Hill's coefficients are dependent on the specimens cut position and size. Thus, when the cladding tube comes from a drilled extruded bar, it is clear that the choice of the mini-cylinders placed in peripheral zone (position 2) is the most adequate to calculate.

3.5 Cyclic constitutive law

This section deals with the experimental cyclic behavior of the investigated ODS steels at room temperature. Two types of test were performed. The first test is a classical tension-compression test. The second test consists in alternated uniaxial compressions along two perpendicular axes. It has been set up in order to *replicate* the loading path induced by the pilgering process. This section describes the specific loading sequence which was designed to determine completely the constitutive model parameters, using only one specimen, for each of the two tests (two samples overall).

3.5.1 Experimental facilities

3.5.1.1 Tension-compression test set up

The cyclic elastic-plastic behavior of the *J05* and *J24* was studied using one cylindrical specimen machined from an extruded bar with dimensions of 6 mm diameter and 10 mm gauge length. The samples were machined parallel to the extrusion direction. The strain rate was fixed at $0.002s^{-1}$ and the amplitude of deformation varied. The transitions from one amplitude to another are made after returning to zero deformation. The sequence of strain range amplitudes is described in Fig. 3.21: ±0.2%, ±0.3%, ±0.4%, ±0.5%, ±0.7%, ±1% before coming back to ±0.5% and finally increasing to ±1.5%. and ±2% The number of cycles at each amplitude is selected so as to stabilize the stress amplitude. The tests were carried out at room temperature and were performed at the CEA/Saclay in collaboration with B. Fournier, C. Caës and L. Toualbi [Toualbi 2010], [Vanegas-Marquez *et al.*, 2011b]

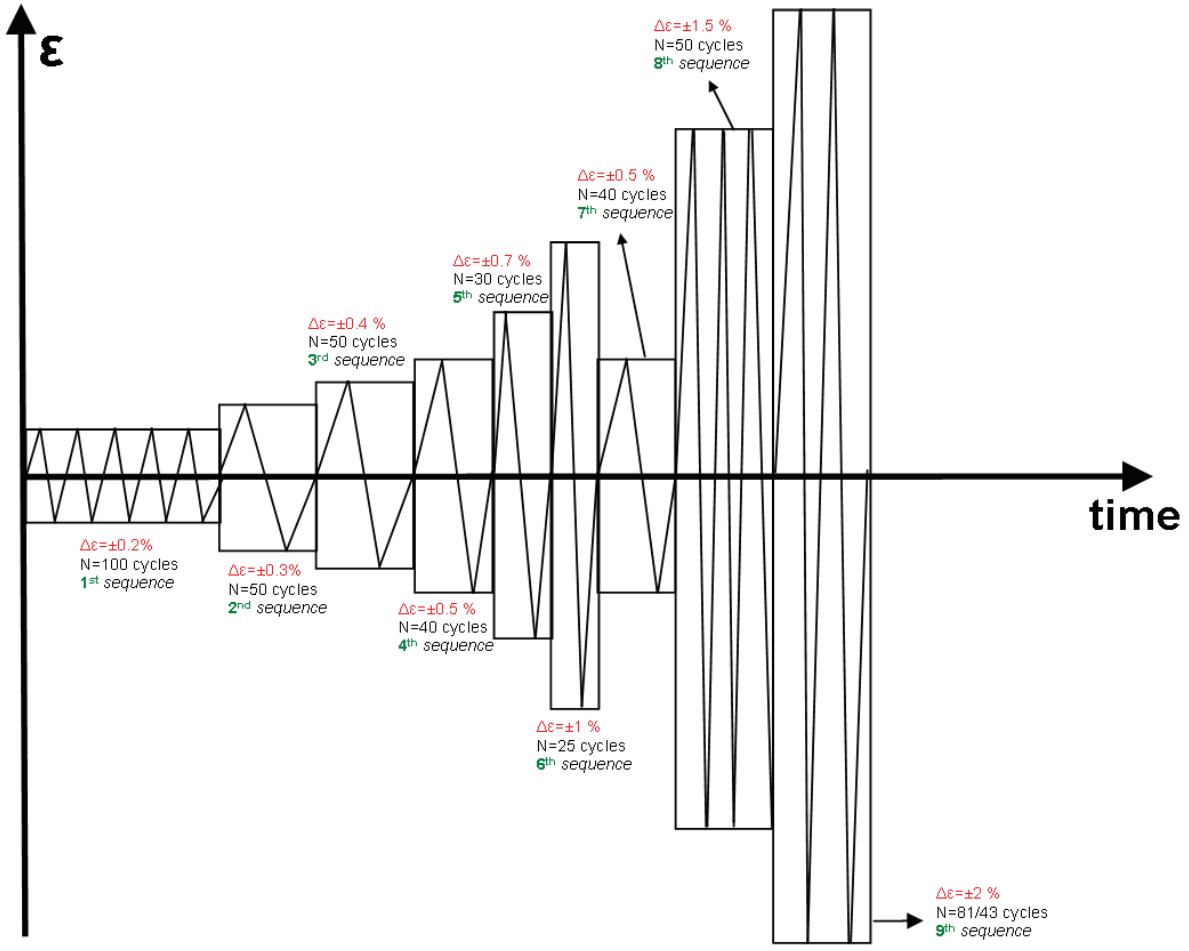

Figure 3.21. Schematic representation of the tension-compression loading sequence.

3.5.1.2 Compression -compression test set up

The cyclic deformation induced by cold pilgering is fairly well approximated by a sequence of compression tests along two perpendicular directions e.g. see [Armstrong 1982], [Huml and Strandell 1984]. The resulting flow stress evolution is expected to be different from the one obtained in monotonic deformation mode [Jiang and Kurath 1997], [Shamsaei *et al.,* 2010]. The non proportionality of the loading path is also likely to influence the mechanical behavior.

Small cubic specimens (10x10x10 mm) were cut from the *J27-M2* extruded bar (see Fig. 3.22).

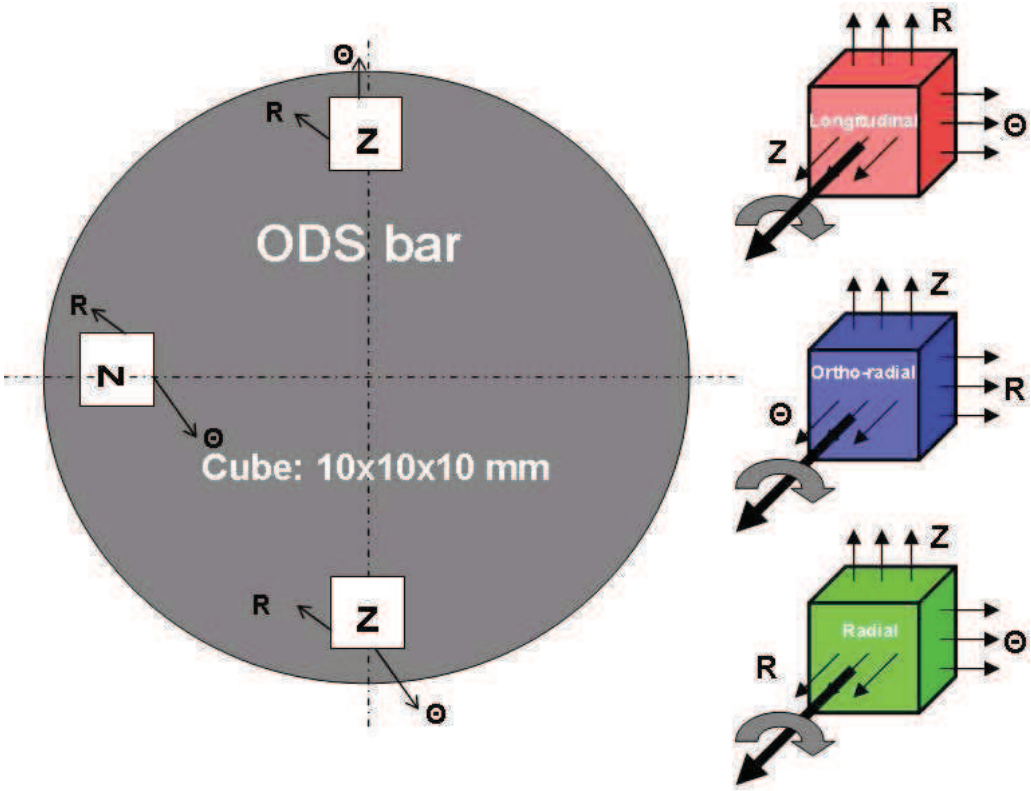

Figure 3.22. Schematic compression-compression test specimens cut from *J27-M2* steel bar.

The alternated loading sequence is schematically illustrated in Fig. 3.23 for the blue sample of Fig. 3.22, rotated by 90° at each compression step around th e ortho-radial direction. Lubrication is applied on each face before compression, in order to keep homogeneous deformation at each 'cycle'.

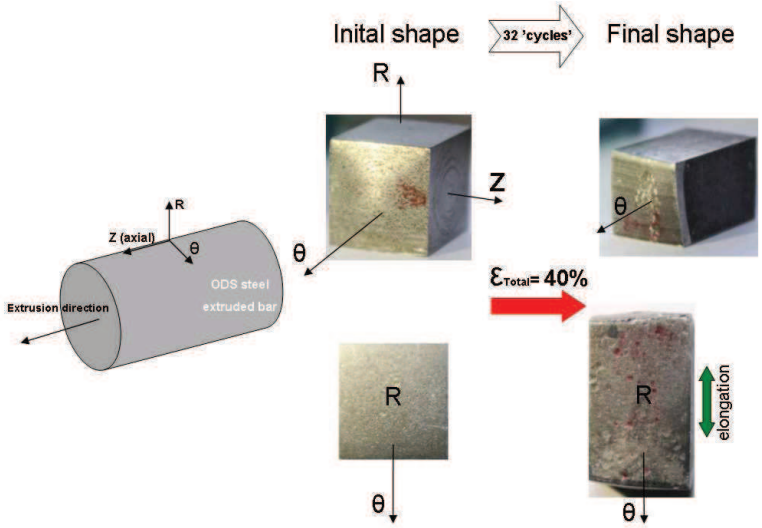

Figure 3.23. Schematic representation of the compression-compression test for the ortho-radial sample (sample rotated around the orthoradial direction).

The experimental test is divided for each specimen in 3 sequences: 1st) 20 cycles at plastic Δε= -1%; 2nd) 8 cycles at plastic Δε= -1.5%; 3th) 4 cycles at plastic Δε= -2%.

3.5.2 Analysis of experimental results

3.5.2.1 Tension-compression test

During the first 3 sequences no plastic strain is noticed. Therefore, the analysis starts from the 4th sequence. The cyclic stress response of *J05* and *J24* at room temperature for different total strain amplitudes is shown in Fig. 3.24. This figure shows the corresponding variations of the half-stress amplitudes vs. the number of cycles.

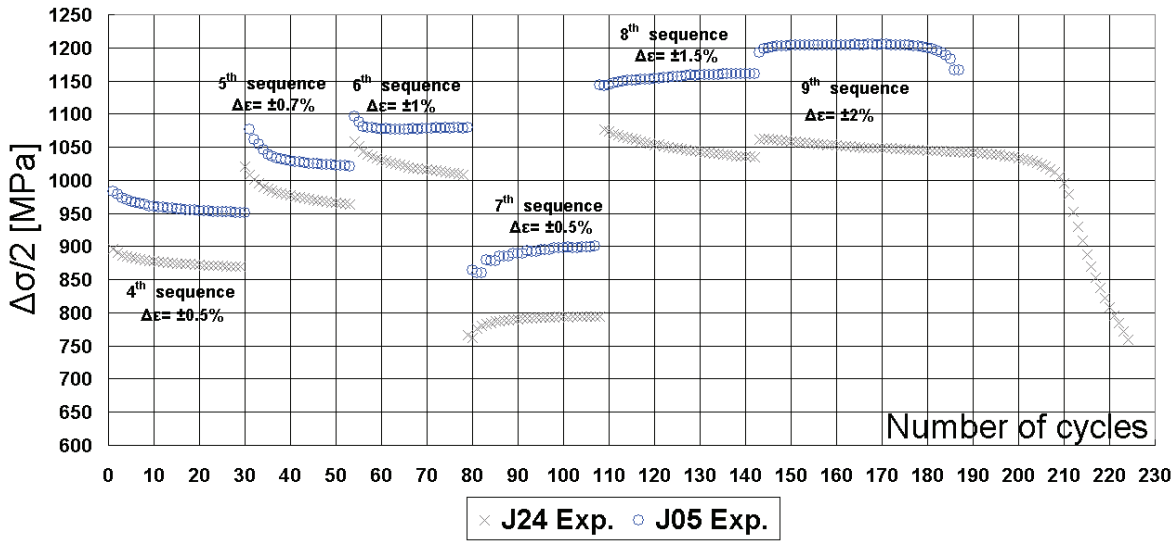

Figure 3.24. *J05* and *J24* experimental response for the considered loading sequence in tension-compression. Half stress amplitude vs. number of cycles.

For all strain ranges, the *J05* specimen exhibits higher strength than *J24* the specimen. The experiments show that the stabilized stress amplitude level (stabilized cycle) is reached within only few cycles (Fig. 3.24) for both studied grades. This is attributable to the excellent microstructure stability produced by the presence of nano-size oxide particles dispersed in ODS steels [Ukai and Ohtsuka 2007]. For sequence 4 and 5 the softening ratio is similar for the two grades, however, in sequence 5, *J05* stabilized faster than *J24*.

The switch from one strain amplitude to another illustrates strain range memory effects. In sequences 4-5-6 of Fig. 3.24, each increase in strain amplitude is followed by a cyclic *softening* until a steady state is reached. In sequence 7, a decrease of strain amplitude leads to a cyclic *hardening*, which then keeps going at sequences 8 and 9 for *J05*, while softening is observed for *J24*.

Cyclic softening (sequences 4^{th}, 5^{th} and 6^{th}) is, in general, attributed to the increase of the mean free motion of dislocations, and/or to the decrease of the back stress, and/or the evolution of precipitates structure. It depends not only on the accumulated plastic strain, but also on the plastic strain amplitude experienced by the material [Fournier *et al.*, 2009], [Kubena *et al.*, 2010]. The cyclic hardening observed from sequence 7 seems, on the other hand, new with respect to the literature data.

It is also concluded observing Fig. 3.25 that the strain recovery (Bauschinger effect) is minimum for these types of ODS grades.

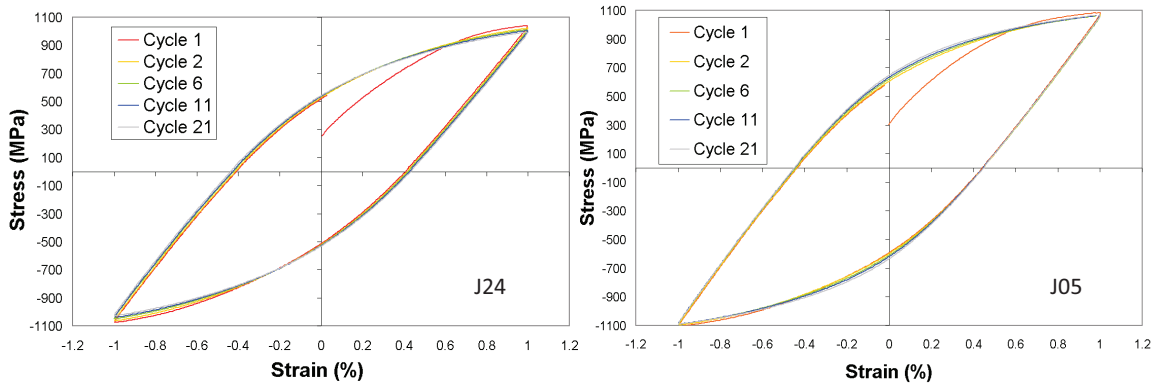

Figure 3.25. Left: *J24* experimental responses at ±1% - Right: J05 experimental responses at ±1% [Toualbi 2010].

The hysteresis loop is composed of three regions for sequences 5, 6 and 8: a linear elastic region, a smooth non-linear elastic-plastic transition, and a non-linear plastic bounding region (Figs. 3.26 and 3.27). On the other hand, the hysteresis loop for sequence 4 and 7 is composed of two regions: a linear elastic region and smooth elastic-plastic region.

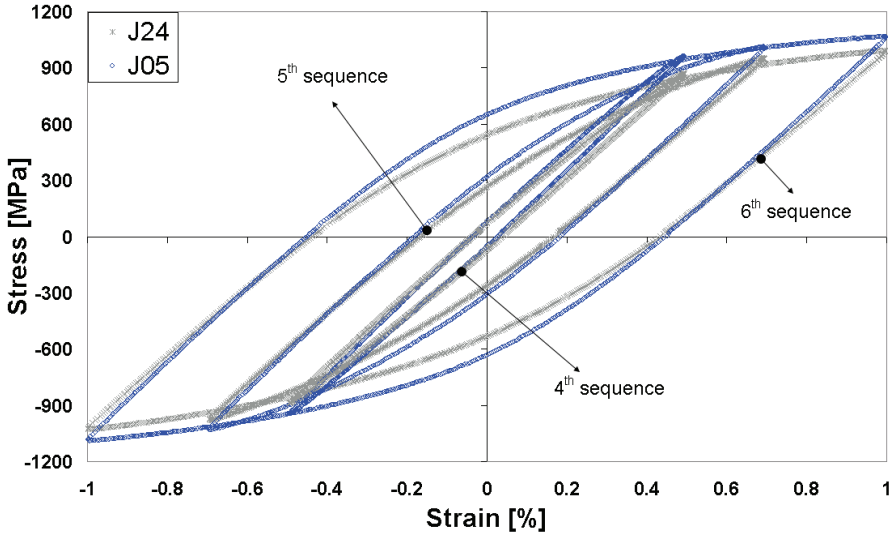

Figure 3.26. *J05* and *J24* experimental response for 3 strain amplitudes (4th, 5th and 6th sequence). Stabilized cycle.

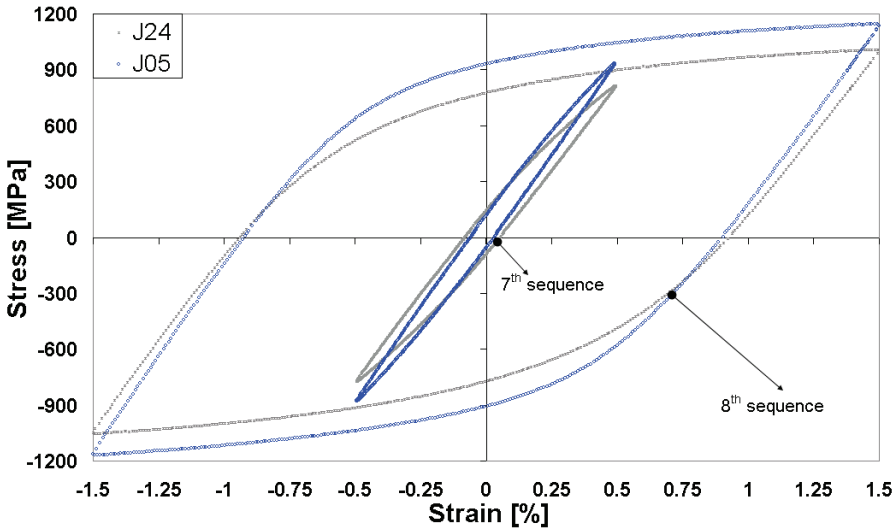

Figure 3.27. *J05* and *J24* experimental response for 2 strain amplitudes (7th and 8th sequence). Stabilized cycle.

The influence of the strain history can be illustrated by comparing hysteresis loops of the 4th and 7th sequences, with equal strain amplitudes of ±0.5% (Fig. 3.28). *J24* steel seems to be more impacted by the plastic strain path than *J05* steel.

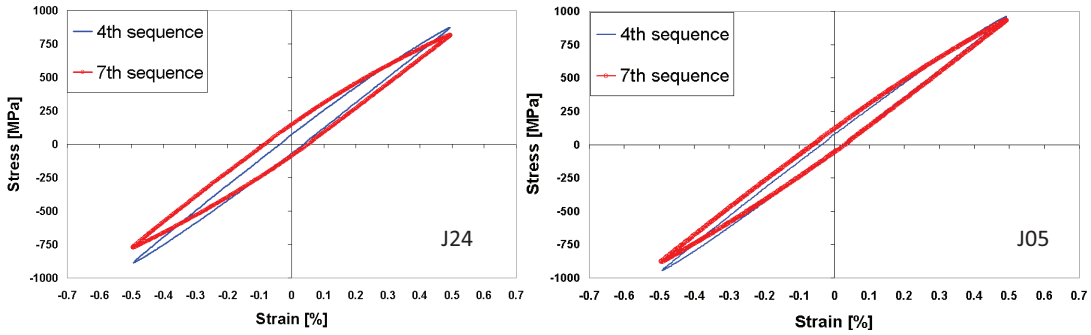

Figure 3.28. Experimental response for strain amplitude equals to ±0.5% (4th and 7th sequence). Stabilized cycle. Left: J24 – Right: J05.

During sequence 9 *J05* exhibits a continuous hardening until 20th cycle. Then some cracks appear leading to a force decrease, followed by sudden failure at 37th cycle. The main cracks appear at 45° from the principal stress dire ction (see Fig. 3.29).

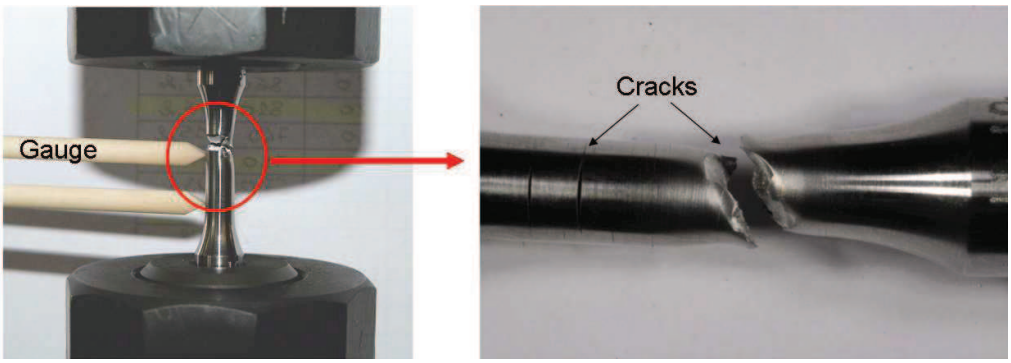

Figure 3.29. Cracks in *J05* during sequence 9 ($\Delta\varepsilon$ = ±2%) [Toualbi 2010].

During sequence 9 *J24* exhibits a continuous softening until the 81st cycle (see Fig 3.24). The test was stopped at this cycle. Two cracks appear (see Fig. 3.30) during cycling leading to a force decrease.

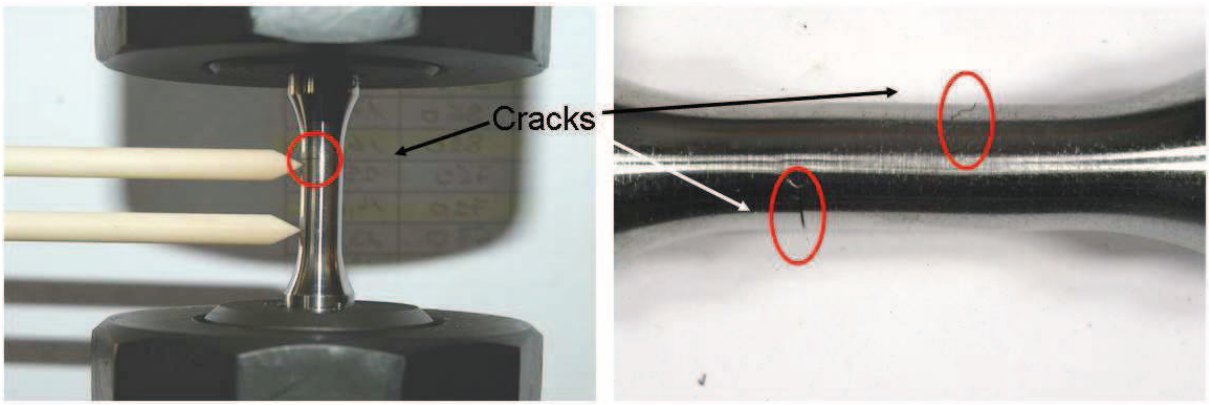

Figure 3.30. 2 cracks appearing in *J24* during sequence 9 ($\Delta\varepsilon$ = ±2%) [Toualbi 2010].

According to these test, *J05* seems to be less resistant to cracks propagation than *J24*.

3.5.2.2 Compression-compression test

Figs. 3.31 and 3.32 show that the compression-compression test sequence systematically leads to cyclic hardening. The work-hardening rate is influenced by the existence of two compression axis. The ortho-radial direction remains the hardest and the longitudinal the weakest, when looking at the first compression in Fig. 3.31. The strong difference in hardening rate with respect to the tension-compression tests may be attributed to dislocation-dislocation interactions increase due to the applied loading path. Cyclic hardening progressively decreases

at each strain amplitude, but regenerates after each increase of the strain amplitude (Fig. 3.34). It is pointed out that in this test no decrease of the strain range was performed.

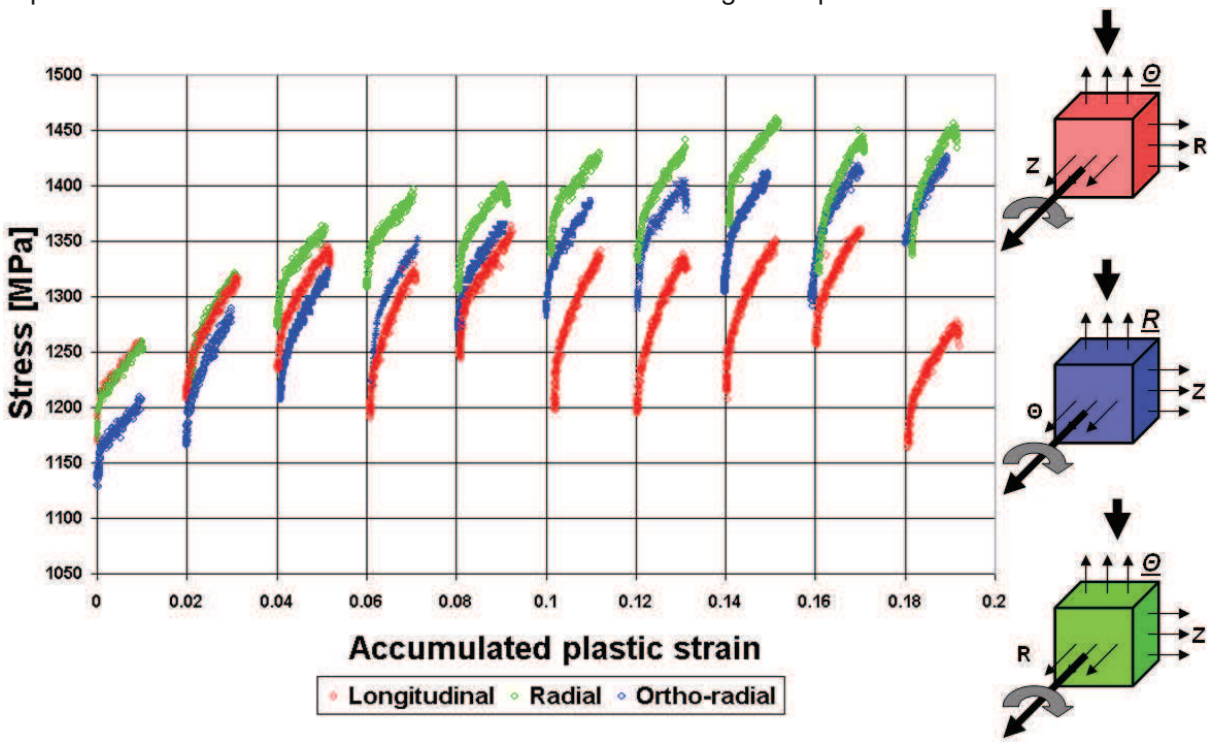

Figure 3.31. *J27-M2* compression-compression test.

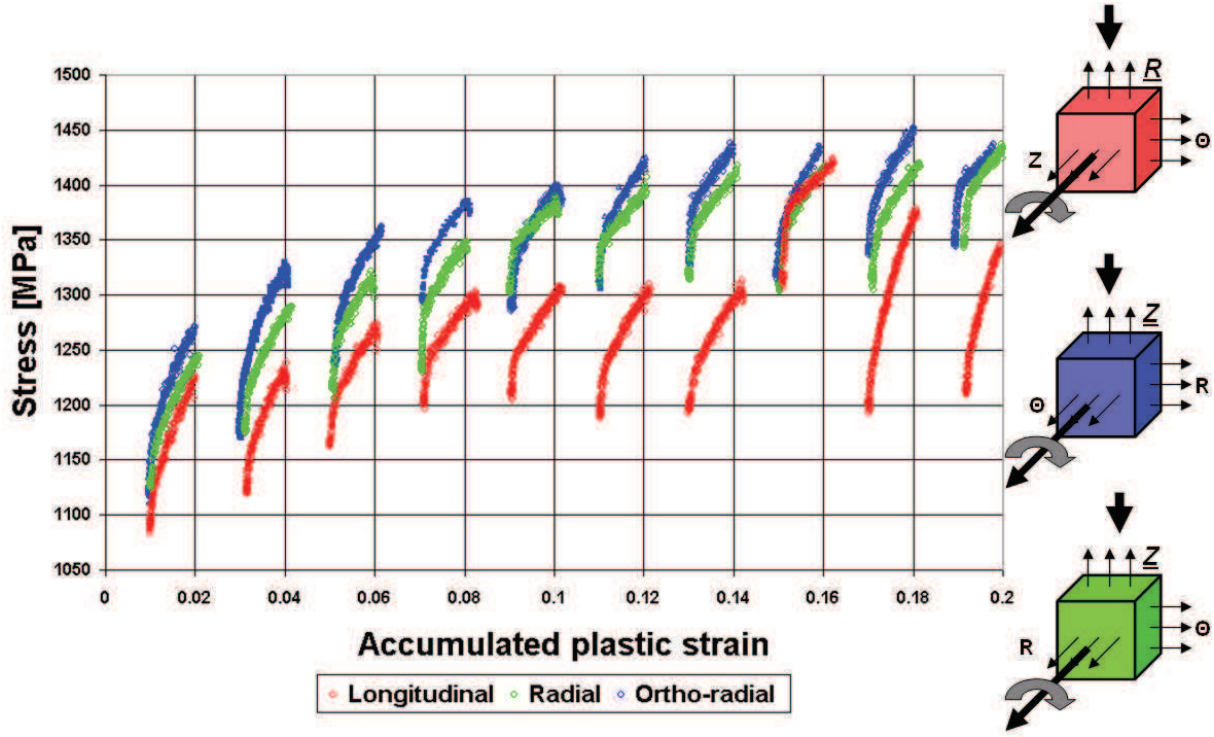

Figure 3.32. *J27-M2* compression-compression test.

It is noted that anisotropy may influence the stress level, i.e. textural effects may lead to stress variations when straining in different directions. When rotating around the longitudinal direction (Z) the final shape is parallelepiped because alternated compression in radial and ortho-radial directions produces similar responses. However, when compression is done in samples rotating around the radial or the ortho-radial direction, the incremental flow is asymmetrical, leading to a *trapezium-shaped* sample (see Fig. 3.33). This asymmetrical flow distribution is more important when rotating around the radial direction because the hardest (ortho-radial) and the weakest (longitudinal) directions are compressed alternately.

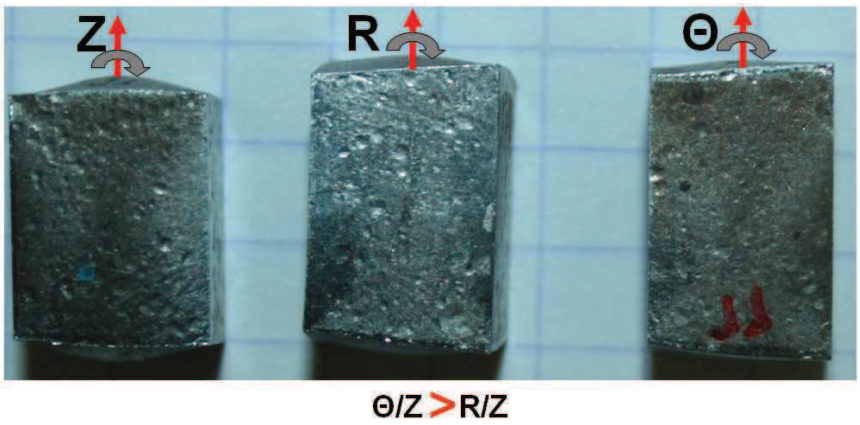

Figure 3.33. *Trapezium-shaped* samples after 40% of plastic strain.

Results are detailed below by looking at compression steps along the Z (longitudinal) direction, which allows strict comparisons with the tension-compression tests, performed along the same direction. The first compression is done along the radial direction (R), the second one is along the axial direction (Z), and so on (Fig. 3.34).

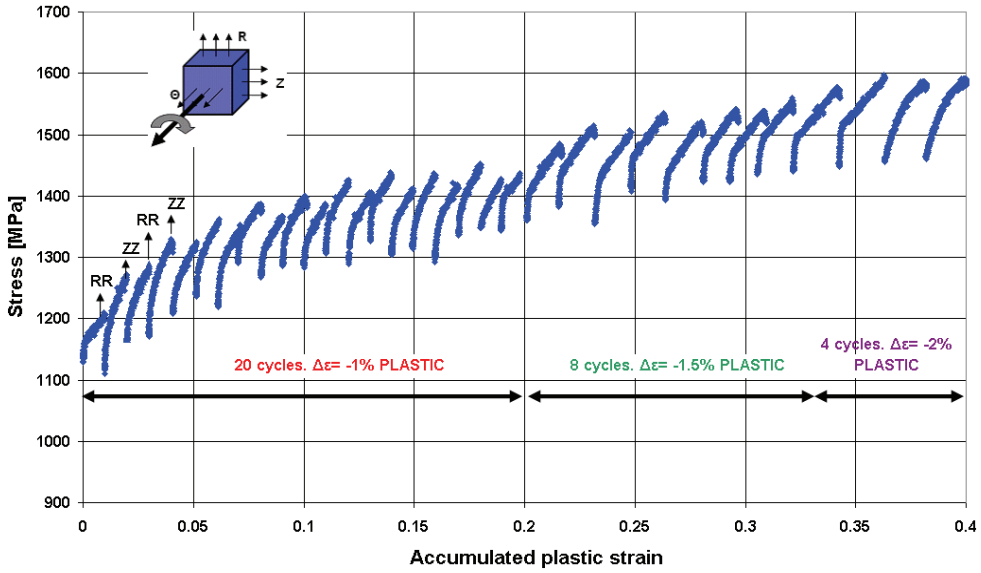

Figure 3.34. Experimental stress response in the compression-compression loading sequence.

Non-proportional cycles generally induce more significant hardening than proportional ones [Tanaka 1994]. In this test, the ability to eliminate or weaken the obstacles to dislocation motion [Huml 1987] is very much reduced compared to the tension-compression tests, leading to much higher hardening rates. For this reason the stress values are very different when performing tension-compression test (maximum stress at Δε= 2%: 1200 MPa) and compression-compression test (maximum stress at Δε= 2%: 1600 MPa).

Similarly to the tension-compression test, stress stabilization is reached within few cycles in the compression-compression test.

3.5.3 Cyclic constitutive equations implementation and numerical resolution

According to the previous experimental behavior, it is proposed to describe the cyclic behavior of ODS steels with an elastic-plastic model developed by Chaboche [Chaboche 1989]. The equations characterizing an individual material and its reaction to applied loads are called *constitutive equations*, since they describe the macroscopic behavior resulting from the internal structure of the material.

The cold pilgering process used for cladding tubes forming involves a sequence of small strain increments of quasi-random amplitudes. For this type of loading, kinematic hardening cannot be neglected and must be introduced into the numerical model [Velay *et al.*, 2006]. The constitutive equations of [Chaboche 1989] use a decomposition of hardening into kinematic and isotropic parts. The standard implementation includes one kinematic hardening variable and one isotropic hardening variable. Nevertheless, it was shown by [Velay *et al.*, 2006] that in many cases two kinematic hardening variables and two isotropic hardening variables are necessary to have a good description of cyclic behaviors.

3.5.3.1 A model of rate-independent elastic-plasticity

The equations of the constitutive law have already been presented in Chapter 2 and are reminded here in order explain their implementation within a FEM formulation. The assumption of the additive decomposition of the strain-rate tensor into elastic and plastic parts leads to:

$$\dot{\underline{\varepsilon}} = \dot{\underline{\varepsilon}}^e + \dot{\underline{\varepsilon}}^p \tag{3.12}$$

The elastic response $\dot{\underline{\varepsilon}}^e$ is described by Hook's law which, for isotropic materials, gives:

$$\dot{\underline{\varepsilon}}^e = \frac{1+\nu}{E}\dot{\underline{\sigma}} - \frac{\nu}{E} tr(\dot{\underline{\sigma}})\underline{I}\,, \tag{3.13}$$

where $\underline{I}$ is the unit (second rank) tensor, E is the elastic modulus and ν the Poisson's ratio, $\dot{\underline{\sigma}}$ the stress rate tensor and $tr(\cdot)$ the trace function. It is considered that the plastic strain rate is normal to the yield surface. The plastic strain rate tensor $\dot{\underline{\varepsilon}}^p$ is written as:

$$\underline{\dot{\varepsilon}}^p = \dot{\lambda}\frac{\partial f}{\partial \underline{\sigma}} = \dot{\lambda}\underline{n}\,, \tag{3.14}$$

where the plastic multiplier $\dot{\lambda}$ is positive. The unit normal $\underline{n}$ to the yield surface has the following form:

$$\underline{n} = \frac{\partial f}{\partial \underline{\sigma}} = \frac{3}{2}\frac{(\underline{s}-\underline{X})}{J_2(\underline{\sigma}-\underline{X})} \tag{3.15}$$

The limit between the elastic domain and the plastic domain is defined by a yield function, which obeys the von Mises criterion [Chaboche *et al.*, 1979], [Chaboche 1991]. The equation of the yield surface can be written as:

$$f = J_2(\underline{\sigma}-\underline{X}) - R - \sigma_y = 0\,, \tag{3.16}$$

where σ_y is the initial yield stress, $\underline{X}$ the kinematic hardening tensor (or back stress tensor). R is the isotropic hardening.

$J_2(\underline{\sigma}-\underline{X})$, second invariant, is defined from the von Mises criterion:

$$J_2(\underline{\sigma}-\underline{X}) = \overline{\sigma} = [\frac{3}{2}(\underline{s}-\underline{X}):(\underline{s}-\underline{X})]^{1/2}\,, \tag{3.17}$$

where $\underline{s}$ is the deviatoric part of the Cauchy stress tensor $\underline{\sigma}$:

$$\underline{s} = \underline{\sigma} - \frac{1}{3}tr\underline{\sigma}\,\underline{I} \tag{3.18}$$

Plastic strain occurs when the state of stress reaches the current yield stress; this corresponds to the yield criterion $f = 0$. The plastic strain continues to grow if the yield criterion is continuously satisfied, that is, if $\dot{f} = 0$.

Due to the incompressibility of plastic deformation, it is useful to decompose the strain rate tensor into spherical and a deviatoric parts.

$$\begin{cases} \underline{\dot{\varepsilon}} = \underline{\dot{e}} + \dfrac{1}{3}tr(\underline{\dot{\varepsilon}})\underline{I} \\ \underline{\dot{\varepsilon}}^e = \underline{\dot{e}}^e + \dfrac{1}{3}tr(\underline{\dot{\varepsilon}}^e)\underline{I}\,, \\ \underline{\dot{\varepsilon}}^p = \underline{\dot{e}}^p \end{cases} \tag{3.19}$$

where $\underline{\dot{e}}$ is the deviatoric strain rate, itself can be decomposed into elastic and plastic part:

$$\underline{\dot{e}} = \underline{\dot{e}}^e + \underline{\dot{e}}^p \tag{3.20}$$

The equivalent accumulated plastic strain rate is expressed as a function of the deviatoric plastic strain rate:

$$\dot{p} = \sqrt{\frac{2}{3}\underline{\dot{e}}^p : \underline{\dot{e}}^p} \tag{3.21}$$

The Lamé parameter μ (or the elastic shear modulus) is given by:

$$\mu = \frac{E}{2(1+\nu)} \tag{3.22}$$

Knowing $\underline{\dot{\varepsilon}}$, if the loading is considered as elastic, $\dot{\lambda} = \dot{p} = 0$, the equations to integrate are:

$$\begin{cases} \underline{\dot{e}}^e = \underline{\dot{e}} \\ \underline{\dot{e}}^p = 0 \\ \dot{P} = -\chi tr(\underline{\dot{\varepsilon}}) \\ \underline{\dot{s}} = 2\mu \underline{\dot{e}}^e \\ \underline{\dot{X}} = 0 \end{cases} \tag{3.23}$$

with χ the elastic compressibility coefficient, its expression is given in section 2.1.1.2 and $\dot{P}$ hydrostatic pressure rate. The kinematic stress tensor $\underline{X}$ expression was given in section 1.4.2.1.2.

If the loading is considered as elastic-plastic, $\dot{\lambda} = \dot{p} > 0$ the equations to integrate are:

$$\begin{cases} \underline{\dot{e}}^e = \underline{\dot{e}} - \underline{\dot{e}}^p \\ \underline{\dot{e}}^p = \dfrac{3\dot{p}}{2\overline{\sigma}}(\underline{s} - \underline{X}_i) \qquad (i = 1, n_1) \\ \dot{P} = -\chi tr(\underline{\dot{\varepsilon}}) \qquad , \\ \underline{\dot{s}} = 2\mu \underline{\dot{e}}^e \\ \underline{\dot{X}}_i = \dfrac{2}{3} C_i \underline{\dot{e}}^p - \gamma_i \underline{X}_i \dot{p} \quad (i = 1, n_1) \end{cases} \tag{3.24}$$

where C_i and γ_i are material parameters dependent. n_1 is the number of kinematic hardening variables. The system of Eqs. (3.24) remains valid if the load is elastic, considering $\dot{p} = 0$. In this case the deviatoric stress $\underline{\dot{s}}$ is linked to the elastic deviatoric strain $\underline{\dot{e}}^e$ by the fourth-order tensor $\underline{\underline{C}}$, often referred to as the continuous tangent modulus:

$$\underline{\dot{s}} = \underline{\underline{C}} : \underline{e}^e \tag{3.25}$$

Since linear isotropic elasticity is considered here (Hooke's law), $\underline{\underline{C}}$ is simply given by:

$$\underline{\underline{C}} = 2\mu\left(\underline{\underline{I}} - \frac{1}{3}\underline{I}\otimes\underline{I}\right), \tag{3.26}$$

where $\underline{\underline{I}}$ is the fourth-order symmetric unit tensor defined as: $I_{ijkl} = \frac{1}{2}\left(\delta_{ik}\delta_{jl} + \delta_{il}\delta_{jk}\right)$.

3.5.3.2 An implicit time integration procedure

It is pointed out first that the mass conservation equation involving the hydrostatic pressure in the system (3.23) and (3.24) is already present in the mechanical equilibrium resolution in Forge3®. The variables $(p_n, \underline{s}_n, \underline{X}_{i_n})$ satisfying the equilibrium at the increment (n), the problem is to determine those variables at the increment $(n+1)$, $(p_{n+1}, \underline{s}_{n+1}, \underline{X}_{i_{n+1}})$. $\underline{\dot{e}}_{n+1}$ is estimated at each iteration of the Newton-Raphson scheme by solving the equilibrium equations of the mechanical problem.

The calculation of the new material state implies, except for simple laws such as elasticity, to carry out the numerical integration of differential equations. The choice of the integration method has an impact on the computing time, the accuracy of the result and the calculation of the elastic-plastic (tangent) modulus. Many authors [Simo and Taylor 1985], [Benallal and Marquis 1987], [Gratacos 1991], [Hartmann at Haupt 1993], [Gay 1995], [Knockaert 2001], [Lange 2006], [Fayolle 2008], [Revil-Baudard 2010] chose to use an implicit integration scheme that has the advantages of numerical stability, robustness, possibility of appending further equations to the existing system of non-linear equations, and together with reasonable computing time.

In this work, we consider the *return mapping algorithm* corresponding to an implicit integration scheme (backward Euler method) for the above variables under the assumption of constant total strain during the increment:

$$\begin{cases} p_{n+1} = p_n + \dot{p}_{n+1}\Delta t \\ \underline{s}_{n+1} = \underline{s}_n + \underline{\dot{s}}_{n+1}\Delta t \\ \underline{X}_{n+1} = \underline{X}_n + \underline{\dot{X}}_{n+1}\Delta t \end{cases} \tag{3.27}$$

$\Delta p = \dot{p}_{n+1}\Delta t = \bar{\varepsilon}^p_{n+1} - \bar{\varepsilon}^p_n$ is the accumulated plastic strain increment to be determined.

The *return mapping algorithm* from a computational standpoint consists in treating the elastic-plastic problem as a strain controlled problem, the stress history being obtained from the strain history by means of an integration algorithm. The basic idea is illustrated in Fig. 3.35. From the converged solution at the increment (n) an *elastic trial stress* $\underline{s}^T_{n+1}$ is computed. If the resulting state defined by $\underline{s}^T_{n+1}$ is outside of the elastic region enclosed by the yield surface, the final state is defined as the closest-point-projection of $\underline{s}^T_{n+1}$ onto the yield surface (see Fig. 3.35). Thus, it is written:

$$\underline{s}^T_{n+1} = \underline{s}_n + 2\mu\Delta t\,\underline{\dot{e}}_{n+1} \tag{3.28}$$

In the particular case of the von Mises yield condition with associated flow rule and isotropic hardening, the closest-point-projection is trivially defined and leads to the so-called *radial return algorithm* [Germain and Muller 1995]. The basic integration scheme, modified to account for two non-linear kinematic hardening variables $(n_1 = 2)$ and two non-linear isotropic hardening variables $(n_2 = 2)$ is summarized below.

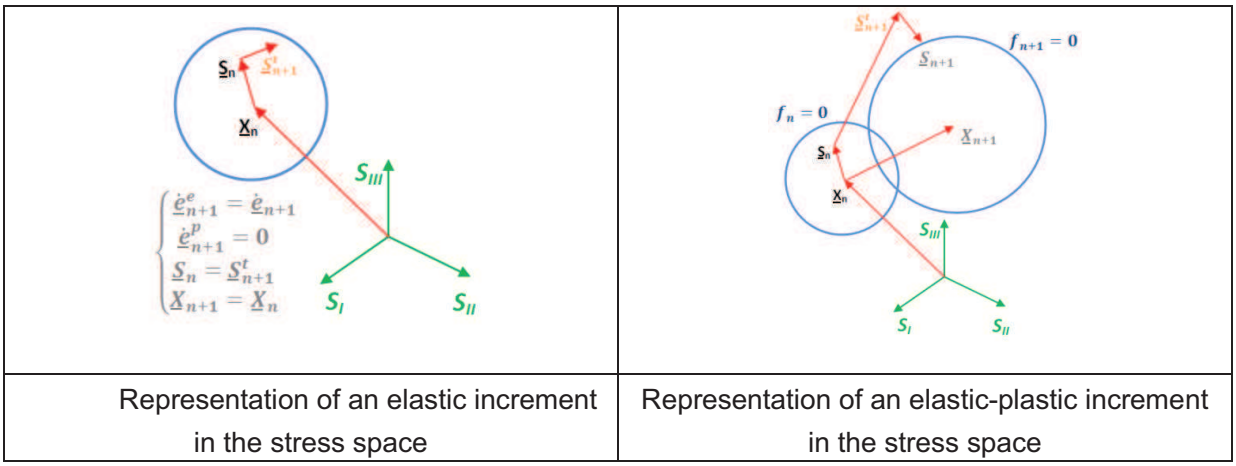

Representation of an elastic increment in the stress space	Representation of an elastic-plastic increment in the stress space

Figure 3.35. Radial return algorithm representation in the stresses space.

By applying this integration scheme, the system becomes:

$$\begin{cases} \dot{\underline{e}}^{e}_{n+1} = \dot{\underline{e}}_{n+1} - \dot{\underline{e}}^{p}_{n+1} \\ \dot{\underline{e}}^{p}_{n+1} = \dfrac{3\dot{p}_{n+1}}{2\overline{\sigma}_{n+1}}(\underline{s}_{n+1} - \underline{X}_{1_{n+1}} - \underline{X}_{2_{n+1}}) \\ \underline{s}_{n+1} = \underline{s}_{n} + 2\mu\Delta t\left[\dot{\underline{e}}_{n+1} - \dfrac{3\dot{p}_{n+1}}{2\overline{\sigma}_{n+1}}\left(\underline{s}_{n+1} - \underline{X}_{1_{n+1}} - \underline{X}_{2_{n+1}}\right)\right] \\ \underline{X}_{1_{n+1}} = \underline{X}_{1_{n}} + \Delta t\left[\dfrac{2}{3}C_1\dot{\underline{e}}^{p}_{n+1} - \gamma_1\underline{X}_{1_{n+1}}\dot{p}_{n+1}\right] \\ \underline{X}_{2_{n+1}} = \underline{X}_{2_{n}} + \Delta t\left[\dfrac{2}{3}C_2\dot{\underline{e}}^{p}_{n+1} - \gamma_2\underline{X}_{2_{n+1}}\dot{p}_{n+1}\right] \end{cases} \tag{3.29}$$

The determination of the unknowns $(\dot{\underline{e}}^{e}_{n+1}, \dot{\underline{e}}^{p}_{n+1})$ is immediate if $(\Delta\bar{\varepsilon}^{p}_{n+1}, s_{n+1}, \underline{X}_{1_{n+1}})$ are known. The problem is therefore to determine these three variables, assuming that the plastic loading criterion is satisfied:

$$\overline{\sigma}_{n+1} - R_{i\,n+1} + \sigma_y = 0$$

The calculation of R_i with $i = n_2 = 2$ will be described in section 3.5.3.4. Rearranging system 3.29:

$$\begin{cases} \underline{s}_{n+1} = \dfrac{\underline{s}^{T}_{n+1} + 2\mu\Delta\lambda(\underline{X}_{1_{n+1}} + \underline{X}_{2_{n+1}})}{(1+2\mu\Delta\lambda)} \\ \underline{X}_{1_{n+1}} = \dfrac{\underline{X}_{1_n} + \dfrac{2}{3}C_1\Delta\underline{e}^{p}_{n+1}}{1+\gamma_1\Delta p_{n+1}} \end{cases}, \tag{3.30}$$

with $\underline{s}^{T}_{n+1}$ the *elastic trial stress* described by Eq. 3.28.

By injecting in $\underline{X}_{1_{n+1}}$ (system (3.30)) the expression of Eqs. (3.14) and (3.15) we obtain:

$$\underline{X}_{1_{n+1}} = \frac{\underline{X}_{1_n} + \dfrac{2}{3}C_1\Delta\lambda\left(\underline{s}_{n+1} - \underline{X}_{2_{n+1}}\right)}{1+\dfrac{2}{3}C_1\Delta\lambda + \gamma_1\Delta p} \tag{3.31}$$

$\underline{s}_{n+1}$ is then obtained by neglecting second order terms:

$$\underline{s}_{n+1} - \underline{X}_{1_{n+1}} - \underline{X}_{2_{n+1}} = \frac{\underline{s}^{T}_{n+1}(1+D\Delta p) - \underline{X}_{2_n}(1+\gamma_1\Delta p) - \underline{X}_{1_n}(1+\gamma_2\Delta p)}{1+\dfrac{2}{3}C\Delta\lambda + D\Delta p + 2\mu\Delta\lambda + \Delta\lambda\Delta p\left[2\mu D + \dfrac{2}{3}(C_1\gamma_2 + C_2\gamma_1)\right]}, \tag{3.32}$$

with $C = C_1 + C_2$ and $D = \gamma_1 + \gamma_2$.

Moreover the equivalent stress is equal to:

$$\bar{\sigma}_{n+1} = \sqrt{\frac{3}{2}\left(\underline{s}_{n+1} - \underline{X}_{1_{n+1}} - \underline{X}_{2_{n+1}}\right) : \left(\underline{s}_{n+1} - \underline{X}_{1_{n+1}} - \underline{X}_{2_{n+1}}\right)} \tag{3.33}$$

Which enables to write down:

$$\bar{\sigma}_{n+1} = \sqrt{\frac{3}{2}\underline{B} : \underline{B}}\,\frac{1}{1+\dfrac{2}{3}C\Delta\lambda + D\Delta p + 2\mu\Delta\lambda + \Delta\lambda\Delta p\left[2\mu D + \dfrac{2}{3}(C_1\gamma_2 + C_2\gamma_1)\right]}, \tag{3.34}$$

with $\underline{B} = \underline{s}^{T}_{n+1}(1+D\Delta p) - \underline{X}_{2_n}(1+\gamma_1\Delta p) - \underline{X}_{1_n}(1+\gamma_2\Delta p)$

Finally,

$$\begin{cases} \underline{s}_{n+1} = \underline{X}_{1_{n+1}} + \underline{X}_{2_{n+1}} + \dfrac{\underline{B}}{1+\dfrac{2}{3}C\Delta\lambda + D\Delta p + 2\mu\Delta\lambda + \Delta\lambda\Delta p\left[2\mu D + \dfrac{2}{3}(C_1\gamma_2 + C_2\gamma_1)\right]} \\ \underline{X}_{1_{n+1}} = \dfrac{1}{1+\gamma_1\Delta p}\left[\dfrac{2}{3}C_1\Delta\lambda\left(\underline{s}_{n+1} - \underline{X}_{1_{n+1}} - \underline{X}_{2_{n+1}}\right)\right] \end{cases} \tag{3.35}$$

The plastic consistency conditions are enforced in order to find the solution that satisfies the plastic von Mises criterion:

$$f(\underline{s}_{n+1},\underline{X}_{1_{n+1}},\underline{X}_{2_{n+1}},p_{n+1})=\sqrt{\frac{3}{2}\left(\underline{s}_{n+1}-\underline{X}_{1_{n+1}}-\underline{X}_{2_{n+1}}\right):\left(\underline{s}_{n+1}-\underline{X}_{1_{n+1}}-\underline{X}_{2_{n+1}}\right)}-R_{1_{n+1}}-R_{2_{n+1}}-\sigma_y=0 \tag{3.36}$$

By injecting in Eq. (3.36) the expression of $\underline{s}_{n+1}$, $\underline{X}_{1_{n+1}}$ from Eq. (3.35), we obtain:

$$g(\Delta p)=\sigma_{0_{n+1}}+\frac{3}{2}C\Delta p+3\mu\Delta p+D\Delta p\sigma_{0_{n+1}}+\frac{3}{2}\Delta p^2\left[2\mu D+\frac{2}{3}(C_1\gamma_2+C_2\gamma_1)\right]-\sqrt{\frac{3}{2}\underline{B}:\underline{B}}=0 \tag{3.37}$$

This equation is solved using a Newton-Raphson scheme. Successive corrections $\partial\Delta p$ on Δp are computed iteratively. For that purpose, it is necessary to differentiate $g(\Delta p)$ with respect to Δp. If Δp is determined, all other quantities are known from Eq. (3.24) and (3.29). Tables **3.15** and **3.16** summarize schematically the proposed algorithm of stress calculation.

Table 3.15. Computation of the accumulated plastic strain by Newton-Raphson scheme

$$\underline{B}=\underline{s}_{n+1}^{T}(1+D\Delta p)-\underline{X}_{2_n}(1+\gamma_1\Delta p)-\underline{X}_{1_n}(1+\gamma_2\Delta p)$$

$$g^k(\Delta p)^{(k)}=\sigma_{0_{n+1}}+\frac{3}{2}C\Delta p+3\mu\Delta p+D\Delta p\sigma_{0_{n+1}}+\frac{3}{2}\Delta p^2\left[2\mu D+\frac{2}{3}(C_1\gamma_2+C_2\gamma_1)\right]-\sqrt{\frac{3}{2}\underline{B}:\underline{B}}$$

$$g'^{(k)}(\Delta p)^{(k)}=\left.\frac{\partial g(\Delta p)}{\partial(\Delta p)}\right|_{(\Delta p)=(\Delta p)^{(k)}}$$

$$(\Delta p)^{(k+1)}=(\Delta p)^{(k)}-\frac{g(\Delta p)^{(k)}}{g'^{(k)}(\Delta p)^{(k)}}$$

If $\left|g^k(\Delta p)^{(k)}\right|\le TOL$ EXIT, otherwise start from the beginning.

Table 3.16. Radial return algorithm. Nonlinear kinematic/isotropic hardening

(i) Calculate *elastic trial stress*: $\underline{s}_{n+1}^{T} = \underline{s}_n + 2\mu\Delta t\,\underline{\dot{e}}_{n+1}$

(ii) Find (Δp) by local iteration, Table **3.15**. Compute the unit normal at (t_{n+1})

$$\underline{n}_{n+1} = \frac{\underline{\underline{B}}}{\left\|\underline{\underline{B}}\right\|}$$

(iii) Calculate stresses with plastic corrector:

$$\underline{s}_{n+1} = \underline{s}_{n+1}^{t} - 2\mu\Delta t\,\underline{\dot{e}}_{n+1}^{p}$$

(iv) Calculate back stress tensor:

$$\underline{X}_{1n+1} = \frac{\underline{X}_{1n} + \frac{2}{3}C_1\left(\sqrt{\frac{3}{2}}\Delta p\,\underline{n}_{n+1}\right)}{1+\gamma_1\Delta p} \qquad \underline{X}_{2n+1} = \frac{\underline{X}_{2n} + \frac{2}{3}C_2\left(\sqrt{\frac{3}{2}}\Delta p\,\underline{n}_{n+1}\right)}{1+\gamma_2\Delta p}$$

It should be noted that due to the assumption of constant total strain during the increment, it is impossible to observe the transition from a plastic to an elastic state during the calculated increment.

3.5.3.3 Consistent tangent elastic-plastic modulus

As shown by Taylor and Simo (Simo and Taylor 1985), to preserve the character of quadratic convergence of the Newton-Raphson method for the global mechanical problem, it is necessary to use discrete tangent elastic-plastic moduli consistent with the integration scheme of the constitutive law. The consistent tangent elastic-plastic modulus $\underline{\underline{\underline{\underline{C}}}}^{d}$ considers the relationship between the stress and the strain rates: ($\dot{s}$ and $\dot{\varepsilon}$ respectively):

$$\underline{\underline{\underline{\underline{C}}}}_{n+1}^{d} = \frac{\partial \dot{s}_{n+1}}{\partial \dot{\varepsilon}_{n+1}} \tag{3.38}$$

After calculations based on the work of [Hartmann and Haupt 1993] for two kinematic hardening variables, the consistent tangent elastic-plastic modulus can be written in our case as:

$$\underline{\underline{\underline{\underline{C}}}}_{n+1}^{d} = 2\mu\left[\beta\left(\underline{\underline{\underline{I}}} - \frac{1}{3}\underline{\underline{I}}\otimes\underline{\underline{I}}\right) - \bar{\gamma}\,n_{n+1}\otimes n_{n+1} - \left(\delta\, s_{n+1}^{t}\otimes n_{n+1} - \delta_1\, X_2\otimes n_{n+1} - \delta_2\, X_1\otimes n_{n+1}\right)\right], \tag{3.39}$$

with

$$\begin{cases} \beta = 1 - \dfrac{3\mu\Delta\bar{\varepsilon}^p A}{\Lambda} \\ \delta = \dfrac{3\mu\Delta\bar{\varepsilon}^p(\gamma_1+\gamma_2)A}{\Lambda\dfrac{\partial g}{\partial\Delta\bar{\varepsilon}^p}} \\ \delta_1 = \dfrac{3\mu\Delta\bar{\varepsilon}^p\gamma_1 A}{\Lambda\dfrac{\partial g}{\partial\Delta\bar{\varepsilon}^p}} \\ \delta_2 = \dfrac{3\mu\Delta\bar{\varepsilon}^p\gamma_2 A}{\Lambda\dfrac{\partial g}{\partial\Delta\bar{\varepsilon}^p}} \\ \bar{\gamma} = \dfrac{3\mu A}{\dfrac{\partial g}{\partial\Delta\bar{\varepsilon}^p}}\left(1 - \dfrac{\dfrac{3}{2}\Delta\bar{\varepsilon}^p}{\Lambda\Psi}\right) \end{cases} \tag{3.40}$$

by affectation:

$$\begin{cases} \Lambda = \bar{\sigma} + C\Delta\bar{\varepsilon}^p + 3\mu\Delta\bar{\varepsilon}^p + D\Delta\bar{\varepsilon}^p\bar{\sigma} + \dfrac{3}{2}\Delta\bar{\varepsilon}^{p2}\left[2\mu D + \dfrac{2}{3}(C_1\gamma_2 + C_2\gamma_1)\right] \\ \Psi = \partial\bar{\sigma} + \dfrac{3}{2}(C_1 + C_2) + \Delta\bar{\varepsilon}^p\partial\bar{\sigma}(\gamma_2+\gamma_1) + 3\mu + \bar{\sigma}(\gamma_2+\gamma_1) + \\ \quad 3\Delta\bar{\varepsilon}^p\left[2\mu(\gamma_2+\gamma_1) + \dfrac{2}{3}(C_1\gamma_2 + C_2\gamma_1)\right] \\ A = 1 + (\gamma_1+\gamma_2)\Delta\bar{\varepsilon}^p \end{cases} \tag{3.41}$$

3.5.3.4 Modeling the isotropic hardening/softening

The modeling of the isotropic hardening/softening behavior is also of the outmost importance for simulations involving metallic materials.

Voce's strain hardening law is usually used in cold forming [Lange 2006]. It has the particularity to model the mechanism of dynamic recovery which is interpreted by a saturation of the isotropic hardening/softening at large deformations. It is also well adapted to model cyclic conditions [Chaboche 1989], i.e. to describe the cyclic hardening phenomenon (increase of strength) or the cyclic softening (decrease). Its evolution is governed by the accumulated plastic strain and the stabilized state is reached when the variables R_i reach the asymptotic values Q_i. The dimension of the elastic domain is controlled by:

$$\dot{R}_i = b_i\left(Q_i - R_i\right)\dot{p} \tag{3.42}$$

or

$$R_i = Q_i(1-\exp(-b_i\, p)) \tag{3.43}$$

with $i = 1, n_2$.

Considering two variables ($n_2 = 2$) for the description of isotropic hardening, we obtain:

$$\sigma_0\left(p\right) = \sigma_y + R_1 + R_2 \tag{3.44}$$

or

$$\sigma_0\left(p\right) = \sigma_y + Q_1(1-\exp(-b_1 p)) + Q_2(1-\exp(-b_2 p)) \tag{3.45}$$

The integration of an isotropic hardening involves the calculation of:

$$\frac{\partial \sigma_0}{\partial \bar{\varepsilon}^p_{n+1}} = b_1 Q_1 \exp(-b_1 p) + b_2 Q_2 \exp(-b_2 p) \tag{3.46}$$

Finally,

$$R = R_1 + R_2 \tag{3.47}$$

3.5.3.5 Validation of the numerical implementation of the cyclic constitutive model into Forge3®

A simple uniaxial tension/compression test schematized on the Fig. 3.36, allowed to validate the implementation of the Chaboche's cyclic elastic-plastic law into Forge3®. A parallelepiped specimen (10x10x20mm) is fixed on one side, the other one being moved with a constant velocity either in tension or in compression. The contact between tools is considered as bilateral sliding. A Lagrangian sensor (moving with the mesh) is positioned at the center of the specimen to follow locally the computation of stress and strain. Two symmetry planes are necessary to avoid side effects and rigid body of motion.

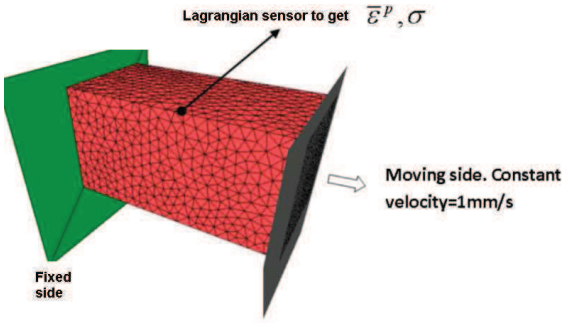

Figure 3.36. Tension/compression test carried out in Forge3®

The implementation started from an existing version using one kinematic hardening variable and one isotropic hardening variable. The designed name of this constitutive law in this work is: *CH*. When setting to zero all the parameters of the second variables (kinematic and isotropic hardening) in the full model (*2CH*); the two models are supposed to be equivalent. The parameters used in the tension/compression test are shown in Table **3.17**.

Table 3.17. Constitutive model parameters taken for the validation material test.

Parameter	σ_y [MPa]	Q_1 [MPa]	b_1	C_1 [MPa]	γ_1
Material test	132	112	14	740	4.2

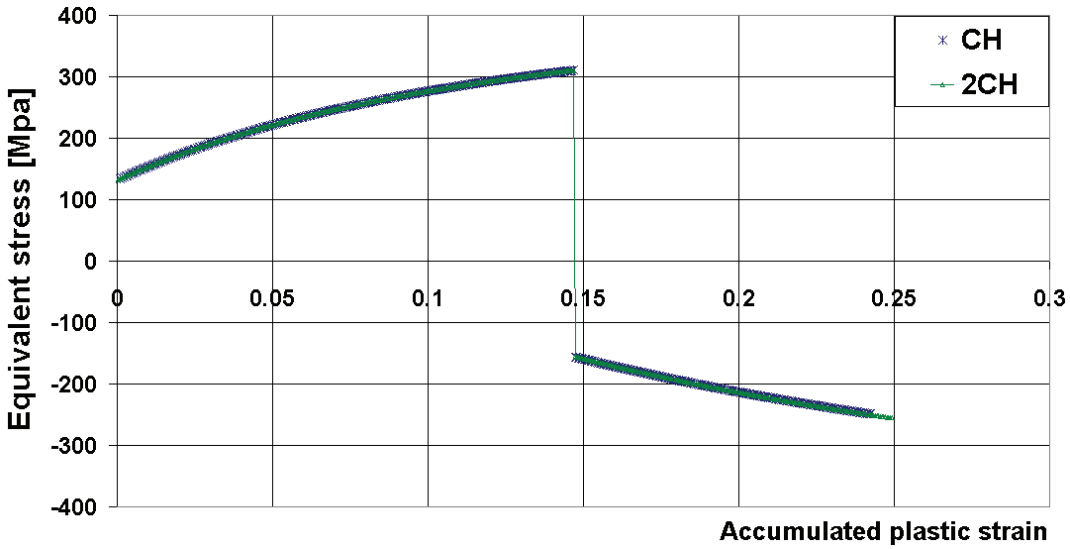

Figure 3.37. CH and 2CH constitutive models response to tension/compression loading with parameters of Table **3.17**.

The comparisons between the tension/compression curves of both models (*CH* and *2CH*) are presented in Fig. 3.37. It shows that curves coincide, which validates partially the model implementation.

To validate the model with two kinematic variables and two isotropic variables, we compare our results with those obtained by [Robin 2006] in Abaqus® for the tension/compression test described below.

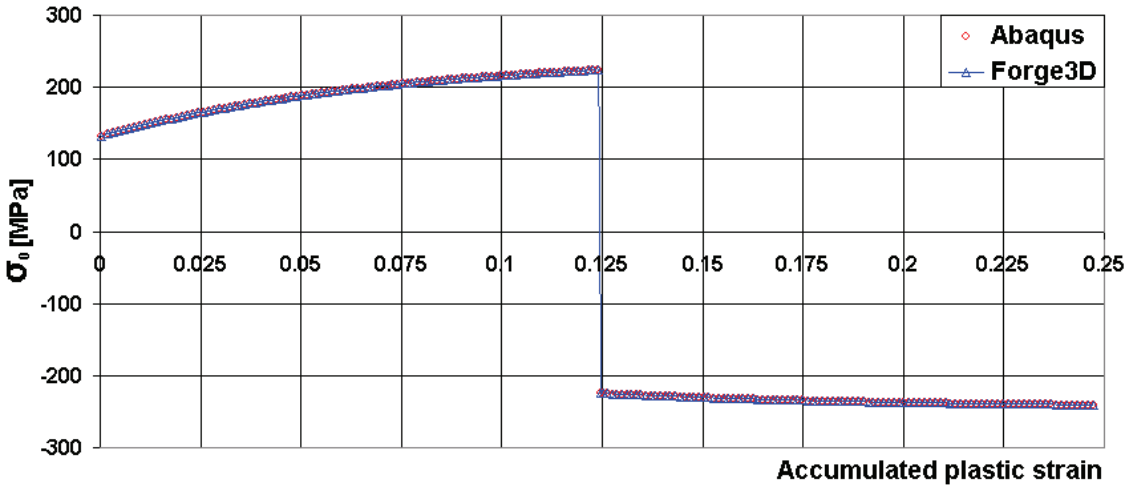

Figure 3.38. σ_0 ($R+\sigma_y$) calculation with Abaqus® and Forge3® for a tension/compression test.

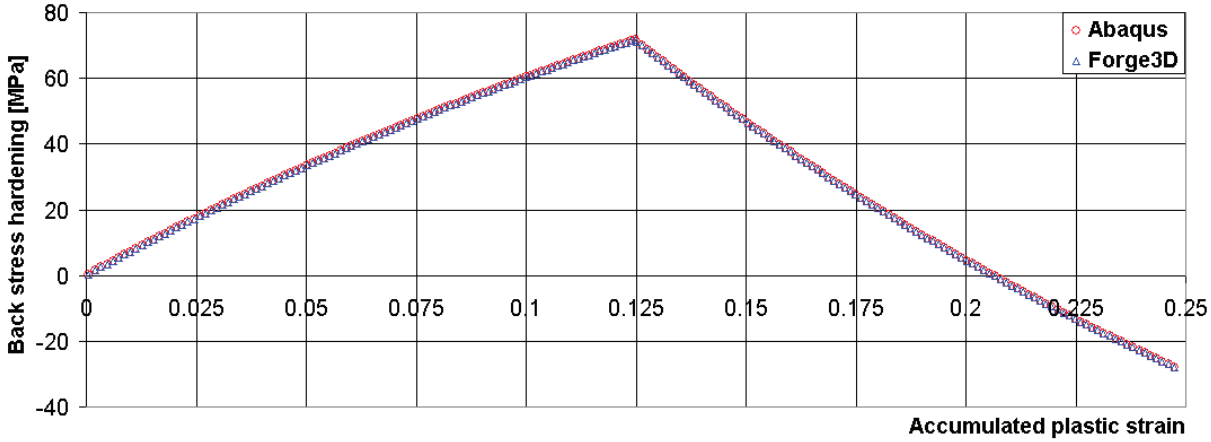

Figure 3.39. Kinematic hardening (X) calculation with Abaqus® and Forge3® for a tension/compression test.

We can see that both calculations of (σ_y, R and X) give similar results with the two codes (Figs. 3.38 and 3.39). The error between the curves does not exceed 0.5 % (average error between values calculated for the same level of strain). We can thus consider that our developments are validated.

3.5.4 Identification methodology of the model parameters

3.5.4.1 Tension-compression tests

The optimum values of the 10 model parameters $\{\sigma_y, E, b_i, Q_i, C_i, \gamma_i$ with $i=1,2\}$ have been identified using a semi-automatic identification process divided in three steps and applied for two ODS grades: *J05* and *J24*. The first and second steps are those proposed by [Velay *et al.*, 2006] schematically illustrated in Fig. 3.40. The third step is proposed in this study to enhance the numerical response of the Chaboche's model in the regime of strain amplitude changes. Each

step of the process was performed using an optimization algorithm based on MAES techniques described in section 3.3.3. The three stages are summarized below:

- The stabilized cycle of sequence 6 illustrated in Fig. 3.26 with ±1% strain amplitude is first considered. Assuming a stable cycle, the isotropic component can be set to a constant value (close to zero for the investigated material). In this first step, σ_y is assumed to correspond to the observed σ_y on the stabilized cycle at ±1% strain amplitude. It is identified graphically using Fig. 3.26 (elastic-plastic transition). The kinematic parameters $C_1, \gamma_1, C_2, \gamma_2$ are identified such as to minimize the gap between calculated and experimental hysteresis loops.

- The previously identified values of the kinematic hardening parameters are kept constant. The isotropic hardening parameters are then adjusted, using R_1 (parameters Q_1 and b_1 according to Eq. (3.42)) to describe the strong softening observed during the first dozens of cycles of loading sequence 6 (Fig. 3.24), and R_2 (parameters Q_2 and b_2) to account for the asymptotic softening (see Fig. 3.24). Besides these isotropic hardening parameters, σ_y and E can also be adjusted at this stage.

- Both kinematic hardening and isotropic hardening parameters are *re-identified* by inverse analysis using the stabilized cycle at ±0.7% (sequence 5), and the first cycle at ±1% (sequence 6). This procedure is used to improve the description of the transient behavior when the strain amplitude is changed (Fig. 3.41).

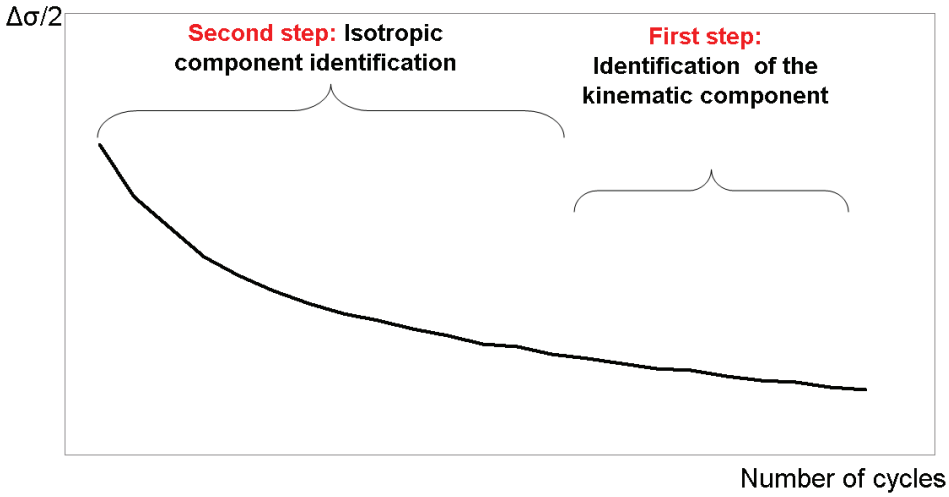

Figure 3.40. Parameter identification methodology from [Velay *et al.*, 2006].

Tables **3.18-3.20** provide the set of parameters identified for the *J05* and *J24* steels with the above semi-automatic identification process.

Table 3.18. Kinematic parameters for the tension-compression test.

	C_1 (MPa)	γ_1	C_2 (MPa)	γ_2
J05	140180	1610	40501	183
J24	120500	1210	39200	100

Table 3.19. Isotropic parameters for the tension-compression test.

	Q_1 (MPa)	b_1	Q_2 (MPa)	b_2
J05	-20	51	-214	15
J24	-80	31	-200	1

Table 3.20. Elastic parameters.

	σ_y (MPa)	E (GPa)	$\nu = 0.30$
J05	960	205	0.30
J24	800	190	0.30

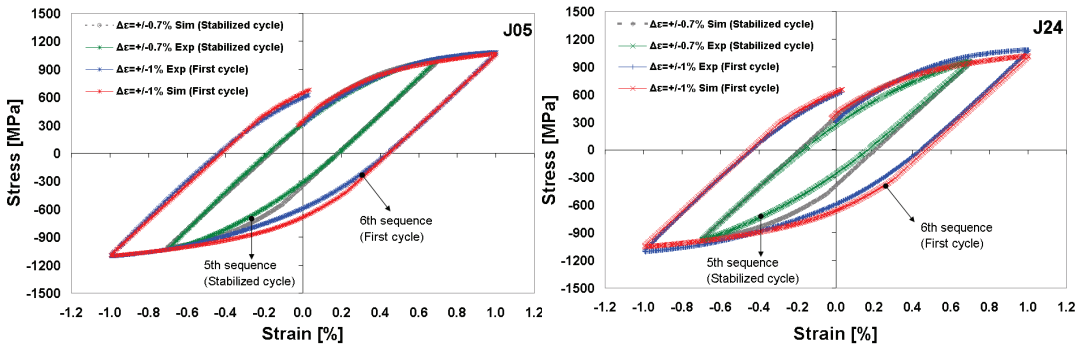

Figure 3.41. Transient behavior due to a change in strain amplitude. Comparison between experimental and calculated hysteresis loops at the stabilized cycle, ± 0.7%, and the first cycle at ± 1%. Left: J05 steel - Right: J24 steel.

The challenge consists in reaching a good description of both asymptotic and transient behaviors. Predicted numerical curve and experimental response are compared in Figs. 3.42-3.45. It can be seen that experimental and predicted results are in good agreement, even when considering loading sequences which were not used for the parameter identification, i.e. other than sequences 5 and 6, with either lower or higher strain amplitudes. Limitations of the constitutive model used in this work are shown in Figs. 3.44 - 3.45. The numerical response shows slight *softening* at sequence 7; rather than the slight cyclic *hardening* obtained experimentally. In sequence 8 of *J05*, cyclic stabilization is obtained numerically instead of the slight hardening measured experimentally. An evolution equation of the isotropic hardening

variable dealing with strain range memory, e.g. as proposed in [Wolf and Taleb 2008], [Taleb and Hauet 2009], [Taleb and Cailletaud 2010], [Sai 2011], might further improve the results (e.g. see [Velay *et al.*, 2006]).

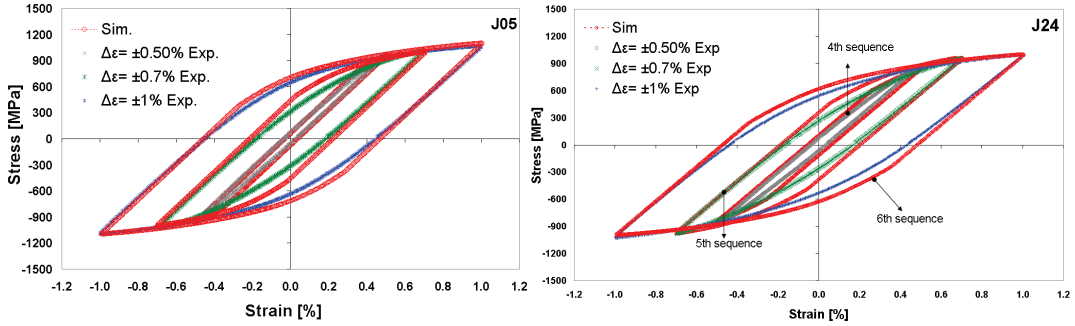

Figure 3.42. Comparison between experimental and calculated hysteresis loops at 4th, 5th and 6th sequences. Left: J05 steel - Right: J24 steel.

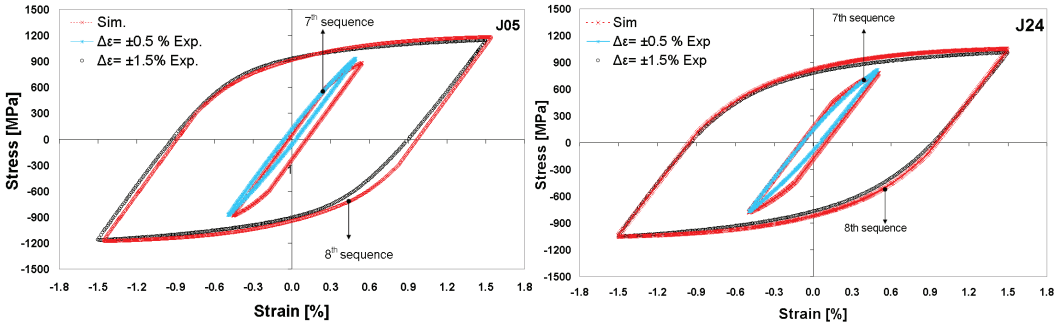

Figure 3.43. Comparison between experimental and calculated hysteresis loops, at 7th and 8th sequences. Left: J05 steel - Right: J24 steel.

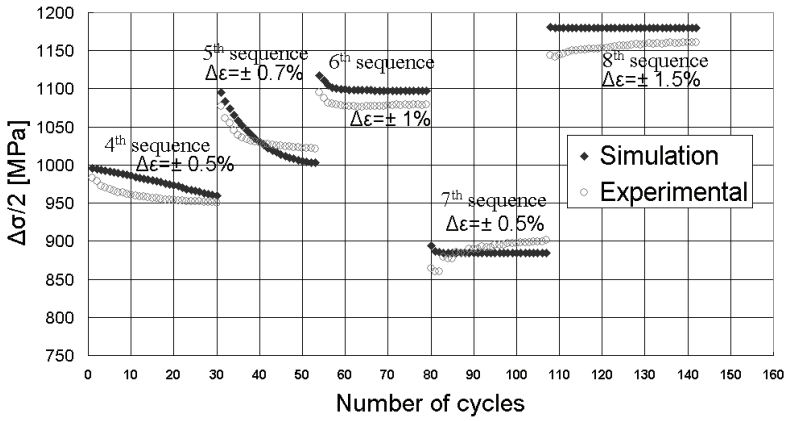

Figure 3.44. Comparison between experimental and calculated responses in the tension-compression loading sequence. J05 steel.

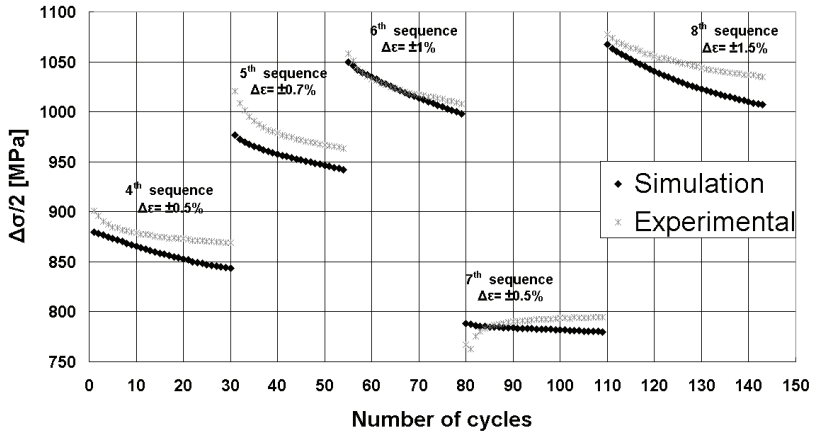

Figure 3.45. Comparison between experimental and calculated responses in the tension-compression loading sequence. J24 steel.

The error (L2 error norm) between the experimental and the numerical curves in Fig. 3.44 and 3.45 is calculated from Eq. (3.48), f_{sim} and $f_{\exp}$ being the simulated and experimental half-stress amplitudes, and i indicating a particular data point in Figs. 3.44 and 3.45. Estimation of the error is 1.95 % for the *J05* steel and 1.8% for the *J24* steel.

$$L2_{error-norm} = 100 \times \frac{\left\| f_{sim} - f_{\exp} \right\|_{L_2}}{\left\| f_{\exp} \right\|_{L_2}} = 100 \times \frac{\sqrt{\sum_{i=1}^{n} (f_{sim}^{i} - f_{\exp}^{i})^2}}{\sqrt{\sum_{i=1}^{n} (f_{\exp}^{i})^2}} \tag{3.48}$$

Besides the good agreement found in Figs. 3.44 and 3.45, the model predicts reasonably well the hysteresis loops, as shown in Figs. 3.42 and 3.43.

3.5.4.2 Compression-compression tests

Using the model parameters of the *J05* steel identified in tension-compression experiments to simulate the compression-compression test does not give good predictions at all (Fig. 3.46). A new parameters identification is therefore performed for this test. The procedure is here divided into two main stages to identify the following set of parameters: $\sigma_y, E, b_i, Q_i, C_i, \gamma_i$ with $i = 1,2$.

- All the strain ranges are considered. Elastic parameters, σ_y and E, are kept to the values identified in section 3.5.4.1 for tension-compression tests. At this stage the kinematic parameters $C_1, \gamma_1, C_2, \gamma_2$ are identified such as to minimize the gap between calculated and experimental stress responses at each cycle (Fig. 3.46).

- The previously identified parameter values describing kinematic hardening are kept constant. The isotropic hardening parameters are then adjusted, using R_1

(parameters Q_1 and b_1) to describe the strong hardening observed during the first cycles of the loading sequence at -1%, and R_2 (parameters Q_2 and b_2) to account for the asymptotic hardening (see Fig. 3.46).

Tables **21** and **22** provide the set of parameters identified with the above semi-automatic identification process and compare with those obtained from the tension-compression test. Agreement between predicted and experimental curves is shown in Fig. 3.46.

Table 21. Kinematic parameters of *J27-M2* steel.

	C_1 (MPa)	γ_1	C_2 (MPa)	γ_2
compression-compression	120000	900	5000	10
tension-compression	140180	1610	40501	183

Table 22. Isotropic parameters of *J27-M2* steel.

	Q_1 (MPa)	b_1	Q_2 (MPa)	b_2
compression-compression	90	51	250	3
tension-compression	-20	51	-214	15

Estimation of the error between the experimental and the numerical curves based on Eq. (3.48) is 4.54 %. The model is able to capture both stabilized values for each amplitude, and the rapid evolution observed when the strain amplitude changes.

In Table **22**, it is pointed out that Q_1 and Q_2 have different signs for the two investigated tests, leading to opposite trends in the cyclic hardening. It is also observed in Table **21** that the magnitudes of kinematic parameters are higher in tension-compression, which is mainly due to the difference in transient behaviors due to strain amplitude changes.

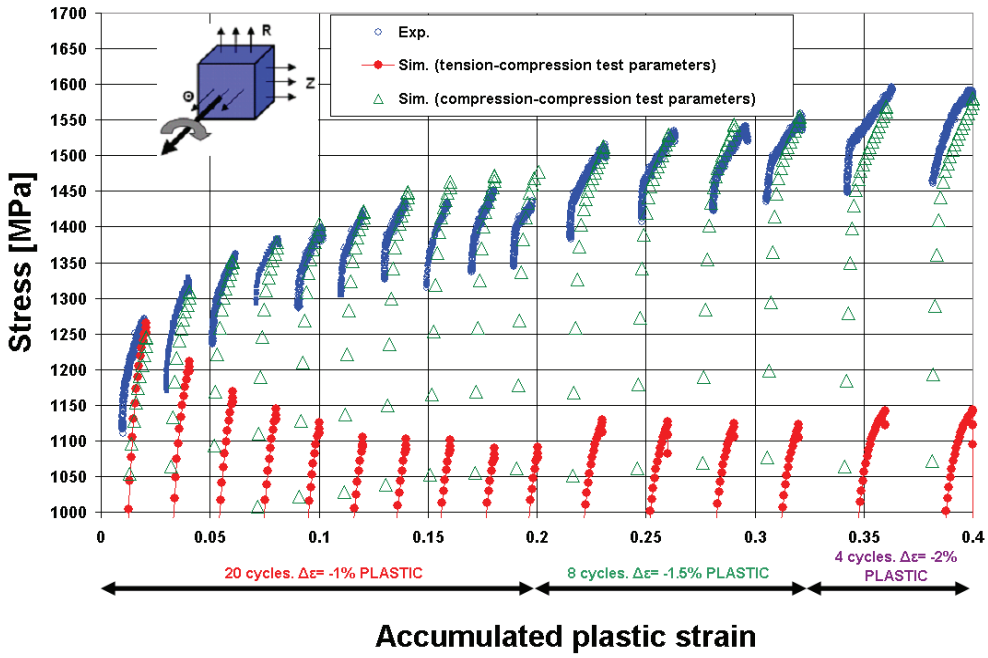

Figure 3.46. Compression-compression loading sequence: comparison between experimental and calculated responses. Simulated curves include the elastic strain.

3.5.5 ODS steel response under cyclic loading: discussion

The ODS steel investigated in this work shows a cyclic behavior which strongly depends on the loading path, the strain amplitudes, and the strain history. Depending on such conditions, the material response may range from significant cyclic softening to very strong cyclic hardening. It is noted that cyclic softening in tension-compression is *not* reported for ODS ferritic steels at high temperature [Ukai *et al.*, 2007], [Kubena *et al.*, 2011], [Kruml *et al.,* 2011], but instead a stable response is observed. At room temperature however, cyclic softening was already pointed out in [Kubena *et al.*, 2011]. The mechanism governing this evolution remains to be further investigated, but one possible explanation would be related to the shearing of nano-sized precipitates, occurring at room temperature and not at higher temperatures.

The proposed constitutive model is simple, and captures well stress changes due to strain amplitude changes. Predicted stabilized loops slightly overestimate the stress level in the elastic-plastic transition range, however in cold pilgering conditions, such a stabilized state is very unlikely to take place. The ability to capture stress changes due to strain amplitude changes is, on the contrary, a more important feature when dealing with this forming process.

The difference in parameter values obtained for tension-compression and compression-compression tests is attributed to the simplicity of the adopted constitutive model, which does not include a direct account of strain range memory effects, and of the degree of non-proportionality of the loading path:

- Strain range memory effects could be introduced as in [Chaboche *et al.*, 1979], but are likely to be inaccurate when dealing with quasi-random non-proportional mechanical loading [Krishna *et al.*, 2009].
- Additional complex mechanical tests with increasing-decreasing non-proportionalities, such as those proposed by Aubin [Aubin *et al.*, 2003a] could be performed in order to analyse further the influence of the degree of non-proportionality of the loading on the model parameters.

Because of the simplicity of the model, and the need to describe complex strain histories, the identified model parameters must be considered as “ad hoc”, i.e. even though they lie in acceptable ranges as compared to other steels [Velay *et al.*, 2006], their exact values cannot be related directly to material properties.

The proposed semi-automatic identification methodology for compression-compression tests could be applied to other ODS steel grades or ODS steels with different microstructures, e.g. recrystallized ferritic ODS steels with equiaxed grains or martensitic ODS steels with isotropic crystallographic and morphological textures. However, the ability to accurately capture transients consecutive to strain amplitude changes should be tested in a systematic way. Anisotropy due to crystallographic and morphological textures inherited from the hot extrusion process or from intermediate cold pilgering passes, as discussed in section 3.4, could be included in future work within the proposed cyclic constitutive law. The *trapezium-shaped* describes in Fig. 3.33 for some the compression-compression tests, could then possibly be modeled.

3.6 Conclusions

Accurate modeling of the material constitutive behavior is one of the most important features needed in order to simulate forming process operations properly. Within the framework of this study, the ODS tubes cold pilgering process is investigated. A volume element typically undergoes several dozens of strokes before deformation is completed. This complex mechanical history may lead to the nucleation of defects (longitudinal cracks) in low-cycle fatigue regime. Anisotropy in the constitutive behavior (crystallographic and morphological textures) and in second phase particles distribution may have a significant influence on this phenomenon. Two ODS steels grades, ferritic (*J05 and J27-M2*) and martensitic (*J24*), were tested, modeled and analyzed in order to identify three different constitutive laws: i) monotonic, ii) anisotropic, iii) cyclic.

First, the monotonic Hansel-Spittel law has been calibrated from tensile tests using an inverse analysis for each ODS grade (*J05* and *J24*). Experimental tensile tests show that *J24* steel has less ductility than *J05* steel but their yield strength are quite similar.

Second, compression tests carried out on cylindrical specimens cut in three different directions (longitudinal, radial and ortho-radial) confirmed the crystallographic texture of the

ferritic ODS steel. These tests result in an ovalization of the cross-section when looking in the radial or ortho-radial directions, and therefore exhibit flow anisotropy. The ovalization ratio is more significant when dealing with the sample cut in the ortho-radial direction. However the yield stress difference between the three loading directions is small. Hill's quadratic plastic anisotropy criterion has been selected to model the different flow patterns in compression. A set of Hill's parameters was identified based on the ovalization shape after upsetting and the stresses recorded from shear tests. Some discrepancy was found between experimental and numerical results. This was explained from three different reasons, one of them being the heterogeneity of crystallographic texture in the samples. It was proposed to assess the influence of the sample size and the cut position into de ODS bar. Furthermore, a Hill's parameters calculation enhancement was performed using the inverse analysis method, which led to an improvement of the correlation between the experimental and numerical results.

Third, strain-controlled cyclic responses of ODS steels, were analyzed and modeled, using two different tests. The first test is a classical tension-compression test, and leads to cyclic *softening* at low to intermediate strain amplitudes. The second test consists in alternated uniaxial compressions along two perpendicular axes. It is based on the similarities with the loading path induced by the pilgering process. The difference of the material response in those two tests is mainly attributed to the loading path. A simple Chaboche type constitutive model involving only 10 parameters was successfully used to describe the experimental trends. This model was implemented in a FEM code with an implicit integration scheme in order to obtain a good accuracy. Its implementation and numerical resolution was detailed. The consistent tangent modulus was also derived in a classical way. In order to check the implementation of Chaboche's model, comparisons with results coming from literature and with Abaqus® were performed.

The model parameters were identified with a semi automated identification procedure involving an inverse analysis method, and considering loading sequences compatible with those encountered in cold pilgering conditions. Experimental and predicted results are in good agreement, but a single set of model parameters could not be identified for both tests. This is mainly attributed to the difference in transient behavior observed in the two tests, when strain amplitudes change. More elaborated constitutive models could be explored in the future, in order to reach a unique model accounting for both tension-compression, and compression-compression tests. Meanwhile, the model obtained from compression-compression test can be used for the full scale simulation of pilgering process.

Due to the limited amount of martensitic grade (*J24*) neither the upsetting test nor the compression-compression test has been performed on this material. Nonetheless, the methodology implemented for the ferritic grade can be applied in a similar way.

The next Chapter will analyze a numerical simulations of ODS tubes cold pilgering considering the three considered constitutive laws in this Chapter, i.e. the monotonic, anisotropic and cyclic behaviors. The influence of these constitutive laws on the mechanical history undergone by a material point during the process will be assessed. This will allow analyzing

conditions for which (a) cracking may develop, and (b) recrystallization may take place upon heat treatment.

3.7 Résumé en français

Une modélisation précise du comportement du matériau est l'une des caractéristiques les plus importantes afin de simuler les procédés de mise en forme correctement. Dans le cadre de cette étude, le procédé de laminage à froid des tubes ODS est étudié. Un élément de volume subit généralement plusieurs dizaines de coups de cage avant que la déformation soit terminée. Cette histoire mécanique complexe peut conduire à la germination de porosités (fissures longitudinales). L'anisotropie dans le comportement mécanique (textures cristallographiques et morphologiques) et dans la distribution des particules de seconde phase peut avoir une influence significative sur ce phénomène. Deux nuances ferritiques d'aciers ODS (J05 et J27-M2) et martensitiques (J24), ont été testées, modélisés et analysées afin d'identifier trois lois de comportement différentes: i) monotone, ii) anisotrope, iii) cyclique.

Premièrement, la loi de comportement de type Hansel Spittel a été utilisée afin de simuler le comportement du matériau à partir des essais de traction simple. L'analyse inverse a permis d'identifier les paramètres matériaux de chaque nuance ODS (J05 et J24). Les essais de traction expérimentaux montrent que l'acier J24 est moins ductile que l'acier J05 mais leur limite élastique sont assez similaires.

Deuxièmement, les tests de compression réalisés sur des échantillons cylindriques prélevés dans trois directions différentes (longitudinal, radial et l'ortho-radiale) ont confirmé la texture cristallographique de l'acier ferritique ODS. Ces tests se traduisent par une ovalisation de la section dans la direction radiale ou ortho-radiale, et présentent donc un écoulement anisotrope de la matière. Le ratio d'ovalisation est plus important lorsqu'il s'agit de l'échantillon prélevé dans le sens ortho-radial. Cependant, la limite élastique dans le trois cas reste proche. Le critère d'anisotropie quadratique de Hill a été choisi pour modéliser les différences d'écoulement en compression. Un ensemble de paramètres de Hill a été identifié, basé sur la forme elliptique et les contraintes à partir d'essais de cisaillement. Un certain écart a été trouvé entre les résultats expérimentaux et numériques. Cela a été expliqué par trois raisons différentes, l'une d'entre elles étant l'hétérogénéité de la texture cristallographique dans les échantillons. Il a été proposé d'évaluer l'influence de la taille de l'échantillon et la position de prélèvement dans la barre d'acier ODS. Par ailleurs, les paramètres du modèle anisotrope ont été recalculés en utilisant la méthode d'analyse inverse, qui conduit à une amélioration de la corrélation entre les résultats expérimentaux et numériques.

Troisièmement, les réponses cycliques à déformation contrôlées des aciers ODS, ont été analysées et modélisées, en utilisant deux tests différents. Le premier test est un test classique de traction-compression. Il conduit à l'adoucissement cyclique à faible amplitude de déformation. Le deuxième test a été mis au point dans cette étude. Il consiste à alterner des compressions

uniaxiales le long de deux axes perpendiculaires. Il est basé sur les similitudes avec le chemin de chargement induit par le procédé de laminage à pas de pèlerin. La réponse du matériau est différente pour les deux tests. Cela est principalement attribué au type de chargement. Un modèle de comportement de type Chaboche impliquant seulement 10 paramètres a été utilisé avec succès pour décrire les tendances expérimentales. Ce modèle a été implémenté dans un code éléments finis avec un schéma d'intégration implicite en vue d'obtenir une bonne précision. Sa mise en œuvre et la résolution numérique ont été détaillées. Le module tangent a également été calculé d'une façon classique. Afin de vérifier la mise en place du modèle de Chaboche, les résultats provenant de la littérature et ceux obtenus avec Abaqus® ont été comparés.

Les paramètres du modèle ont été identifiés avec une procédure d'identification semi-automatique impliquant une méthode d'analyse inverse. Les résultats expérimentaux et numériques sont en accord, mais un seul jeu de paramètres n'a pas pu être identifié pour les deux essais mécaniques. Ceci est principalement attribuable à la différence de comportement transitoire observée dans les deux essais, lorsque l'amplitude de déformation change. Des modèles plus élaborés de comportement de matériaux pourraient être explorés dans l'avenir, afin d'avoir un modèle unique pour les deux essais, tension-compression et compression-compression. D'ici là, le modèle obtenu avec l'essai de compression alternée de cubes, peut être utilisé pour la simulation complète du laminage à pas de pèlerin.

En raison de la quantité limitée de matière de la nuance martensitique (J24), l'essai de compression alternée de cubes a été effectué sur une nuance ferritique. Néanmoins, la méthodologie mise en œuvre sur la nuance ferritique peut être appliquée d'une façon similaire pour une autre nuance ODS.

Chapter 4

Pilgering process analysis

4.1 Introduction

Longitudinal defects may occur in cold pilgering of ODS tubes caused by the stress and strain history. Because of rare occurrences, these defects are really difficult to be study directly. A model has been built in Chapter 2 to describe the mechanical conditions that prevail during a forming pass. In this Chapter the influence of the ferritic ODS constitutive law, on the prediction of defect, is assessed. The constitutive law is shown to control the strain path, and hence the tendency to develop cracks. Experimental observations have been performed (longitudinal strain, number of pilgering marks, and micro-hardness). They provide data which can be used to identify the most accurate constitutive law. The distribution of strains and stresses is discussed as well. A damage criterion risk is finally defined and computed. The third pass of the fabrication route is more specifically studied here.

4.2 Experimental measurements

4.2.1 Strain measurements

To observe the strain path in a Zircaloy-4 tube during cold pilgering, [Aubin *et al.*, 1995], [Girard *et al.*,1993], [Mulot *et al.*, 1996], [Aubin *et al.*, 2000], [Girard *et al.*, 2001], [Osika and Swiatkowski 2003], [Osika *et al.*, 2009] drilled pieces of rods (markers) in the thickness of the tube. This technique is also used here to analyze and validated the proposed HPTR cold pilgering FEM model. The amount of ODS steel being limited, a Zircaloy tube is used instead.

The Zircaloy tube has been prepared by drilling 59 holes (diameter: 1mm) aligned along the axis of the tube. A hole is drilled every 8 mm. Due to the character of the tube rolling process (small diameter-thickness reduction and tube elongation) the markers should be properly located. The choice of material marker has been done taking into account that it should have a different color to be easily identified in the tube material. Its mechanical properties should be as similar as possible compared to the tube. If the marker is too soft it is difficult to put it into the hole and it could leave the hole during pilgering. If the material is too hard, then it will significantly affect the flow of the tube material. In our case the holes were filled with pieces of stainless steel (316L) because its yield stress is close to the Zircaloy one.

The tube has been partially rolled with the HPTR mill available at CEA/Saclay. Evolution of location and shape of the inserts (markers) are revealed by microscopic examination.

4.2.1.1 Longitudinal strain

The Zy-4 partially rolled tube is showed in Fig. 4.1. The initial marker shape is displayed in Fig. 4.1(a). During rolling, some markers were ejected from the initial hole (see e.g. Fig. 4.1(b)), markers were pulled out and then smashed over the tube by the dies (see e.g. Fig. 4.1(c)).

Despite these losses, there were enough markers left to measure and analyze the strain path in the longitudinal direction. Indeed, initial circular markers become ellipses (see e.g. Fig. 4.1(d)-(e)). The longitudinal elongation allows calculating the longitudinal strain using the following equation:

$$\varepsilon_{zz}(z) = \ln\left(1 + \frac{\left(l_f(z) - l_0\right)}{l_0}\right) \tag{4.1}$$

where l_f is the long axis of the measured ellipse at a given position z (on the tube working zone) and l_0 is the marker initial diameter. Thus, the experimental longitudinal strain can be quantified along the length of the partially rolled tube (see Fig. 4.2).

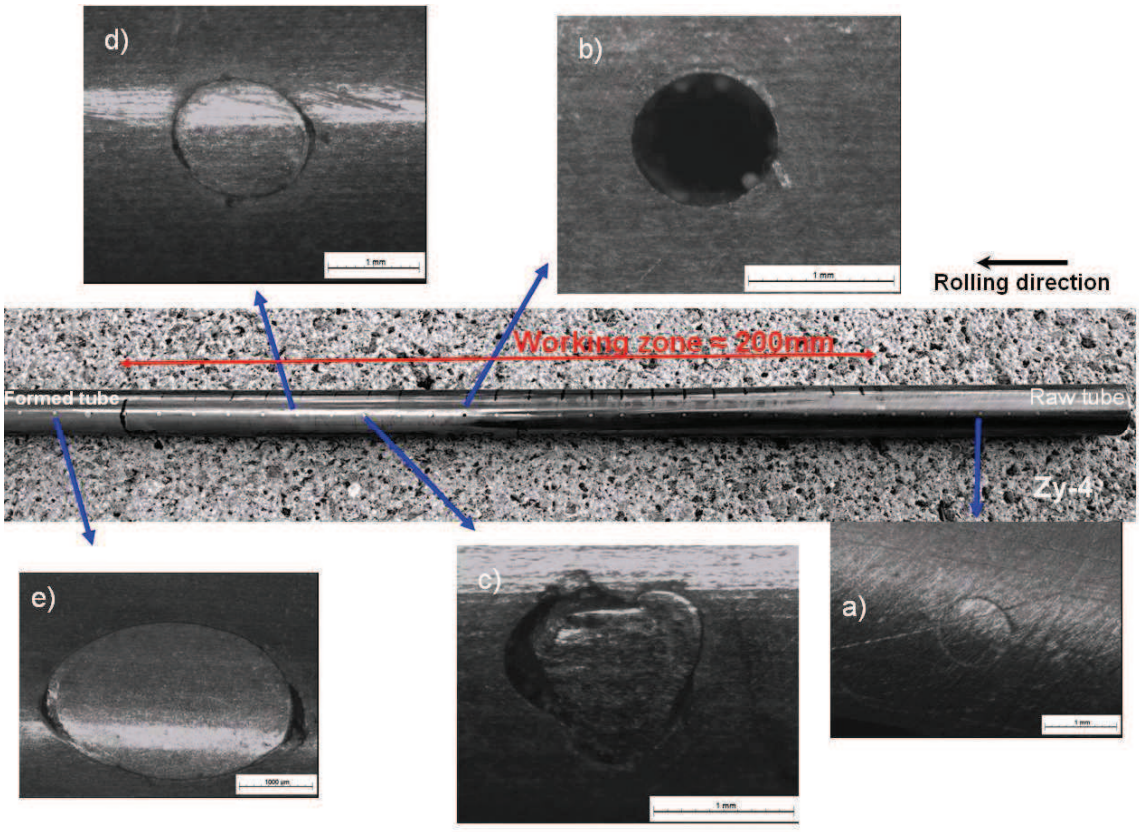

Figure. 4.1. Partially rolled tube showing the working zone and the 316L cylindrical markers evolution. a) initial shape and position of a given marker b) marker has disappeared c) marker smashed by the dies after being pulled out d) good marker deformation in the working zone e) final shape (elliptical) of the marker.

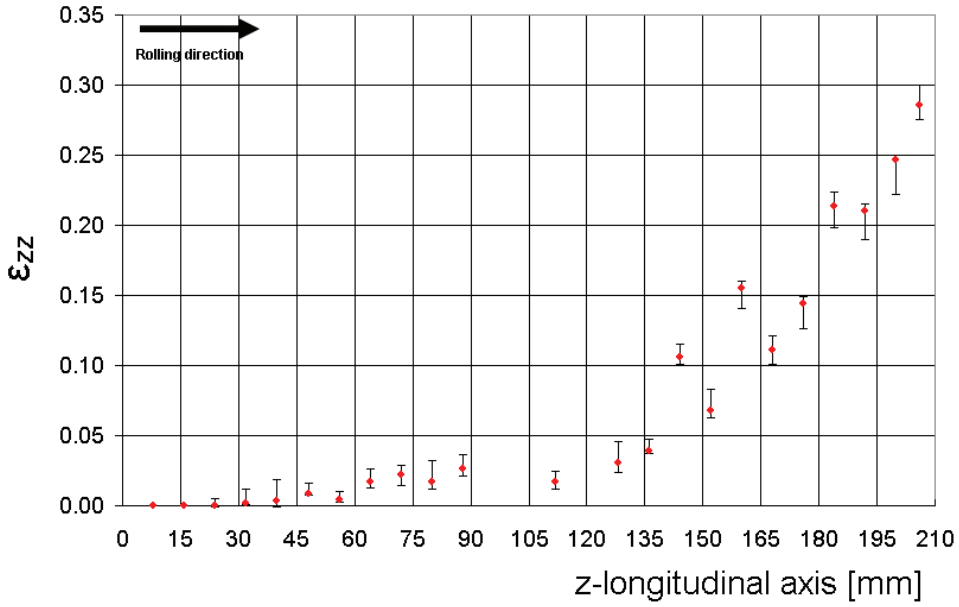

Figure 4.2. Experimental longitudinal strain evolution along the length of a partially rolled tube.

From Fig. 4.2, the first half of the working zone ($0 < z < 135mm$) deals with a small elongation in the rolling direction. This means that the HPTR process works mainly on the diameter and thickness changes in this area. From $z > 135mm$ the elongation of the tube becomes more significant because the tube is in contact with the mandrel and, by mass conservation effect, the material flows in the rolling direction. It is pointed out from Fig. 4.1 that the markers remained aligned in the axial direction, i.e. the orthoradial position of the holes did not change during HPTR pilgering.

4.2.1.2 $\varepsilon_{\theta z}$ (Rolling helix)

Torsion of the tube (pilgering helix) is a known phenomenon that occurs during VMR pilgering [Girard 1993], [Mulot *et al.*, 1996], [Aubin *et al.*, 2000], [Girard *et al.*, 2001], [Osika *et al.*, 2009]. In order to check this observation in the HPTR pilgering, a straight channel (0.4 mm depth and 0.4mm width) was machined in the raw tube at 180° of the holes alignment described above. After pilgering, the initial straight channel does not change to an helix (see Fig. 4.3) as in the VMR case (e.g. see [Aubin *et al.*, 1994]). In the VMR case, a cross-section of the tube at a given position in the rolling direction, z, remains slightly elliptical. Therefore, during a VMR stroke , a significant transverse shift of the dies (transverse force) can appear, and partially explains the sense of the twisting of the tube (pilgering helix, see section 1.3.1). On the other hand, for HPTR pilgering, a cross-section of the tube at a given position in the rolling direction, z, remains slightly clover; with a 120° rotation symmetry. Therefore, d uring a HPTR stroke, the 3 dies are less subjected to transverse forces, avoiding thus a material twist.

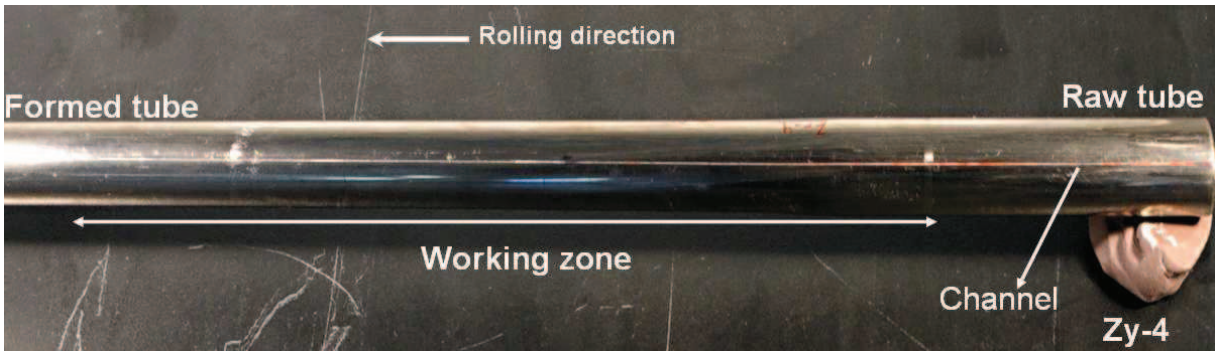

Figure 4.3. Partially rolled tube showing the evolution of the straight initial channel. It remains straight after rolling, showing no torsion of the tube.

4.2.2 Stress measurement

Hardness measurements provide an easy way of obtaining the increase of the yield strength in cold-formed products, since their use is very simple and inexpensive. Vickers hardness number is used in this work.

The Vickers Pyramid Number (Hv) is expressed in $kgf.mm^{-2}$ ($1\,kgf.mm^{-2} \approx 9.81 MPa$). Hv is directly calculated with respect to the applied force in kgf and the average diagonal value of the square-based pyramid.

It is common to express Hv in MPa. These measures allow characterizing the rheological properties of work-pieces surfaces. The flow stress can be indeed related to the Vickers hardness [Tabor 1950] using:

$$\sigma_0 \approx \frac{Hv[MPa]}{c} \tag{4.2}$$

where c is a material parameter, often close to 3. In the case of ferritic ODS (not recrystallized), it was found $c = 3.14$. Micro-hardness (Vickers) measures were carried out in the partially rolled ferritic ODS tube at the CEA/SRMA/LA2M Saclay [LA2M 2011]. For this purpose, a piece (*ring*) of tube was cut from the formed tube. The *ring* was then polished. Afterwards, micro-hardness measures at different locations into the *ring* wall thickness were performed. A force of $1\,kgf$ during 15s was used. The hardness measurements are only available after the *pass 2* and the subsequent intermediate heat treatment, and after the *pass 4*. They are summarized in Table **4.1**. The hardness increases from the internal to the external tube surface (see Fig. 4.4). A small hardness increase (<7%) of ODS steels is observed and this was also pointed out in the literature (see e.g. [Toualbi *et al.*, 2011]).

Table 4.1. Ferritic ODS tube micro-hardness [H_{V1}] before and after cold pilgering.

Position from the internal diameter [mm]	Raw tube hardness [$kgf.mm^{-2}$] (*Pass 2* + heat treatment)	Formed tube hardness *(Pass 4)* [$kgf.mm^{-2}$]	Hardness increases [$kgf.mm^{-2}$]	Hardness increases (%)
0.1	369.1	393.8	24.7	6.7
0.3	397.4	405.3	7.9	1.98
0.5	397.9	421.5	23.6	5.9
0.7	396.3	418.2	21.9	5.52
0.8	405.2	-	-	-

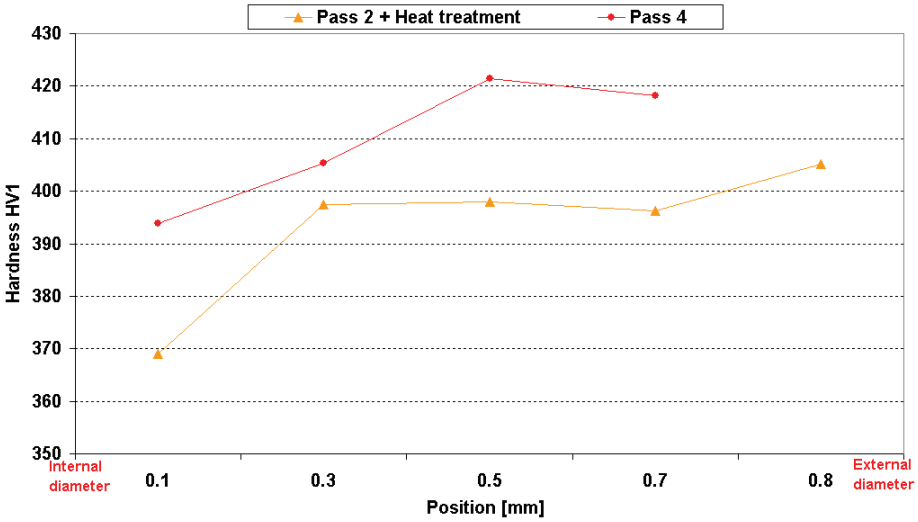

Figure 4.4. Hardness [H_{V1}] evolution over the tube wall thickness from [LA2M 2011].

Table 4.2. Ferritic ODS tube σ_0 [MPa] before and after cold pilgering, computed from Table **4.1**.

Position from the internal diameter [mm]	Raw tube σ_0 [MPa] (*Pass 2* + heat treatment)	Formed tube σ_0 [MPa] *(Pass 4)*
0.1	1153	1230
0.3	1241	1266
0.5	1243	1317
0.7	1238	1306
0.8	1266	-

After heat treatment (following *pass 2*), σ_0 remains high (see Table **4.2**) in relation with the initial yield limit extruded bar (960 MPa) (see Chapter 3). This means that the heat treatment is unable to significantly soften the material, in the absence of recrystallization.

4.2.3 Clover marks periodicity

In a partially rolled tube clover marks dashed by the shoulders die are easily observed (see Fig. 4.5). The number of marks does not depend on the material because they are observed in both Zircaloy and ODS tubes. Indeed, their numbers depend of the rotation angle at each stroke. For the investigated fabrication route, the rotation angle is 39° leading to 9 clover marks (360⁄39° ≈9).

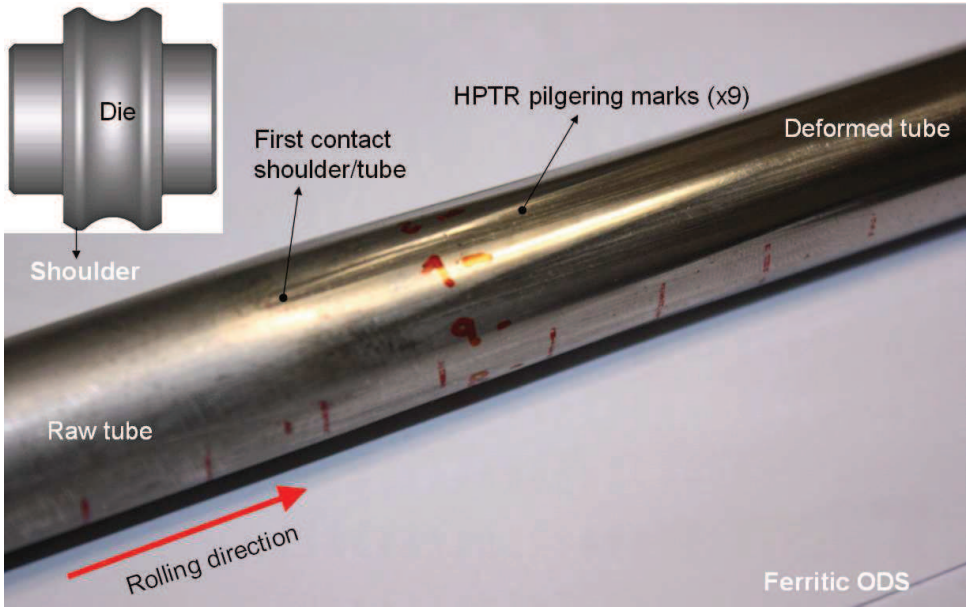

Figure 4.5. HPTR pilgering marks on partially rolled ferritic ODS tube. 9 marks are visible when rotating 39° the tube after each stroke.

The depth of HPTR pilgering marks should be measured as it could be material dependent. This measurement can be used to validate, partially, the adopted constitutive law.

4.3 Mechanical analysis

4.3.1 Simulation set up

Taking into account Chapter 2 conclusions, we will consider here a 20 mm tube initial length. The tube is space discretized with an anisotropic structured mesh, with 4 elements over the thickness, 60 elements over the length and 100 elements over the circumference. Mesh characteristics are summarized in Table **4.3**. For this study the time step is fixed to 0.001s managed with the adaptive time step method described in section 2.3.4. Coulomb friction is assumed with $\mu = 0.1$. *Pass 3* of the fabrication route (see section 2.3.1) is simulated. The process total time is 98s. The tube is turned 39° and moved forward (feed) 1.7 mm after each stroke. A material point takes 120 strokes to pass through the working zone.

Table 4.3. Mesh characteristics.

	Number of elements	Number of nodes	Element type
Tube	144000	30500	3D tetrahedral
Dies	3 x 20294	3 x 10199	2D triangles
Mandrel	60000	30100	2D triangles

Lagrangian numerical sensors have been placed at the mid-length of the tube at different angles (0°-19.5°-39°-90°-180°-270°) (see Fig. 4.6) to avoid edge effects. Four sensors are placed over the thickness at the Gauss point as illustrated in Fig. 4.6. In order to analyze the process over the circumference 6 sensors rows are placed in the $r(\theta)$ cross-section plane. Each row (called R) leads to four sensors (called S). Thus, R1 contains S1-4 counted from the external surface to the internal surface; R2 contains S5-8 and so on.

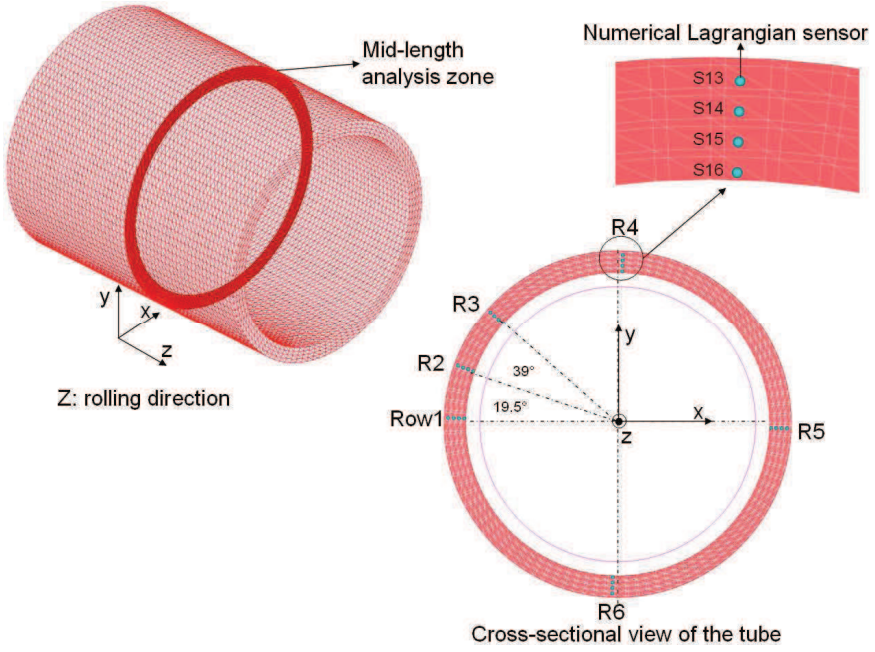

Figure 4.6. Lagrangian numerical sensors placed at the mid-length of the tube at different angles (0°-19°-39°-90°- 180°-270°).

The aim of this section is to assess the influence of the constitutive law on the mechanical history of a material point in pilgering conditions, and to identify the critical mechanical conditions corresponding to the highest risk of cracking.

Referring to Chapter 3, the ferritic ODS steel will be considered here using different constitutive laws:

- Chaboche type constitutive model. Materials parameters identification coming from a classical tension/compression test (named: *Cyclic T/C*).
- Chaboche type constitutive model. Materials parameters identification coming from alternated uniaxial compressions along two perpendicular axes (named: *Cyclic C/C*).
- Hill's quadratic plastic anisotropy criterion. Materials parameters identification coming from upsetting tests of cylindrical specimens cut in three different directions.

Shear parameters are assumed to be the same as for an isotropic material (named: *anisotropic monotonic*).

- Hansel-Spittel behavior law. Materials parameters identification from tensile test (named: *isotropic monotonic*).

4.3.2 Cyclic material point history induced by pilgering

4.3.2.1 Stress

The sensor S2 stress history is monitored and is illustrated in Fig. 4.7. The axial stress is tensile when the material is located in the side relief, and compressive over the die shoulder. A material point will experience cycles of tension and compression, potentially inducing fatigue phenomena during the pilgering process. The 120 positive (tensile) and negative (compressive) peaks appear in Fig. 4.7; in the compressive case, high and low peaks alternate, because the material point varies, depending on the successive rotations. The largest stress is experienced in the last cycles because the thickness reduction is larger and the material is strongly work-hardened.

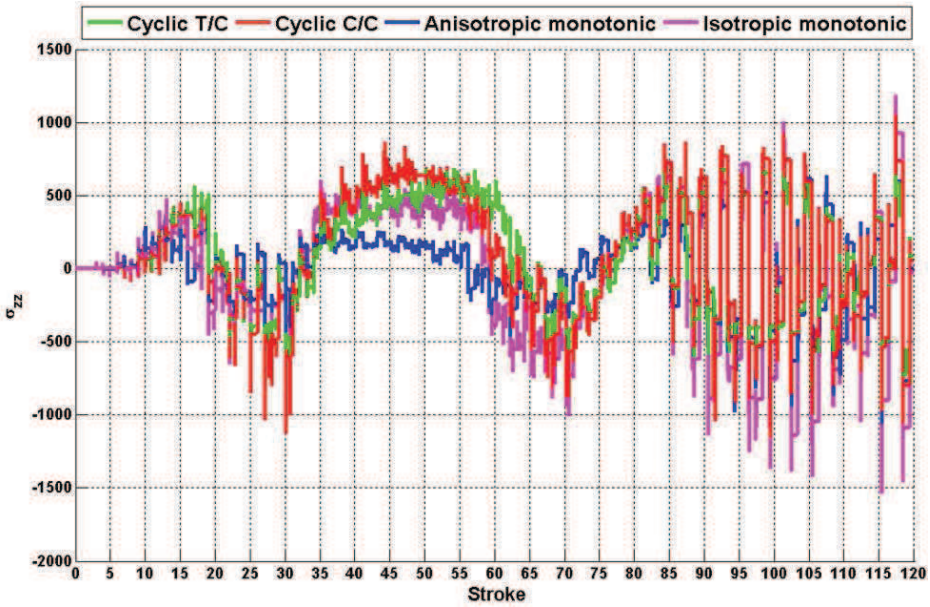

Figure 4.7. Sensor S2 longitudinal stress (in MPa) history for different ferritic ODS constitutive laws.

Fig. 4.8 displays the dies and tube position when the longitudinal stress is maximum according to Fig. 4.7, using the cyclic C/C constitutive law. In the deformation zone under the die, the longitudinal stress σ_{zz} is tensile in the side relief area, and compressive in the groove bottom (see Fig. 4.9).

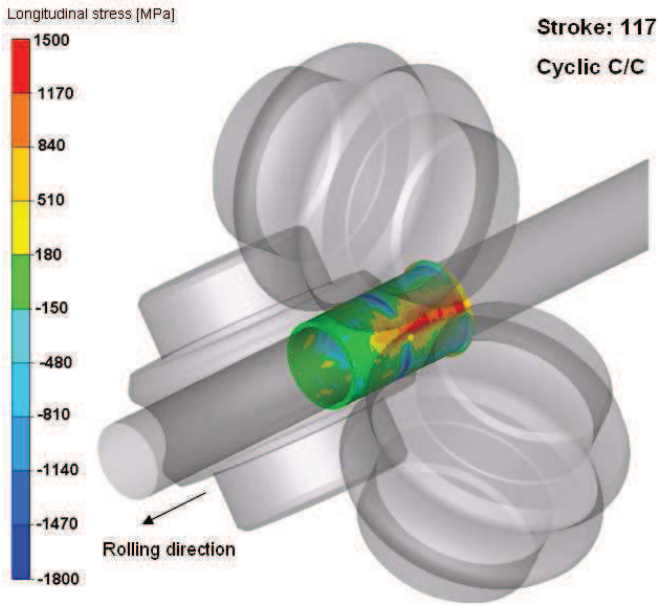

Figure 4.8. Longitudinal stress isovalues (in MPa) showing the high compression in the groove bottom and the high tensile material state in the side relief when using the cyclic C/C constitutive law. Stroke 117 corresponds to the moment when the tensile stresses are highest for the Cyclic C/C constitutive law.

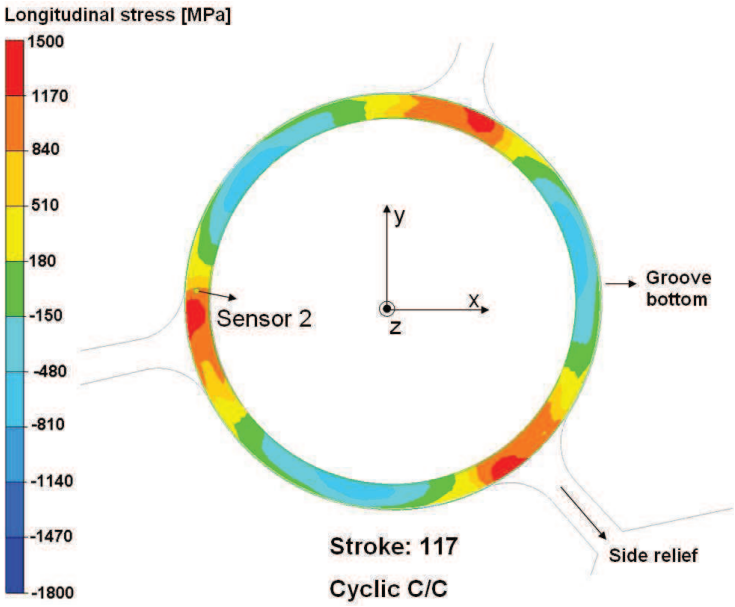

Figure 4.9. Cross-section at the stroke 117 where the longitudinal stress is maximum (in MPa), on sensor S2 according to Fig. 4.7. Cyclic constitutive law.

When analyzing the maximum value of the equivalent stress at each stroke for each constitutive law (see Fig. 4.10), both isotropic monotonic and anisotropic monotonic laws provide overestimated stress values in the last strokes. Indeed, the equivalent stress value increases sharply from the 85th stroke. From, the mathematically point of view, the computation is correct because the flow stress equation is given by a power law, therefore the more the strain increases, the more the stress increases. On the other hand, when dealing with Chaboche's constitutive

model, no more hardening is possible because of stabilization of the isotropic hardening variables (the asymptotic value is reached, see section 1.4.2.1.1).

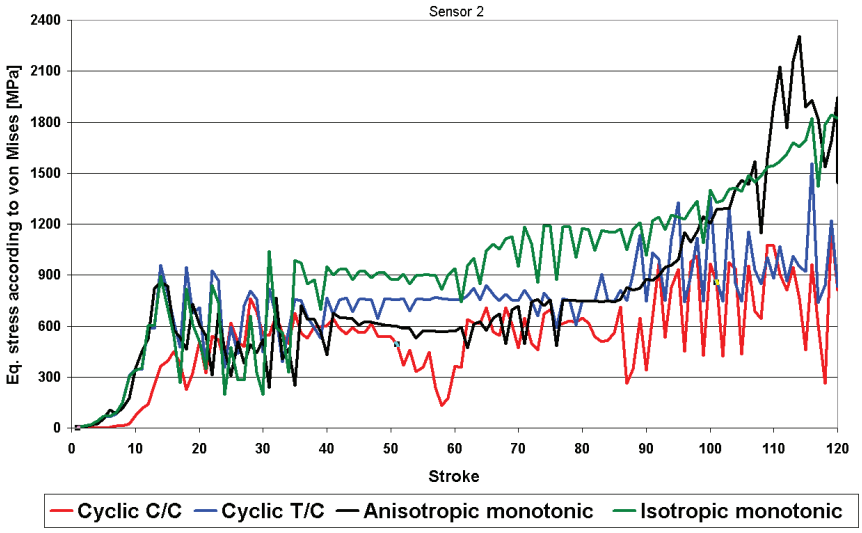

Figure 4.10. Sensor 2: maximum equivalent stress (in MPa) at each stroke for a ferritic ODS HPTR pilgered tube.

Different isotropic hardening evolutions are observed in Fig. 4.11 when considering the two cyclic laws. For the cyclic T/C constitutive law the yield surface size decrease during pilgering. This is coherent with the fact that the material parameters were identified through the classical uniaxial tension-compression test, where cyclic softening occurs. On the other hand, when dealing with the cyclic C/C constitutive law, the material parameters were identified through alternating uniaxial compressions along two perpendicular axes of a cube. In that case, cyclic hardening was observed.

From Fig. 4.11 the fast stabilization of the first isotropic variable apparent in both cases. It was reached after only 14 strokes leading to plastic strain. However, the second variable evolves differently, i.e. much faster in the cyclic T/C constitutive law. In the cyclic C/C constitutive law, it does not even saturate, which leaves space for further strain hardening.

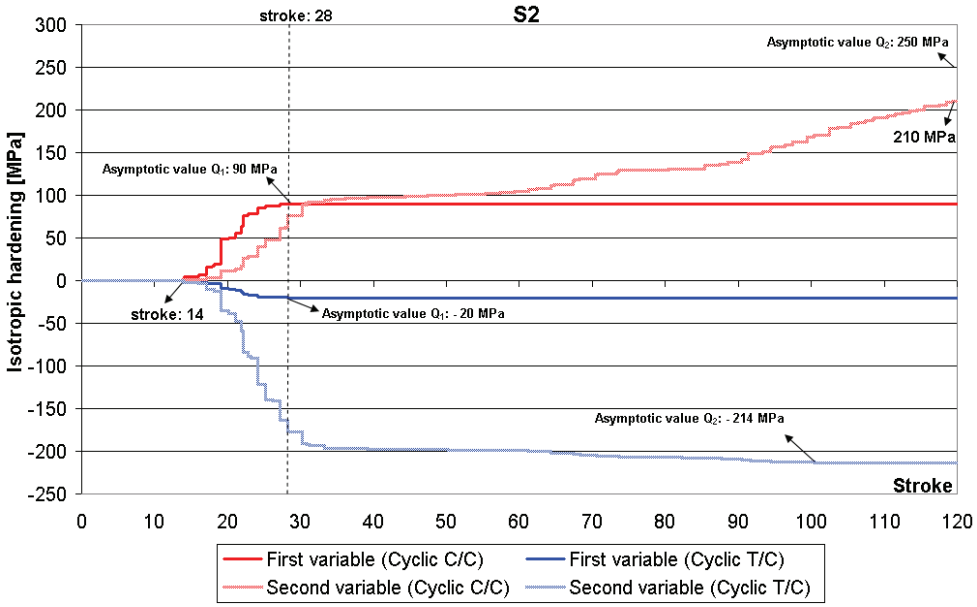

Figure 4.11. Sensor 2: isotropic hardening (in MPa) variables history for both cyclic T/C and cyclic C/C constitutive laws.

Now, when comparing the flow stress σ_0 value experimentally and numerically identified (at the external surface of the tube wall thickness, see Fig. 4.12), it is observed that the cyclic T/C constitutive law does not manage to model the final state of the ferritic ODS tube. In the case of monotonic constitutive laws, the difference is even larger when comparing to the final experimental yield stress of the formed tube (see Table **4.2**). On the other hand, the cyclic C/C constitutive law is much closer. In Fig. 4.13, the initial yield stress (960 MPa) identified from the compression-compression test is however lower that measured (1238 MPa). The tube has indeed already undergone two forming passes and a subsequent heat treatment (without any recrystallization).

Fig. 4.14 analyzes the flow stress (σ_0) evolution as a function of the wall thickness level. The larger values are located close to the external tube surface. Simulation and experimental results are in agreement on this. However, some disagreements appear when approaching the internal tube surface. The numerical value of σ_0 decreases from the external surface to the center of the tube, and then, close to the internal tube surface it increases slightly. This increase is not measured experimentally. It should be noticed again that we are comparing the numerical *pass 3* with measurements done after *pass 4*, so final conclusions are difficult to reach.

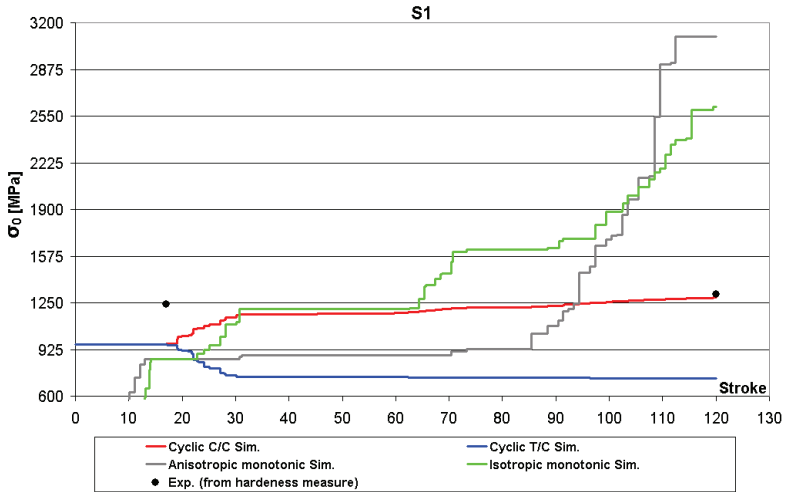

Figure 4.12. Sensor 1: stress σ_0 (in MPa) numerical and experimental response comparison for different constitutive laws.

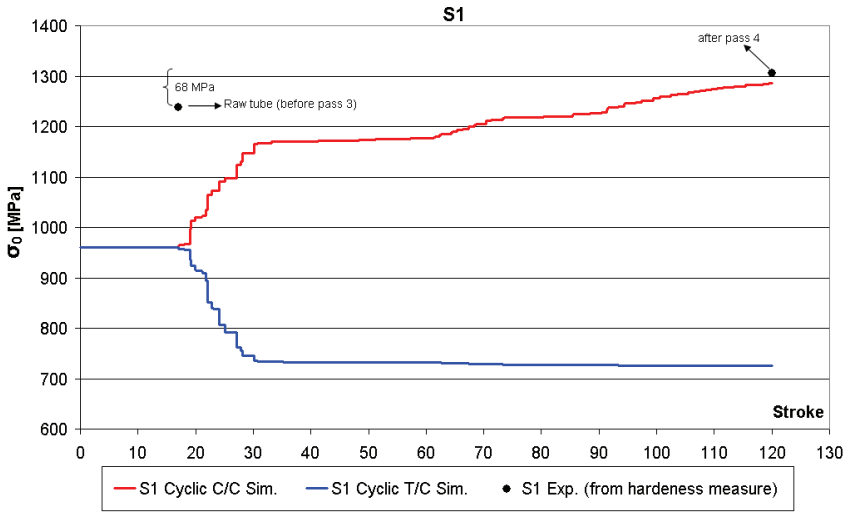

Figure 4.13. Sensor 1: stress σ_0 (in MPa) numerical and experimental response comparison for cyclic T/C and cyclic C/C constitutive laws.

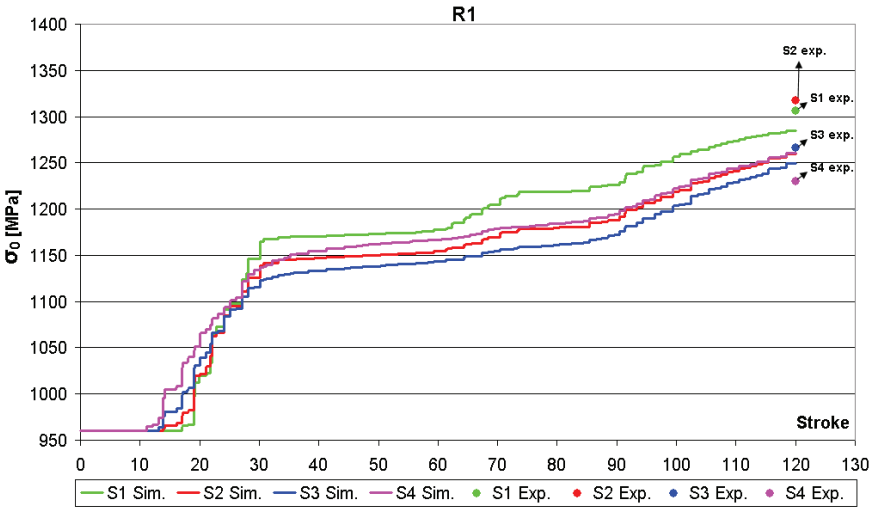

Figure 4.14. Row 1: stress σ_0 (in MPa) numerical and experimental response comparison for the cyclic C/C constitutive law.

Despite the possible discrepancy between the cyclic C/C constitutive law and the experimental yield stress calculated from hardness measurements, the Chaboche's cyclic constitutive model, involving material parameters identified from alternated uniaxial compressions along two perpendiculars axes, proved to be by far the most accurate model.

4.3.2.2 Strain rate

The quasi-random loading of a material point under pilgering conditions is observed in Fig. 4.15. The highest strain rate values are found in the last strokes when the HPTR process leads to thickness reduction. Although the tube is rolled on the forward and return stroke, the major deformation is mainly undergone during the forward stroke (see stroke 70 zoom in Fig. 4.15).

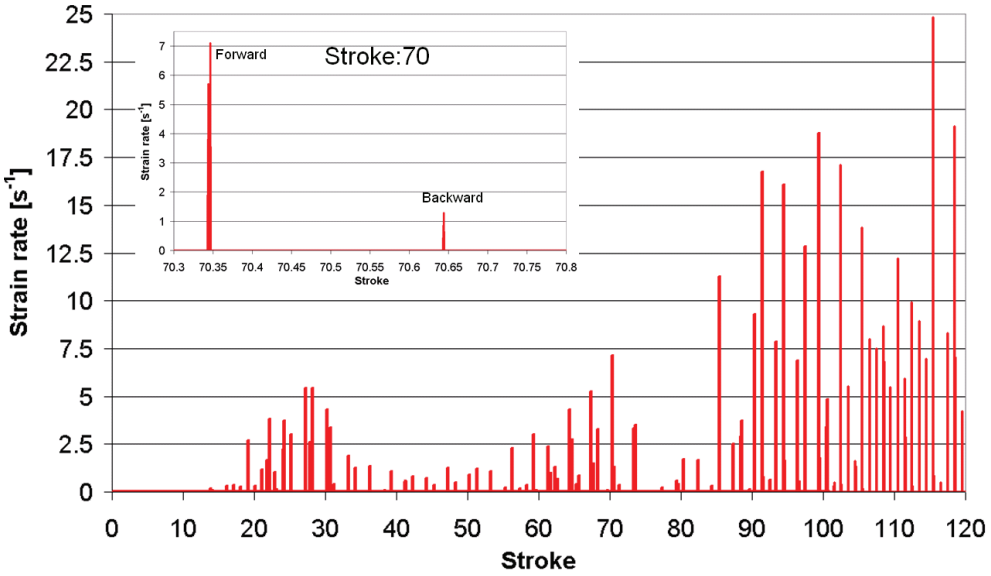

Figure 4.15. Sensor 2 strain rate history for the Cyclic C/C behavior law.

The random-loading intensity can vary from one side of the tube to the other. The maximum strain rate value is mostly located at the external tube surface. This observation is valid with any constitutive law used in this work (Fig. 4.16).

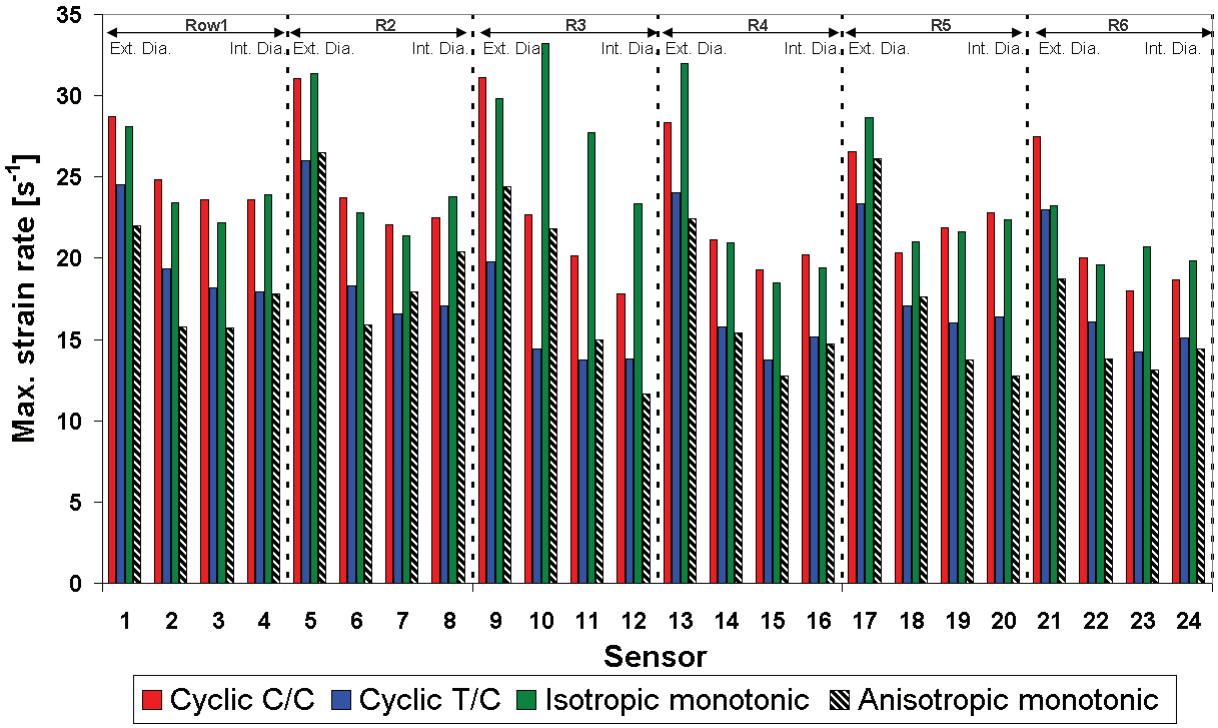

Figure 4.16. Maximum strain rate in the sensors (S1-S24).

The maximum strain rate remains high for cold deformation of hard materials. Nevertheless, from Fig. 4.17, it can be observed that 62% of the strokes are performed with strain rates from 0 to 1.5 s^{-1}. Few isolated high strain rate strokes (e.g. stroke: 85, 92, 95, 101, 116, 118) could increase the risk of damage and cracking (see Fig. 4.15).

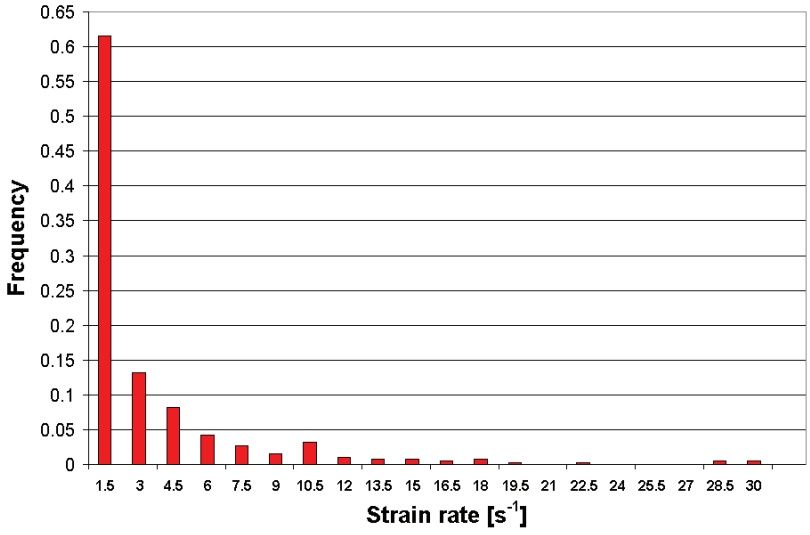

Figure 4.17. Strain rate frequency (S2). Cyclic C/C behavior law.

Fig. 4.18 shows at which stroke the maximum strain rate is undergone by each sensor placed over the tube when using the cyclic C/C constitutive law. This helps identifying the "risky"

strokes. With this law, strokes 112,116 and 117 are particularly dangerous. Nevertheless, strain rate alone does not tell the story about damage risks. This point is discussed later in this Chapter.

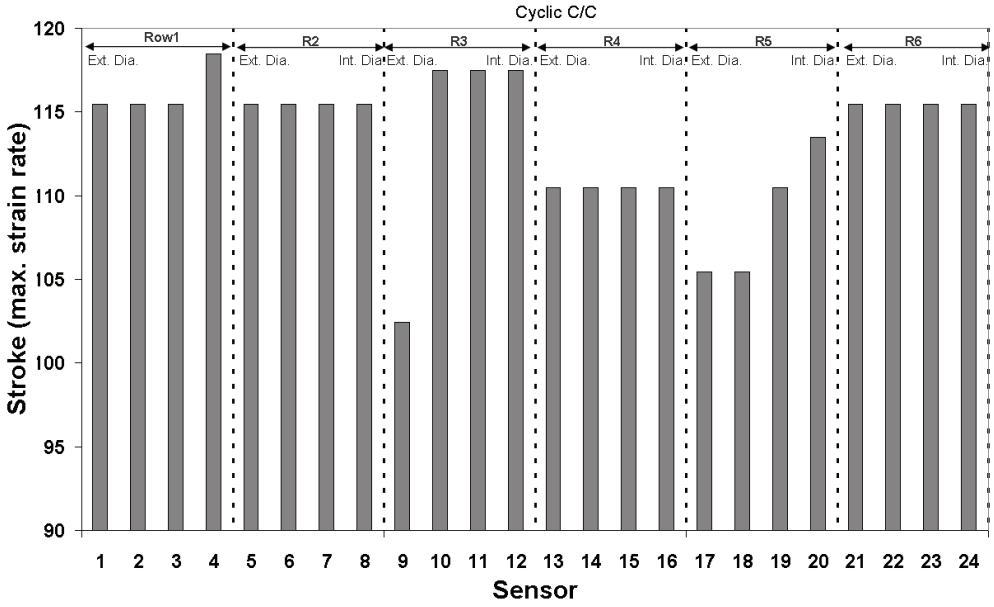

Figure 4.18. Strokes exhibiting maximum strain rate for the Cyclic C/C behavior law..

4.3.2.3 Strain

Figs. 4.19-4.22 show the time integrated values of four components of the strain rate tensor in cylindrical coordinates. It is noticed that before 85th stroke the dies mainly lead to a diameter reduction of the tube, after this stroke $\varepsilon_{\theta\theta}$ decreases markedly (see Fig. 4.20). On the other hand ε_{rr} increases during the first 85 strokes, leading to an increase of the tube thickness (see Fig. 4.19), resulting in a *clover-shape* tube. Most of the deformation is then performed after the 85th stroke by compression between the dies and the mandrel resulting in an extension in the axial (z) direction (see Fig. 4.21). Furthermore; $\varepsilon_{\theta\theta}$ can be locally in tension in the finishing zone, at the side relief (e.g. see strokes 100-105 in Fig. 4.20).

The above general analysis is valid for the different constitutive laws investigated in this study whereas the distribution of deformation can change from one constitutive law to another. Differences can be found when looking closer at the deformation path. In Fig. 4.19, the radial deformation value is more or less the same for all cases except for the anisotropic monotonic constitutive law for which the 56th stroke exhibits a positive strain increment, indicating either a tensile stress in the radial direction or a volume conservation effect. The other constitutive laws do not predict such a radial strain at the 56th stroke. At the 27th stroke, the difference in the material flow can be pointed out again for the anisotropic monotonic law. The radial strain is almost twice as compared to the isotropic monotonic case. This is a consequence of the Hill's parameters which largely control the 3D material flow. This can be observed in strokes 30-58 and 67-85. The radial strain increment, $\Delta\varepsilon_{rr}$, are compressive in the anisotropic monotonic case, while they remain close to zero in the other cases.

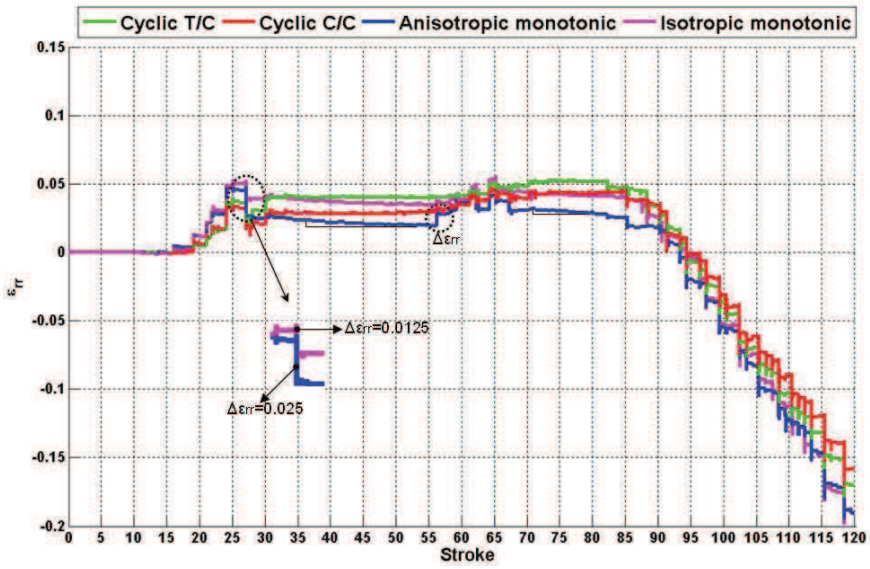

Figure 4.19. Radial strain $\mathcal{E}_{rr}$ path undergone by a volume element (sensor 2) during HPTR cold pilgering of a ferritic ODS cladding tube.

In Fig. 4.20, the ortho-radial deformation history is roughly the same for the two cyclic constitutive laws. However, some differences can be found with monotonic constitutive laws, more specifically for the 18th, 24th, 27th and 64th strokes (circled on the Figure). Positive orthoradial strain increments, $\Delta\varepsilon^{+}_{\theta\theta}$, are again noticed in the anisotropic case.

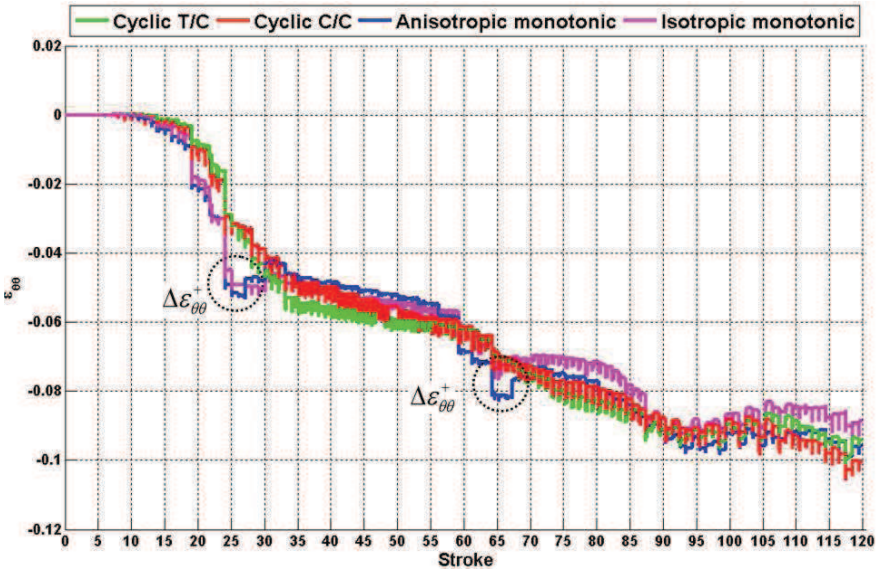

Figure 4.20. Ortho-radial strain $\mathcal{E}_{\theta\theta}$ path undergone by a volume element (sensor 2) during HPTR cold pilgering of a ferritic ODS cladding tube. Most of the strokes involve compressive strains along the ortho-radial direction.

The longitudinal strain history seems independent of the constitutive law choice (see Fig. 4.21). It is mainly prescribed by the HPTR pilgering process parameter (e.g. die geometries, dies kinematics, feed, rotation…).

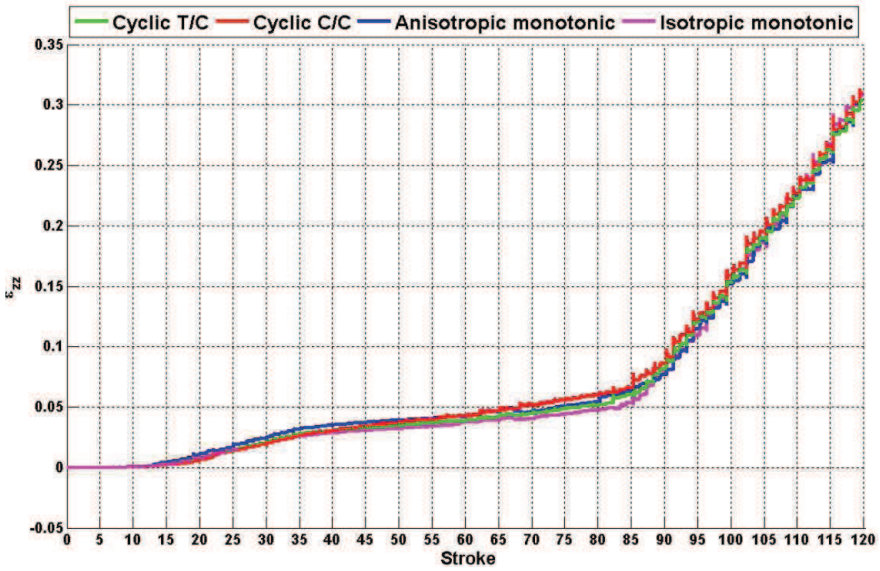

Figure 4.21. Longitudinal strain ε_{zz} path undergone by a volume element (sensor 2) during HPTR cold pilgering of a ferritic ODS cladding tube.

In Fig. 4.22, it is noticed that the relative ε_{rz} increment values change more than those of ε_{zz}. However the values of $\Delta\varepsilon_{rz}$ could have modifications in the same way in absolute values. The observed values of ε_{rz} (0.03-0.05) are smaller than those reported in the literature (0.5-0.6) for VMR pilgered Zyrcaloy tubes [Aubin *et al.*, 1994]. Unfortunately no reference value is available in the literature for the HPTR process.

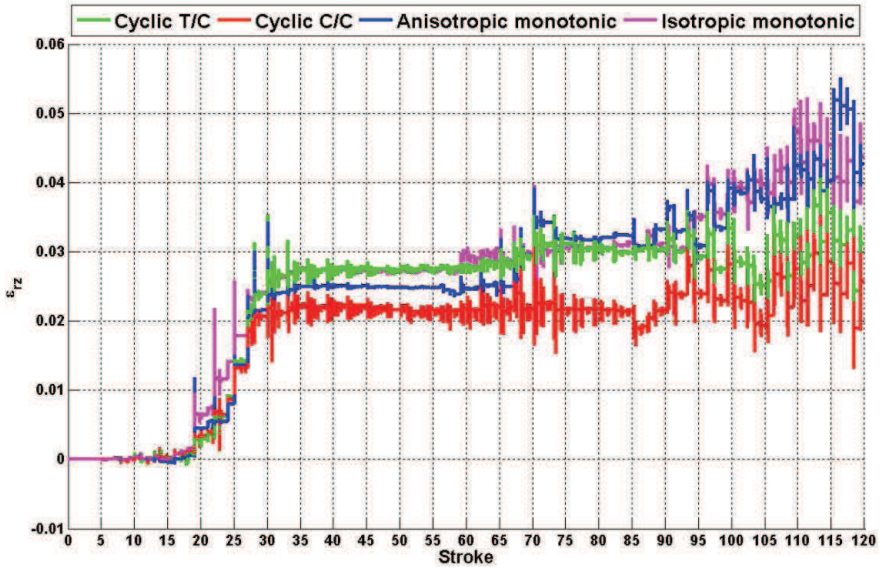

Figure 4.22. Shear strain ε_{rz} path undergone by a volume element (sensor 2) during HPTR cold pilgering of a ferritic ODS cladding tube.

Concerning the two others shear strains $\varepsilon_{\theta z}$ and $\varepsilon_{r\theta}$: the first one is insignificant from the experimental measurements. It can also be confirmed from the numerical model because the

original sensor row rotation is negligible. Sensor 2 $\varepsilon_{\theta z}$ is shown in Fig. 4.24. It slightly depends on the constitutive law but values remain low.

On the other hand, the numerical model displays a 4° $r(\theta)$ plane rotation after 120 strokes (see Fig. 4.23). Hence, very small strain increments occur in $r(\theta)$. The shear $\varepsilon_{r\theta}$, computed with the cyclic C/C constitutive law (see Fig. 4.25), is small in magnitude for the cyclic laws. For the monotonic cases, however $\varepsilon_{r\theta}$ values can be four times as high.

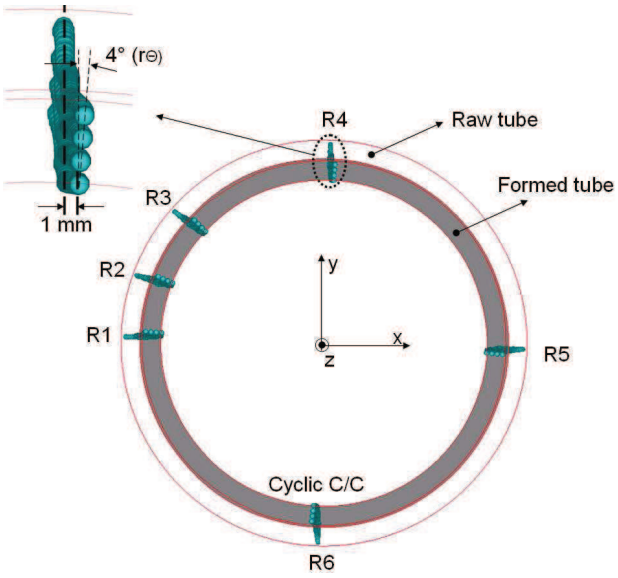

Figure 4.23. Numerical displacement undergone by each sensor during HPTR cold pilgering looking at the $r(\theta)$ planes.

It is concluded that for the cyclic C/C behavior law, the shear values $\varepsilon_{\theta z}$ and $\varepsilon_{r\theta}$ remain low in magnitude as compared to the other components. For this reason, in the remainder of this work these two components are not analyzed.

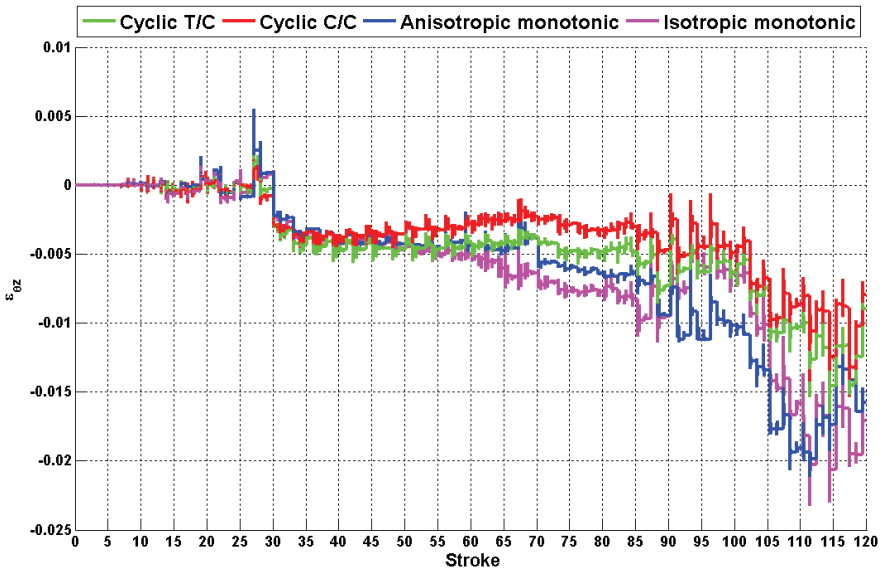

Figure 4.24. Shear strain $\varepsilon_{\theta z}$ path undergone by a volume element (sensor 2) during HPTR cold pilgering of a ferritic ODS cladding tube.

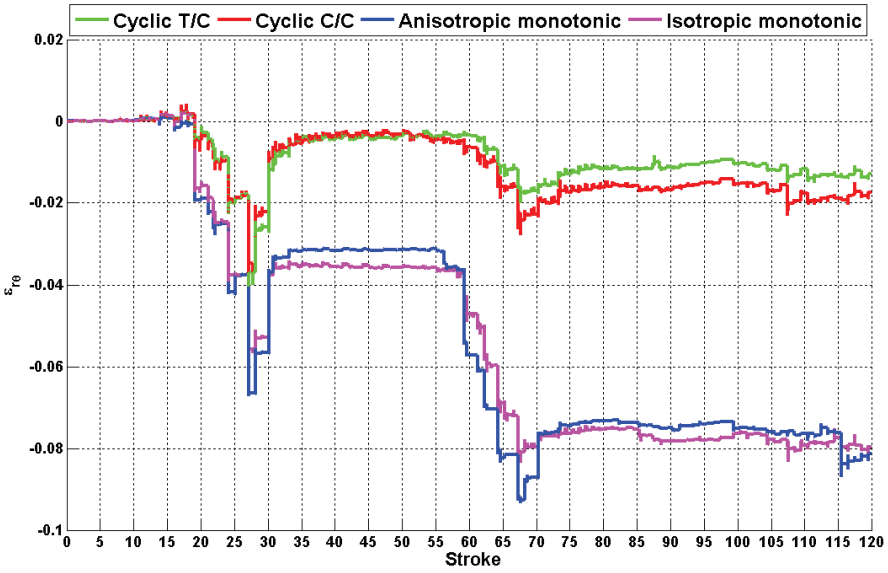

Figure 4.25. Shear strain $\mathcal{E}_{r\theta}$ path undergone by a volume element (sensor 2) during HPTR cold pilgering of a ferritic ODS cladding tube.

Considering the equivalent strain evolutions, two *plateaus* are observed in Fig. 4.26. The first one, between 33rd and 53rd strokes and the second one between 70th and 85th strokes. This could be explained by the fact that the material locally hardens during cold deformation, therefore the force applied to the material in these two *plateaus* is not enough to deform plastically through the whole thickness of the tube. This is clear when looking at stroke 80 with the Cyclic C/C behavior law in Fig. 4.27. S1 and S2 do not deform plastically whereas S3 and S4 do. During the process plastic deformation is located on the external surface, then on the inner surface. From Fig. 4.27 one can also see that the external surface of the tube is much more deformed as compared to the other thickness levels.

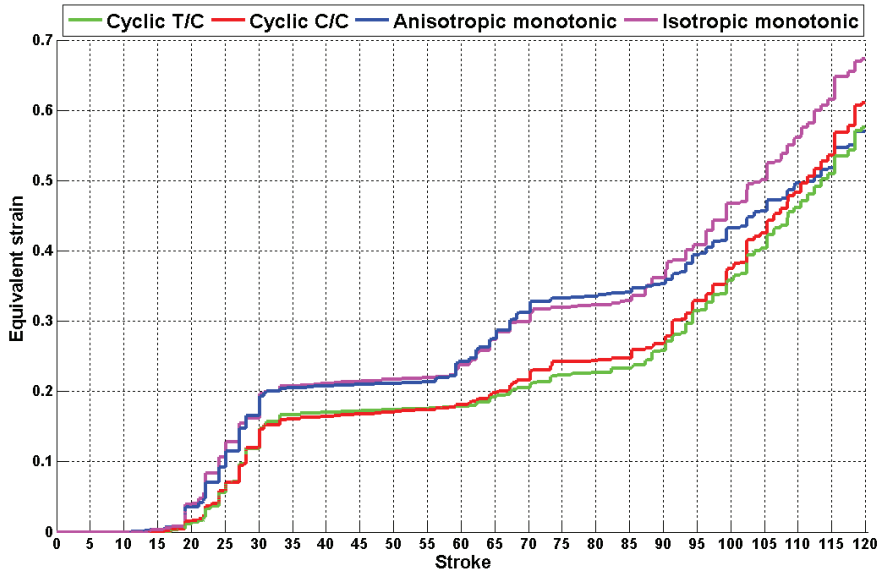

Figure 4.26. Equivalent strain path undergone by a volume element (sensor 2) during HPTR cold pilgering of a ferritic ODS cladding tube.

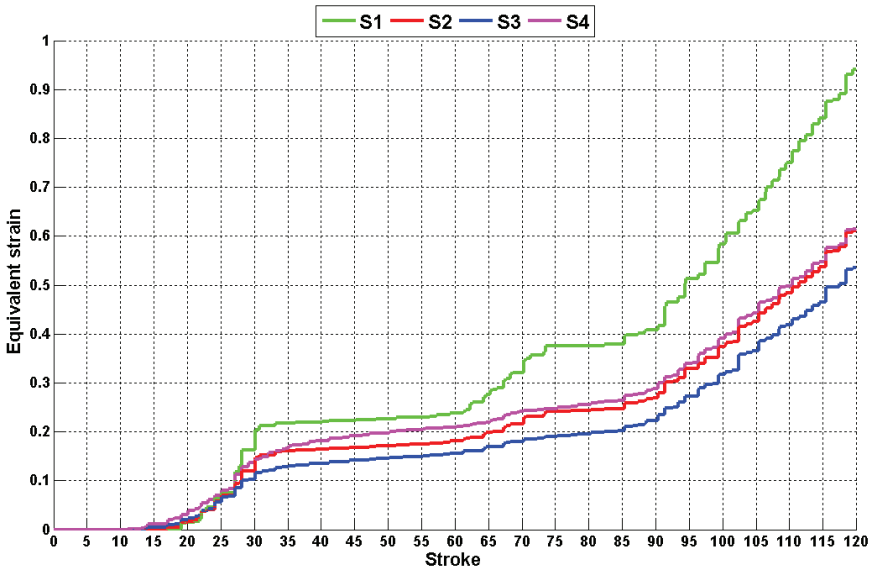

Figure 4.27. Cyclic C/C behavior law: equivalent strain path undergone by sensors along the raw 1 (R1) during HPTR cold pilgering of a ferritic ODS cladding tube.

Comparison between predicted and measured longitudinal strain

Experimental evaluation of plastic longitudinal strains due to cold pilgering of a Zy-4 cladding tubes has been performed in section 4.2. Experimental and simulated values are displayed in Fig. 4.28. As shown previously, the numerical longitudinal strain is slightly sensitive to the choice of the constitutive law. The numerical HPTR pilgering model overestimates longitudinal strains at the beginning of the process. More than a half of the working zone ($0 < z < 135$ mm) leads mainly to diameter reduction with very limited tube elongation. For $z > 135$ mm the tube elongates consequently, and this captured by the model. Overall, the trend is well predicted.

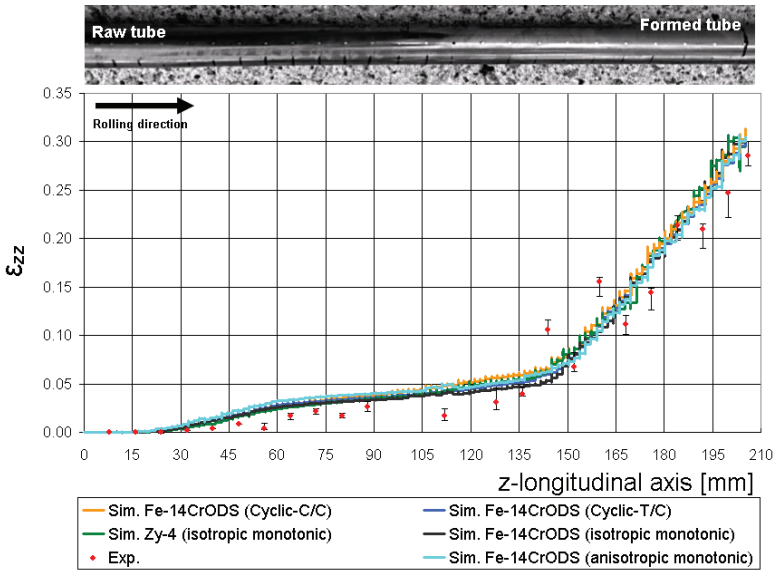

Figure 4.28. Comparison between predicted and measured longitudinal strain. Numerical results correspond to S2.

The identification of the deformation path was the first step toward a better understanding of the critical conditions leading to damage and cracking. A more systematic analysis of all cycles can help to define which cycles (strokes) may contribute to the oligocyclic fatigue of the material. This leads to the need for a damage criterion. Integration of a proper damage law or failure criterion into the proposed numerical model may lead to the numerical optimization of the process in terms of maximum acceptable deformation before heat treatment, and detailed cold pilgering conditions (tools kinematics, dies profile optimization, etc.).

4.3.2.4 Damage

The criterion introduced by Latham and Cockroft and used in this work establishes the damage function from the principal stresses [Cockroft and Latham 1968]. This damage criterion was already used for VMR cold pilgering (e.g. [Aubin *et al.*, 2000], [Girard *et al.*, 2001]) and seems to be a good indicator to predict defects frequency. Compressive stresses have a negligible effect on damage compared with tensile ones; so in its original version this criterion does not take them into account. The classical damage function used in [Girard *et al.*, 2001] is the sum of the product of the maximum tensile stress at each stroke. This function represents an indicator of the material state. The expression was already given in section 1.3.3.

Considering the HPTR cold pilgering process, and the experimental evidence of longs cracks along the rolling axis, it is proposed to consider each strain increments in all directions ($\Delta\varepsilon_i$, $i = rr, \theta\theta, zz, r\theta, \theta z, rz$), instead of the equivalent strain ε_{eq}. Similarly, the expression of the maximal stress is modified in order to consider only positive stress components. Finally, authors have shown that damage occurs for mechanical states where the triaxiality is higher than -1/3 [Bao and Wierzbicki 2004].

A modified cumulative damage function (Lat&Co) is then proposed:

$$Lat\ \&\ Co_{(i)} = \sum_{\substack{Stroke \\ triaxiality \geq -1/3}} \sigma_i^+ * \Delta\varepsilon_i^+ \tag{4.3}$$

where $i = rr, \theta\theta, zz, r\theta, \theta z, rz$, $\sigma_i^+ = \max(0, \sigma_i)$, $triaxiality = \sigma_H / \sigma_{eq}$ with σ_H the hydrostatic pressure and σ_{eq} the equivalent stress. Thus, it is possible to obtain a cumulative damage field in each mechanical solicitation direction. These damage functions have been implemented in the FEM software Forge3®.

Comparing Figs. 4.29-4.32, it is observed that the longitudinal damage function is maximal in magnitude regardless of the constitutive law. Fig. 4.29 shows the sensor 2 longitudinal damage function evolution, computed with Eq. (4.3), for each constitutive law.

Longitudinal damage is highest for the cyclic C/C behavior law. Even with the huge stress values predicted by monotonic laws; the longitudinal damage value is lower than for both cyclic laws. Hence, when the cyclic constitutive law is taken into account, the material follows more

damaging situations. Additionally, the anisotropic monotonic case seems to decrease damage risks. This point will be discussed later.

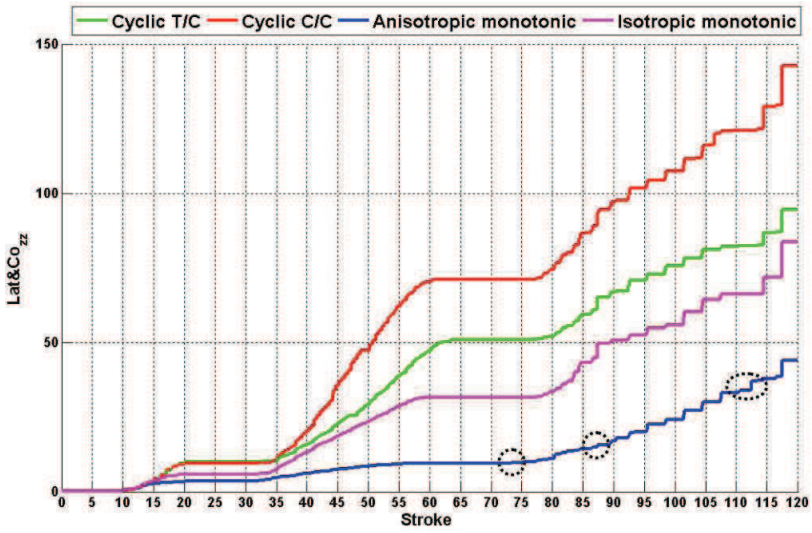

Figure 4.29. Longitudinal damage function history in sensor S2 (in MPa).

Dashed circles in Figs. 4.29-4.32 show damage increments observed for one constitutive law while they are absent for the others. For example, in Fig. 4.29 two strokes (74 and 113) cause longitudinal damage only in the anisotropic monotonic case. On the other hand, stroke 87 causes a very small damage increment in comparison with other cases. That can be explained by the different 3D material flow. The damage increments in those three particular strokes remain however limited in magnitude.

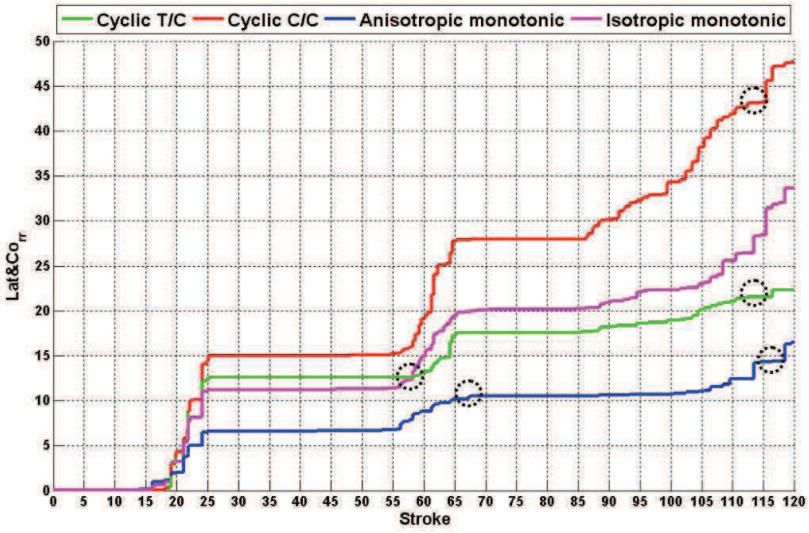

Figure 4.30. Radial damage function history in sensor S2 (in MPa).

Looking at Fig. 4.30 and Fig. 4.31 and considering the cyclic C/C behavior law, damage functions increase dramatically between strokes 57-65 for the radial component, and 75-78 for the ortho-radial component. Other laws also lead to an increase, but with lower intensity.

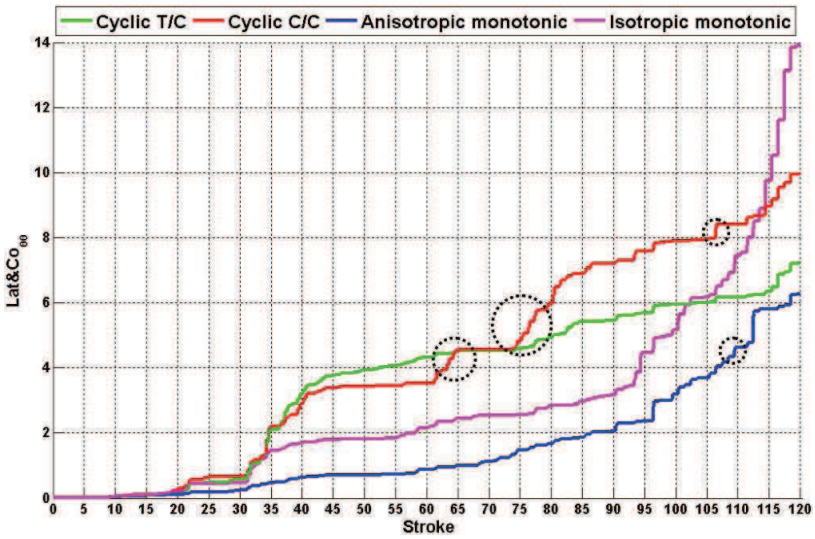

Figure 4.31. Ortho-radial damage function history in sensor S2 (in MPa).

The damage associated to shear rz is higher in magnitude than the damage function in the ortho-radial directions, and that is true for any constitutive law used in this work. This shows the importance of lubrication in this process. The magnitude is actually comparable to that of the radial component.

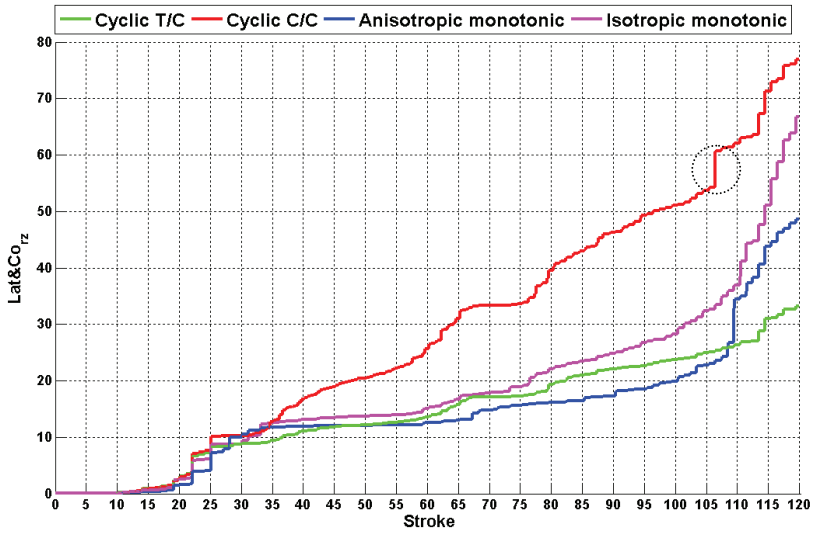

Figure 4.32. Shear ε_{rz} damage function history in sensor S2 (in MPa).

4.3.3 Geometry evolution

Whereas the mandrel and the dies are axisymmetric, the die shoulder and the conic profile of the die cams ensure the deformation of the tube. Therefore, the tube cross-section has a clover shape at the beginning of the process. The *cloverty* tube shape vanishes continuously until the end of the reduction zone, as the final tube must have a circular section. The clover shape is clearly seen, at the external and internal tube surfaces, in Figs. 4.33-4.35 for the 36th

stroke. A more complex evolution takes place in the first strokes, where the tube is rolled without being reduced by a mandrel-tube-die contact. This shape can contribute to damage because some materials points are in tension (see Fig. 4.8).

Nine marks can be observed on the tube with the model (see Fig. 4.33-4.35). The depth marks depend of the constitutive law used in the numerical simulation. It varies from 5-8µm for the cyclic C/C behavior law to 10-12µm with the isotropic monotonic behavior law. Nine marks were also measured experimentally in the tube partly rolled on an HPTR mill.

Fig. 4.35 shows the internal and the external surfaces radii obtained with the cyclic C/C constitutive law. The *clover-shaped* tube is clearly observed. Both internal and external surfaces oscillate. The thickness is not homogeneous circumferentially and may be locally higher than the initial one (0.99 mm), in agreement with the history of ε_{rr} in Fig. 4.19.

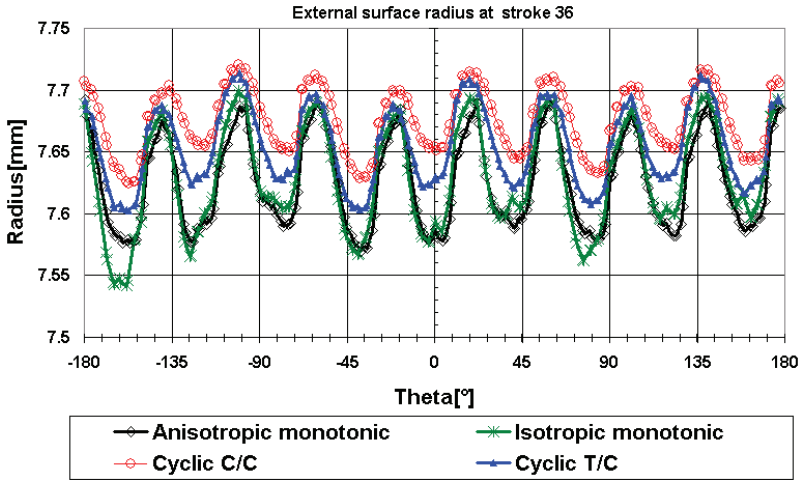

Figure 4.33. External surface radius at stroke 36th.

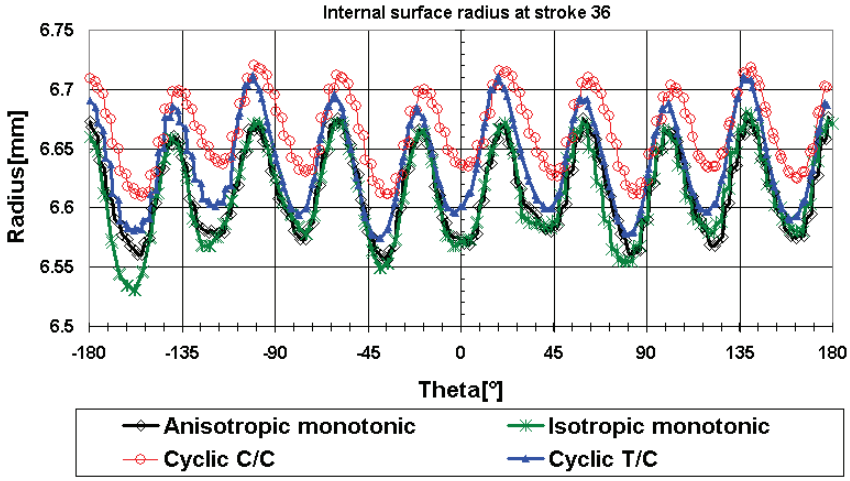

Figure 4.34. External surface radius at stroke 36th.

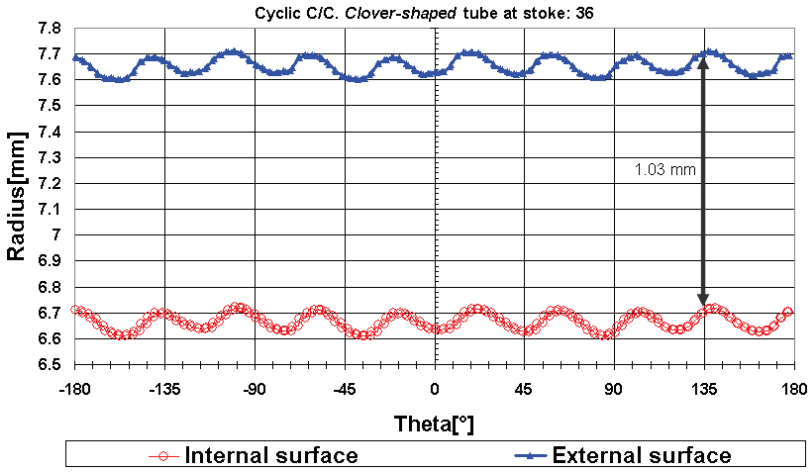

Figure 4.35. External and internal surfaces radius at stroke 36th for the Cyclic C/C constitutive law.

The more the tube advance in the reduction area the more the tube becomes circular. Fig. 4.36 displays the cross-sectional shapes $r(\theta)$ at the 96th stroke. At this moment the tube is in contact with the mandrel, therefore bulges start being compressed. The marks depth varies now from 2 to 3.5µm.

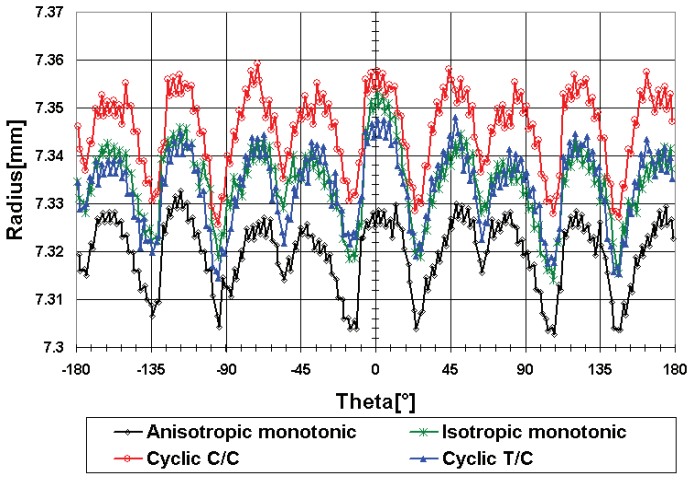

Figure 4.36. External surface radius at stroke 96th.

At the end of the process (120 strokes) the tube is circular for any constitutive law. The marks are still present (their depth varies from 1 to 2µm), but only 3 marks are left instead of 9 (see Fig. 4.37). These 3 marks correspond to the number of side relief zones of the HPTR cold pilgering process (see Fig. 4.38). The side relief at a half-stoke is about 3.2 mm wide.

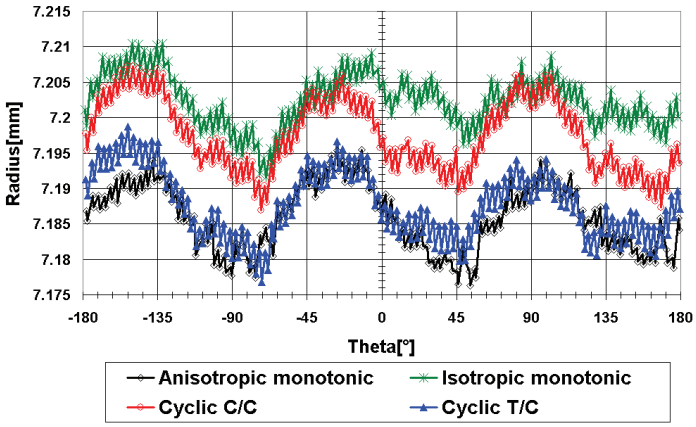

Figure 4.37. External surface radius at stroke 120th.

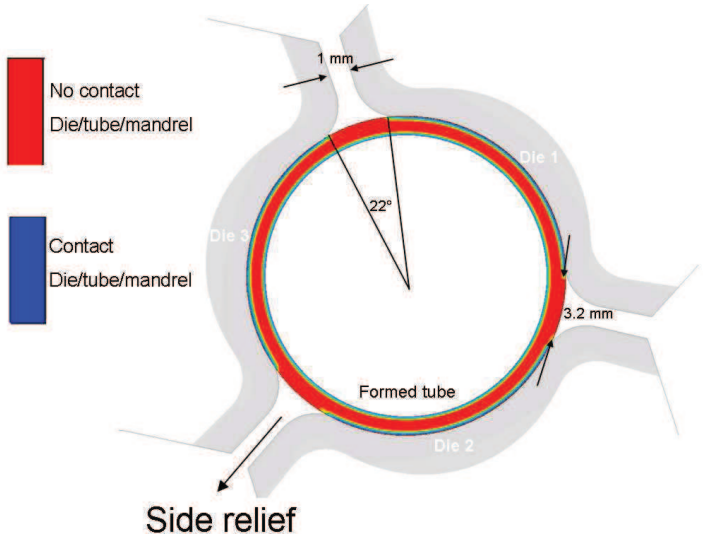

Figure 4.38. Cross-sectional view of the tube and dies at the end of the forward pass of the stroke 120, showing full conformation of the tube inside the three grooves with the three side relief spaces. Note the homogeneous thickness reduction.

Up to now, the mechanical analysis focused on the evolution of stress, strain and damage function undergone by a volume element. In the next section, the mechanical and damage state of the final tube is analyzed.

4.3.4 Formed tube mechanical state

In order to analyze the mechanical conditions of the formed tube over the circumference and also over the thickness, five layers are selected (see Fig. 4.39). These layers do not coincide exactly with the sensor position in order to analyze more accurately what happens at the external and internal surfaces. The eight apparent layers result from a 2D cut of a 3D mesh with 4 parallepipeds in the thickness, each one divided into 5 tetrahedra. The analysis will be done at mi-length of the tube to avoid edge effects.

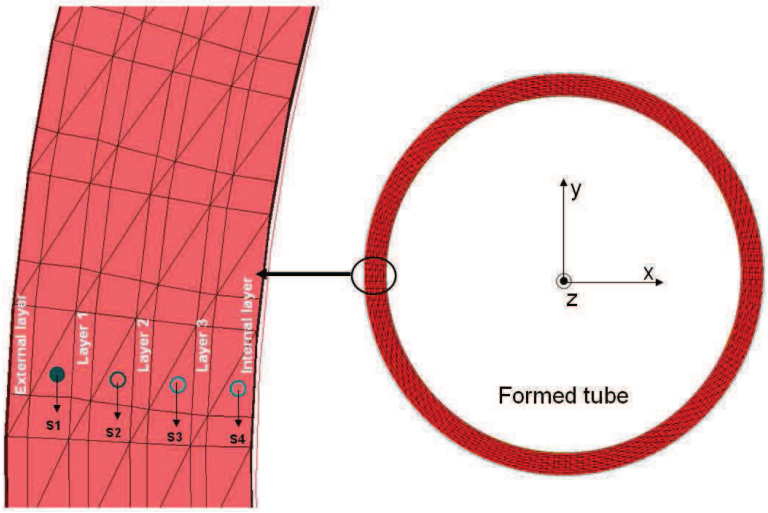

Figure 4.39. Formed tube and selected layers used to analyze the wall thickness and the circumference.

4.3.4.1 Strain

Fig. 4.40 illustrates the influence of side effects (manipulator and free end) on the distribution of accumulated strain and the stabilized state at mid-length. Axial rolling marks with a high accumulated equivalent strain also appear in Fig. 4.40 and are due to the die shoulder which induces non homogeneous deformations in the first strokes. Nevertheless, their intensity varies from one behavior law to another. For example, when comparing cyclic behavior laws, the rolling marks intensity are higher in cyclic C/C than in cyclic T/C. The reason is clear; the material cyclically hardens in the first case whereas it tends to soften in the second case. With the isotropic monotonic law, quasi-homogeneous deformation can be noted (excepted for the borders). In the anisotropic case, rolling marks are visible but with low intensity.

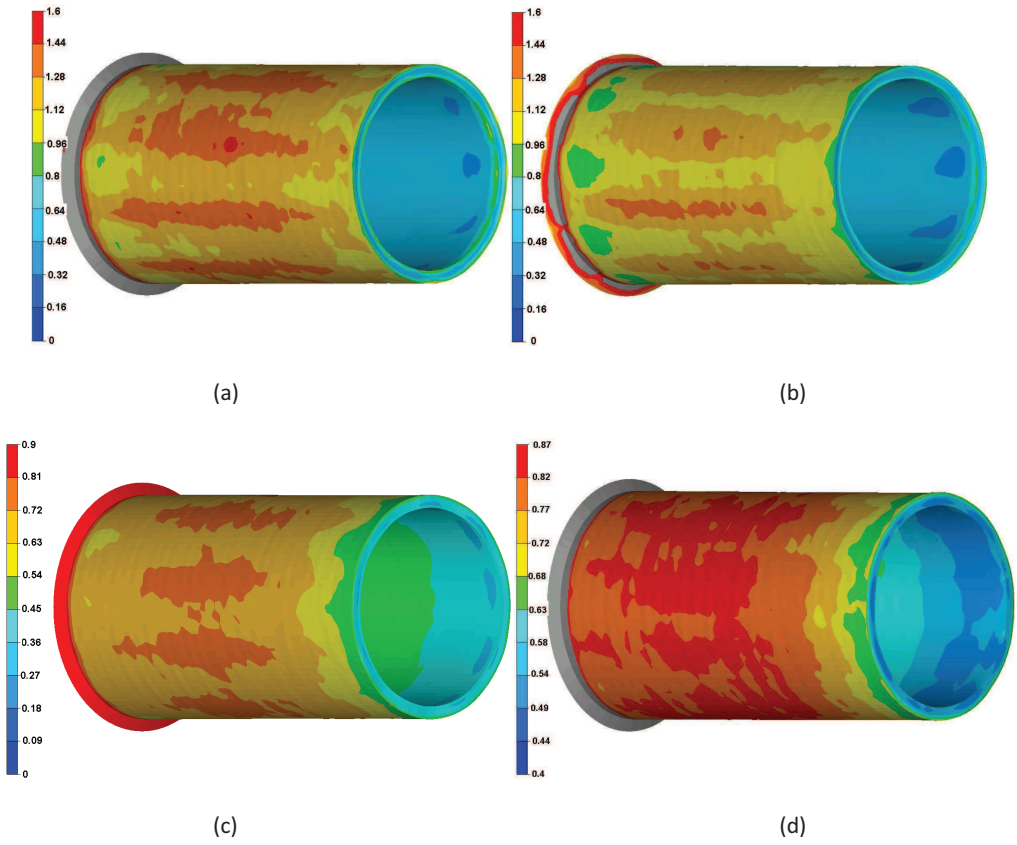

Figure 4.40. Formed tube equivalent strain a) cyclic C/C b) cyclic T/C c) anisotropic monotonic d) isotropic monotonic.

Equivalent strain, at mid-length of the tube, is displayed in Fig. 4.41. The equivalent strain evolves over the wall thickness and is not totally homogeneous in the ortho-radial direction, with a 40° (39°) periodicity. The maximum values are locat ed in the external tube surface.

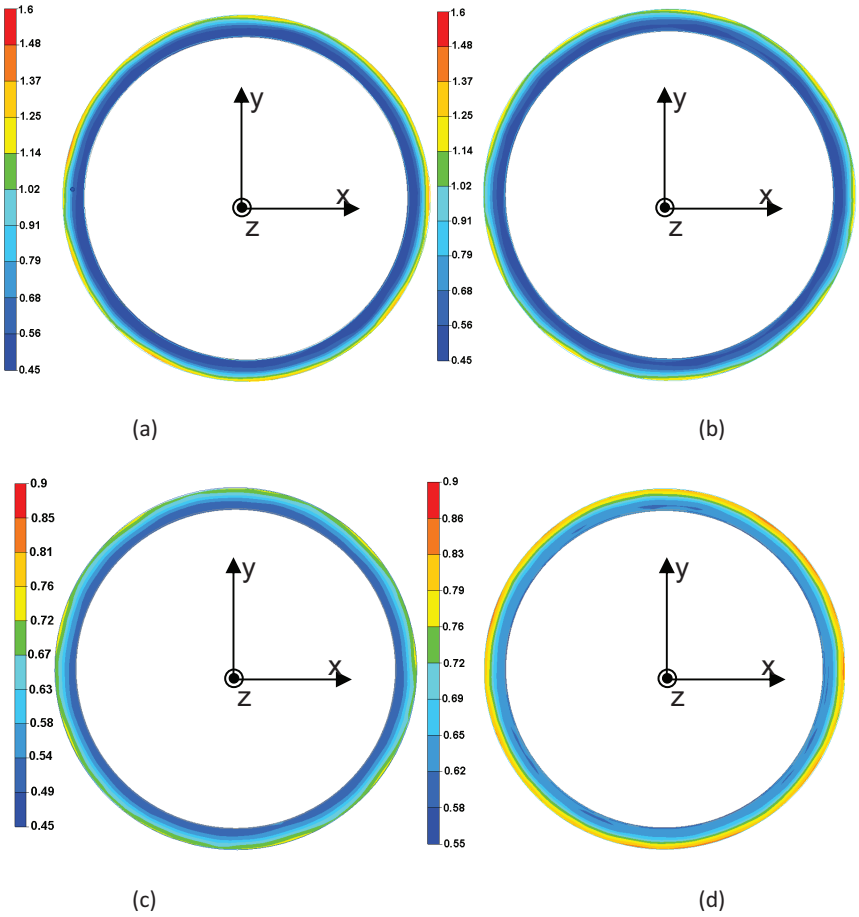

Figure 4.41. Cross-section view of the formed tube equivalent strain a) cyclic C/C b) cyclic T/C c) anisotropic monotonic d) isotropic monotonic

Another view on the strain distribution over the tube wall thickness and along the circumference is given in Figs. 4.42 to 4.45. For the cyclic constitutive laws, Figs. 4.42-4.43, the equivalent strain gradient between the internal and the external tube surface is higher than for both monotonic cases, Figs. 4.44-4.45.

The deformation along the circumference is confirmed to be non homogeneous with cyclic constitutive laws, the external surface exhibits three peaks, corresponding to the side relief zones Fig. 4.37.These peaks are less apparent in the monotonic cases, as already discussed in Fig. 4.40.

It is also pointed out that the strain in the internal layer is equal or even larger, in some cases, than the one in layers 2 and 3. Therefore, the tube “core” has undergone lower deformation than the external and internal surfaces.

The above remarks are not in agreement with the assumptions made in the analytical models proposed in the literature for VMR pilgering (see Chapter 1).

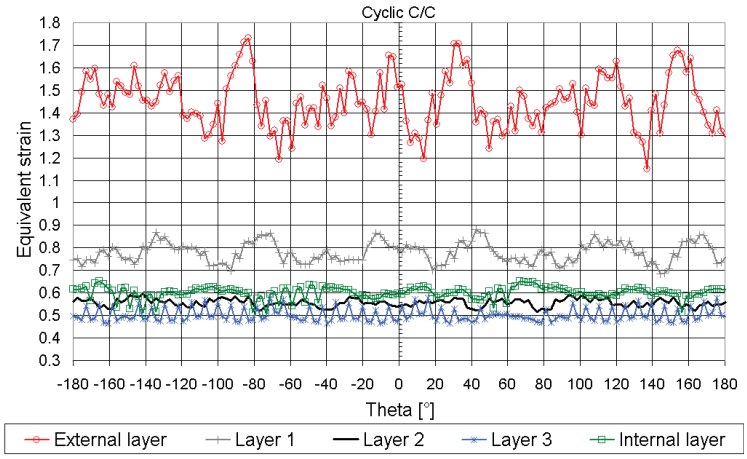

Figure 4.42. Cyclic C/C constitutive law case: circumferential distribution of the equivalent strain in the formed tube.

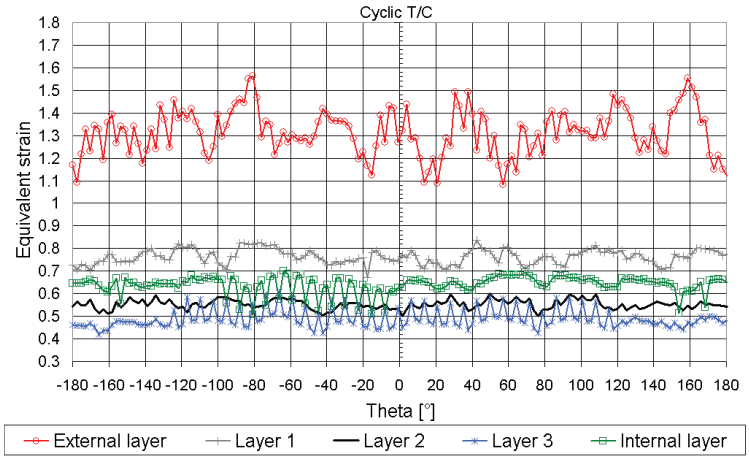

Figure 4.43. Cyclic T/C constitutive law case: circumferential distribution of the equivalent strain in the formed tube.

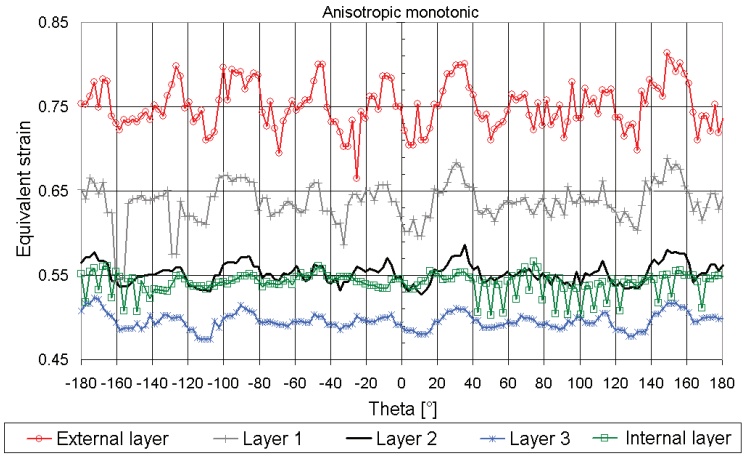

Figure 4.44. Anisotropic monotonic constitutive law case: circumferential distribution of the equivalent strain in the formed tube.

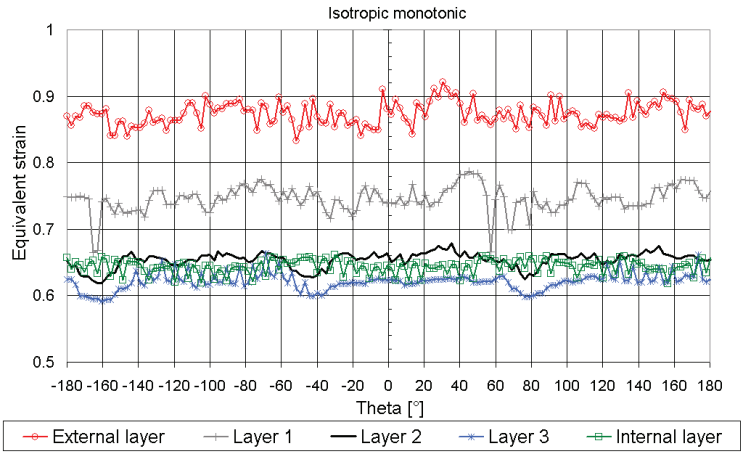

Figure 4.45. Isotropic monotonic constitutive law case: circumferential distribution of the equivalent strain in the formed tube.

4.3.4.2 Damage

Nine marks with higher values of the axial damage function are visible in the formed tube for all the investigated constitutive laws (see Fig. 4.46). For the cyclic C/C behavior law their intensity is much higher than for the cyclic T/C. On the other hand, the isotropic monotonic case leads to higher values than the anisotropic monotonic one where the marks are barely visible. The modified material flow caused by the anisotropic yield function leads to predict lower risks of damage.

It would be interesting to combine the cyclic C/C law with a Hill criterion. Anisotropy would probably reduce the predicted risks of damage.

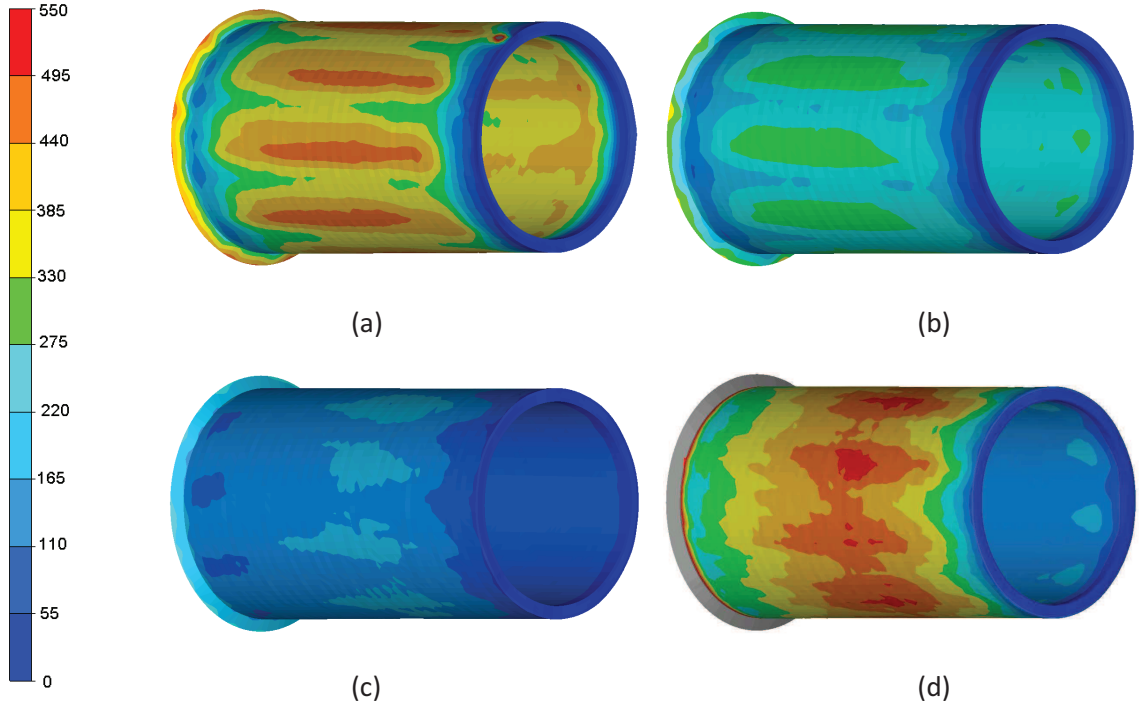

Figure 4.46. Formed tube axial damage function. a) cyclic C/C b) cyclic T/C c) anisotropic monotonic d) isotropic monotonic law.

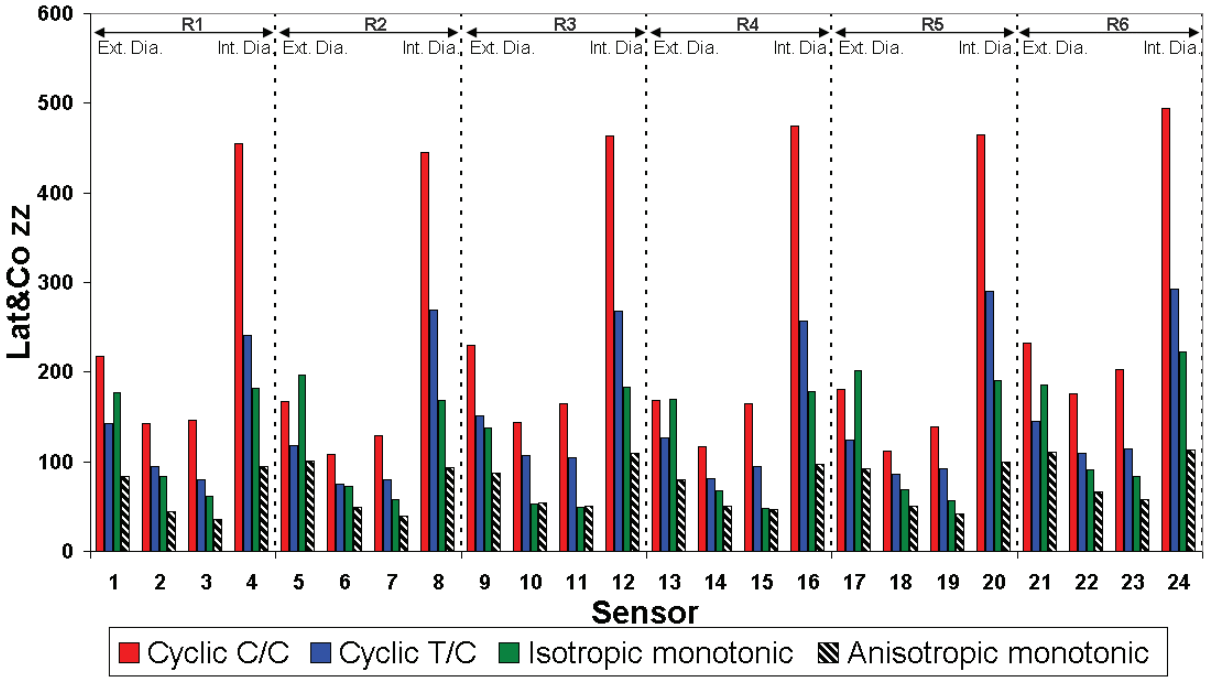

Figure 4.47. Axial damage function in the formed tube (in MPa).

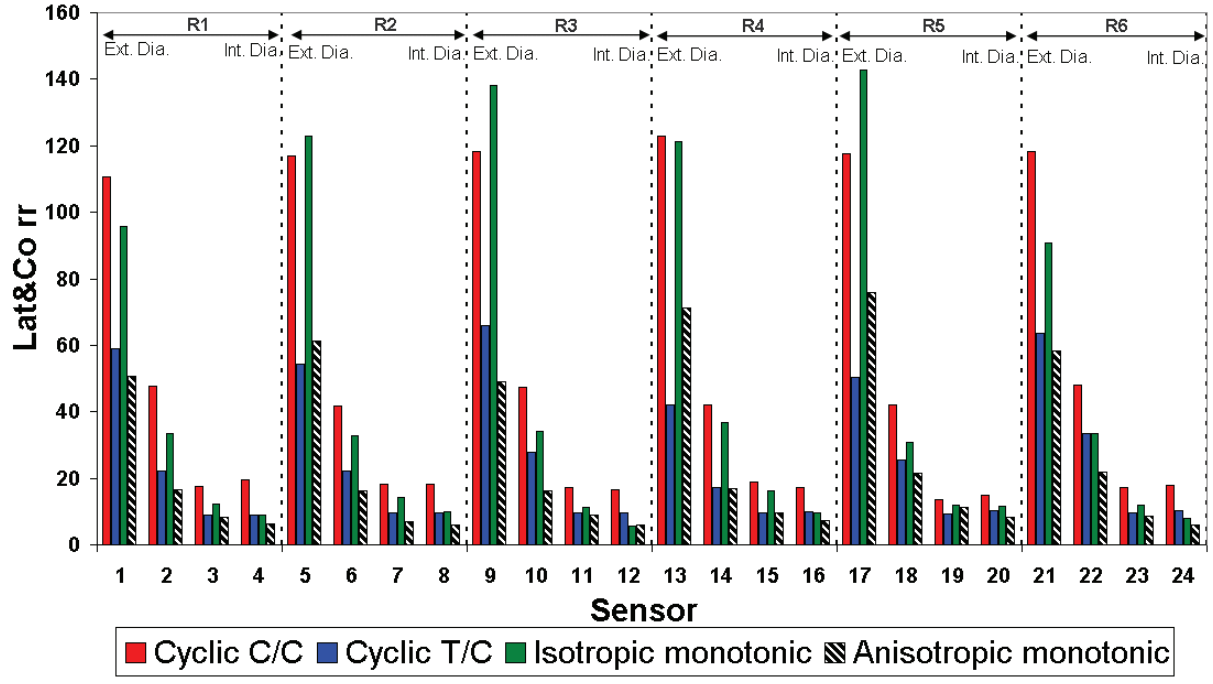

Figure 4.48. Radial damage function in the formed tube (in MPa).

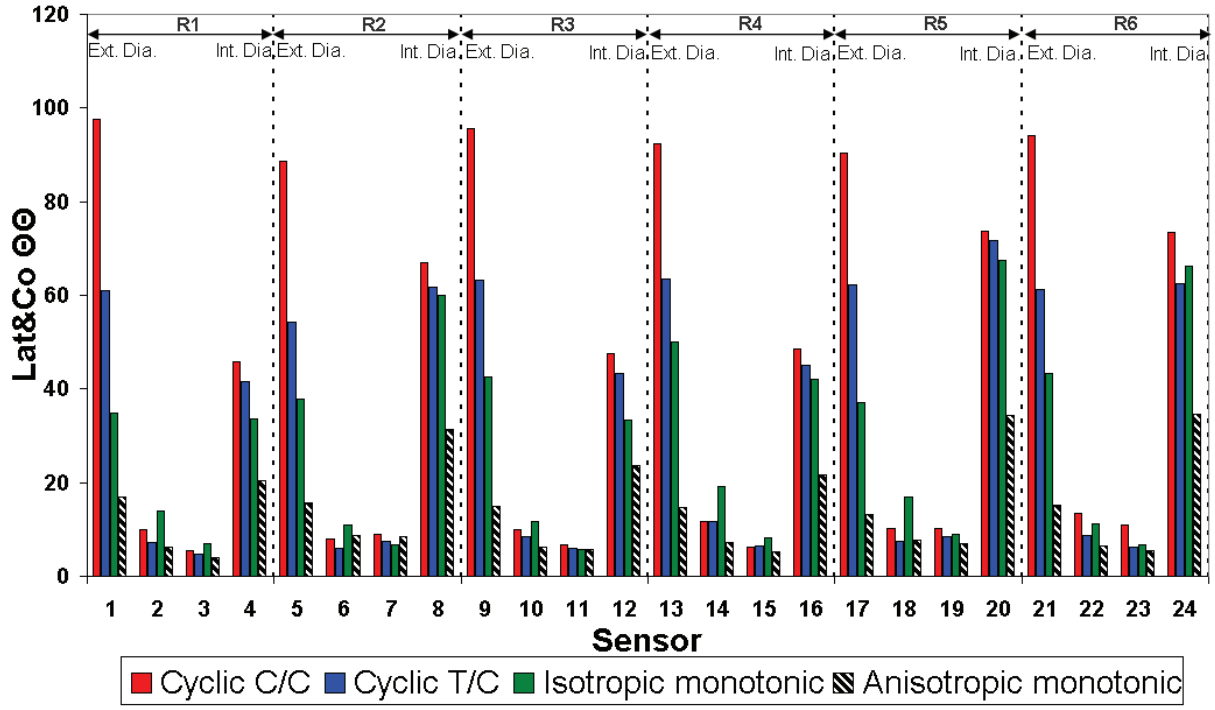

Figure 4.49. Ortho-radial damage function in the formed tube (in MPa).

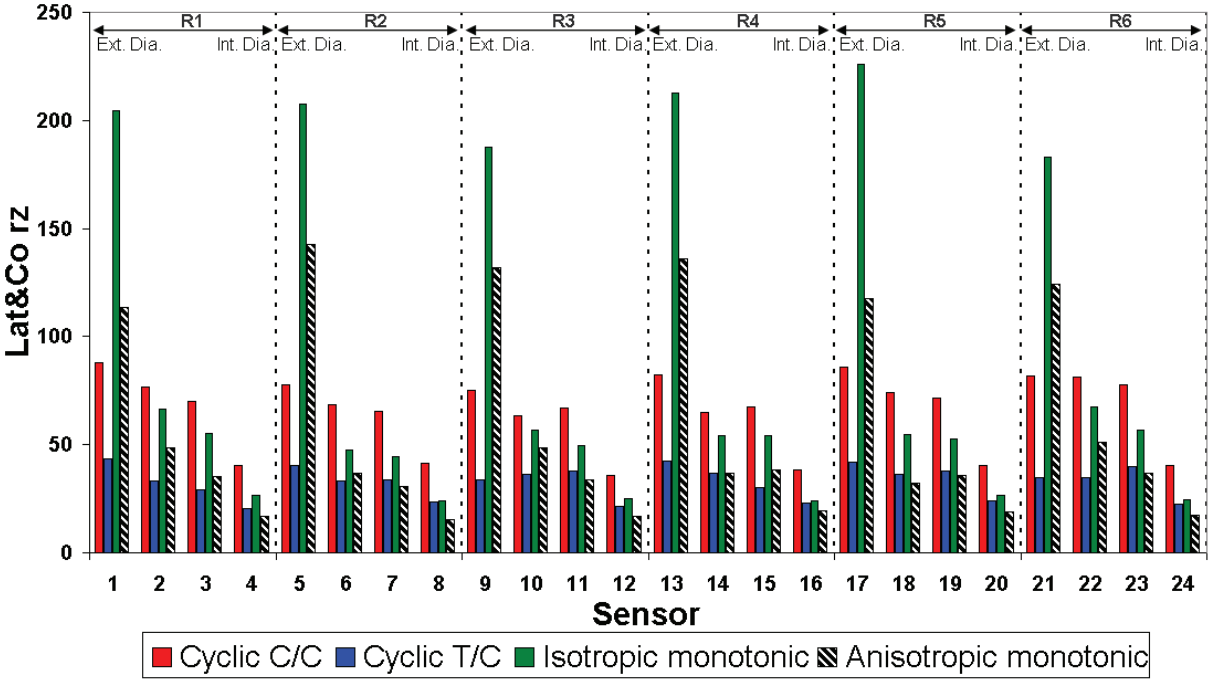

Figure 4.50. Shear damage function in the formed tube (in MPa).

Figs. 4.47-4.50 display the final damage function value at each numerical sensor for each constitutive law studied. The conclusion can be summarized as follows:

- For any sensor and any constitutive law, the maximum damage function value is found in the longitudinal or axial (z) component.

- The maximal longitudinal damage is found at the internal tube surface for any sensor and any constitutive law. Moreover, the longitudinal damage function value is lower in the center (core) of the tube wall thickness.
- For the cyclic C/C constitutive law, damage risks at the internal surface are strongly increased as compared to the other constitutive laws. Voids nucleation could be triggered from longitudinal loading in this case.
- In most cases, damage values obtained with the anisotropic monotonic constitutive law are lower than for the other cases. It can be concluded that the anisotropy due to hot extrusion seems to be beneficial for cracking risks.
- From the above remark, it seems necessary to introduce an anisotropic-cyclic constitutive law in the FEM software in order to have more accurate results.
- Shear damage (rz) is maximal at the external surface of the tube, then it decreases gradually to the internal layer. It can be explained by the die/tube contact conditions.
- Shear damage (rz) is maximal for monotonic constitutive laws in the external surface and much higher in magnitude as compared to the other cases. With the cyclic laws the shear damage (rz) values remain significant as compared to radial and ortho-radial components.
- Ortho-radial damage in the tube thickness core is lower than for the other components. The significant values at the external and internal surfaces are related to the clover tube shape in the deformation zone.
- The trend and conclusions are reproducible from one row of sensors to another one.

4.3.4.3 Residual stress

Residual stresses are generated, following plastic deformation induced by pilgering. The magnitude and distribution of residual stresses after pilgering are analyzed in this section based on data at stroke 139.

Longitudinal residual stress

Fig. 4.51 shows the residual longitudinal stresses after pilgering. Overestimated values given by the isotropic monotonic case are noticed. They are twice as large as than the initial yield stress (960MPa). On the other hand, results obtained with the cyclic C/C behavior law show a residual stress level in the longitudinal direction close to 600 MPa in some regions at mid-length of the tube. This corresponds approximately to a half of the final yield limit (1300 MPa) of the formed tube.

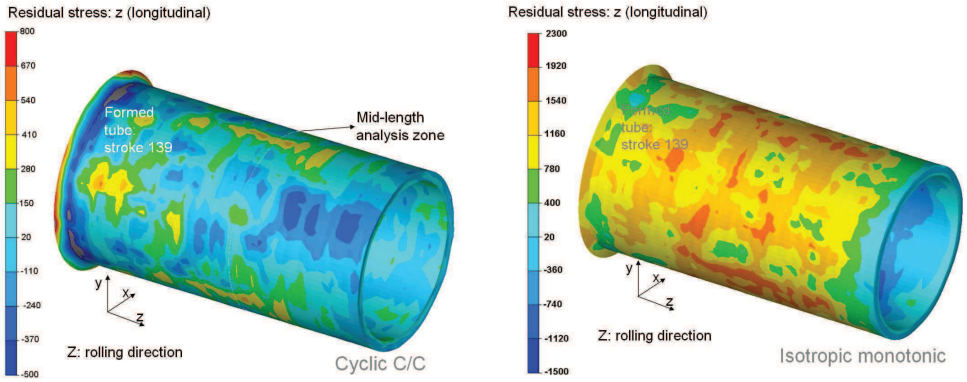

Figure 4.51. Longitudinal residual stress (in MPa) for the cyclic C/C (left) and isotropic monotonic (right) constitutive laws in the formed tube at stroke: 139.

A high compressive state in the inner layer of the tube is observed in three regions in Fig. 4.52, at about 120° from each other. Likewise, there are three regions exhibiting tensile states, also with a three-fold symmetry. This periodicity corresponds to the number of bottom groove and side relief zones.

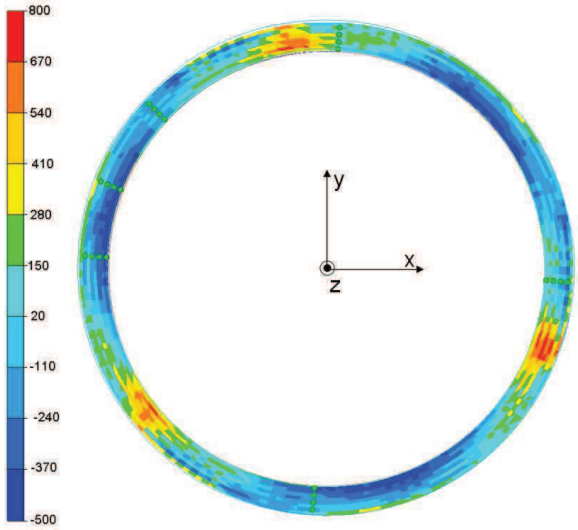

Figure 4.52. Cyclic C/C constitutive law: residual longitudinal stress (in MPa).

Fig. 4.53 shows the residual longitudinal stresses along the circumference using the cyclic C/C law. The larger values for both tensile and compression states are located in the inner layer. Moreover, tensile values are larger than compressive ones.

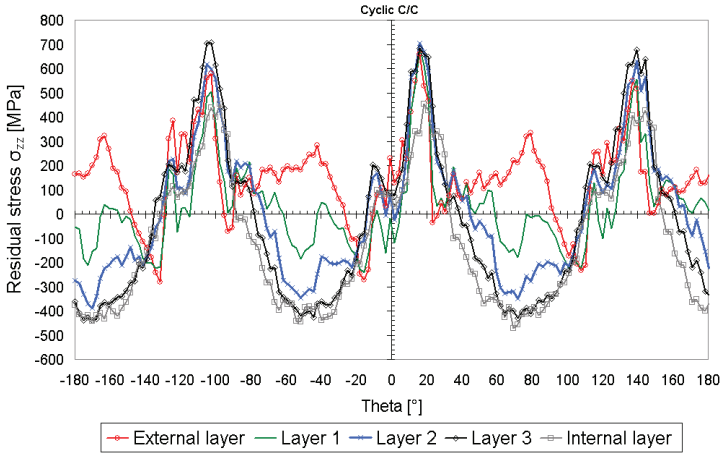

Figure 4.53. Cyclic C/C constitutive law: residual longitudinal stress along the circumference (in MPa).

Ortho-radial residual stress

Fig. 4.54 shows the residual ortho-radial stresses after pilgering. Similar patterns as for longitudinal stresses are noted. However, residual stresses magnitudes are slightly lower.

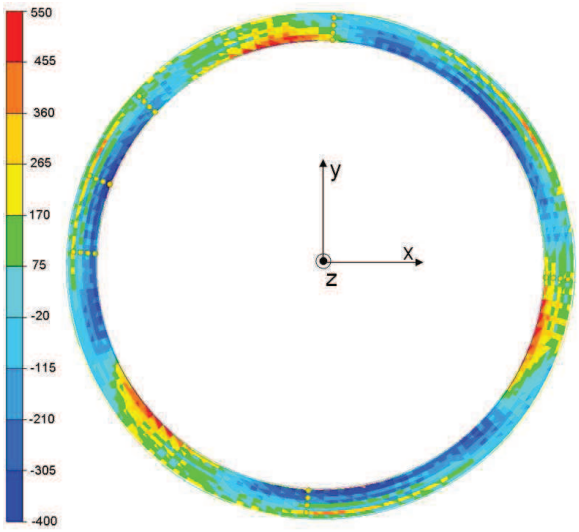

Figure 4.54. Cyclic C/C constitutive law: residual ortho-radial stress (in MPa).

Another view of the residual ortho-radial stresses along the circumference is given in Fig. 4.55. The larger values for both tensile and compression states are again located at the inner layer. Tensile values are again larger than compressive ones.

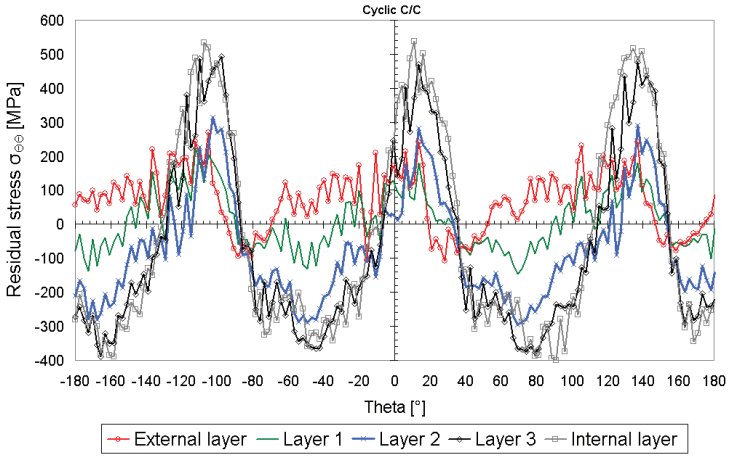

Figure 4.55. Cyclic C/C constitutive law: residual ortho-radial stress along the circumference (in MPa).

Radial residual stress

Fig. 4.56 shows the residual radial stresses after pilgering. A more random distribution is observed when comparing the previous cases. Lower magnitudes for the tensile states are also pointed out. Typical values range around 125 MPa.

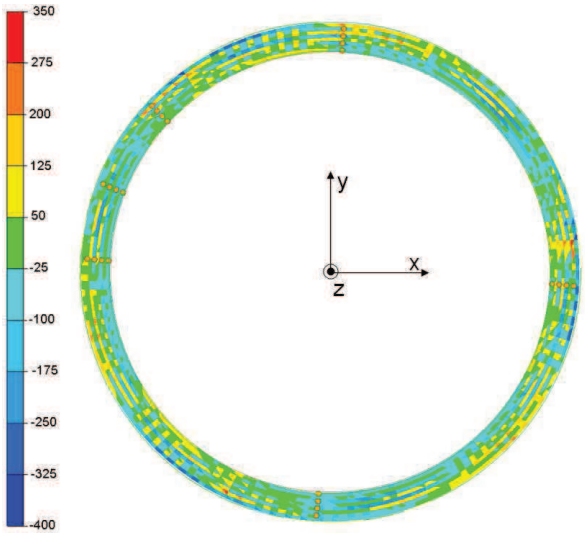

Figure 4.56. Cyclic C/C constitutive law: residual radial stress (in MPa).

Fig. 4.57 shows that excepted for the external surface, the residual radial stresses are more homogeneous than in the previous cases. The magnitudes remains lower, around 1/5 of the final yield limit (1300 MPa).

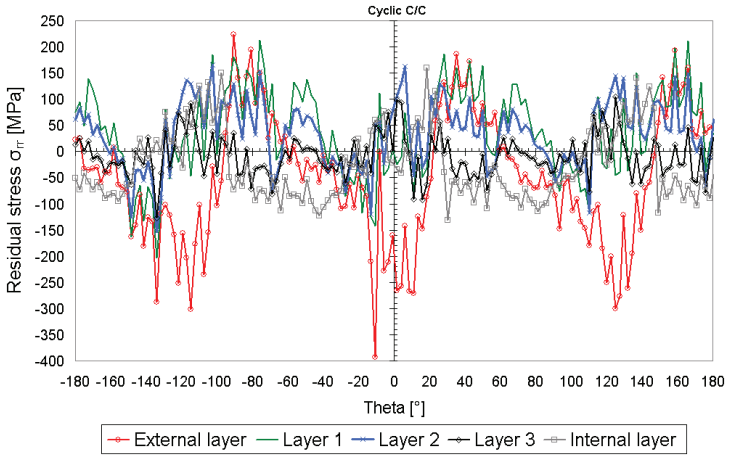

Figure 4.57. Cyclic C/C constitutive law: residual radial stress along the circumference (in MPa).

Shear residual stress

Fig. 4.58 shows the residual shear (rz) stresses along the circumference. The internal layer shear stress has a sign opposite to that of the other layers.

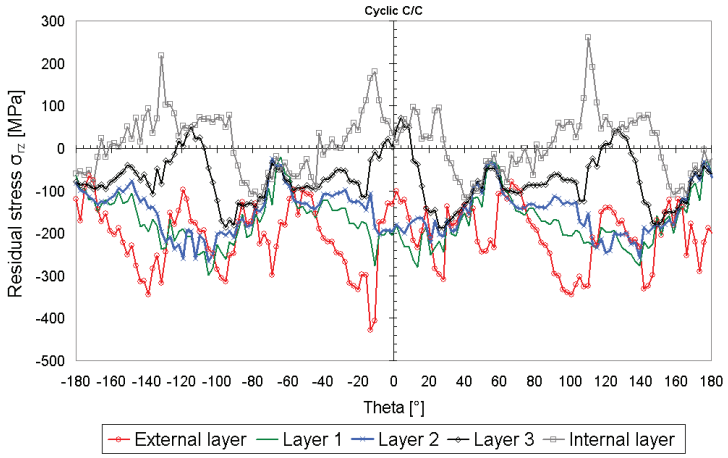

Figure 4.58. Cyclic C/C constitutive law: residual shear stress along the circumference (in MPa).

4.3.4.4 Cracks origin possible explanation

The damage criterion used in this work revealed maximum values, along the longitudinal direction, in the inner region of the formed tube. Therefore, voids nucleation could be formed there during the process. Additionally, the residual stress analysis shows three zones of tensile residual stresses regions in both longitudinal and ortho-radial directions.

In general, tensile residual stresses tend to open crack and promote cracks propagation. Experimental data indicates a tendency for crack opening in the axial direction (see Fig. 4.59), hence under the influence of orthoradial loading ($\sigma_{\theta\theta}$). Predicted magnitudes of residual stresses are similar in the θ and z directions, however one has to keep in mind that alignment of second

phase particles in the axial direction lead to anisotropic toughness of ODS steels, with the weakest value corresponding to a circumferential stress.

This analysis during pilgering enables to conclude on the probable fracture areas. The ferritic ODS tube crack could initiate during rolling close to the inner surface, and then the propagation could be driven by the residual stresses in the orthoradial direction. A fracture area analysis is necessary to validate this scenario.

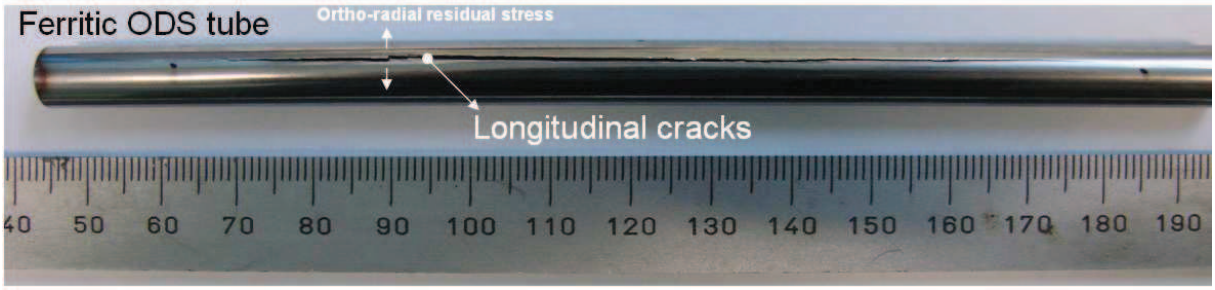

Figure 4.59. Longitudinal cracks after pilgering.

4.4 Conclusion

In this Chapter; a deep analysis of the HPTR pilgering process has been achieved. The aim was to:

- Assess the impact of the constitutive law choice on the prediction of the mechanical history undergone by a material point during the process,
- Analyze the mechanical state of the HPTR pilgered tube,
- Identify the most damaged regions of the tube and the possible origin of cracks,
- Analyze damage evolution during pilgering.

Accurate modeling of the material constitutive behavior is one of the most important features needed in order to simulate the process properly. Full numerical simulations considering the monotonic, anisotropic and cyclic constitutive behavior of ODS steels (identified in Chapter 3) were carried out.

It was shown in this study that monotonic constitutive laws lead to non physical stress values during pilgering. The formalism fails because cold pilgering involves a sequence of small strain increments. For this type of loading, kinematic hardening cannot be neglected and must be introduced in the numerical model. Thus, a simple Chaboche-type constitutive model is preferred.

It was found that the cyclic C/C constitutive law, identified with a specific compression/compression procedure, leads to better results in terms of stresses than a cyclic T/C constitutive law, identified with a classical tension/compression test. Measurements performed before and after pilgering have shown that the ferritic ODS tube undergoes hardening.

Experimental and “cyclic C/C predicted” stress results are in good agreement. Therefore, the compression-compression procedure based on the similarities with the loading path induced by pilgering seems to be quite accurate to represent the ODS steels hardening.

A systematic analysis of all strokes has helped defining which stroke could contribute mainly to the oligocyclic fatigue of the material. A modified Latham and Cockroft damage function has been computed from positive strains and stresses. The damage accumulation is done only if stroke triaxiality is higher than -1/3. With the current FEM meshes and the cyclic C/C constitutive law, it was possible to predicted that voids nucleation should originate in the internal surfaces of the tubes.

The study of the residual stress state of the formed tube led to reporting high longitudinal and ortho-radial tensile stresses in the internal surface of the tube. Thus, the experimental longitudinal cracks observed on ferritic ODS tubes could be explained by the fact that some voids are nucleated during rolling and that the ortho-radial residual stresses can promote crack propagation.

For all considered constitutive laws in this Chapter and the rolling *pass 3* the wall thickness center is the region with lowest plastic strain and damage function intensity.

The friction coefficient was taken from literature in the case of VMR pilgered Zyrcaloy tubes. The shear damage (rz) function remains high and not negligible when simulating HPTR process. Therefore, the friction coefficient should be identified more accurately.

The anisotropic constitutive law used in this Chapter supposed that shear Hill’s model parameters were those in an isotropic case. Other solutions could be tested. One important conclusion seems to be that anisotropy inherited from extrusion is favorable, i.e. it decreases cracking risks. Identification of the quadratic Hill model parameters from tubes instead of bars to confirm these conclusions. However, cylindrical sample upsetting is not appropriate when using tubes. Polycrystalline models (e.g. see [Lebensohn and Tomé 1993]) could be use to compute Hill’s anisotropic parameters through tube texture measurement. Moreover, taking into account the anisotropy in the cyclic C/C case could improve the numerical results and damage prediction.

The results are encouraging but more experimental data, e.g. pilgered marks depth, partially rolled tube hardness evolution, residual stresses, shear strains, longitudinal cracks analysis, dies forces, mandrel forces, are necessary to assess the accuracy of the current calculations and conclusions.

The current work focused on the mechanical analysis of a laboratory pilgering mill, HPTR. However, in the context of the Stratotube project, a parallel numerical study was performed for the VMR cold pilgering process. This study was partially based on the work described in this document and some numerical code improvements were also carried out in order to simulate properly this particular process. The reader can refer to [Veysset 2011] for more details of this work. The numerical VMR model predicts the pilgering helix observed in the industrial VMR mill

(see Fig. 4.60). In addition, the so called pilgering waves were also predicted. This phenomenon was observed experimentally: several inserts positioned initially at the same z position were no more aligned after pilgering, i.e. z positions were different (see Fig. 4.60 and Fig. 4.61). These two mechanical phenomena observed in the real pilgered tube are not observed in the case of HPTR pilgered tubes. This study pointed out the difference in strain path between HPTR and VMR pilgering.

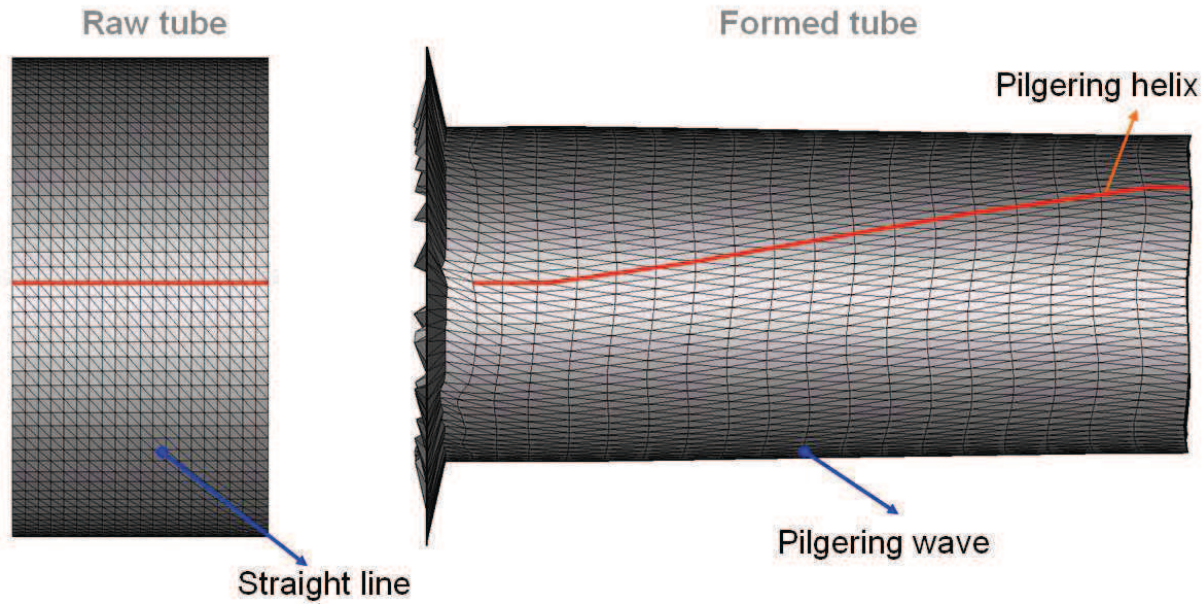

Figure 4.60. The pilgering helix (in red) and pilgering wave observed in the VMR pilgering numerical model.

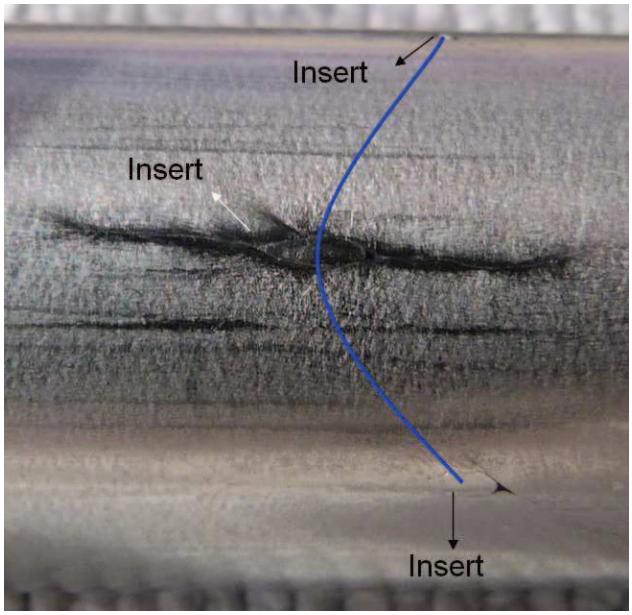

Figure 4.61. Final shape and locations of three inserts placed originally in the same cross-section. After VMR pilgering they are placed at different Z positions.

4.5 Résumé en français

Dans ce Chapitre, une analyse détaillée du procédé de laminage HPTR a été réalisée. L'objectif était de:

• Évaluer l'impact du choix de la loi de comportement sur la prédiction de l'histoire mécanique subie par un point matériel au cours du procédé,
• Analyser l'état mécanique du tube après un passe de laminage à pas de pèlerin,
• Identifier les régions les plus endommagées du tube et la possible origine des fissures,
• Analyser l'évolution des dommages lors du laminage.

Une modélisation précise du comportement du matériau est l'une des caractéristiques les plus importantes et nécessaires afin de simuler la mise en forme correctement. Des simulations numériques complètes en prenant en compte le comportement monotone, anisotrope et cyclique des aciers ODS (identifiés dans le chapitre 3) ont été réalisées.

Dans cette étude il a été démontré que la loi de comportement isotrope monotone mène à des valeurs de contraintes non physiques au cours du laminage. Le formalisme échoue car le laminage à froid implique une séquence de petites déformations incrémentales. Pour ce type de chargement, l'écrouissage cinématique ne peut pas être négligé et doit être introduit dans le modèle numérique. Ainsi, un simple modèle de comportement de type Chaboche est préférable.

On a constaté que le modèle de comportement cyclique, basé sur les essais de compression alternée de cubes (cyclique C/C), conduit à de meilleurs résultats en termes de contraintes que le modèle de comportement cyclique basé sur les essais de traction/compression (cyclique T/C). Les mesures effectuées avant et après laminage ont montré que le tube ferritique ODS subit un durcissement. Les valeurs de contrainte expérimentales et numériques "cyclique C/C" sont en bon accord. Par conséquent, l'essai de compression-compression basé sur les similitudes avec le chemin de chargement induit par laminage semble être assez précis pour représenter le durcissement des aciers ODS.

Une analyse systématique de tous les coups de cage a permis de définir les situations qui pourraient contribuer principalement à la fatigue oligocyclique du matériau. Le critère de Latham et Cockroft modifié a été calculé à partir de déformations positives et leurs contraintes. L'accumulation des dommages se fait seulement si la triaxialité est supérieure à -1/3. Avec le maillage utilisé et le comportement cycliques C/C, il a été possible de prévoir que la germination de porosités devrait se créer dans la surface interne des tubes. L'étude de l'état de contrainte résiduelle du tube formé conduit à des valeurs de contraintes de traction longitudinales et des contraintes de traction ortho-radiales dans la surface interne du tube. Ainsi, les fissures longitudinales expérimentales observées sur des tubes ODS ferritiques pourraient s'expliquer par le fait qu'un endommagement initial soit apparu pendant le laminage, et que les contraintes résiduelles ortho-radiales aient ensuite conduit à la propagation des fissures.

Chapter 5

Conclusions and outlooks

This thesis aimed at providing a better understanding of deformation paths which may lead to crack growth in ODS tubes HPTR pilgering. To reach such goal three main steps were undertaken:

i) Creating a robust and reliable finite element model of pilgering.

ii) Characterization of the mechanical behavior of ODS steels under monotonic and cyclic loadings.

iii) Sensitivity analysis of the different constitutive laws on the deformation path undergone by a volume element.

The present study has demonstrated the feasibility of detailed FEM mechanical analysis of the HPTR cold pilgering of tubes. Complete simulations of HPTR pilgering have been presented using a *short tube* approach. The length reduction allowed saving considerable CPU time and permitted to simulate all strokes. The main results have shown that the formed tube has non-homogenous strain in the radial, circumferential and axial directions. A complex mechanical history undergone by a material point has been detailed. A sensitivity analysis on the mesh sizes, time step, type of mesh and length of the tube was performed in order to assess the accuracy of the calculations. Bases on this analysis, an HPTR pilgering model was proposed which gives a good compromise between CPU cost and accuracy.

A comparison between predicted and measured pilgered steady state tube geometry as well as the experimental evaluation of plastic longitudinal strains due to cold pilgering allowed validating the dies kinematics.

A detailed mechanical analysis of the process requires a realistic constitutive law. ODS steels are considered in this study and a detailed study of their mechanical behavior was carried out :

Since ODS tubes reveal mechanical anisotropy, compression and shear tests of cylindrical specimens cut in three different directions (longitudinal, radial and ortho-radial) were performed. Hill's quadratic plastic anisotropy criterion was selected to account for the observed anisotropy. A set of Hill's parameter was identified based on the ovalization shapes of cross sections after compression, with the option of considering yield stress in shear tests. Furthermore, a Hill's parameter calculation enhancement was performed using an inverse analysis method, which led to an improvement of the correlation between experimental and numerical results.

The strain-controlled cyclic characteristics of ODS steels were analyzed and modeled, using two different tests. The first test is a classical tension-compression test. The second test consists in alternated uniaxial compressions along two perpendicular axes. It has been developed based on the similarities with the loading path induced by the pilgering process. The cyclic behavior of ODS steels was modeled using an elastic-plastic model developed by Chaboche. This model was implemented in a FEM code. The constitutive model involves only 10 parameters and nevertheless successfully describes the experimental trends. The model

parameters were identified with a semi automated identification process involving an inverse analysis method, and considering loading sequences compatible with those which can be encountered in cold pilgering conditions. Experimental and predicted results are in good agreement, but a single set of model parameters could not be identified for both tests. This is mainly attributed to the difference in transient behavior observed in the two tests, when strain amplitudes change. The set of parameters identified with the compression/compression procedure leads to much more accurate results in terms of stresses than those identified from the classical tension/compression test.

It was shown in this study that monotonic constitutive laws lead to non physical stress values during pilgering.

A systematic analysis of all strokes has helped defining which stroke could contribute mainly to the oligocyclic fatigue of the material. A modified Latham and Cockroft damage function has been computed considering only the contribution of positive strains and stresses, and when the stress triaxiality is higher than -1/3. With the current FEM meshes and the cyclic (compression/compression) constitutive law, it was possible to predict that damage is likely to initiate in the internal surfaces of the tubes. The predicted residual stress state of the formed tube results in high longitudinal and ortho-radial tensile stresses in the internal surface of the tube. Therefore, the experimental longitudinal cracks observed in ferritic ODS tubes could be explained by damage initiation during rolling and subsequent crack growth after forming, assisted by the ortho-radial residual stresses, and considering the anisotropic toughness of the material.

More experimental data is needed to validate the proposed model, e.g. longitudinal cracks analysis, dies forces, mandrel forces, pilgered marks depth, partially rolled tube hardness evolution, residual stresses, shear strains, friction characterization. Nonetheless, the present HPTR numerical model has already proved enough accuracy to be considered for numerical optimization, looking at quantities such as tools kinematics dies profile, lubricant, feed, rotation angle and Q factor, etc. Optimization objectives may be related to cracking risks (which was the main focus in this work), but also to intermediate heat treatments. Indeed, maximum hardness values have been identified, and these may be correlated to the calculated evolution of the material yield strength in the process. The possibility to trigger recrystallization during the heat treatment is linked to the material hardness, but also to the strain path undergone by a volume element, since it dictates the final crystallographic texture. Since heterogeneous textures are favorable for triggering recrystallization, one interesting outcome of this study could be a proposed fabrication route where the strain path changes from one pass to another. This would effectively reduce the recrystallizing temperature. Calculated textures from the predicted strain paths, using polycrystalline models, could therefore be part of the optimization program.

Future work should definitely include a numerical simulation of ODS tubes cold pilgering using the Chaboche cyclic constitutive law combined with the Hill's anisotropic criterion. Indeed, both the cyclic nature of the loading and the material anisotropy have been shown to significantly influence the mechanical history undergone by a material point during the process.

The proposed test considering alternated uniaxial compressions along two perpendicular axes, and the associated semi-automatic identification methodology, could be applied to other ODS steels with different microstructures, e.g. recrystallized ferritic ODS steels with equiaxed grains or martensitic ODS steels with isotropic crystallographic and morphological textures. This would then lead to an overall optimization of fabrication routes, considering both the forming parameters, and the material choice.

More elaborated constitutive models could be explored in the future, in order to reach a unique model accounting for both tension-compression, and compression-compression tests. A memory effect could be introduced to take into account the influence of the plastic strain range on the amount of cyclic hardening. The effect of the degree of non-proportionality of the loading path could also be studied in more details. Interesting bibliography references have been already identified on that subject.

More complex tools kinematics could be studied in the future, by which the tube may be advanced and rotated not only before the forward stroke, but also between the forward and the backward stroke.

The modified Latham and Cockroft damage function delivers qualitative results. A non-linear damage model for ductile fracture based on the continuum damage mechanics formulation could be introduced in the model, and associated to the Chaboche cyclic constitutive law. However two limitations of such an approach should be kept in mind:

- the directional spatial distribution of second phase particles in the investigated ODS steels would call for an anisotropic damage law, which significantly increases the complexity of the model [Lemaître *et al.*, 1999], [Benzerga *et al.*, 2004a], [Benzerga *et al.*, 2004b];
- ductile fracture in ODS steels is not yet confirmed when deformation is at room temperature, with large strain rates. Toughness might be a more appropriate property to consider.

Finally, this thesis focused mainly on the laboratory HPTR mill available at CEA/Saclay. The proposed constitutive law identified from alternated compressions, as well as the modified Latham & Cockroft damage function, could be used as well when modeling the industrial VMR mill, and lead to an optimization with objectives similar to those described for the HPTR process.

Bibliography

[Abdel-Karim 2010a**]** : M. Abdel-Karim, *An extension for the Ohno-Wang kinematic hardening rules to incorporate isotropic hardening*, International Journal of Pressure Vessels and Piping 87, pp.170 - 176, 2010a.

[Abdel-Karim 2010b**]** : M. Abdel-Karim, *An evaluation for several kinematic hardening rules on prediction of multiaxial stress-controlled ratchetting*, International Journal of Plasticity 26, pp.711 - 730, 2010b.

[Abdel-Karim 2009**]** : M. Abdel-Karim, *Modified kinematic hardening rules for simulations of ratchetting*, International Journal of Plasticity 25, pp.1560 - 1587, 2009.

[Abdul-Latif 1996**]** : A. Abdul-Latif, *Constitutive equations for cyclic plasticity of Waspaloy*, International Journal of Plasticity 12, pp.967 - 985, 1996.

[Abdul-Latif and Saanouni 1996**]** : A. Abdul-Latif, K. Saanouni, *Micromechanical modeling of low cycle fatigue under complex loadings - Part II. Applications*, International Journal of Plasticity 12, pp.1123 - 1149, 1996.

[Abe *et al.,* 1993**]** : H. Abe, K. Matsuda, T. Hama, T. Konishi, M. Furugen, *Fabrication process of high nodular corrosion resistant Zircaloy-2 tubing*, Tenth International Symposium of Zirconium A.S.T.M Baltimore 1245, pp. 285 - 306, 1993.

[Alamo *et al.,* 2004**]** : A. Alamo, V. Lambard, X. Averty, M. Mathon, *Assessment of ODS-14%Cr ferritic alloy for high temperature applications*, Journal of Nuclear Materials 329-333, Part A, pp.333 - 337, 2004.

[Alamo *et al.,* 2007**]** : A. Alamo, J. Bertin, V. Shamardin, P. Wident, *Mechanical properties of 9Cr martensitic steels and ODS-FeCr alloys after neutron irradiation at 325℃ up to 42dpa* , Journal of Nuclear Materials 367-370, Part A, pp.54 - 59, 2007.

[Aliaga 2000**]** : C. Aliaga, *Simulation numérique par éléments finis en 3D du comportement thermomécanique au cours du traitement thermique d'aciers : application à la trempe de pièces forgées ou coulées*, **PhD report**, MinesParistech, France, 2000. In french.

[Armstrong 1982**]** : P. Armstrong, *Large strain multidirectional deformation of 1100 aluminum at 300 K*, Journal of Mechanics Physics of Solids 30, pp.37 - 58, 1982.

[Armstrong and Frederick 1966**]** : P. Armstrong, C. Frederick, *A mathematical representation of the multiaxial bauschinger effect*, CEGB Report No. RD/B/N 731, Berkeley Nuclear Laboratories , pp.Berkeley, UK., 1966.

[Aubin *et al.,* 1994**]** : J.-L. Aubin, E. Girard, P. Montmitonnet, *Modeling of damage in cold pilgering*, in: A.M. Garde, E. Bradley (Eds.), Zirconium in the Nuclear Industry, ASTM STP 1245, ASTM, Philadelphia, 1994.

[Aubin *et al.,* 2000**]** : J.-L. Aubin, P. Montmitonnet, S. Mulot, *Zirconium alloy cold pilgering process control by modeling*, in: Proceedings of the Conference on Zirconium in the Nuclear Industry, Toronto, Canada, 1999, ASTM STP 1354, ASTM, West Conshohocken, USA, 2000.

[Aubin 2001**]** : V. Aubin, *Plasticité cyclique d'un acier inoxydable austeno-ferritique sous le chargement biaxial nonproportionnel*, **PhD report**, Ecole Centrale de Lille, France, 2001. In french.

[Aubin *et al.,* 2003a**]** : V. Aubin, P. Quaegebeur, S. Degallaix, *Cyclic behaviour of a duplex stainless steel under multiaxial loading: Experiments and modelling*. Andrea Carpinteri, M. d. F. and Spagnoli, A., eds. Biaxial/Multiaxial Fatigue and Fracture 6th International Conference on Biaxial/Multiaxial Fatigue and Fracture, Elsevier, 401 – 422, 2003a.

[Aubin *et al.,* 2003b**]** : V. Aubin, P. Quaegebeur, S. Degallaix, *Cyclic plasticity of a duplex stainless steel under non-proportional loading*, Materials Science and Engineering: A 346, pp.208 - 215, 2003b.

[Babuska 1973**]** : I. Babuska, *The finite element method with penalty,* Mathematics of computation 27, pp.221-228, 1973.

[Baluc *et al.,* 2011**]** : N. Baluc, J. Boutard, S. Dudarev, M. Rieth, J.B. Correia, B. Fournier, J. Henry, F. Legendre, T. Leguey, M. Lewandowska, R. Lindau, E. Marquis, A. Muñoz, B. Radiguet, Z. Oksiuta, *Review on the EFDA work programme on nano-structured ODS RAF steels*, Journal of Nuclear Materials 417, pp.149 - 153, 2011.

[Banabic *et al.,* 2003**]** : D. Banabic, T. Kuwabara, T. Balan, D. Comsa, D. Julean, *Non-quadratic yield criterion for orthotropic sheet metals under plane-stress conditions*, International Journal of Mechanical Sciences 45, pp.797 - 811, 2003.

[Bao and Wierzbicki 2004**]** : Y. Bao, T. Wierzbicki, *On fracture locus in the equivalent strain and stress triaxiality space*, International Journal of Mechanical Sciences 46, pp.81 - 98, 2004.

[Bari and Hassan 2000**]** : S. Bari, T. Hassan, *Anatomy of coupled constitutive models for ratcheting simulation*, International Journal of Plasticity 16, pp.381 - 409, 2000.

[Bari and Hassan 2001**]** : S. Bari, T. Hassan, *Kinematic hardening rules in uncoupled modeling for multiaxial ratcheting simulation*, International Journal of Plasticity 17, pp.885 - 905, 2001.

[Bari and Hassan 2002**]** : S. Bari, T. Hassan, *An advancement in cyclic plasticity modeling for multiaxial ratcheting simulation*, International Journal of Plasticity 18, pp.873 - 894, 2002.

[Barlat and Brem 1991**]** : F. Barlat, D. Brem, *A six components yield function for anisotropic materials*, International Journal of Plasticity 7, pp.693 - 712, 1991.

[Barlat *et al.,* 2003**]** : F. Barlat, J.F. Duarte, J. Gracio, A. Lopes, E. Rauch, *Plastic flow for non-monotonic loading conditions of an aluminum alloy sheet sample*, International Journal of Plasticity 19, pp.1215 - 1244, 2003.

[Ben-Tahar 2005**]** : M. Ben-Tahar, *Contribution à l'étude et la simulation du procédé d'hydroformage*, **PhD report**, MinesParistech, France, 2005. In french.

[Benallal *et al.,* 1989**]** : A. Benallal, P.L. Gallo, D. Marquis, *An experimental investigation of cyclic hardening of 316 stainless steel and of 2024 aluminium alloy under multiaxial loadings*, Nuclear Engineering and Design 114, pp.345 - 353, 1989.

[Benallal and Marquis 1987**]** : A. Benallal, D. Marquis, *Constitutive Equations for Nonproportional Cyclic Elasto-Viscoplasticity*, Journal of Engineering Materials and Technology 109, pp.326 - 337, 1987.

[Benzerga *et al.*, 2004a**]** : A.A. Benzerga, J. Besson, A. Pineau, Anisotropic ductile fracture Part I: experiments, Acta Materialia 51, pp.4623 – 4638, 2004a.

[Benzerga *et al.*, 2004b**]** : A.A. Benzerga, J. Besson, A. Pineau, Anisotropic ductile fracture Part II: theory, Acta Materialia 52, pp.4639 – 4650, 2004b.

[Bocher *et al.,* 2001**]** : L. Bocher, P. Delobelle, P. Robinet, X. Feaugas, *Mechanical and microstructural investigations of an austenitic stainless steel under non-proportional loadings in tension-torsion-internal and external pressure*, International Journal of Plasticity 17, pp.1491 - 1530, 2001.

[Bouchou and Delobelle 1996a**]** : A. Bouchou, P. Delobelle, *Behaviour and modelization of a 17-12 SPH stainless steel under cyclic, unidirectional and bidirectional anisothermal loadings*, Nuclear Engineering and Design 162, pp.21 - 45, 1996a.

[Bouchou and Delobelle 1996b**]** : A. Bouchou, P. Delobelle, *Behavior and modeling of a 17-12 SPH stainless steel under cyclic, uni and bidirectional, anisothermal loadings. Part I: Behavior*, International Journal of Plasticity 12, pp.295 - 309, 1996b.

[Boussetta 2005**]** : R. Boussetta, *Estimateurs d'erreur et remaillage adaptatif : application à la simulation 3D des procédés de mise en forme des matériaux*, **PhD report**, MinesParistech, France, 2005. In french.

[Caillet 2007**]** : N. Caillet, *Prise en compte des specifités des pièces forgées en fatigue illimitée*, **PhD report**, MinesParistech, France, 2007. In french.

[Cailletaud 1992**]** : G. Cailletaud, *A micromechanical approach to inelastic behaviour of metals, International Journal of Plasticity* 8, pp.55 - 73, 1992.

[Cailletaud *et al.,* 2003**]** : G. Cailletaud, S. Forest, D. Jeulin, F. Feyel, I. Galliet, V. Mounoury, S. Quilici, *Some elements of microstructural mechanics*, Computational Materials Science 27, pp.351 - 374, 2003.

[Cailletaud and Sai 2008**]** : G. Cailletaud, K. Saï, *A polycrystalline model for the description of ratchetting: Effect of intergranular and intragranular hardening*, Materials Science and Engineering: A 480, pp.24 - 39, 2008.

[Cailletaud and Sai 1995**]** : G. Cailletaud, K. Saï, *Study of plastic/viscoplastic models with various inelastic mechanisms*, International Journal of Plasticity 11, pp.991 - 1005, 1995.

[Calloch and Marquis 1997**]** : S. Calloch, D. Marquis, *3D experimental and numerical investigations to test constitutive equations for nonproportional cyclic plasticity*, In proceedings: Transactions of the 14th International Conference on structural Mechanics in Reactor Technology (SMiRT 14), Lyon, France, August 17 – 22, 1997.

[Calloch and Marquis 1999**]** : S. Calloch, D. Marquis, *Triaxial tension-compression tests for multiaxial cyclic plasticity*, International Journal of Plasticity 15, pp.521 - 549, 1999.

[Cazacu *et al.,* 2006**]** : O. Cazacu, B. Plunkett, F. Barlat, *Orthotropic yield criterion for hexagonal closed packed metals*, International Journal of Plasticity 22, pp.1171 - 1194, 2006.

[Chaboche 1986**]** : J.-L. Chaboche, *Time-independent constitutive theories for cyclic plasticity, International Journal of Plasticity* 2, pp.149 - 188, 1986.

[Chaboche 1989**]** : J.-L. Chaboche, *Constitutive equations for cyclic plasticity and cyclic viscoplasticity*, International Journal of Plasticity 5, pp.247 - 302, 1989.

[Chaboche 1991**]** : J.-L. Chaboche, *On some modifications of kinematic hardening to improve the description of ratchetting effects*, International Journal of Plasticity 7, pp.661 - 678, 1991.

[Chaboche 1996**]** : J.-L. Chaboche, *Unified Cyclic Viscoplastic Constitutive Equations: Development, Capabilities, and Thermodynamic Framework*. Krausz, A. and Krausz, K., eds. Unified Constitutive Laws of Plastic Deformation, Academic Press, San Diego, 1 – 68, 1996.

[Chaboche 2008**]** : J.-L. Chaboche, *A review of some plasticity and viscoplasticity constitutive theories*, International Journal of Plasticity 24, pp.1642 - 1693, 2008.

[Chaboche and Cailletaud 1986**]** : J. Chaboche, G. Cailletaud, *On the calculation of structures in cyclic plasticity or viscoplasticity*, Computers & Structures 23, pp.23 - 31, 1986.

[Chaboche and Cailletaud 1996**]** : J. Chaboche, G. Cailletaud, *Integration methods for complex plastic constitutive equations*, Computer Methods in Applied Mechanics and Engineering 133, pp.125 - 155, 1996.

[Chaboche *et al.,* 1979**]** : J.-L. Chaboche, K. Dang-Van, G. Cordier, *Modelization of the strain memory effect on the cyclic hardening of 316 stainless steel*, In: Proceedings of the Transactions of the 5th International Conference on Structural Mechanics in Reactor Technology, Berlin, No. Div L in 11/3., 1979.

[Chen and Jiao 2004**]** : X. Chen, R. Jiao, *Modified kinematic hardening rule for multiaxial ratcheting prediction*, International Journal of Plasticity 20, pp.871 - 898, 2004.

[Chenot *et al.,* 2002**]** : J.-L. Chenot, L. Fourment, K. Mocellin, *Numerical treatment of contact and friction in FE simulation of forming processes*, Journal of Materials Processing Technology 125-126, pp.45 - 52, 2002.

[Coupez *et al.,* 1998**]** : T. Coupez, L. Fourment, J.-L. Chenot, *Adaptive solutions in industrial forming process simulation*. Advances in Adaptive Computational Methods in Mechanics, Elsevier, pp365 – 381, 1998.

[Coupez *et al.,* 2000**]** : T. Coupez, H. Digonnet, R. Ducloux, *Parallel meshing and remeshing,* Applied Mathematical Modelling 25, pp.153 - 175, 2000.

[Cockroft and Latham 1968**]** : M.G. Cockcroft, D.J. Latham, *Ductility and the workability of metals. Journal of the Institute of Metals* 96, pp,33 - 39, 1968.

[Davies *et al.,* 2002**]** : R.W. Davies, M.A. Khaleel, W.C. Kinsel, H.M. Zbib, *Anisotropic Yield Locus Evolution During Cold Pilgering of Titanium Alloy Tubing*, Journal of Engineering Materials and Technology 124, pp.125 - 135, 2002.

[de Carlan *et al.,* 2009**]** : Y. de Carlan, J.-L. Bechade, P. Dubuisson, J.-L. Seran, P. Billot, A. Bougault, T. Cozzika, S. Doriot, D. Hamon, J. Henry, M. Ratti, N. Lochet, D. Nunes, P. Olier, T. Leblond, M. Mathon, *CEA developments of new ferritic ODS alloys for nuclear applications*, Journal of Nuclear Materials 386-388, pp.430 - 432, 2009.

[Dubuisson *et al.,* 2011a**]** : P. Dubuisson, Y. de Carlan, V. Garat, M. Blat, *ODS Ferritic / Martensitic alloys for Sodium Fast Reactor fuel pin cladding*, oral contribution to DIANA I workshop "Dispersion Strengthened steels for advanced nuclear applications", Aussois (France) April 4-8, 2011a.

[Dubuisson *et al.,* 2011b**]** : P. Dubuisson, Y. de Carlan, V. Garat, M. Blat, *ODS Ferritic / Martensitic alloys for Sodium Fast Reactor fuel pin cladding*, Proceedings of DIANA I workshop "Dispersion Strengthened steels for advanced nuclear applications", Aussois (France) April 4-8, 2011b, *in Press*.

[Ducloux *et al.,* 2010**]** : R. Ducloux, L. Fourment, S. Marie, D. Monnereau, *Automatic Optimization Techniques Applied to a Large Range of Industrial Test Cases*, International Journal of Material Forming 3, pp.53 - 56, 2010.

[Eberl *et al.,* 1998**]** : F. Eberl, F. Feyel, S. Quilici, G. Cailletaud, *Approches numériques de la plasticité cristalline*, Journal of Physics IV France 08, pp.5 - 25, 1998. In french.

[Estrin 1998**]** : Y. Estrin, Dislocation *theory based constitutive modelling: foundations and applications*, Journal of Materials Processing Technology 80-81, pp.33 - 39, 1998.

[Fayolle 2008**]** : S. Fayolle, *Etude de la modélisation de la pose et de la tenue mécanique des assemblages par déformation plastique*, **PhD report**, MinesParistech, France, 2008. In french.

[Fazio *et al.,* 2009**]** : C. Fazio, A. Alamo, A. Almazouzi, S.D. Grandis, D. Gomez-Briceno, J. Henry, L. Malerba, M. Rieth, *European cross-cutting research on structural materials for Generation IV and transmutation systems*, Journal of Nuclear Materials 392, pp.316 - 323, 2009.

[Flores *et al.,* 2007**]** : P. Flores, L. Duchêne, C. Bouffioux, T. Lelotte, C. Henrard, N. Pernin, A.V. Bael, S. He, J. Duflou, A. Habraken, *Model identification and FE simulations: Effect of different yield loci and hardening laws in sheet forming*, International Journal of Plasticity 23, pp.420 - 449, 2007.

[Forest and Cailletaud 1995**]** : S. Forest, G. Cailletaud, *Strain Localization in Single Crystals: Effect of Boundaries and Interfaces*, European Journal of Mechanics A/Solids 14, pp.747 - 771, 1995.

[Fourment *et al.,* 1999**]** : L. Fourment, J.-L. Chenot, K. Mocellin, *Numerical formulations and algorithms for solving contact problems in metal forming simulation*, International Journal for Numerical Methods in Engineering 46, pp.1435 - 1462, 1999.

[Fourment *et al.,* 2010**]** : L. Fourment, R. Ducloux, S. Marie, M. Ejday, D. Monnereau, T. Massé, P. Montmitonnet, *Mono and multi-objective optimization techniques applied to a large range of industrial test cases using Metamodel assisted Evolutionary Algorithms*, in: Proceedings of the 10th International Conference on Numerical Methods in Industrial Forming Processes Dedicated to Professor O. C. Zienkiewicz (1921–2009), 2010.

[Fourment *et al.,* 2009**]** : L. Fourment, T. Massé, S. Marie, R. Ducloux, M. Ejday, C. Bobadilla, P. Montmitonnet, *Optimization of a range of 2D and 3D bulk forming processes by a meta-model assisted evolution strategy*, International Journal of Material Forming 2, pp.343 - 346, 2009.

[Fournier *et al.,* 2009**]** : B. Fournier, M. Sauzay, A. Renault, F. Barcelo, A. Pineau, *Microstructural evolutions and cyclic softening of 9%Cr martensitic steels*, Journal of Nuclear Materials 386 - 388, pp.71 - 74, 2009.

[Furugen and Hayashi 1984**]** : M. Furugen, C. Hayashi, *Application of the theory of plasticity to the cold pilgering of tubes*, Journal of Mechanical Working Technology 10, pp.273-286, 1984.

[Gay 1995**]** : C. Gay, *Contribution à la simulation numérique tridimensionnelle du forgeage à froid*, **PhD report**, MinesParistech, France, 1995. in french.

[Geleji 1955**]** : A. Geleji, *die Berechnung der Kräfte und des Leistungsbedarfs beim Kaltpilgern von Rohren*, Acta Techn. Ac. Sci. Hung Budapest 11, pp.461 - 478, 1955.

[Germain and Muller 1995**]** : P. Germain, P. Muller, *Introduction à la mécanique des milieux continus*, Masson, 1995. In french.

[Girard 1993**]** : E. Girard, *Etude mécanique théorique et expérimentale du laminage à pas de pèlerin: Application à l'endommagement de la surface externe des tubes en Zircaloy 4*, **PhD report**, Ecole Centrale de Nantes, France, 1993. In french.

[Girard *et al.,* 2001**]** : E. Girard, R. Guillén, P. Weisbecker, M. François, *Effect of plastic shearing on damage and texture on Zircaloy-4 cladding tubes: experimental and numerical study*, Journal of Nuclear Materials 294, pp.330 - 338, 2001.

[Gratacos 1991**]** : P. Gratacos, *Un problème de déformation couplée: modélisation elasto-plastique par éléments finis du laminage à froid de bande mince*, **PhD report**, MinesParistech, 1991. In french.

[Hamilton *et al.,* 2000**]** : M.L. Hamilton, D.S. Gelles, R.J. Lobsinger, M.M. Paxton, W. F. Brown, Fabrication Technology for ODS Alloy MA957, PNL-13165. - Richlands, VA : Batelle Pacific Northwest Lab.,February 2000

[Hacquin *et al.,* 1996**]** : A. Hacquin, P. Montmitonnet, J.-P. Guillerault, *A steady state thermo-elastoviscoplastic finite element model of rolling with coupled thermo-elastic roll deformation*, Journal of Materials Processing Technology 60, pp.109 - 116, 1996.

[Hacquin *et al.,* 1998**]** : A. Hacquin, P. Montmitonnet, J. Guillerault, *A three-dimensional semi-analytical model of rolling stand deformation with finite element validation*, European Journal of Mechanics - A/Solids 17, pp.79 - 106, 1998.

[Harada *et al.,* 2005**]** : M. Harada, A. Honda, S. Toyoshima, *Simulation of cold pilgering process by a generalized plane strain FEM*, Journal of ASTM International 2(3), pp. 233 - 247, 2005.

[Hartmann and Haupt 1993**]** : S. Hartmann, P. Haupt, *Stress computation and consistent tangent operator using non-linear kinematic hardening models*, International Journal for Numerical Methods in Engineering 36, pp.3801-3814, 1993.

[Hassan *et al.,* 2008**]** : T. Hassan, L. Taleb, S. Krishna, *Influence of non-proportional loading on ratcheting responses and simulations by two recent cyclic plasticity models*, International Journal of Plasticity 24, pp.1863 - 1889, 2008.

[Hill 1948**]** : R. Hill, *A Theory of the Yielding and Plastic Flow of anisotropic metals*, In: Proceedings of the Royal Society of London. Series A, 1948.

[Hill 1979**]** : R. Hill, *Theoretical plasticity of texture aggregates, Mathematics and Theoretical Physics* 85, pp.179 - 191, 1979.

[Hill 1990**]** : R. Hill, *Constitutive modelling of orthotropic plasticity in sheet metals*, Journal of the Mechanics and Physics of Solids 38, pp.405 - 417, 1990.

[Hosford 1972**]** : W. Hosford, *A generalized isotropic yield criterion*, Journal of Applied Mechanics 39, pp.607 - 610, 1972.

[HPTR CEA/LTMEX**]** : HPTR mill technical manual at CEA/LTMEX Saclay.

[Hu 2007**]** : W. Hu, *Constitutive modeling of orthotropic sheet metals by presenting hardening-induced anisotropy*, International Journal of Plasticity 23, pp.620 - 639, 2007.

[Huml 1987**]** : P. Huml, *The influence of strain path on wire properties*, Advanced Technology of Plasticity 2, pp.827-833, 1987.

[Huml 1997**]** : P. Huml, *Control and characterisation of mechanical properties under cold rolling conditions*, Scandinavian Journal of Metallurgy 26, pp.224 - 230, 1997.

[Huml and Fogelholm 1994**]** : P. Huml, R. Fogelholm, *Simulation model of cold pilgering*, Journal of Materials Processing Technology 42, pp.167 - 173, 1994.

[Huml *et al.,* 1993**]** : P. Huml, R. Fogelholm, A. Salwen, *Optimization of Cold Rolling of Precision Tubes*, CIRP Annals - Manufacturing Technology 42, pp.283 - 286, 1993.

[Huml and Lindegren 1992**]** : P. Huml, M. Lindegren, *Properties of Cold-Formed Metal Products*, CIRP Annals - Manufacturing Technology 41, pp.267 - 270, 1992.

[Huml and Strandell 1984**]** : P. Huml, P.O. Strandell, *Utilization of Flow Stress in Metal Forming Calculations*, CIRP Annals Manufacturing Technology 33, pp.147 - 149, 1984.

[Inoue *et al.,* 2007**]** : M. Inoue, T. Kaito, S. Ohtsuka, *Research and development of oxide dispersion strengthened ferritic steels for sodium cooled fast breeder reactor fuels*, Materials for Generation IV Nuclear Reactors, Cargese, Corsica, 2007.

[Inoue *et al.,* 2008**]** : M. Inoue, T. Kaito, S. Ohtsuka, *Research and development of oxide dispersion strengthened ferritic steels for sodium cooled fast breeder reactor fuels, Materials Issues for Generation IV Systems*, Springer Netherlands, pp 311 - 325, 2008.

[Iracane *et al.,* 2006**]** : D. Iracane, H. Abderrahim, F. Carré, P. Chaix, J. Seran, and P. Yvon, *Generation IV systems R&D needs and research reactors policy*. IAEA Technical committee meeting on "research reactors support needed for innovative nuclear power reactors and fuel cycles" Vienna, Austria, November 20th to 22nd, 2006.

[Jiang and Kurath 1997**]** : Y. Jiang, P. Kurath, *Nonproportional cyclic deformation: critical experiments and analytical modeling*, International Journal of Plasticity 13, pp.743 - 763, 1997.

[Kang *et al.,* 2004**]** : G. Kang, Q. Gao, X. Yang, *Uniaxial and non-proportionally multiaxial ratcheting of SS304 stainless steel at room temperature: experiments and simulations*, International Journal of Non-Linear Mechanics 39, pp.843 - 857, 2004.

[Kang *et al.,* 2002**]** : G. Kang, Q. Gao, X. Yang, *A visco-plastic constitutive model incorporated with cyclic hardening for uniaxial/multiaxial ratcheting of SS304 stainless steel at room temperature*, Mechanics of Materials 34, pp.521 - 531, 2002.

[Karafillis and Boyce 1993**]** : A. Karafillis, M. Boyce, *A general anisotropic yield criterion using bounds and a transformation weighting tensor*, Journal of the Mechanics and Physics of Solids 41, pp.1859 - 1886, 1993.

[Karas**]** : L. Karas, *Development and evaluation of a model for a new cold pilger process*, **PhD report**, AGH University of Science and Technology, Poland-TU Clausthal, Germany, to be defended.

[Kimura *et al.,* 2011**]** : A. Kimura, R. Kasada, N. Iwata, H. Kishimoto, C. Zhang, J. Isselin, P. Dou, J. Lee, N. Muthukumar, T. Okuda, M. Inoue, S. Ukai, S. Ohnuki, T. Fujisawa, T. Abe, *Development of Al added high-Cr ODS steels for fuel cladding of next generation nuclear systems*, Journal of Nuclear Materials 417, pp.176 - 179, 2011.

[Klueh *et al.,* 2005**]** : R. Klueh, J. Shingledecker, R. Swindeman, D. Hoelzer, *Oxide dispersion-strengthened steels: A comparison of some commercial and experimental alloys*, Journal of Nuclear Materials 341, pp.103 - 114, 2005.

[Knockaert 2001**]** : R. Knockaert, Numerical and experimental study of the strain localization during sheet forming operations, **PhD report**, MinesParistech, France, 2001.

[Krishna *et al.,* 2009**]** : S. Krishna, T. Hassan, I.B. Naceur, K. Saï, G. Cailletaud, *Macro versus micro-scale constitutive models in simulating proportional and nonproportional cyclic and ratcheting responses of stainless steel 304*, International Journal of Plasticity 25, pp.1910 - 1949, 2009.

[Krempl and Lu 1984**]** : E. Krempl, H. Lu, *The hardening and rate dependence behavior of fully annealed AISI Type 304 stainless steel under biaxial in-phase and out-of-phase strain cycling at room temperature*. ASME Journal of Engineering Materials and Technology 106, pp.376 – 382, 1984.

[Kruml *et al.,* 2011**]** : T. Kruml, I. Kubena, J. Polak, *Fatigue behaviour and surface relief in ODS steels*, Procedia Engineering 10, pp.1685 - 1690, 2011.

[Kubena *et al.,* 2010**]** : I. Kubena, T. Kruml, P. Spätig, N. Baluc, Z. Oksiuta, M. Petrenec, K. Obrtlík, J. Polák, *Fatigue behaviour of ODS ferritic-martensitic Eurofer steel*, In proceedings: Procedia Enginnering Fatigue 2010, 2, pp.717 - 724, 2010.

[Kubena *et al.,* 2011**]** : I. Kubena, T. Kruml, B. Fournier, J. Polák, *Cyclic plasticity of a duplex stainless steel under non-proportional loading*, Key Engineering Materials 465, pp.556 - 559, 2011.

[Lange 2006**]** : C. Lange, *Etude physique et modélisation numérique du procédé de sertissage de pièces de carrosserie*, **PhD report**, MinesParistech, France, 2006. In french.

[LA2M 2011**]** : Fiche d'essai dureté Vickers tube J37 - référence No DT LA2M : 633C DMN/SRMA/LA2M CEA/Saclay, 2011.

[Lebensohn *et al.,* 1996**]** : R. Lebensohn, M. Gonzalez, C. Tomé, A. Pochettino, *Measurement and prediction of texture development during a rolling sequence of Zircaloy-4 tubes*, Journal of Nuclear Materials 229, pp.57 - 64, 1996.

[Lebensohn and Tomé 1993**]** : R. Lebensohn, C. Tomé, *A self-consistent anisotropic approach for the simulation of plastic deformation and texture development of polycrystals: Application to zirconium alloys*, Acta Metallurgica et Materialia 41, pp.2611 - 2624, 1993.

[Lemaître and Chaboche 1994**]** : J. Lemaître, J.-L. Chaboche, *Mechanics of Solid Materials*, Press Sindicate of the University of Cambridge, 1994.

[Lemaître *et al.,* 1999**]** : J. Lemaître, R. Desmorat, M. Sauzay, *Loi d'évolution de l'endommagement anisotrope*, Mécanique des solides et des structures, C.R. Académie de Sciences Paris, t. 327, Série II b, pp. 1231 – 1236, 1999. In french.

[Lodej *et al.,* 2006**]** : B. Lodej, K. Niang, P. Montmitonnet, J.-L. Aubin, *Accelerated 3D FEM computation of the mechanical history of the metal deformation in cold pilgering of tubes*, Journal of Materials Processing Technology 177, pp.188 - 191, 2006.

[McDowell 1985**]** : D.L. McDowell, *A two surface model for transient nonproportional cyclic plasticity*, Part I: Development of appropriate equations, ASME Journal of Applied Mechanics 52, pp.298 – 302, 1985.

[Malaplate *et al.,* 2011**]** : J. Malaplate, F. Mompiou, J.-L. Béchadechade, T.V.D. Berghe, M. Ratti, Creep behavior of ODS materials: *A study of dislocations/precipitates interactions*, Journal of Nuclear Materials 417, pp.205 - 208, 2011.

[Massé 2010**]** : T. Massé, *Study and optimization of high carbon steel flat wires*, **PhD report**, MinesParistech, France, 2010.

[Massé *et al.,* 2011**]** : T. Massé, Y. Chastel, P. Montmitonnet, C. Bobadilla, N. Persem, S. Foissey, *Impact of mechanical anisotropy on the geometry of flat-rolled fully pearlitic steel wires*, Journal of Materials Processing Technology 211, pp.103 - 112, 2011.

[Mises 1928**]** : R. von Mises, *Mechanik der plastischen Forrnmnderung von Kristallen*, Z. Angew math. Mech. 8, pp.161-185, 1928.

[Mocellin 1999**]** : K. Mocellin, *Contribution à la simulation numérique tridimensionnelle du forgeage à chaud: étude du contact et calcul multigrille*, **PhD report**, MinesParistech, France, 1999. In french.

[Montmitonnet 2007**]** : P. Montmitonnet, *From steady-state to cyclic metal forming processes*, In: Proceedings of the Materials Processing and Design, Modeling, Simulation and Applications, NUMIFORM '07: 9th International Conference on Numerical Methods in Industrial Forming Processes, Porto, Portugal, 2007.

[Montmitonnet and Aubin 2008**]** : P. Montmitonnet, J.-L. Aubin, *Formage des tubes métalliques*, Techniques de l'ingénieur Doc M 3 068, 2008. In french.

[Montmitonnet and Chenot 1995**]** : P. Montmitonnet, J.-L. Chenot, *Introduction of anisotropy in viscoplastic 2D and 3D finite-element simulations of hot forging*, Journal of Materials Processing Technology 53, pp.662 - 683, 1995.

[Montmitonnet *et al.,* 2002**]** : P. Montmitonnet, R. Logé, M. Hamery, Y. Chastel, J.-L. Doudoux, J.-L. Aubin, *3D elastic-plastic finite element simulation of cold pilgering of zircaloy tubes*, Journal of Materials Processing Technology 125-126, pp.814 - 820, 2002.

[Mulot 1997**]** : S. Mulot, *Etude théorique et expérimentale du laminage à pas de pèlerin de tubes en zircalloy 4*, **PhD report**, MinesParistech, France, 1997. In french.

[Mulot *et al.,* 1996**]** : S. Mulot, A. Hacquin, P. Montmitonnet, J.-L. Aubin, *A fully 3D finite element simulation of cold pilgering*, Journal of Materials Processing Technology 60, pp.505 - 512, 1996.

[Narita *et al.,* 2004**]** : T. Narita, S. Ukai, T. Kaito, S. Ohtsuka, T. Kobayashi, *Development of Two-Step Softening Heat Treatment for Manufacturing 12Cr-ODS Ferritic Steel Tubes*, Journal of Nuclear Science and Technology 41, pp.1008 - 1012, 2004.

[Nerino *et al.,* 2011**]** : A. Nerino, M. Deaver, C. Nagele, J. Reinhart, *HPTR's past, present, and future*, The Tube and Pipe Journal July/August, 20 - 24, 2011.

[Nouailhas 1988**]** : D. Nouailhas, *Modélisation de l'écrouissage et de la restauration en viscoplasticité cyclique*, Physics Applied 23, pp.339 - 349, 1988. In french.

[Nouailhas *et al.,* 1985a**]** : D. Nouailhas, G. Cailletaud, H. Policella, D. Marquis, J. Dufailly, H. Lieurade, A. Ribes, E. Bollinger, *On the description of cyclic hardening and initial cold working*, Engineering Fracture Mechanics 21, pp.887 - 895, 1985a.

[Nouailhas *et al.,* 1985b**]** : D. Nouailhas, J. Chaboche, S. Savalle, G. Cailletaud, *On the constitutive equations for cyclic plasticity under nonproportional loading*, International Journal of Plasticity 1, pp.317 - 330, 1985b.

[Ohno 1997**]** : N. Ohno, *Current state of the art in constitutive modeling for ratcheting*, In: Proceedings of the 14th International Conference on SMiRT, Lyon, France, 1997.

[Oksiuta *et al.,* 2009**]** : Z. Oksiuta, P. Olier, Y. de Carlan, N. Baluc, *Development and characterisation of a new ODS ferritic steel for fusion reactor application*, Journal of Nuclear Materials 393, pp.114 - 119, 2009.

[Olier *et al.,* 2009**]** : P. Olier, A. Bougault, A. Alamo, Y. de Carlan, *Effects of the forming processes and Y2O3 content on ODS-Eurofer mechanical properties*, Journal of Nuclear Materials 386-388, pp.561 - 563, 2009.

[Osika and Libura 1992**]** : J. Osika, W. Libura, *Mathematical model of tube cold rolling in pilger mill*, Journal of Materials Processing Technology 34, pp.1239 - 1251, 1992.

[Osika *et al.,* 2009**]** : J. Osika, H. Palkowski, K. Swiatkowski, D. Pociecha, A. Kula, *Analysis of material deformation during the new cold tube rolling process realized on the new generation of pilger mills*, Archive of Metallurgy and Materials 54, pp.325 - 332, 2009.

[Osika and Swiatkowski 2003**]** : J. Osika, K. Swiatkowski, *An investigations of displacements and deformation during cold rolling of tubes in pilgering process*, Archives of Metallurgy 48, pp.269 - 276, 2003.

[Parmentier *et al.,* 2002**]** : P. Parmentier, A. Alamo, N. Llorca, *Optimisation de l'élaboration et de la mise en forme d'aciers renforcés par dispersion d'oxydes (ODS)*, In: Proceedings of the Matériaux 2002, 21-25 october,Tours, France, 2002.

[Park *et al.,* 2005**]** : H. J. Park, S. S. Kim, S. Lee, T. H. Choi, H. W. Lee, S. J. Lim, E. Z. Kim, K. H. Na, C. S. Han, *Optimum design of a pilger mill process for wire forming using CAD/CAE*, In proceedings: Materials Science Forum 475-479, pp.3275 – 3278, 2005.

[Perchat 2000**]** : E. Perchat, *Mini-élément et factorisations incomplètes pour la parallélisation d'un solveur de Stokes 2D. Application au forgeage*, **PhD report**, Mines Paristech, France, 2000. In french.

[Prager 1945**]** : W. Prager, *Strain hardening under combined stress*, Journal Applied Physics 16, pp.837, 1945.

[Praud 2011**]** : M. Praud, *document technique DMN/SRMA/LA2M/NT/11-3190/A*, 2011.

[Praud *et al.,* 2011**]** : M. Praud, F. Mompiou, J. Malaplate, D. Caillard, J. Garnier, A. Steckmeyer, B. Fournier, *Study of the deformation mechanisms in a Fe-14%Cr ODS alloy*, Proceedings of DIANA I workshop "Dispersion Strengthened steels for advanced nuclear applications", Aussois (France) April 4-8, 2011, *in Press*.

[Ratti 2009**]** : M. Ratti, *Développement de nouvelles nuances d'aciers ferritiques/martensitiques pour le gainage d'éléments combustibles des réacteurs à neutrons rapides au sodium*, **PhD report**, Institute Polytechnique de Grenoble, France, 2009. In french.

[Ratti *et al.,* 2009**]** : M. Ratti, D. Leuvrey, M. Mathon, Y. de Carlan, *Influence of titanium on nano-cluster (Y, Ti, O) stability in ODS ferritic materials*, Journal of Nuclear Materials 386-388, pp.540 - 543, 2009.

[Rauch *et al.,* 2011**]** : E.F. Rauch, J.J. Gracio, F. Barlat, G. Vincze, *Modelling the plastic behaviour of metals undercomplex loading conditions*, Modelling and Simulation in Materials Science and Engineering 19, 035009 (18pp), 2011.

[Réglé 1994**]** : H. Réglé*, Alliages ferritiques 14/20% de chrome renforcés par dispersion d'oxydes. Effets des procédés de mise en forme sur les textures de déformation, la recristallisation et les* propriétés de traction, Rapport CEA-R-5675, **PhD report**, Université de Paris-sud UFR scientifique d'Orsay, France, 1994. In french.

[Revil-Baudard 2010**]** : B. Revil-Baudard, *Simulation du comportement mécanique des alliages de titane pour les procédés de mise en forme à froid*, **PhD report**, MinesParistech, France, 2010. In french.

[Robin 2006**]** : M.C. Robin, rapport technique première année de thèse, *Etude de la durée de vie de collecteurs d'échappement*. MinesParistech, France, 2006. In french.

[Saanouni and Abdul-Latif 1996**]** : K. Saanouni, A. Abdul-Latif, *Micromechanical modeling of low cycle fatigue under complex loadings - Part I. Theoretical formulation*, International Journal of Plasticity 12, pp.1111 - 1121, 1996.

[Sai 2011**]** : K. Saï, Multi-mechanism models: *Present state and future trends*, International Journal of Plasticity 27, pp.250 - 281, 2011.

[Serrano *et al.,* 2011**]** : M. Serrano, M. Hernandez-Mayoral, A. Garcia-Junceda, *Microstructural anisotropy effect on the mechanical properties of a 14Cr ODS steel*, Journal of Nuclear Materials, 2011, *in Press*.

[Shamsaei *et al.,* 2010**]** : N. Shamsaei, A. Fatemi, D.F. Socie, *Multiaxial cyclic deformation and non-proportional hardening employing discriminating load paths*, International Journal of Plasticity 26, pp.1680 - 1701, 2010.

[Siebel and Neumann 1954**]** : E. Siebel, F. Neumann, *das Kaltpilgern von Rohren-Versuchergebnße und Untersuchungen über dem Walzvorgang*, Stahl und Eisen 74, pp.139 - 145, 1954.

[Simo and Taylor 1985**]** : J. Simo, R. Taylor, *Consistent tangent operators for rate-independent elastoplasticity*, Computer Methods in Applied Mechanics and Engineering 48, pp.101 - 118, 1985.

[Sornin and Couvrat 2010**]** : D. Sornin, M. Couvrat, *Numerical simulation of hot extrusion consolidation of PM ferritic ODS stainless steels*, In: Proceedings of the World PM2010 Conference– EPMA, Florence, 10th - 14th October, 2010.

[Steckmeyer *et al.,* 2010**]** : A. Steckmeyer, M. Praud, B. Fournier, J. Malaplate, J. Garnier, J. Béchade, I. Tournié, A. Tancray, A. Bougault, P. Bonnaillie, *Tensile properties and deformation mechanisms of a 14Cr ODS ferritic steel*, Journal of Nuclear Materials 405, pp.95 - 100, 2010.

[Strehlau 2006**]** : Strehlau,O., www.thefabricator.com/article/tubepipeproduction/introducing-cold-pilger-mill-technology, Introducing cold pilger mill technology, 2006.

[Tabor 1950**]** : D. Tabor, *The hardness of metals*, Clarendon Press, Oxford, 1950.

[Taleb and Cailletaud 2010**]** : L. Taleb, G. Cailletaud, *An updated version of the multimechanism model for cyclic plasticity*, International Journal of Plasticity 26, pp.859 - 874, 2010.

[Taleb *et al.,* 2006**]** : L. Taleb, G. Cailletaud, L. Blaj, *Numerical simulation of complex ratcheting tests with a multi-mechanism model type*, International Journal of Plasticity 22, pp.724 - 753, 2006.

[Taleb and Hauet 2009**]** : L. Taleb, A. Hauet, *Multiscale experimental investigations about the cyclic behavior of the 304L SS*, International Journal of Plasticity 25, pp.1359 - 1385, 2009.

[Tanaka 1994**]** : E. Tanaka, *A non-proportionality parameter and a viscoplastic constitutive model taking into account amplitude dependences and memory effects of isotropic hardening*, European Journal of Mechanics,A/Solids 13, pp.155 - 173, 1994.

[Tanaka *et al.,* 1985**]** : E. Tanaka, S. Murakami, M. Ooka, *Effects of strain path shapes on non-proportional cyclic plasticity*, Journal of the Mechanics and Physics of Solids 33, pp.559 - 575, 1985.

[Toualbi 2010**]** : L. Toualbi, *document technique DEN/DANS/DNM/SRMA/LA2M/NT/2010-3179/A*, 2010.

[Toualbi *et al.,* 2011**]** : L. Toualbi, P. Olier, Y. de Carlan, D. Bossu, E. Rouesne, R. Logé, *Assessment of a new fabrication route for Fe-9Cr-1W ODS cladding tubes*, Proceedings of DIANA I workshop "Dispersion Strengthened steels for advanced nuclear applications", Aussois (France) April 4-8, 2011, *in Press*.

[Tresca 1868**]** : H. Tresca, *Mémoire sur l'écoulement des solides*, 18, pp.733 - 799, 1868.

[Turker and Hughes 1995**]** : M. Turker, T.A. Hughes, *Oxidation Behavior of Three Commercial ODS Alloys at 1200℃*, Oxidations of Metals 44, pp.Nos.5/6, 1995.

[Ukai and Fujiwara 2002**]** : S. Ukai, M. Fujiwara, *Perspective of ODS alloys application in nuclear environments*, Journal of Nuclear Materials 307-311, Part 1, pp.749 - 757, 2002.

[Ukai *et al.,* 1993a**]** : S. Ukai, M. Harada, H. Okada, M. Inoue, S. Nomura, S. Shikakura, K. Asabe, T. Nishida, M. Fujiwara, *Alloying design of oxide dispersion strengthened ferritic steel for long life FBRs core materials*, Journal of Nuclear Materials 204, pp.65 - 73, 1993a.

[Ukai *et al.,* 1993b**]** : S. Ukai, M. Harada, H. Okada, M. Inoue, S. Nomura, S. Shikakura, T. Nishida, M. Fujiwara, K. Asabe, *Tube manufacturing and mechanical properties of oxide dispersion strengthened ferritic steel*, Journal of Nuclear Materials 204, pp.74 - 80, 1993b.

[Ukai *et al.,* 1998**]** : S. Ukai, T. Nishida, T. Okuda, T. Yoshitake, *R&D of oxide dispersion strengthened ferritic martensitic steels for FBR*, Journal of Nuclear Materials 258-263, pp 1745 - 1749, 1998.

[Ukai *et al.,* 2002**]** : S. Ukai, S. Mizuta, M. Fujiwara, T. Okuda, T. Kobayashi, *Development of 9Cr-ODS Martensitic Steel Claddings for Fuel Pins by means of Ferrite to Austenite Phase Transformation*, Journal of Nuclear Science and Technology 39, pp.778 - 788, 2002.

[Ukai *et al.,* 2004**]** : S. Ukai, T. Narita, A. Alamo, P. Parmentier, Tube *manufacturing trials by different routes in 9CrW-ODS martensitic steels*, Journal of Nuclear Materials 329-333, Part A, pp.356 - 361, 2004.

[Ukai and Ohtsuka 2007**]** : S. Ukai, S. Ohtsuka, *Low cycle fatigue properties of ODS ferritic-martensitic steels at high temperature*, Journal of Nuclear Materials 367-370, Part A, pp.234 - 238, 2007.

[Ukai *et al.,* 2009**]** : S. Ukai, S. Ohtsuka, T. Kaito, H. Sakasegawa, N. Chikata, S. Hayashi, S. Ohnuki, *High-temperature strength characterization of advanced 9Cr-ODS ferritic steels*, Materials Science and Engineering: A 510-511, pp.115 - 120, 2009.

[Vanegas *et al.,* 2011a**]** : E. Vanegas, K. Mocellin, R. Logé, *Identification of cyclic and anisotropic behaviour of ODS steels tubes*, Procedia Engineering 10, pp.1208 - 1213, 2011a.

[Vanegas-Marquez *et al.,* 2011b**]** : E. Vanegas-Márquez, K. Mocellin, L. Toualbi, Y. de Carlan, R.E. Logé, *A simple approach for the modeling of an ODS steel mechanical behavior in pilgering conditions*, Journal of Nuclear Materials doi: 10.1016/j.jnucmat.2011.10.013, 2011b, *in Press*.

[Velay 2003**]** : V. Velay, *Modélisation du comportement cyclique et de la durée de vie d'aciers à outils martensitiques*, **PhD report**, MinesParistech, France, 2003. In french.

[Velay *et al.,* 2006**]** : V. Velay, G. Bernhart, L. Penazzi, *Cyclic behavior modeling of a tempered martensitic hot work tool steel*, International Journal of Plasticity 22, pp.459 - 496, 2006.

[Veysset 2011**]** : J. Veysset, *Simulation Numérique du Laminage à pas de Pelèrin VMR de Tubes ODS*, Rapport mastère Compumech in the context of Stratotube project, MinesParistech, 2011. In french.

[Wolff and Taleb 2008**]** : M. Wolff, L. Taleb, *Consistency for two multi-mechanism models in isothermal plasticity*, International Journal of Plasticity 24, pp.2059 - 2083, 2008.

[Yoshida *et al.,* 1975**]** : H. Yoshida, T. Matsui, T. Otani, K. Mandai, *Experimental investigation of the cold pilgering of copper tubes*, Ann. CIRP 24, pp.191-197, 1975.

Annexes

Annex 1: HPTR/LTMEX cam geometry

Profiled cams are 3 slopes with different angles. HPTR/LMTEX cam length: 191 mm

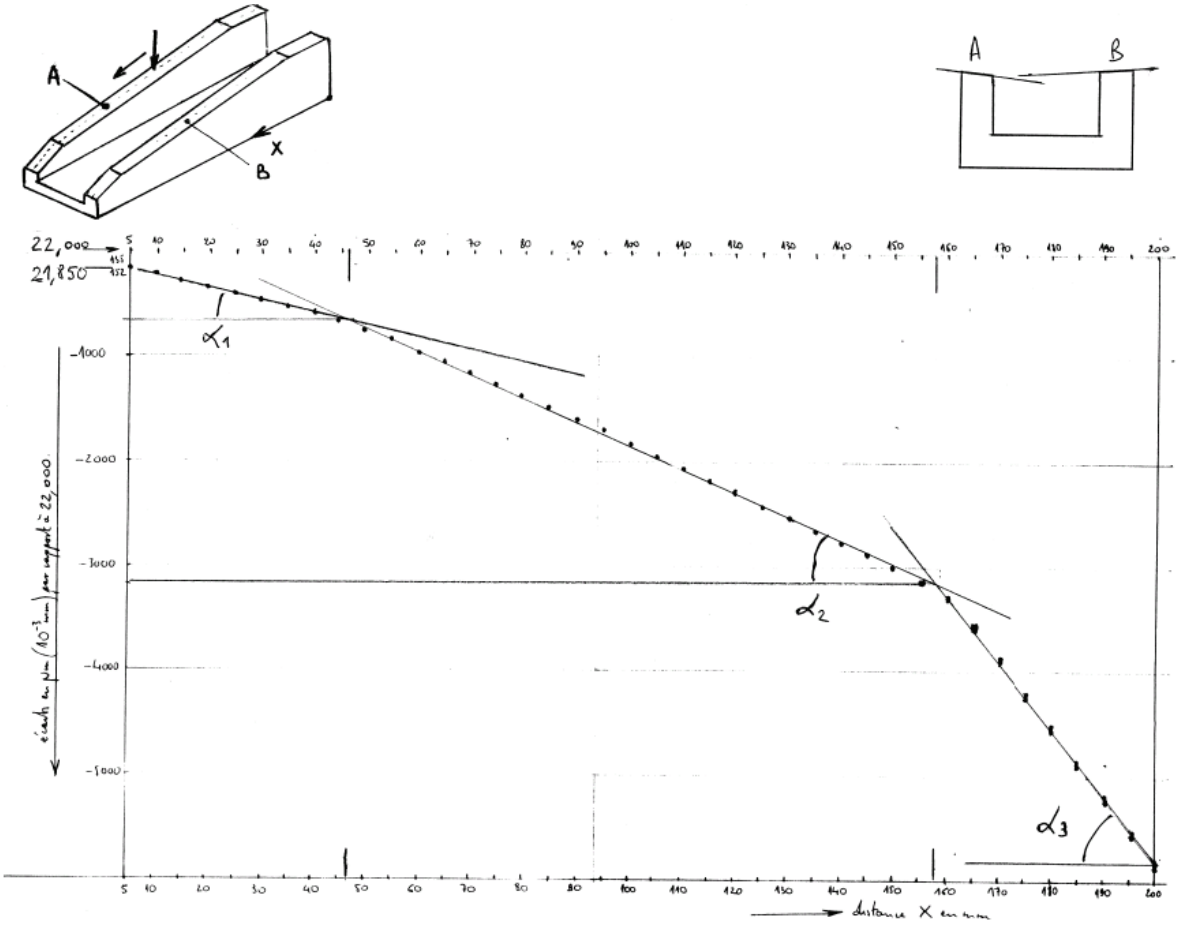

Figure A.1. Profiled cams are 3 slopes with different angles.

The corresponding angles in Fig. A.1 are:

α_1 = 0.682°
α_2 = 0.1290°
α_3 = 3.653°

Annex 2: Cam dilatation factor

Denis Sornin at CEA / DEN/DMN/SRMA/LTMEx laboratory calculated the dilatation cam factor (f_x) in relation with the formed external tube diameter. f_x is computed thanks to dimensions of the crankpin systems of the HPTR mill which varies from one final diameter to another (see [HPTR CEA/LTMEX]).

Table A.1. the dilatation factor (f_x) to apply at the real cam length

Formed external tube diameter [mm]	Factor (f_x)	Theoretical cam working zone length [mm]
8	**1,552**	296,7
9	**1,526**	291,7
10	**1,494**	285,6
11	**1,463**	279,6
12	**1,436**	274,6
13	**1,405**	268,5
14	**1,373**	262,5
15	**1,347**	257,5

Numerical modeling of ODS steel tubes pilgering

ABSTRACT : For new fast-neutron sodium-cooled Generation IV reactors, the candidate cladding materials for the very strong rates of combustion are the ferritic and martensitic oxide dispersion strengthened (ODS) grades. Classically the cladding tube is cold formed by a sequence of cold pilger rolling passes with intermediate heat treatments. Within the framework of a finite element model, the cold pilgering process is investigated. The numerical model takes into account the complex kinematics of the process as well as the material constitutive behavior under cyclic elastic-plastic loadings. Cyclic behaviour of ODS steels was modeled using an elastic-plastic model developed by Chaboche. A procedure for identifying the model parameters was proposed using an inverse analysis method. This procedure was applied to the experimental cyclic test data of only one specimen, using a sequence of cycles with several strain amplitudes. Moreover, the use of numerical sensors to follow the deformation path of a volume element during the process allows estimating the nature and the amplitude of the cyclic deformations. The identification of the deformation path is the first step toward a better understanding of the critical conditions leading to damage and cracking. The ODS steel is highly textured and mechanically anisotropic. Therefore, the possible influence of this anisotropy on the deformation path is analyzed using (i) an isotropic constitutive law, and (ii) an anisotropic law using the Hill quadratic criterion. Integration of a proper damage law or failure criterion as well as the choice of an appropriated constitutive model into the proposed numerical model leads to the possibility of analyzing conditions for which (a) cracking may develop, and (b) recrystallization may take place upon heat treatment.

Keywords : 9-14 % Cr steels, tube, cold pilgering, low-cycle fatigue, constitutive law, finite element method, ODS, damage, cracking.

Modélisation numérique du laminage à pas de pèlerin de tubes en acier ODS

RESUME : Pour les nouveaux réacteurs à neutrons rapides refroidis au sodium de Génération IV, les matériaux de gainage de référence pour les très forts taux de combustion sont les nuances ferritiques et martensitiques renforcés par une dispersion d'oxydes nanométriques (ODS). A l'heure actuelle le tube de gainage est mis en forme à froid à partir d'une ébauche tubulaire par une succession de passes de laminage à pas de pèlerin et de traitements thermiques intermédiaires. La modélisation numérique du procédé de laminage à pas de pèlerin pour ces nuances a été entreprise. Le modèle numérique d'élément finis tient compte de la cinématique complexe du procédé ainsi que du comportement du matériau sous chargements cycliques élasto-plastiques. Pour cela, le comportement cyclique des aciers ODS a été modélisé à l'aide d'un modèle élasto-plastique développé par Chaboche. Une procédure d'identification des paramètres du modèle a été proposée en utilisant une méthode d'analyse inverse. Cette procédure a été appliquée aux données expérimentales issues d'un essai cyclique sur une seule éprouvette. Utilisant une séquence de différentes amplitudes de déformations. Par ailleurs, l'utilisation de capteurs numériques a permis de suivre le chemin de déformation d'un élément de volume au cours du procédé afin d'estimer la nature et l'amplitude des déformations cycliques. L'identification du chemin de déformation est la première étape vers une meilleure compréhension des conditions critiques menant à des dommages et de fissures. L'acier ODS est également fortement texturé et mécaniquement anisotrope. Par conséquent, la possible influence de cette anisotropie sur le chemin de déformation est analysée en utilisant (i) une loi de comportement isotrope, et (ii) une loi anisotrope basée sur le critère de Hill quadratique. L'intégration d'une loi adaptée pour la prédiction de dommages ainsi que le choix d'une loi de comportement appropriée dans le modèle numérique proposé conduisent à la possibilité d'analyser les conditions pour lesquelles les fissures peuvent se développer, et la recristallisation peut avoir lieu au moment des traitements thermiques.

Mots clés: aciers 9-14 % Cr, tube, laminage à pas de pèlerin, fatigue oligocyclique, loi de comportement, méthode des éléments finis, ODS, endommagement, fissures.

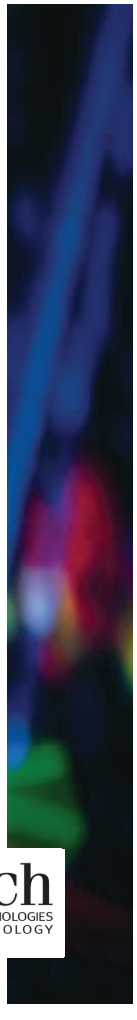

MINES ParisTech

ParisTech
INSTITUT DES SCIENCES ET TECHNOLOGIES
PARIS INSTITUTE OF TECHNOLOGY